Fabrication, Optical Analysis and Photonic Applications of Certain Metallic Nanostructure-Integrated Dye Doped Polymer Optical Fibers

Ph D Thesis submitted to

Cochin University of Science and Technology

In partial fulfilment of the requirements for the award of the Degree of

Doctor of Philosophy

Suneetha Sebastian

Reg. No: 4065

International School of Photonics
Cochin University of Science and Technology
Cochin -682022, Kerala, India

June 2015

Fabrication, Optical Analysis and Photonic Applications of Certain Metallic Nanostructure-Integrated Dye Doped Polymer Optical Fibers

Ph D thesis in the field of Photonics

Author:

Suneetha Sebastian
Research Fellow
International School of Photonics
Cochin University of Science & Technology
Cochin -682022, Kerala, India
sunikutty@gmail.com

Research Advisor:

Dr. M. Kailasnath
Assistant Professor
International School of Photonics
Cochin University of Science & Technology
Cochin -682022, Kerala, India
kailas@cusat.ac.in, mkailasnath@gmail.com

International School of Photonics
Cochin University of Science & Technology
Cochin -682022, Kerala, India
www.photonics.cusat.edu

June 2015

Cover images

Front page: Laser emission from polymer optical fiber doped with dyes and Ag nanosphere

Back page (photo courtesy to Amendola, Vincenzo, PhD Thesis): Laser ablation of Au nanoparticles using nanosecond pulsed laser at 1064nm.

Dedicated to dearest Daddy, Ichayan and rest of my family……

INTERNATIONAL SCHOOL OF PHOTONICS
COCHIN UNIVERSITY OF SCIENCE AND TECHNOLOGY
COCHIN -682022, KERALA, INDIA

Dr. M. Kailasnath
Assistant Professor

Certificate

This is to certify that the thesis entitled **"Fabrication, Optical Analysis and Photonic Applications of Certain Metallic Nanostructure-Integrated Dye Doped Polymer Optical Fibers"** submitted by **Ms. Suneetha Sebastian**, is a bonafide record of research work carried out by her under my guidance and supervision in partial fulfilment of the requirement of the degree of Doctor of Philosophy of Cochin University of Science and Technology, under the Faculty of Technology and has not been included in any other thesis submitted previously for the award of any degree.

Cochin-682022
23 - 06- 2015

Dr. M. Kailasnath
(Supervising guide)

Phone: +91 484 2575848 Fax: 0091-484-2576714.
Email: kailas@cusat.ac.in, mkailasnath@gmail.com

INTERNATIONAL SCHOOL OF PHOTONICS
COCHIN UNIVERSITY OF SCIENCE AND TECHNOLOGY
COCHIN -682022, KERALA, INDIA

Dr. M. Kailasnath
Assistant Professor

Certificate

This is to certify that the thesis entitled **"Fabrication, Optical Analysis and Photonic Applications of Certain Metallic Nanostructure-Integrated Dye Doped Polymer Optical Fibers"** submitted by **Ms. Suneetha Sebastian**, has incorporated all the relevant corrections and modifications suggested by the audience during the pre-synopsis seminar and recommended by the Doctoral Committee.

Cochin-682022
23- 06- 2015

Dr. M. Kailasnath
(Supervising guide)

Phone: +91 484 2575848 Fax: 0091-484-2576714.
Email: kailas@cusat.ac.in, mkailasnath@gmail.com

Declaration

I, Suneetha Sebastian, do hereby declare that the thesis entitled "**Fabrication, Optical Analysis and Photonic Applications of Certain Metallic Nanostructure-Integrated Dye Doped Polymer Optical Fibers**" is a genuine record of research work done by me under the supervision of Dr. M. Kailasnath, Assistant Professor, International School of Photonics, Cochin University of Science and Technology, Cochin–22, India and it has not been included in any other thesis submitted previously for the award of any degree.

Cochin- 682022 **Suneetha Sebastian**
22- 06- 2015

Acknowledgement

At the very outset, let me express my sincere thanks to my research supervisor Dr. M Kailasnath, who gave me an opportunity to start my research career at this famed department of Photonics. His untainted support and guidance throughout the work helped me for the completion of my research at CUSAT.

I gratefully remember the expertise advice of Prof. C.P Girijavallabhan during my work and his succor while writing the journal papers. According to him a top-notch paper is like a building made of bricks with little empty space. His vision on science and technology really inspired me all time in my work. I am fortunate enough to meet such a prominent person like him.

I would like to signify my regard to Prof. V.P.N Nampoori who always motivated me through his vast knowledge of science. His suggestions during the research really helped me to improve the quality of my work and thesis. I am also thankful to Prof. P Radhakrishnan for his good suggestions during the work and his undelayed review on journal papers and thesis.

I remember all the members of the department including office staffs who helped me in different capacities all throughout my career here. I also extend my sincere thanks to Murali Sir, Department of Instrumentation, for the realisation of research tools. I would also thank STIC CUSAT, Spectroscopy/ Analytical Test facility IISc and Centre for Nanoscience and Nanotechnology MG University for providing the facilities for sample characterisations.

Regarding my colleagues, both seniors and juniors, I have no words to express my gratitude. But for their selfless service I could not have finished my work. I will be failing in my duty if I do not mention the names of at least a few of them like Lins, Indu Chechy, Nideep Chettan, Roopa, Ajina, Divya, Sister Rosmin, Aparna Chechy,

Bejoy Chettan, Bobby Chettan, Mathew Chettan, Bini Chechy, Jessy, Jaison Chettan, Retheesh Chettan and Pradeep Chettan.

Before I conclude, may I express my most sincere gratitude from the bottom of my heart to God Almighty, my Daddy who always stood as a pillar in my life, my beloved and doting Ichayan, who always inspired me for the completion of my work, Lee Chettan and Jyotsna Chechy for their constant support, and last but not the least Mathu, Liya Chechy, Mosuttan, Babu Chettan, Jaicy Chechy, Jamon Chettan, Simi Chechy and all my loving family members for their unconditional love.

Suneetha Sebastian

List of Journal Publications

Suneetha Sebastian, Ajina C, C. P. G Vallabhan, V. P. N. Nampoori, P. Radhakrishnan, M. Kailasnath "Fabrication and Photostability of Rhodamine-6G Gold Nanoparticle Doped Polymer Optical Fiber" **CHIN. PHYS. LETT. Vol. 30, No. 11 (2013) 118101**

S Sebastian, C L Linslal, C P G Vallabhan, V P N Nampoori, P Radhakrishnan and M Kailasnath "Random lasing with enhanced photostability of silver nanoparticle doped polymer optical fiber laser" **Laser Phys. Lett. 11 (2014) 055108**

Suneetha Sebastian, C. Ajina, C.P.G. Vallabhan, V.P.N. Nampoori, P. Radhakrishnan, M. Kailasnath "Femtosecond laser induced emission enhancement in Rhodamine6G" **Journal of Photochemistry and Photobiology A: Chemistry 288 (2014) 34–38**

Suneetha Sebastian, C.L Linslal, C.P.G Vallbhan, V.P.N Nampoori, P Radhakrishnan, M Kailasnath "Laser Induced Augmentation of Silver Nanospheres to Nanowires in Ethanol Fostered by Poly Vinyl Pyrrolidone" **Applied Surface Science 320 (2014) 732–735**

Suneetha Sebastian, C.L Linslal, C.P.G Vallabhan, V.P.N Nampoori, P.Radhakrishnan, M Kailasnath "Formation of Au-Ag nanoalloy through Au core/Ag shell intermediate phase by laser ablation" **Chemical Physics Letters 628 (2015) 25–29**

Linslal, C. L., **S. Sebastian**, S. Mathew, P. Radhakrishnan, V. P. N. Nampoori, C. P. Girijavallabhan, and M. Kailasnath. "Microring embedded hollow polymer fiber laser." **Applied Physics Letters 106, no. 13 (2015): 131101**

Suneetha Sebastian, Sooraj S, Animesh Aaryan, Jaison Peter, V.P.N Namboori, C.P.G. Vallaban, P. Radhakrishnan, M. Kailasnath "Impact of laser ablated gold nanoparticles on absorption and fluorescence of Rhodamine6G in Methyl Methacrylate" **IEEE Optical Engineering special edition**

Suneetha Sebastian, Animesh Aaryan, SorajS, V.P.NNamboori and MKailasnath "Pulsed Laser Ablation in Methyl Methacrylate to Produce Spherical Gold Nanoparticles and Fluorescent Nanodots"**International Conference on Fiber Optics and Photonics,OSA2012**

.

List of Conferences

Suneetha Sebastian, V.P.N Nampoori, M Kailasnath "Lifetime reduction of Rhodamine6G doped in MMA solution by laser ablated silver nanoparticles" National Conference on Advanced Materials and Applications, April 04-05, 2013, NIT Trichy

Suneetha Sebastian, Ajina C, M Kailasnath "Fabrication of Gold Nanoparticle Doped Polymer Optical Fiber" National Seminar on Recent Trends in Conducting Polymers and Polymer Nano Structures, Cochin

Suneetha Sebastian, Joseph John, M Kailasnath "Curcumin Doped Polymer Optical Fiber" Indian Association of Physics Teachers Convention and Seminar, November 2-4, 2012, International School of Photonics, CUSAT, Cochin

Suneetha Sebastian, V.P.N Namboori, M Kailasnath "Quenching of Rhodamine 6G Doped Methyl Methacrylate Solution by Laser Ablated Silver Nanoparticles " National Laser Symposium, NLS-21, February 6-8, 2013, Bhabha Atomic Research Centre, Trombay, Mumbai, India

Suneetha Sebastian, Ajina C, M Kailasnath "Ultrashort pulse mediated ablation in liquid to spawn variable size silver nanoparticles" International Conference on Nano Materials: Science, Technology and Applications 2013 (ICNM'13)

Suneetha Sebastian, Linslal C.L, M Kailasnath "Ag nanoparticle mediated random lasing in polymer optical fiber laser" International Conference on Optics and Opto-Electronics (ICOL-2014), DRDO

List of Figures

Figure 1.1: Classification of Polymer Optical Fibers 3

Figure 1.2: Chemical structure of PMMA 3

Figure 1.3: Attenuation spectrum of PMMA showing different transmission windows 5

Figure 1.4: Schematic of conventional POF heat drawing process 7

Figure 1.5: Energy level diagram of dye laser.....8

Figure 1.6: Light trapped inside a spherical microcavity by total internal reflection....9

Figure 1.7: (a) First order WGM modes and (b) Second order WGM modes formed at 482nm inside microdisk 11

Figure 1.8: Absorption spectra of Au nanoparticles differing in size and shape.....12

Figure 1.9: Schematic of plasmon resonance taking place due to the coherent interaction.....13

Figure 1.10: Growth of nanoparticles inside the cavitation bubble during laser ablation 18

Figure 1.11: Pictorial representation of formation of nanoparticles.....18

Figure 2.1: (a) Experimental setup for Laser Ablation in Liquid and (b) Photograph showing the image of metal targets 30

Figure 2.2: Schematic of particle size analyser 33

Figure 2.3: Amplitude of autocorrelation function with respect to the delay time.....34

Figure 2.4: Experimental setup for coherent back scattering 35

Figure 2.5: Schematic of conventional POF drawing tower.....36

Figure 2.6: Experimental setup for lasing from POFs.....38

Figure 2.7: Experimental setup for Spontaneous Raman Scattering 39

Figure 3.1: (A) Optical extinction spectra and (B) Normalised extinction spectra of Au nanoparticles.....43

Figure 3.2: (A) Optical absorption spectra and (B) Normalised extinction spectra of Ag nanoparticles.....44

Figure 3.3: Photograph showing the colour of (A) Au nanoparticles and (B) Ag nanoparticles.....44

Figure 3.4: (A) Representative TEM image of Au nanoparticles in MMA (B) High Resolution TEM image (C) Size distribution of nanoparticles and (D) EDS of Au nanoparticles.....45

Figure 3.5: (A) TEM image of Ag nanoparticles in MMA and (B) High Resolution TEM (C) Histogram (D) EDS. 46

Figure 3.6: Formation of electrical double layer on the surface of nanoparticle.....47

Figure 3.7: Dipole moment Vs. FWHM and maximum optical extinction of Au nanoparticles in different environment.....48

Figure 3.8: Relative abundance of Au nanoparticles generated in different liquid environment.....49

Figure 3.9: (A) Optical absorption spectra of Au nanoparticles produced by LAL in water at different wavelength and (B) Normalised extinction spectra 50

Figure 3.10: (A) Optical extinction of Ag nanoparticles produced in water at different wavelength and (B) Normalised extinction spectra.....52

Figure 3.11: (A) Optical absorption spectra of Au nanoparticles produced in water at different laser energy (B) Plot of ablated mass in gram vs. laser energy 53

Figure 3.12: Abundance of Au nanoparticles produced in MMA with respect to number of laser shots.....54

Figure 3.13: Full width at half maximum of Au nanoparticles produced in different volume of MMA.....54

Figure 3.14: Schematic of the experimental setup for laser ablation using fs laser pulses.....55

Figure 3.15: Optical extinction spectra of Ag nanoparticles in ethanol produced by positioning the target above and below the focal plane of the lens.....56

Figure 4.1: Molecular orbital schematic for resonance energy transfer 65

Figure 4.2: Experimental setup for photostability and LIF measurements.....67

Figure 4.3: (A) Representative TEM image of Au nanoparticles produced in Rh6G doped MMA solution (B) HRTEM image (C) Particle size distribution (D) EDS 68

Figure 4.4: Extinction spectra showing the plasmon band of Au nanoparticles produced in (a) MMA (b) Rh6G doped MMA solution.....69

Figure 4.5: (A) Optical extinction and (B) emission spectra of Rh6G in the absence and presence of Au nanoparticles formed directly in the solution 69

Figure 4.6: Optical extinction spectra of Au nanoparticles produced in MMA at different concentrations.....70

Figure 4.7: (A) Spectral absorption and (B) Emission of Rh6G-Au nanoparticle system in MMA.....70

Figure 4.8: Spectral overlap between (a) plasmon absorption band of Au nanoparticles and (b) emission band of Rh6G.....71

Figure 4.9: Decay curves of Rh6G doped MMA solution in the absence and presence of laser ablated gold nanoparticles 73

Figure 4.10: Absorbance versus integrated fluorescence intensity of Rh6G (A) in water and (B) in MMA.....74

Figure 4.11: Optical absorption of the plasmon band of Au nanoparticles (a) in MMA (b) in PMMA.....77

Figure 4.12: LIF of Rh6G in PMMA film with and without Au nanoparticles.....78

Figure 4.13: Photostability of Rh6G-Au nanoparticle based POFs 78

Figure 4.14: Emission from polymer fiber containing (A) Rh6G only (B) Rh6G-Au nanoparticles in the gain medium.....79

Figure 4.15: Photograph of Au nanoparticles doped hollow fiber.....80

Figure 4.16: Emission spectra of (A) Hollow fiber filled with Rh6G (B) Au doped hollow fiber filled with Rh6G 81

Figure 5.1: Interaction of metal nanoparticle with incident electric field.....86

Figure 5.2: Modified Jablonski diagram which includes metal–fluorophore interactions. 87

Figure 5.3: Schematic of the experimental setup for lasing from polymer fibers 89

Figure 5.4: (A) Optical absorption spectra and (B) Emission spectra of Rh6G in the presence and absence of Ag nanoparticles in MMA 89

Figure 5.5: Spectral overlap between the absorption spectra of Ag nanoparticles and emission spectra of Rh6G.....90

Figure 5.6: Ratio of intensity of Rh6G in the presence and absence of acceptor with respect to the concentration of Ag nanoparticles.....91

Figure 5.7: (A) Optical absorption and (B) Emission spectra of Rh6G in the absence and presence of Ag nanoparticles produced in ethanol by fs laser.....93

Figure 5.8: Time resolved fluorescence spectra of (a) Rh6G alone (b) Rh6G containing Ag nanoparticles produced in ethanol by fs laser.....94

Figure 5.9: Enhancement factor of the emission with respect to the concentration of the dye at fixed concentration of Ag nanoparticles 95

Figure 5.10: (A) and (B) Representative TEM image of Ag nanoparticles generated in ethanol by nanosecond laser (C) Histogram.....96

Figure 5.11: Spectral emission of cylindrical rods of Rh6G in the absence and presence of Ag nanoparticles.....97

Figure 5.12: (A) Spectral emission and (B) Normalised emission spectra of fibers ..98

Figure 5.13: Emission intensity vs pump energy of fibers R_1, R_2, R_3 and R_4.....98

Figure 5.14: Evolution of linewidth with energy of the pumping laser.....99

Figure 5.15: Emission spectra of R_4 with varying pump energy 100

Figure 5.16: Emission spectra of R4 fibers when pumped 100

Figure 5.17: Lasing of fiber R_4 collected from the surface of the fiber.....101

Figure 5.18: Photostability curves of pure Rh6G doped polymer optical fiber and Rh6G–Ag nanoparticle doped POF 102

Figure 6.1: Chemical structure of Poly Vinyl Pyrrolidone.....109

Figure 6.2: Optical absorption spectra of Ag nanoparticles produced in pure ethanol and in ethanolic solution of PVP of various concentrations.....110

Figure 6.3: (A)Representative TEM image of Ag nanoparticles in ethanolic solution of PVP (B) HRTEM (C) SAED pattern and (D) Histogram 111

Figure 6.4: Optical absorption spectra of Au nanoparticles generated in ethanol and ethanol containing PVP 112

Figure 6.5: (A) TEM image of Au nanoparticles produced in 0.6mM PVP solution. And (B) Histogram 113

Figure 6.6: Optical absorption spectra of (a) physical mixture of Au and Ag and (b) core-shell bimetallic nanostructure produced by irradiating the physical mixture.....114

Figure 6.7: Image showing the colour of Au nanoparticles, Ag nanoparticles and alloy of AuAg in PVP solvent 115

Figure 6.8: (A) Optical absorption spectra showing the formation of Au-Ag nanoalloy and (B) Peak position of alloy plasmon band against the mole fraction of Ag 115

Figure 6.9: Representative TEM image of (A) Au core/Ag shell nanocomposites (B) Magnified image of core/shell structure (C) Lattice image of Ag shell and (D) Size distribution carried out on TEM images of Au core/Ag shell nanocomposites.....117

Figure 6.10: Schematic of the formation of core/shell and alloy of Au-Ag nanoparticles.....118

Figure 6.11: (A) Representative TEM image of Au-Ag alloy nanostructure formed by ablating Ag and (B) HRTEM (C) Size distribution and (D) EDS pattern. 119

Figure 6.12: Emission spectra of 5 cm long fiber containing (A) Rh6G only (B) Rh6G-Ag nanoparticles 120

Figure 6.13: (A) Linewidth of the emission spectrum for different samples with varying pump energy (B) Integrated intensity of emission of different POFs 121

Figure 6.14: (A) WGM lasing from Au core/Ag shell incorporated POFs with varying pump energy and (B) enlarged version of WGM lasing.....122

Figure 6.15: Photostability of POFs recorded with respect to pulse count.....123

Figure 6.16: Lasing emission from (A) Bare Rh6G doped POF and (B) Rh6G-Au-Ag nanoalloy doped POFs 124

Figure 7.1: Schematic for the irradiation of Rh6G 130

Figure 7.2: Molecular structure of Rh6G 131

Figure 7.3: Peak fluorescence intensity of Rh6G vs. Irradiation time of the dye. 132

Figure 7.4: The difference in peak fluorescence intensity between the non-irradiated sample and 5 min irradiated samples vs. concentration of the dye.....133

Figure 7.5: Variation of fluorescence intensity with pump power density. 0W/cm^2 corresponds to the fluorescence intensity of non-irradiated sample.....133

Figure 7.6: (A) Optical absorption spectra of Rh6G before and after irradiation with fs laser pulses and (B) Width of absorption band of dye is plotted as a function of irradiation time. 134

Figure 7.7: FTIR spectra of non-irradiated and irradiated Rh6G in MMA by fs laser pulses 135

Figure 7.8: Time resolved fluorescence spectra of modified Rh6G 136

Figure 7.9: (A) Emission spectra and (B) Absorption spectra of Rh6G in MMA irradiated by ns laser at various time intervals 138

Figure 7.10: FTIR spectra of Rh6G irradiated by ns laser.....139

Figure 7.11: (A) Lasing emission from pure Rh6G doped POF and modified Rh6G doped POFs and (B) WGM lasing from modified Rh6G doped POF 139

Figure 7.12: Emission of fibers containing (a) modified Rh6G and (b) pure Rh6G with respect to log of pump energy. 140

Figure 7.13: Photostability curves of modified as well as pure Rh6G doped POFs..141

Figure 8.1: Schematic representation of Ag nanowires (A) Inside and (B) Outside the polymer preforms 148

Figure 8.2: (A) Particle size distribution of Ag nanoparticles generated in ethanolic solution of PVP (B) Auto correlation function g2(T) vs. delay time 148

Figure 8.3: (A) Optical absorption spectra of Ag nanoparticles in ethanolic solution of PVP recorded after irradiation using xenon lamp and (B) Position and FWHM of plasmon band with respect to irradiation time.....149

Figure 8.4: Representative TEM images of Ag nanoparticles (A) Irradiated by xenon lamp for 7h (B) Magnified image and (C) SAED pattern 149

Figure 8.5: Plasmon absorption band of Ag nanocolloids (a) generated by laser ablation (b) nanocolloids irradiated by 532nm for 45min (c) for 9h (d) for 18h.....150

Figure 8.6: (A) TEM image of nanocolloids irradiated for 45 minutes by ns laser pulses at 532nm and (B) Distribution of nanoparticles 151

Figure 8.7: TEM image of Ag nanoparticles irradiated by laser pulses for 9 hours (A) assembly of unstable nanoparticles via laser radiation and (B) Enlarged view.....151

Figure 8.8: TEM images of Ag nanocolloids irradiated for 18 h (A) Ag nanowires formed through ripening mechanism (B) Cross section of the nanowires (C) Aspect ratio distribution and (D) SAED pattern.....152

Figure 8.9: Photograph of the Ag colloidal solution before and after irradiation.....153

Figure 8.10: Optical absorption spectra of Ag nanowires dispersed in 2-propanol...154

Figure 8.11: (A) Representative TEM image of Ag nanowires and (B) HRTEM....154

Figure 8.12: Coherent back scattering cones obtained from Ag nanowires 155

Figure 8.13:Lasing obtained from Rh6G in MMA solution (A) without Ag nanowires and (B) with 0.032M Ag nanowires 157

Figure 8.14: Time resolved fluorescence spectra of Rh6G doped polymer rods with and without Ag nanowires.....158

Figure 8.15: Electric field distribution at wavelength of 350nm calculated for (A) Ag nanowire and (B) Ag nanospheres.....159

Figure 8.16: SEM image of a portion of POF containing Ag nanowires 160

Figure 8.17: Distribution of the electric field intensity normalized by the incoming field near the pure Ag nanowires 161

Figure 8.18: Integrated emission intensity of fibers as a log function of pump energy 161

Figure 8.19: WGM lasing from (A) Ag nanowire doped POF lasers and (B) Bare dye doped POFs 162

Figure 8.20: Lasing emission from (a) bare Rh6G doped POFs and (b) Ag nanowires outside bare dye doped POFs 163

Figure 8.21: Photostability curves of Rh6G doped POFs in the presence and absence of Ag nanowires. 164

Figure 8.22: Recorded Raman spectra of POF 164

Figure 8.23: Variation of Raman intensity at 2957cm^{-1} with diameter of the polymer fiber 165

Figure 8.24: (A) Raman scattering intensity of PMMA POFs (a) normal Raman (b) SERS in the presence of Ag nanowires and (B) Enhancement factor of SERS with respect to concentration of Ag nanowires 167

Figure 8.25: Raman scattering of PMMA rods (a) in the absence and in the presence of (b) Ag nanowires.....167

List of Tables

Table 1.1:Properties of PMMA 4

Table 1.2:Bulk properties of Ag and Au.....12

Table 3.1:Variation of peak of SPR band, bandwidth and mass ablated from the plate during ablation of Au and Ag nanoparticles in different liquid media. 49

Table 3.2:Variation of particle size with laser wavelength.....52

Table 3.3:Variation of position of plasmon band, bandwidth and particle size with target position 58

Table 4.1:Sample designation, concentration of dye and concentration of Au nanoparticles.....66

Table 4.2:Time-resolved quenching studies of Rh6G containing different concentration of Au nanoparticles.....73

Table 4.3:Variation of spectral overlap, Förster distance, lifetime, QY and transfer efficiency with respect to gold nanoparticle concentration 76

Table 5.1:Variation of efficiency of energy transfer between Rh6G and Ag nanoparticles and QY of the dye with varying concentration of Ag nanoparticles 91

Table 5.2:Concentration of Rh6G and Ag nanoparticles with corresponding enhancement factor of emission 97

Table 6.1:Variation of plasmon band position and width, ablated mass of Ag nanoparticles with respect to PVP concentration in ethanol 112

Table 7.1:Variation of QY, lifetime, radiative and non-radiative decay rate of modified Rh6G 137

Table 8.1:Multi exponential analysis of intensity decay of Rh6G doped polymer rods with and without Ag nanowires 158

Table 8.2:Quantum yield (QY), radiative decay rate and non-radiative decay rate of Rh6G in the presence and absence of Ag nanowires.....159

CONTENTS

Preface

Chapter 1 : Overview on Polymer Optical Fibers and Metal Nanoparticles

1.1 Introduction to Polymer Optical Fibers 1

1.2 Fabrication of POFs 5

1.2.1 Extrusion method 5

1.2.2 Preform drawing method 5

1.3 Dye doped POFs 7

1.3.1 Whispering Gallery Resonators and modes 8

1.4 Introduction to metal nanoparticles 11

1.4.1 Surface Plasmon Resonance 13

1.4.2 Mie theory 13

1.4.3 Applications of metal nanoparticles 15

1.5 Method of synthesis of metal nanoparticles 16

1.5.1 Chemical reduction method 16

1.5.2 Physical method 17

1.6 Scope of the thesis 20

Chapter 2 : Fabrication and characterisation tools of metal nanoparticles and polymer fibers

2.1 Preparation of metal nanoparticles by laser ablation 30

2.2 Characterisation of metal nanoparticles 31

2.2.1 Absorption spectrograph 31

2.2.2 Photoluminescence Spectrograph 31

2.2.3 Transmission Electron Microscopy 31

2.2.4 Time Resolved Fluorescence Spectroscopy 32

2.2.5 Scanning Electron Microscopy 32

2.2.6 Fourier Transform Infra Red Spectroscopy (FTIR) 32

2.2.7 Particle size analyzer 32
2.2.8 High Resolution Raman Spectroscopy 34
2.2.9 Coherent back scattering 34
2.3 Fabrication and characterisation of POFs.....35
2.3.1 Preform fabrication.....35
2.3.2 Fiber drawing.....36
2.3.3 Attenuation measurement using cut-back method.....37
2.3.4 Lasing and photostability study of optical fibers.....37
2.3.5 Spontaneous Raman Scattering from POFs.....38

Chapter 3 : Generation of Metallic Nanoparticles by Laser Ablation-Effect of experimental parameters

3.1 Introduction 42
3.2 Experimental Section.....42
3.3 Result and Discussions 43
3.3.1 Effect of generation media on the SPR tunability of metal nanoparticles.....43
3.3.2 Effect of laser wavelength 50
3.3.3 Effect of energy of laser pulses 52
3.3.4 Effect of number of laser shots.....53
3.3.5 Effect of volume of liquid media.....54
3.3.6 Effect of pulse width 55
3.4 Conclusions 58

Chapter 4 : Effect of Au nanoparticles on the optical properties of laser dye

4.1 Introduction 63
4.2 Experimental Section.....65
4.3 Result and Discussions 67
4.3.1 Optical characterisation of Rh6G-Au nanoparticle system 67
4.3.1.1 Optical absorption spectroscopy, fluorescence spectroscopy and TEM...67

4.3.1.2 Time- Resolved Fluorescence Spectroscopy 72
4.3.1.3 Quantum yield of Rh6G and Rh6G-Au nanoparticles in MMA.....74
4.3.1.4 Calculation of Overlap integral, Förster distance and Transfer efficiency 75
4.3.2 Optical properties of Rh6G-Au nanoparticle based planar waveguide 76
4.3.3 Rh6G-Au nanoparticles based cylindrical waveguides 78
4.3.4 Lasing from Au doped hollow POFs filled with Rh6G 80
4.4 Conclusions 81

Chapter 5 : Impact of Silver Nanoparticles on Dye Doped Polymer Optical Fibers

5.1 Introduction 86
5.1.1 Metal Enhanced Fluorescence 86
5.1.2 Nanomaterial Surface Energy Transfer 87
5.2 Experimental Section.....88
5.3 Result and discussions.....89
5.3.1 Fluorescence quenching by Ag nanoparticles by NSET 89
5.3.2 Metal Enhanced Fluorescence by Ag nanoparticles.....92
5.3.3 MEF by Ag nanoparticles in ethanol produced by ns laser 96
5.3.4 Application of MEF in POFs.....96
5.4 Conclusions 102

Chapter 6 : Synthesis of Au-Ag core/shell and alloy nanostructures for metal enhanced fluorescence applications

6.1 Introduction 108
6.2 Experimental Section.....109
6.3 Results and Discussions 109
6.3.1 Formation of Ag nanoparticles in ethanolic solution of PVP.....109
6.3.2 Formation of Au nanoparticles in PVP solution.....112
6.3.3 Formation of Au-Ag core/shell nanostructure by laser irradiation.....113

6.3.4 Formation of Au-Ag alloy through Au core/Ag shell intermediate phase in ethanolic solution of PVP by ablation 115
6.3.5 Formation of Au-Ag nanoalloy in ethanol by laser ablation 119
6.3.6 Application of bimetallic nanostructures in MEF 120
6.4 Conclusions 124

Chapter 7 : Structural modification of Rhodamoine6G under femtosecond laser irradiation

7.1 Introduction 130
7.2 Experimental section 130
7.3 Results and Discussions..... .135
7.3.1 Irradiation using femtosecond laser pulses.....131
7.3.1.1 Effect of irradiation time 132
7.3.1.2 Effect of concentration of the dye 133
7.3.1.3 Effect of distance from the focal point (Z) 133
7.3.1.4 Structural modifications in Rh6G.....134
7.3.2 Irradiation using Nd-YAG laser 137
7.3.3 Lasing properties and photostability of modified Rh6G in POFs 139
7.4 Conclusions..... 160

Chapter 8 : Formation of Ag nanowires from nanospheres- its Applications in lasing and SERS

8.1 Introduction 146
8.2 Experimental Section.....147
8.3 Results and Discussions 148
8.3.1 Post-irradiation of Ag nanospheres using Xenon lamp 148
8.3.2 Post irradiation of Ag nanospheres using 532nm laser pulses.....150
8.3.3 Optical characterisation of Ag nanowires dispersed in 2-propanol.....154
8.3.4 Ag nanowires doped polymer rods and polymer fibers.....157
8.3.4.1 Surface Enahnced Raman Scattering of PMMA 164

8.4 Conclusions 168

Chapter 9 : General conclusions and future prospects.....175

Appendix : 179

Preface

Polymer Optical Fibers have occupied historically a place for large core flexible fibers operating in short distances. In addition to their practical passive application in short-haul communication they constitute a potential research field as active devices with organic dopants. Organic dyes are preferred as dopants over organic semiconductors due to their higher optical cross section. Thus organic dyes as gain media in a polymer fiber is used to develop efficient and narrow laser sources with a tunability throughout the visible region or optical amplifier with high gain. Dyes incorporated in fiber form has added advantage over other solid state forms such as films since the pump power required to excite the molecules in the core of the fiber is less thereby utilising the pump power effectively. In 1987, Muto et.al investigated a dye doped step index polymer fiber laser. Afterwards, numerous researches have been carried out in this area demonstrating laser emission from step index, graded index and hollow optical fibers incorporating various dyes. Among various dyes, Rhodamine6G is the most widely and commonly used laser dye for the last four decades. Rhodamine6G has many desirable optical properties which make it preferable over other organic dyes such as Coumarin, Nile Blue, Curcumin etc. The research focus on the implementation of efficient fiber lasers and amplifiers for short fiber distances.

Developing efficient plastic lasers with electrical pumping can be a new proposal in this field which demands lowest possible threshold pump energy of the gain medium in the cavity as an important parameter. One way of improving the efficiency of the lasers, through low threshold pump energy, is by modifying the gain of the amplifiers in the resonator/cavity. Success in the field of Radiative Decay Engineering can pave way to this problem. Laser gain media consisting of dye-nanoparticle composites can improve the efficiency by lowering the lasing threshold and enhancing the photostability. The electric field confined near the surface of metal nanoparticles due to Localized Surface Plasmon Resonance can be very effective for the excitation of active centers to impart high optical gain for lasing. Since the Surface Plasmon Resonance of nanoparticles of gold and silver lies in the visible range, it can affect the spectral emission characteristics of organic dyes such as Rhodamine6G through plasmon field generated by the particles. The change in emission of the dye placed near metal nanoparticles depend on plasmon field strength which in turn depends on the type of metal, size of nanoparticle, surface modification of the particle and the wavelength of incident light. Progress in fabrication of different types of nanostructures lead to the advent of nanospheres, nanoalloys, core-shell and nanowires to name a few. The thesis deals with the fabrication and characterisation of polymer optical fibers with various metallic and bimetallic nanostructures incorporated in the gain media for efficient fiber lasers with low threshold and improved photostability.

Chapter 1: Gives a basic idea about Polymer Optical Fibers and potential application of dye doped optical fibers. Glimpse on the laser cavity supported by optical fibers are discussed. Since plasmon resonance of metal nanoparticles can affect the spectral properties of gain medium in a cavity, a brief idea about the plasmon field generated on the surface of metal nanoparticles is considered. Various applications of metal nanoparticles are discussed with focus on its application in Radiative Decay Engineering and Surface Enhanced Raman Scattering.

Chapter 2: Experimental setup used for the fabrication of metallic nanostructures by physical method is detailed in this chapter. Also the chapter overviews various characterisation techniques, used to investigate and characterise the nanostructures, in brief. Fabrication of polymer optical fibers doped with dyes and nanoparticles are also detailed. Experimental setups used to characterise the fiber lasers are described along with the setup for Raman scattering of polymer fibers.

Chapter 3: Chapter gives an idea about various advantages of physical method like laser ablation in liquid over chemical method of synthesis of nanostructures. Optimisation of various parameters affecting the size and shape of nanostructures during laser ablation is an important step towards its practical applications. So the chapter deals with those parameters such as carrier media, wavelength of laser source, pulse counts, fluence at the target, volume of the liquid media and pulse width influencing the formation of nanostructures. Optical characteristics of the nanostructures synthesised are also discussed.

Chapter 4: Gold nanoparticles affect the spectral characteristics of dyes like Rhodamine6G. The chapter gives a complete analysis of the variation of spectral absorption, emission, lifetime and quantum yield of the dye in the presence of Au nanoparticles. Spectral overlap integral, Forster distance and efficiency of the system are also calculated. With these inferences the system of dye-nanoparticles are polymerised into planar waveguides and their optical emission spectra are recorded. Polymer fibers with Au nanoparticle integrated gain medium are heat drawn and its optical characterisations are done.

Chapter 5: Silver nanoparticles have the highest surface plasmon strength among other metal nanoparticles and are widely used in Radiative Decay Engineering. The environment of the nanoparticles plays an important role in determining spectral characteristics of the dye. So the optical properties of dye in presence of Ag nanoparticles synthesised in Methyl Methacrylate and ethanol are studied. The spectral emission and photostability studies of optical fibers doped with dye-Ag nanoparticles system have been discussed.

Chapter 6: Various applications in the field of nanotechnology demand the synthesis of various bimetallic nanostructures such as nanoalloys and core/shell nanostructures. In this chapter we introduce a simple method for the synthesis of Au-Ag nanoalloy through the intermediate phase of Au core/Ag shell nanostructures by direct laser ablation and its optical characterisations are done. Core/shell and alloy nanostructures are integrated into polymer optical fiber based lasers and its lasing and photostability measurements are recorded.

Chapter 7: The intense electric field of femtosecond pulses can cause bond breaking and rearrangement of molecular structure in many systems. We have systematically studied the effect of time of irradiation, pump power density and concentration of Rhodamine6G upon irradiation on its optical properties. Optical characterisation is done using optical absorption spectra and FTIR spectra. Rhodamine6G is also irradiated using nanosecond pulsed laser and its optical characterisations have also been done. We have also demonstrated lasing properties of polymer fibers doped structurally modified Rhodamine6G in this chapter.

Chapter8: The chapter deals with the formation of well defined nanowires by laser induced irradiation of already prepared Ag nanocolloidal solution containing nanospheres. Scattering strength of Ag nanowires has been calculated from mean free path. Metal Enhanced Fluorescence using Ag nanowires has been demonstrated and its practical applications in lasing have been discussed. Surface Enhanced Raman Scattering studies on polymer optical fibers doped with Ag nanowires is also performed.

Chapter 9: Work performed in this thesis are concluded and summarised in this chapter and future prospects are discussed.

Chapter 1:

Overview on Polymer Optical Fibers and Metal Nanoparticles

An overview of polymer optical fibers mainly emphasising on the properties of Poly Methyl Methacrylate based polymer fibers are discussed along with its method of fabrication. Characteristics of dye doped polymer fiber lasers with special mention to whispering gallery resonators are presented. Noble metal nanoparticles are introduced with a few of its applications and preparation methods along with a theoretical aspect of formation of metal nanoparticles using laser ablation in liquid technique.

1.1 Introduction to Polymer Optical Fibers

The term 'optical fiber' in general gives us an idea of silica fibers which is most widely used in data communication and sensing. But apart from these glass fibers there exists a prominent class of plastic/polymer fibers which, apart from its high attenuation and low bandwidth as compared to the former, is widely used in Local Area Networks and sensors. The development of Polymer Optical Fibers (POFs) started at the middle of 20^{th} century when it was first introduced by DuPont in the mid 1960s. Progress in the field of POFs after its introduction [1-2] has brought down the attenuation considerably. Currently Poly Methyl Methacrylate (PMMA) based POFs typically has attenuation in the range of 80 to 120dB/km in the transmission window (visible region) [3]. With the development of fluorinated polymer, which has excellent chemical, thermal, electrical and surface properties, further reduction of attenuation in polymer based fibers is achieved [4-5].

Advantages of POFs

Major advantages of POFs over silica fibers are high mechanical resilience, high numerical aperture, low bending loss, ease of tooling, use of visible light as sources, easy installation, water resistance and doping with organic compounds. Inherent property of flexibility of plastic as compared to glass allows the rough handling of plastic fibers such as acute bending and stressing. Due to large numerical aperture, certain mismatch occurring while aligning with transmitters and receivers avoids the use of expensive precision tools for connectorization. Large core diameter of POFs (nearly 1mm) permits certain bending tolerance as compared to silica fibers and installation of fibers can be done at a better rate with low cost and less skill. Plastic fibers can be cut using conventional scissors or blades and polishing can be done using sand papers. Plastic fibers making use of PMMA allows the use of sources in the visible spectral region because of its transmission window in the visible range. POFs due to its water resistance property are thus suitable for marine applications. Low processing temperature of POFs as compared to silica fibers allows quantum dots, nanoparticles and organic compounds to survive the fiber drawing process without degradation [6].

Classification of POFs

POFs can be categorised on the basis of specific material and refractive index profile for several applications as given in fig.1.1. The type of material selected essentially determines the attenuation and the thermal stability of the fiber, whereas the optical bandwidth/transmission capacity is solely determined by the type of profile such as step index (SI) or graded index (GI). Two main classes of POFs based on material are PMMA based fibers and perfluorinated fibers. Fig 1.2 shows the chemical structure of PMMA. Attenuation of PMMA based fibers (~150dB/km) is due to the

presence of CH bonds which causes overtone absorption corresponding to their stretching vibrational mode in the visible wavelength region [7].

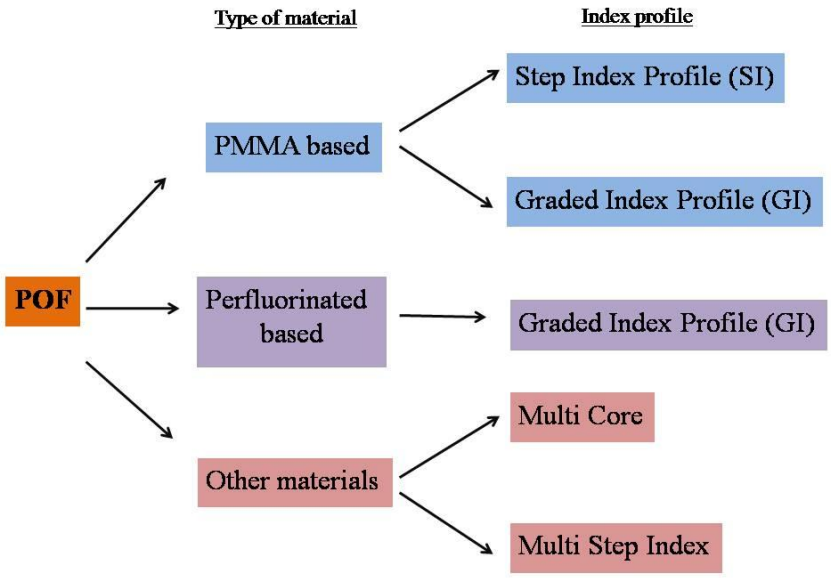

Figure 1.1: Classification of Polymer Optical Fibers.

The most effective way of reducing attenuation is the replacement of hydrogen atoms in the fiber material by heavier atoms like fluorine [8-9]. Thus perfluorinated fibers reduce attenuation arising from CH stretching vibrations of PMMA POFs. CYTOP (Cyclic Transparent Optical Fiber, which is a perfluorinated polymer fiber) offers low attenuation upto 40dB/km at 650nm, 16dB/km at 850nm and 20dB/km at 1300nm [10].

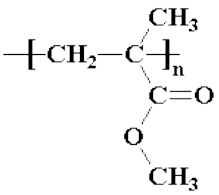

Figure 1.2: Chemical structure of PMMA.

Other two major types of POFs based on refractive index profile are SI and GI POFs. SI POFs are characterised by a constant uniform core refractive index which is greater than that of cladding and the refractive index drops sharply at the interface. GI POFs exhibit a gradient refractive index profile with maximum index near the core centre

and decreases gradually towards the cladding. SI POFs exhibits bit rate of 500 Mbps (in a 100m length) whereas the GI POFs exihibits 10 Gbps [11]. The fabrication method is different for different types of fibers and SI POFs are easier to fabricate. SI POFs find applications in automotive and industrial applications where bandwidth requirement is less.

Third type of POFs includes multi core and multi step index POFs which overcome the bending sensitivity, manufacturing cost and difficulty of GI POFs. Another promising class of POFs which find tremendous current applications is Microstructured POFs (MPOFs). MPOF/Photonic Crystal Fibers (PCF) obtains their waveguide property from a closely spaced arrangement of air holes which runs throughout the fiber length. Air holes form an internal microstructure within the fiber which provides another dimension of light control [12]. Novel features associated with MPOFs are endlessly single mode nature, tailorizable dispersion and high or low non-linearity (depending on the hole design) [13].

Among the various types of POFs, PMMA POFs has received considerable attention in this category. Certain physical, electrical, optical and thermal properties of PMMA are listed in table.1.1. PMMA is a transparent polar material with a refractive index of 1.49. PMMA absorbs very little light in the visible region with a transmission of 80-93% as its transmission window lies in the visible region. It has a glass transition temperature at 105^0C and a melting point at 130^0C. From the attenuation plot of PMMA with respect to the wavelength as shown in fig.1.3, it can be seen that green and blue windows are characterised by the lowest attenuation of nearly 80dB/km [6].

Table 1.1: Properties of PMMA.

Properties	**Value**
Density	1.15 - 1.19 g/cm3
Melt Flow	0.9 – 27 g/10 min
Water absorptivity	0.3%
Dielectric Constant	2.8 - 4
Melting Point	130°C
Glass transition temperature	100 - 105 °C
Vicat Softening Point	47 - 117 °C
Haze	1 - 96 %
Transmission, Visible	80 - 93 %
Refractive Index	1.49 - 1.498

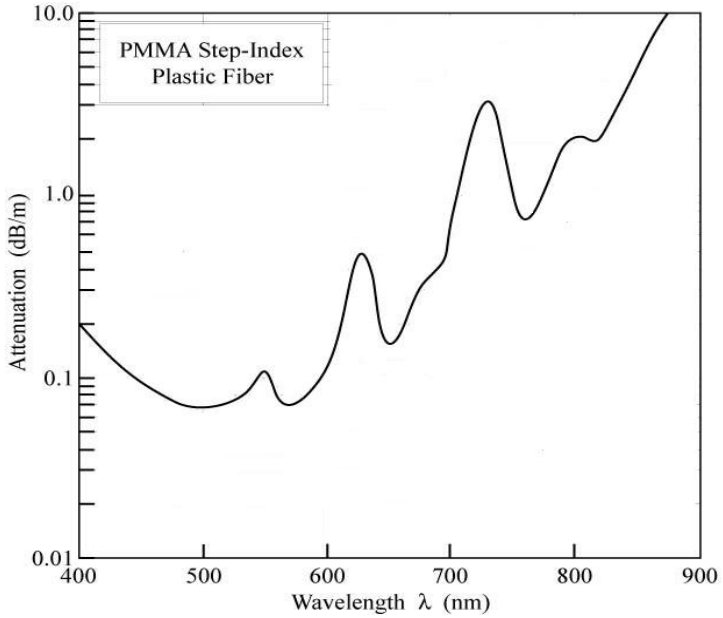

Figure 1.3: Attenuation spectrum of PMMA showing different transmission windows.

1.2 Fabrication of POFs

PMMA, which is the most common material for core of POFs are fabricated mainly using two methods, extrusion method and preform drawing method [14-16].

1.2.1 Extrusion method

This can be either continuous or batch extrusion types. The former is an efficient method for the fabrication of SI POF since the method eliminates the extrinsic loss factors from the fiber caused by organic impurities, dust or bubbles in the fiber core. This method makes use of a single system, from the initial step of monomer purification to the final process of fiber drawing. Monomer such as Methyl Methacrylate (MMA) with polymerisation initiator and chain transfer agents (CTA) are continuously fed into the reactor followed by gear pumping from the reactor to the core extruder at typical reactor temperature of 180^0C [14]. The fiber core is immediately cladded with another polymer of lower refractive index through another extruder. Thus SI POFs are obtained with high production rate. But this method suffers from thermal degradation of the materials used for the extrusion.

1.2.2 Preform drawing method

The method involves two steps, viz., preform fabrication and fiber drawing. The former involves the production of a transparent cylindrical rod and the latter is followed by its drawing into optical fibers.

1.2.2.1 Preform fabrication

There are several methods for preform fabrication in the case of glass fibers such as Chemical Vapour Deposition (CVD), Outside Vapour Deposition (OVD), photo co-polymerisation, diffusion and Vapour Phase Axial Deposition (VAD) [15]. In the case of POFs fabrication, one of the promising method is Teflon technique [17]. The method involves the fixation of a smooth teflon rod of desirable diameter at the centre of a test tube and filling the rest of the test tube with purified monomer, initiator and chain CTA. Suitable initiators like Benzoyl Peroxide (BPO) or Azobisisobutyronitrile (AIBN) are used to start the polymerisation process. BPO is preferred over AIBN since in the former case no gas such as nitrogen is released during polymerisation thus avoiding of bubbles in the preform [17]. Initiation process is followed by termination in order to control the molecular weight of the polymer. Thus along with the initiator, CTA such as n-butyl mercaptan is added to regulate and terminate the polymerisation process. With an appropriate combination of initiator and CTA, the molecular weight and thereby the thermal and mechanical stability of the drawn fibers can be controlled [17]. Moreover the amount of initiator and CTA determines the speed of polymerisation of MMA at a particular temperature. It is reported on the basis of material characterisation and drawing tests that a readily drawable preform has a glass transition temperature Tg around 100^0C and average molecular weight in between 60000 and 100000[17]. In the case PMMA Tg lies around 105^0C.

The test tube is then placed in a constant temperature oil bath for thermal polymerisation. When polymerisation is over, the teflon rod is removed from the test tube obtaining a hollow preform which serves as the cladding. Now the hollow portion is filled with monomer of higher refractive index and a second polymerisation is done. When polymerisation is complete, a step index polymer preform is obtained. The major advantage of the technique is that it gives a good core-cladding interface thereby reducing losses due to scattering [18].

1.2.2.2 Fiber drawing

Preforms thus obtained are drawn using conventional POF drawing tower and the drawing process is schematically depicted in fig.1.4. The preform is held vertically using a preform holder and is placed at the middle of the furnace leaving behind a small portion of the preform unheated. Processing temperature of POFs are around 200^0C whereas silica fibers have high processing temperature around 1200^0C. When the heated portion of the preform reaches beyond its softening point, it tumbles down due to gravity. Once the preform is pulled down by its own weight, the drawing is thereafter controlled by fiber puller and feeder. For a given preform, the diameter of the fibers can be varied by controlling the draw rate and feed rate using [18] the equation

$$\frac{D^2}{d^2} = \frac{V_d}{V_f} \tag{1.1}$$

where D is the diameter of the preform, d is the diameter of the drawn fiber, V_d is the draw rate of fiber and V_f is the feed rate of the preform. Thus depending on the diameter of the drawn fibers, either single mode or multimode GI/SI POFs can be obtained.

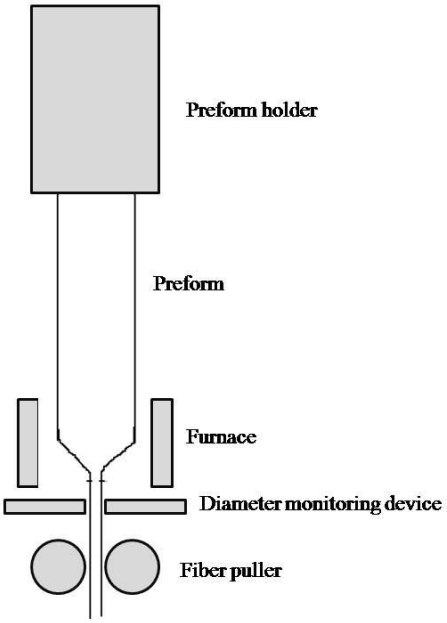

Figure 1.4: Schematic of conventional POF heat drawing process.

1.3 Dye doped POFs

Emergence of POFs in LAN demands the development of them as promising active devices such as fiber lasers and amplifiers for short haul communication. Low processing temperature of POFs allows incorporation of organic dyes as the gain media. High gain of such lasers and amplifiers is due to the large absorption and emission cross section of organic dyes as compared to rare earth elements in silica fibers. Among various dyes, Rhodamine6G (Rh6G) is the most widely and commonly used laser dye for the last four decades. Rh6G has many desirable properties such as high quantum efficiency, increased photostability and good lasing action [19-20] which make it preferable over other organic dyes such as Coumarin, Nile Blue, Curcumin etc. Fig. 1.5 shows the energy level diagram of a dye laser [21]. Molecules get excited to the higher energy singlet state S_1 when pumped by an external source

such as flash lamp. The excited molecules relax to the lowest vibronic energy level of the excited electronic state (S_1) within picoseconds (ps). The molecules residing in this state are stimulated by another spontaneously emitted photon and thus results in lasing. Due to losses such as internal conversion and intersystem crossing, the non-radiative decay rate is increased reducing the radiative decay rate (emission).

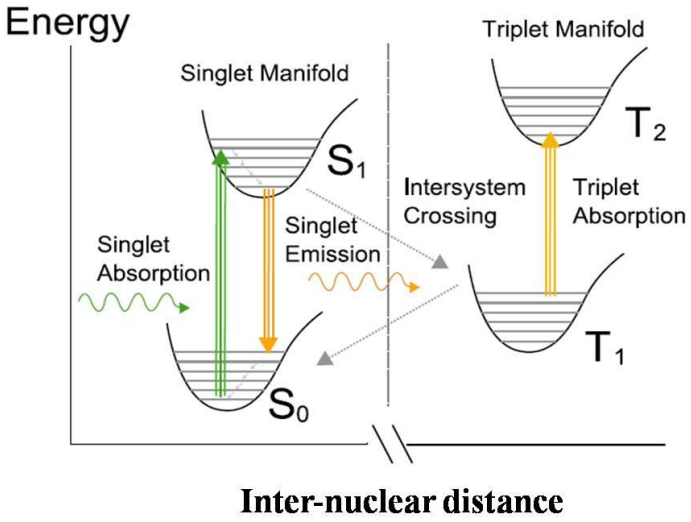

Figure 1.5: Energy level diagram of dye laser [21].

Thus laser dyes can be used to develop efficient and narrow laser sources with a tunability throughout the visible region or optical amplifier with high gain. Solid state dye gain media attracts the interest of recent research due to its inherent advantages such as compatibility, mechanical stability and safe handling compared to their counterpart in liquid medium [17, 22-25]. There are already a number of reports on solid state dye gain media after its first demonstration in 1967 [26] by Soffer and McFarland. Advantage of incorporating dyes in fiber form is the lower pump power required to excite the molecules in the core of the fiber when compared to other solid state forms like films and thereby, utilising the pump power more effectively. In 1987, Muto et.al investigated a dye-doped step index polymer fiber laser [27]. Afterwards a lot of research has been carried out in this area demonstrating laser emission from step index, graded index solid and hollow fibers incorporating various organic dyes [28-35].

1.3.1 Whispering Gallery Resonators and modes

Laser oscillations need a cavity to provide optical feedback. The cavity provides resonance and thus establishes a well defined spectral mode structure and an associated highly directional emission pattern. The cylindrical curved surface of the

fiber provides an excellent microcavity for the efficient coupling of spontaneous emission into lasing modes [36-38]. Such a cylindrical cavity supports whispering gallery modes (WGM) and thus acts as whispering gallery resonators. First observation on WGM was made by Lord Rayleigh about a century back, who studied the propagation of sound waves over a curved gallery surface [39-42]. WG resonators with high Quality (Q) factor and small mode volume are highly important in the fundamental studies of light-matter interaction and in applications such as microcavity lasers [43-44], optical filters and modulators [45-47], mechanical, chemical and biological sensors [48-50], non-linear optics [51-52] and quantum optics [53-55]. WGM is a resonance of light wave that is trapped inside the curved surface such as dielectric spheres, disks or cylinders by total internal reflection as shown in fig.1.6. The resonance condition is satisfied for the circulating light if it reaches the original point with the same phase after one circulation.

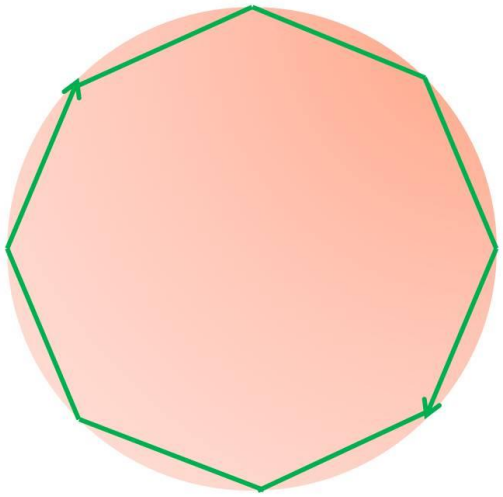

Figure 1.6: Light trapped inside a spherical microcavity by total internal reflection and giving rise to resonant modes known as whispering gallery modes.

The Q value of laser modes are usually used to characterise the quality of the modes and is defined as the number of optical cycles needed for the cavity mode field to decay to 1/e of its initial value times 2π [36,56] and is given by

$$Q = \frac{\lambda}{\delta\lambda} \tag{1.2}$$

where $\delta\lambda$ is the linewidth of the mode at wavelength λ. Q factor mainly depends on the cavity quality [36,57] and is given by

$$Q^{-1} = Q_{abs}^{-1} + Q_s^{-1} + Q_r^{-1} \tag{1.3}$$

where first term in the right hand side corresponds to loss due to optical absorption in the cavity, second term corresponds to losses due to light scattering by surface roughness as well as Rayleigh scattering inside the microcavity and the last term is due to the intrinsic diffraction leakage. Thus the losses in the cavity restrict the Q factor of WGM modes or in other words, the Q factor can be improved by improving the quality of the resonator.

The peak of lasing spectra occurs at the maximum of optical gain spectrum of the amplifier, $\gamma(\lambda)$. We have noticed that lasing occurs at λ where $\gamma(\lambda)$ exceeds the losses in the cavity and this condition [53] is given by

$$\gamma \geq \frac{2\pi n_p}{\lambda Q} \tag{1.4}$$

where n_p is the refractive index of the cavity. The resonant lasing frequencies that can be supported by the polymer fiber cavity are given by

$$\nu_m = \frac{mc}{\pi D n_{eff}} \tag{1.5}$$

where m is an integer, c is the speed of light in vacuum and n_{eff} is the effective index of refraction of the cavity medium. For a thick cavity n_{eff} may be approximated to $n_{eff} \approx n_p(1\text{-}d/D) \approx n_p$. Using this approximation in eqn (1.5), we calculate the intermodal spectral spacing [53] as $\Delta\nu = \nu_m - \nu_{m-1} = \frac{c}{\pi D n_{eff}}$.

Fig.1.7 shows the WGM at 428nm from a microdisk [58]. In principle second order modes always coexist with the first order but it has low Q factor as compared to first and so higher lasing threshold is needed for its excitation [59]. WGM are characterised by the polarisation (p) (Transverse Electric or Transverse Magnetic), the angular (m) and radial momentum numbers (r) and the value of these integers represent the intensity distribution of resonant modes in the cavity. WGM positions for TE and TM are different in general [59].

Thus it can be understood that WG resonators in fiber provides low threshold lasing with high Q factor. Lowering the threshold pump energy needed for lasing has become a crucial to open the possibility of electrical pumping of plastic lasers [36] in the near future. Success in the field of Radiative Decay Engineering (RDE) making use of metal nanoparticles can pave the way to this problem. Metal nanoparticles can

modify the spectral emission characteristics of the dye through its plasmon resonance by increasing or decreasing radiative decay rate of the dye/fluorophore.

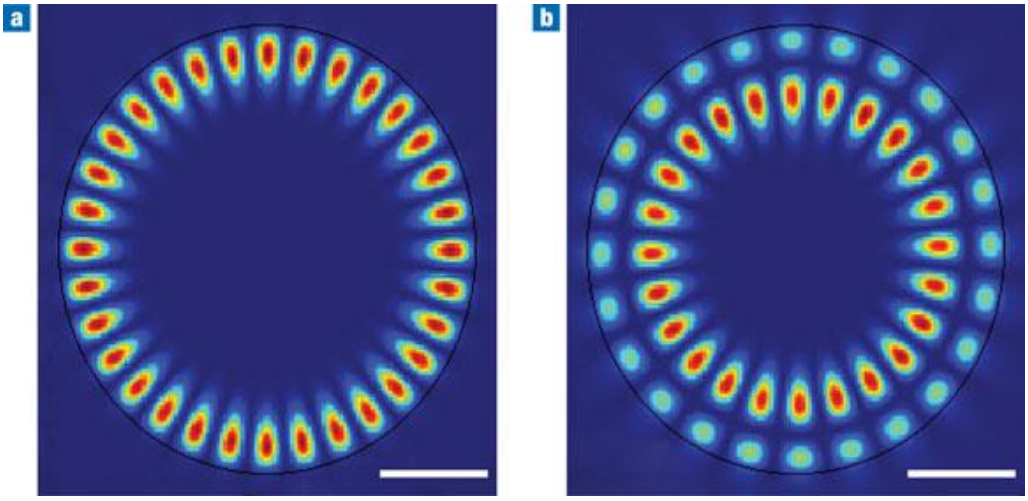

Figure 1.7: (a) First order WGM modes and (b) Second order WGM modes formed at 482nm inside microdisk. Red portion corresponds to the highest intensity of the mode and blue that of lowest intensity. Black edge around the modes represents the edge of the microdisk [58].

1.4 Introduction to metal nanoparticles

Metal nanoparticles have attracted the attention of the scientific world by its fascinating colour long before it became an integral part of modern nanotechnology. Application of colloidal metal nanoparticles can be dated back to 17th century when it was used for staining the glass [60]. Faraday was the first person who recognized that the ruby red colour of Au colloid was due to the presence of minute size of Au particles [61]. Gustav Mie in 1908 explained this phenomenon theoretically by solving Maxwell's equation and the theory has found wide applicability, since it allows the calculation of particle extinction spectra provided, the material dielectric function is known and the size of the particle is less than the wavelength of light [61]. The physical origin of the colour of colloidal metal nanoparticles such as ruby red colour of Au and yellow colour of Ag is due to the collective oscillation of electrons in the conduction band which is known as Surface Plasmon Resonance (SPR) [62-63]. This plasmon oscillation frequency for gold, silver and copper lies in the visible range of electromagnetic spectrum giving a very strong absorption. SPR absorption of silver nanoparticles lies in the blue region (~ 400nm), that of gold nanoparticles lies in the green region (~520nm) and copper nanoparticles in the yellow region (~560nm). Thus the origin of properties in the nanoscale for noble metals and semiconductors are different. In metals SPR give rise to the colour whereas in semiconductors the

emission due to the band gap is responsible for the colour. Depending on the size and shape of metal nanoparticles the SPR absorption band can be tuned as shown in the fig 1.8 [60].

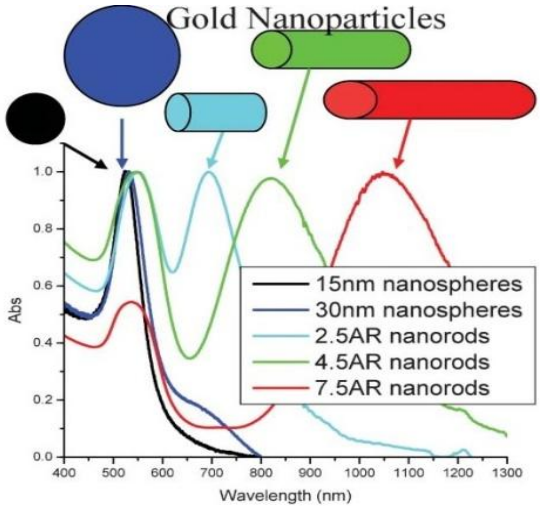

Figure 1.8: Absorption spectra of Au nanoparticles differing in size and shape [60].

Nanospheres exhibit a single plasmon band wheras nanorods exhibit two plasmon bands tunable with respect to the aspect ratio (AR) of the rod. The absorption coefficient/extinction coefficient of metal nanoparticles is of several orders of magnitude higher than the strongest absorbing fluorophore [63]. With change in the shape from isotropic such as nanospheres to anisotropic structure such as nanowires, nanorods etc the absorption can be increased further. Table 1.2 gives the bulk properties of Au and Ag [64].

Table 1.2: Bulk properties of Ag and Au.

Bulk properties	**Silver**	**Gold**
Electronic configuration	$4d^{10}5s^{1}$	$5d^{10}6s^{1}$
Atomic weight	107.87 a.u	196.97 a.u
Lattice	fcc	fcc
Lattice parameter	0.409 nm	0.408 nm
Density	10.50 g/cm^3	19.28 g/cm^3

1.4.1 Surface Plasmon Resonance

SPR of metal nanoparticles are the in phase collective oscillations of conduction free electrons when exposed to external electric field [65-69]. Plasmon resonances of very small metal nanoparticles are strongly damped and that of bigger particles, of the order of tens of nanometer, are excited with visible light [70]. The surface plays a crucial role in determining the position of surface plasmon resonance as it alters the boundary condition for the polarizability of metal [70]. SPR is definitely not a quantum size effect since metal nanoparticles do not display SPR when their size is less than 2nm [70].

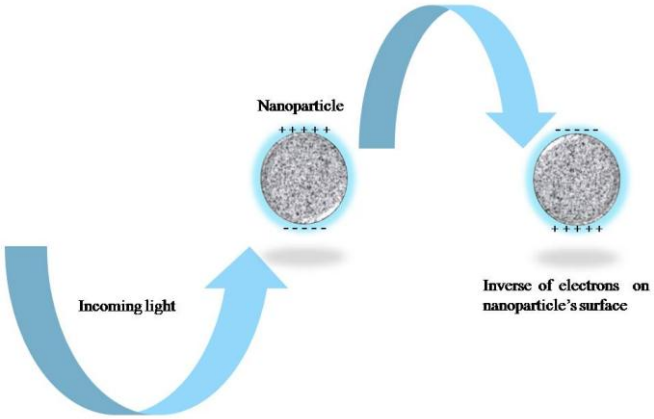

Figure 1.9: Plasmon resonance taking place due to the coherent interaction of electrons in the conduction band of metal nanoparticles with light.

Fig.1.9 shows schematically how plasmon resonance takes place in a simpler manner. The electric field of the incoming light induces a polarisation for the conduction band (free) electrons with respect to its much heavier ionic core. This net charge difference taking place at the surface (boundary) of nanoparticles in turn acts as a restoring force to polarisation. In this manner a dipolar oscillation is created with a period same as that of incoming light. Resonance plasmon oscillations take place when the natural period of oscillation of dipole matches with the period of incoming light. The molar extinction coefficient for a metal nanoparticle of 20nm diameter is of the order of 10^9 $M^{-1}cm^{-1}$ [71] which is three to four orders of magnitude higher than that of very strong absorbing organic dye molecules. SPR is one of the most important characteristics of metal nanoparticles which can be explained using Mie theory.

1.4.2 Mie theory

Mie was the first one to explain the red colour of gold nanoparticle solution [72]. He solved Maxwell's equation for an electromagnetic field interacting with small spheres which are having same macroscopic frequency dependent material dielectric

constant as in the case of the bulk metal. The solutions to these calculations for spherical objects lead to a series of multipole oscillations for the extinction coefficient [73]. By series expansion of fields involved in the partial wave analysis, we can obtain the expressions for extinction cross section σ_{ext} and scattering cross section σ_{sca} [73] as

$$\sigma_{ext} = \frac{2\pi}{|k|^2} \sum_{L=1}^{\infty} (2L+1)\mathrm{Re}\left(a_L + b_L\right) \tag{1.6}$$

$$\sigma_{sca} = \frac{2\pi}{|k|^2} \sum_{L=1}^{\infty} (2L+1)\left(|a_L|^2 + |b_L|^2\right) \tag{1.7}$$

with $\sigma_{abs} = \sigma_{ext} - \sigma_{sca}$ and

$$a_L = \frac{m\Psi_L(mx)\Psi_L'(x) - \Psi_L'(mx)\Psi_L(x)}{m\Psi_L(mx)\eta_L'(x) - \Psi_L'(mx)\eta_L(x)}$$

$$b_L = \frac{\Psi_L(mx)\Psi_L'(x) - m\Psi_L'(mx)\Psi_L(x)}{\Psi_L(mx)\eta_L'(x) - m\Psi_L'(mx)\eta_L(x)}$$

where $m=n/n_m$ with n, the refractive index of the particle and n_m, the refractive index of the surrounding medium, k the wave vector, $x=|k|r$ with r, the radius of the nanoparticle under consideration, ψ_L and η_L are the Ricatti-Bessel cylindrical functions [70]. The prime in the expressions indicate differentiation with respect to the arguments in the brackets. L is the summation index of the partial waves and L=1 corresponds to dipole oscillations of the free conduction electrons in the metal nanoparticles and L=2 corresponds to quadrupole oscillations and so on [70]. For nanoparticles with size much smaller than the wavelength of incoming light ($2r \ll \lambda$) only the dipole oscillations contribute to the extinction cross section [65-67,73] and the Mie theory for total extinction reduces to the following expression under dipole approximation

$$\sigma_{ext}(\omega) = 9\frac{\omega}{c}\varepsilon_m^{3/2} V \frac{\varepsilon_2(\omega)}{\left[\varepsilon_1(\omega) + 2\varepsilon_m(\omega)\right]^2 + \varepsilon_2(\omega)^2} \tag{1.8}$$

where ω is the angular frequency of the incoming light, V is the particle volume, c is the speed of light and ε_m and $\varepsilon(\omega)=\varepsilon_1(\omega)+i\varepsilon_2(\omega)$ are the dielectric functions of the surrounding medium and material composing the particle respectively. Dielectric function of the surrounding medium is assumed to be frequency independent whereas that of the material is frequency dependent and is complex. Resonance condition is satisfied when $\varepsilon_1(\omega) = -2\varepsilon_m(\omega)$ and if ε_2 is small or weakly dependent on ω [74].

Thus eqn (1.8) is widely and extensively used to explain the plasmon absorption spectra of small nanoparticles [74]. As the particle size increases, dipole approximation becomes invalid since the plasmon resonance depends explicitly on the size of the nanoparticles (as x is a function of r). When the particle size is large, higher order modes come into play since the incoming light can no longer polarize the particles homogeneously. The higher order modes peak at lower energies and thus the plasmon band gets red shifted with increase in size [68,73]. Also the bandwidth of the plasmon absorption increases with increase in particle size as the absorption spectra depend directly on its size [73].

1.4.3 Applications of metal nanoparticles

In addition to the various applications of metal nanoparticles as catalysts [75], areas of solar energy conversion [76], ultrafast data communication and optical data storage [77-78], it finds tremendous applications in Surface Enhanced Raman Scattering (SERS) [79-82] and in Radiative Decay Engineering (RDE) [83], due to the plasmon field on their surface.

1.4.3.1 Fluorescence manipulation and RDE

As the plasmon field generated in the metal nanoparticles lies in the visible region of the spectrum, it can affect the optical properties of organic dyes by spectral emission quenching or enhancement. Fluorophores, placed within a distance of 5nm with respect to the metal nanoparticles, suffer from emission quenching whereas that placed at a distance about 10nm or above, undergoes emission enhancement upto 100 fold. When the fluorophores are too close to the metal nanoparticles, they interact electronically with the metal surface and thus transferring the excited electrons in the fluorophores to the metal and thereby reducing the fluorescence emission of the dye. However as the distance of separation between the nanoparticles and fluorophores is increased, the plasmon field generated in the nanoparticles are still strong enough to enhance the emission and will not interact directly with the electrons of the fluorophores [60]. Such enhancement is caused by change in radiative decay rate of the fluorophore. This is by providing additional radiative decay paths in the presence of metal nanoparticles (further details are provided in chapter 5). Thus by placing the fluorophores at proper distance with respect to the nanoparticles, fluorescence can be enhanced several orders of magnitude through enhanced radiative decay and this field

is known as RDE. In addition to the distance between the nanoparticles and fluorophore, the change in emission of the dye (gain medium) depends on the plasmon field strength also. And the plasmon field strength in turn depends on the type of metal, size of nanoparticle, surface modification of the particle and the wavelength of incident light [84].

1.4.3.2 Surface Enhanced Raman Scattering

SERS is a Raman Spectroscopic technique which gives intense Raman signal from Raman active molecule that is adsorbed on to metal nanoparticles [81]. SERS was first discovered in 1970's, when molecules of pyridine adsorbed on to roughened silver electrode showed intense Raman scattering [81]. Recently it is found that anisotropic nanostructures give enhanced Raman signal than isotropic nanostructures. This is due to the higher electric field generated at the corners of the former. SERS has been developed as a powerful diagnostic tool for the detection of trace molecules [82].

There are two main factors which are responsible for the enhanced Raman signal intensity. They are chemical enhancement and electromagnetic field enhancement [81]. The chemical effect contributing to the enhancement is of an order or two in magnitude. The chemical enhancement includes changes in the electronic state of the adsorbate which is due to the chemisorptions of the analyte molecule. The electromagnetic field enhancement which is the dominant mechanism in the Raman signal enhancement is due to the local field strength produced by the surface plasmon oscillations [81]. There are 'hot spots' on the surface of anisotropic structures as well as on metal aggregates which will further enhance Raman signal.

1.5 Method of synthesis of metal nanoparticles

Synthesis methods of metal nanoparticles in solution are broadly divided into chemical method and physical method. Chemical method involves the reduction of metal ions (Au^+ or Ag^+) and the chemisorption of ligands on the surface of metal ions to prevent them from coagulation. Physical method makes uses of different approaches such as evaporation/condensation and laser ablation of metal targets.

1.5.1 Chemical reduction method

Chemical reduction method is the most frequently used method for the synthesis of metal nanoparticles as stable nanocolloids. It offers several advantages such as variety of choice over solvents and ligands, high control over size and shape of the nanoparticles, production of mono-dispersive nanoparticles and production of nanoparticles in large scale.

1.5.1.1 Citrate reduction

The most popular chemical method for the production of metal nanoparticles is citrate reduction method introduced by Turkevich. This method involves heating of aqueous solution of Auric chloride ($HAuCl_4$) to its boiling followed by the rapid addition of sodium citrate solution [85]. The process involves a colour change of pale yellow of the initial solution first to colourless on addition of sodium citrate followed by gray, blue, purple and finally to wine red colour of gold nanoparticles. Different colour of the solution during the process attributes to formation of intermediate nanostructure prior the formation gold nanospheres [85]. Same procedure can be used to reduce silver salt also. But the method results in the formation of larger nanoparticles with poly dispersive nature.

Besides the advantages of chemical method as mentioned above, it has some drawbacks. The chemicals involved such as metal precursors, reducing and stabilizing agents etc are very expensive. Similarly pollutant waste involved in the final purification and need of a stabilizing agent in order to prevent their agglomeration are other drawbacks. Physical method for the generation of metal nanoparticles overcomes most of the limitations of chemical method.

1.5.2 Physical method

Evaporation/condensation method makes use of solid metal target, in a boat which is centred at the furnace, is vaporized into a carrier gas and it is deposited at the target. Various nanoparticles such as Au, Ag and Cu can be prepared by this technique [86]. The disadvantages of this method is that it occupies a large space, takes a lot of time to achieve thermal stability, consumes a lot of electricity etc. Another physical method is Laser Ablation in Liquid (LAL) technique making use of a laser source for ablating the metal target placed inside a liquid environment. The nanoparticles produced in the liquid medium are found to be stable without any stabilizers.

1.5.2.1 Laser Ablation in Liquid

Different models have been developed by scientists to explain the formation mechanism of nanoparticles by LAL technique. A model based on the observations of microsecond (μs) and nanosecond (ns) time-resolved shadowgraph imaging and spectrographic observations of LAL has been developed [87]. From the observations it is found that plasma which is generated during the ablation of target by laser pulses is more dense in liquid environment than in gaseous medium. The enhanced plasma density is due to the confinement provided by the liquid medium. This confinement is mainly due to the high density of liquid around the plasma. Following the generation of plasma plume, shock wave with high pressure is observed and this indicates a high pressure induced by laser ablation of metal targets in the liquid medium. At the next stage, cavitation bubble is observed and its size is enlarged with respect to time and

eventually the cavitation bubble shrank and collapsed. Cavitation bubble seems close to the ablation spot and it is generated by the expansion of ejected material by ablation and local heating of the solvent in the vicinity of spot. When the bubble gets collapsed another shock wave seems to generate and this indicates that impulsive high pressure is again liberated. Also it is observed that nanoparticles are produced inside the cavitation bubble through collision of ejected matter and the nanoparticles are dispersed into the liquid environment only when the bubble is collapsed. Fig 1.10 shows the growth of nanoparticles inside the cavitation bubble.

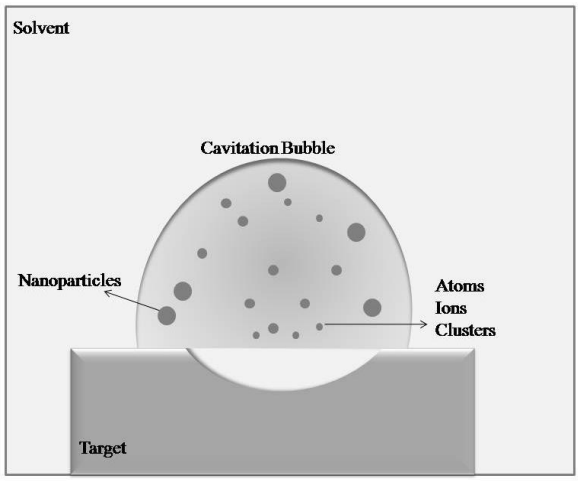

Figure 1.10: Growth of nanoparticles inside the cavitation bubble during laser ablation.

From the above observations, the formation mechanism of nanoparticles by LAL can be concluded as follows. There are three mechanisms for the ablation of target during LAL. Firstly, direct ablation of the target by laser pulses. Secondly, secondary ejection caused by the high pressure of the plasma and thirdly, secondary ejection caused high pressure generated during the collapse of cavitation bubbles. All materials ejected via the above mentioned processes are confined within the cavitation bubble and is dispersed into the medium only through its collapse [87].

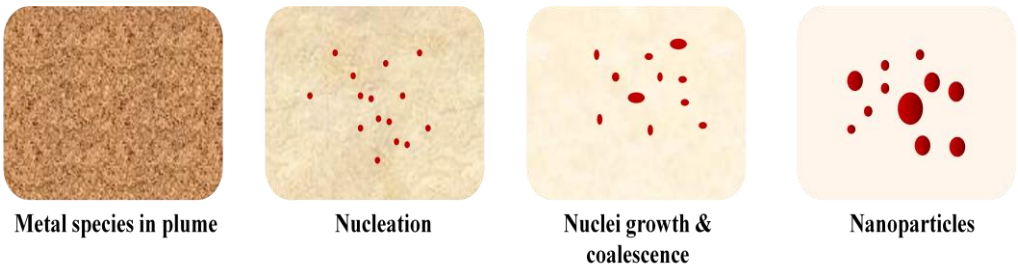

Figure 1.11: Pictorial representation of formation of nanoparticles.

Mafune et al. [88] developed another model for explaining and studying the mechanism behind the formation and growth of nanoparticles produced by laser ablation of metal targets in liquid. According to this model plasma, which contains small clusters, atoms and ions, is generated during the ablation of target by laser pulses and it expands under liquid environment. Small clusters and atoms contained in the plume collide with each other and nucleate to form nanoparticles. A schematic of nucleation of metal species to form nanoparticles is shown in fig.1.11. For the first few pulses liquid medium surrounds the plume and the nanoparticles formed at this time disperses into the liquid medium and it serves as the nucleation centers for the further coming metal species generated after this first few pulses. At this stage, two mechanisms contribute to the nucleation process of metal species. First is the direct nucleation of ablated species in the condensed plume which is very similar to the first stage. Second is the inclusion of metal atoms or clusters to the particles that are formed before. This process promotes the growth of nanoparticles already formed and thus when both these mechanisms occur, broad size distribution is obtained. Growth rate of nanoparticles depend on the number of nanoparticles produced in the first stage and polarity of the surrounding medium [89].

By studying the particle size distribution and morphology of target after LAL, two synthesis mechanisms have been proposed [64]. First one is explosive mechanism and the second is vaporisation mechanism. In the first mechanism nanoparticles are formed by nanometric melted fragments of ablated matter and in the second mechanism nucleation and growth of particles are due to cooling and supersaturation of plasma plume [64]. When both mechanisms occur at the same time, bimodal distribution of particle size is observed because both mechanisms produce nanoparticles with different sizes [64]. In the vaporisation regime, type of solvent media plays a crucial role since the free energy barrier (ΔG_N), the minimum radius of the nuclei (R_N) and the speed of nucleation process (J_N) depend on metal-liquid interface energy ($\gamma_{S\text{-}L}$) [90] as

$$\Delta G_N \propto \frac{\gamma_{S-L}^3}{\left(K_B T \ln\left[\frac{P}{P_0}\right]\right)^2} \tag{1.9}$$

$$R_N \propto \frac{\gamma_{S-L}}{K_B T \ln\left[\frac{P}{P_0}\right]} \tag{1.10}$$

$$J_N \propto \exp\left[\frac{-\Delta G_N}{K_B T}\right] \tag{1.11}$$

where K_B is the Boltzmann constant, T is the temperature and P/P_0 is the ratio of partial vapour pressure P to the equilibrium vapour pressure P_0 and it represents the supersaturation of the metal vapour. Growth of nuclei takes place from the minimum radii R_N with respect to time as

$$R(t) = R_N + kV_a d(t)\nu t \tag{1.12}$$

where k is the sticking probability of each atom on the particle surface, V_a is the effective volume of a single atom, d(t) is the free atom density in solution at time t and ν is the diffusion velocity of metal atoms to the already existing metal nanoparticles with a radius R_N [91-92]. Size and shape of the nanoparticles produced by LAL strongly depends on laser parameters like wavelength, pulse duration, fluence etc and the properties of the surrounding liquid medium such as its viscosity and polarity. Thus controlling such parameters can yield nanoparticles with desirable size and shape.

1.6 Scope of the thesis

POF based dye lasers have added advantage over other solid state dye lasers like the low pump energy needed for the excitation of the gain medium due to the effective confinement. Because of the low threshold energy needed for the excitation, another problem with regard to solid state dye lasers like photobleaching can be reduced in POF based lasers. Besides, thermally induced photobleaching can be reduced due to the long and thin fiber geometry. Whispering gallery resonators in the fiber provide the efficient coupling of amplified spontaneous emission from the fluorophores to lasing. WG resonators provide high quality factor and narrow linewidth of lasing modes. With the modification of the gain media in the fiber microcavity, laser efficiency can be improved. Metal nanoparticles incorporated in the gain medium can engineer the emission of the fluorophores thereby affecting the net gain of the medium. Depending on the type of metal nanoparticles (gold or silver), shape of the nanoparticles (nanospheres or nanowires etc) and distance of separation between metal nanoparticles and fluorophores, emission enhancement or quenching is resulted. Emission enhancement of the gain medium results in low threshold lasing and metal nanoparticles found to improve the photostability of the fluorophores. Such low threshold pumping of the gain medium in the presence of nanoparticles can pave way to electrical pumping of polymer lasers from the conventional optical pumping in the near future. The work done in this thesis aims at the fabrication of different metal nanoparticles such as gold and silver with different nanostructures like nanospheres, nanowires, nanoalloys, nano core/shell etc by laser ablation. Different metal nanostructures incorporated into plastic fibers acts as efficient gain medium providing lasing and enhanced photostability. The results can open a new era of plastic fibers

incorporating nanoparticles in the gain medium for efficient fiber lasers and amplifiers.

References

[1] C. Emslie, "Review Polymer Optical Fibers," Journal of Materials Science 23, (1988). 2281-2293.

[2] Kaino, Toshikuni, Kaname Jinguji, and Shigeo Nara. "Low loss poly (methylmethacrylate-d8) core optical fibers." Applied Physics Letters 42, no. 7 (1983): 567-569.

[3] Chang, Xinlong, Ming Li, and Xuanzi Han. "Recent development and applications of polymer optical fiber sensors for strain measurement." Frontiers of Optoelectronics in China 2, no. 4 (2009): 362-367.

[4] Koike, Y. "Progress in GI-POF-Status of high speed plastic optical fiber and its future prospect." In Proceedings of the Ninth International Conference on Plastic Optical Fibres and Applications-POF'00, Boston, Massachusetts, pp. 1-5. 2000.

[5] Monroy, I. Tafur, H. P. A. Vd Boom, A. M. J. Koonen, G. D. Khoe, Y. Watanabe, Y. Koike, and T. Ishigure. "Data transmission over polymer optical fibers." Optical Fiber Technology 9, no. 3 (2003): 159-171.

[6] Abrate, Silvio, Roberto Gaudino, and Guido Perrone. "Step-index PMMA fibers and their applications." (2013): 177-202.

[7] Takahashi, Ami, Azusa Inoue, Takafumi Sassa, and Yasuhiro Koike. "Fluorination effects on attenuation spectra of plastic optical fiber core materials." Optical Materials Express 3, no. 5 (2013): 658-663.

[8] Koike, Kotaro, Takahiro Kado, Zen Satoh, Yoshiyuki Okamoto, and Yasuhiro Koike. "Optical and thermal properties of methyl methacrylate and pentafluorophenyl methacrylate copolymer: Design of copolymers for low-loss optical fibers for gigabit in-home communications." Polymer 51, no. 6 (2010): 1377-1385.

[9] Takezawa, Yoshitaka, Seikichi Tanno, Noriaki Taketani, Shuichi Ohara, and Hideki Asano. "Plastic optical fibers with fluoroalkyl methacrylate copolymer as their core." Journal of applied polymer science 42, no. 12 (1991): 3195-3203.

[10] Argyros, Alexander. "Microstructures in polymer fibres for optical fibres, THz waveguides, and fibre-based metamaterials." ISRN Optics 2013 (2013).

[11] Ziemann, Olaf, Jürgen Krauser, Peter E. Zamzow, and Werner Daum. POF handbook: optical short range transmission systems. Springer Science & Business Media, 2008.

[12] Keiser, Gerd. Optical fiber communications. John Wiley & Sons, Inc., 2003.

[13] Large, Maryanne CJ, Martijn A. van Eijkelenborg, Alexander Argyros, Joseph Zagari, Steven Manos, Nader A. Issa, Ian M. Bassett et al. "Microstructured polymer optical

fibers: progress and promise." In International Symposium on Biomedical Optics, pp. 105-116. International Society for Optics and Photonics, 2002.

[14] Koike, Yasuhiro. Fundamentals of Plastic Optical Fibers. John Wiley & Sons, 2014.

[15] Ferenets, Marju, Hanna Myllymäki, Kirsi Grahn, Auli Sipilä, and Ali Harlin. "Manufacturing Methods for Multi Step Index Plastic Optical Fiber Materials." Autex Research Journal (2004).

[16] Moradi, S., N. G. Ebrahimi, N. A. Granpayeh, and M. K. Moravveg. "A Fast And Simple Method For Fabrication of Polymer Optical Fiber." (2006).

[17] Peng, Gang Ding, Pak L. Chu, Zhengjun Xiong, Trevor W. Whitbread, and Rod P. Chaplin. "Dye-doped step-index polymer optical fiber for broadband optical amplification." Lightwave Technology, Journal of 14, no. 10 (1996): 2215-2223.

[18] Rajesh, M., and V. P. N. Nampoori. "Fabrication and characterisation of polymer optical fibers for smart sensing and optical amplification." PhD diss., Cochin University of Science & Technology, 2006.

[19] Avnir, David, David Levy, and Renata Reisfeld. "The nature of the silica cage as reflected by spectral changes and enhanced photostability of trapped rhodamine 6G." The Journal of Physical Chemistry 88, no. 24 (1984): 5956-5959.

[20] Rajesh, M., K. Geetha, M. Sheeba, CP G. Vallabhan, P. Radhakrishnan, and V. P. N. Nampoori. "Characterization of rhodamine 6G doped polymer optical fiber by side illumination fluorescence." Optical Engineering 45, no. 7 (2006): 075003-075003.

[21] Chen, Ellen Yi. "Design and Characterization of a Flashlamp-Pumped Organic Dye Laser." (2009).

[22] Kuriki, Ken, Takeyuki Kobayashi, Nana Imai, Toshihiko Tamura, Yasuhiro Koike, and Yoshi Okamoto. "Organic dye-doped polymer optical fiber laser."Polymers for Advanced Technologies 11, no. 8-12 (2000): 612-616.

[23] Maslyukov, A., S. Sokolov, M. Kaivola, K. Nyholm, and S. Popov. "Solid-state dye laser with modified poly (methyl methacrylate)-doped active elements."Applied optics 34, no. 9 (1995): 1516-1518.

[24] Lo, D., J. E. Parris, and J. L. Lawless. "Laser and fluorescence properties of dye-doped sol-gel silica from 400 nm to 800 nm." Applied Physics B 56, no. 6 (1993): 385-390.

[25] Costela, A., F. Florido, I. Garcia-Moreno, R. Duchowicz, F. Amat-Guerri, J. M. Figuera, and R. Sastre. "Solid-state dye lasers based on copolymers of 2-hydroxyethyl methacrylate and methyl methacrylate doped with rhodamine 6G."Applied Physics B 60, no. 4 (1995): 383-389.

[26] McFarland, B. B. "Laser Second-Harmonic-Induced Stimulated Emission of Organic Dyes." Applied Physics Letters 10, no. 7 (1967): 208-209.

[27] Muto, S., A. Ando, O. Yoda, T. Hanawa, and H. Ito. "Tunable laser by sheet of dye doped plastic fibers." Trans. Inst. Electron. Inf. Commun. Eng. J70-C(1987): 1479-1484.

[28] Koike, Yasuhiro, Takaaki Ishigure, and Eisuke Nihei. "High-bandwidth graded-index polymer optical fiber." Lightwave Technology, Journal of 13, no. 7 (1995): 1475-1489.

[29] Ishigure, Takaaki, Eisuke Nihei, and Yasuhiro Koike. "Graded-index polymer optical fiber for high-speed data communication." Applied optics 33, no. 19 (1994): 4261-4266.

[30] Tagaya, Akihiro, Takeyuki Kobayashi, Shiro Nakatsuka, Eisuke Nihei, Keisuke Sasaki, and Yasuhiro Koike. "High gain and high power organic dye-doped polymer optical fiber amplifiers: Absorption and emission cross sections and gain characteristics." Japanese journal of applied physics 36, no. 5R (1997): 2705.

[31] Kuriki, Ken, Takeyuki Kobayashi, Nana Imai, Toshihiko Tamura, Susumu Nishihara, Yukihisa Nishizawa, Akihiro Tagaya, Yasuhiro Koike, and Yoshi Okamoto. "High-efficiency organic dye-doped polymer optical fiber lasers."Applied Physics Letters 77, no. 3 (2000): 331-333.

[32] Sheeba, Mavila, Kannampuzha J. Thomas, Mandamparambil Rajesh, Vadakkedathu PN Nampoori, Chakkalakkal PG Vallabhan, and Padmanabhan Radhakrishnan. "Multimode laser emission from dye doped polymer optical fiber." Applied optics 46, no. 33 (2007): 8089-8094.

[33] Linslal, C. L., S. Mathew, P. Radhakrishnan, V. P. N. Nampoori, C. P. Girijavallabhan, and M. Kailasnath. "Laser emission from the whispering gallery modes of a graded index fiber." Optics letters 38, no. 17 (2013): 3261-3263.

[34] Linslal, C. L., Jaison Peter, S. Mathew, and M. Kailasnath. "Multimode laser emission from dye-doped hollow polymer optical fibre." Pramana 82, no. 2 (2014): 233-236.

[35] Peter, Jaison, P. Radhakrishnan, V. P. N. Nampoori, and M. Kailasnath. "Multimode laser emission from free-standing cylindrical microcavities." Journal of Luminescence 149 (2014): 204-207.

[36] Frolov, S. V., M. Shkunov, Z. V. Vardeny, and K. Yoshino. "Ring microlasers from conducting polymers." Physical Review B 56, no. 8 (1997): R4363.

[37] Chang, Richard Kounai, and Anthony J. Campillo. Optical processes in microcavities. World scientific, 1996.

[38] Knight, J. C., H. S. T. Driver, and G. N. Robertson. "Morphology-dependent resonances in a cylindrical dye microlaser: mode assignments, cavity Q values, and critical dye concentrations." JOSA B 11, no. 10 (1994): 2046-2053.

[39] Rayleigh, John William Strutt. "The theory of sound, vol. 1." New York: McMillan 34 (1945).

[40] Rayleigh, Lord. "IX. Further applications of Bessel's functions of high order to the Whispering Gallery and allied problems." The London, Edinburgh, and Dublin Philosophical Magazine and Journal of Science 27, no. 157 (1914): 100-109.

[41] Rayleigh, Lord. "CXII. The problem of the whispering gallery." The London, Edinburgh, and Dublin Philosophical Magazine and Journal of Science 20, no. 120 (1910): 1001-1004.

[42] Matsko, A. B., A. A. Savchenkov, D. Strekalov, V. S. Ilchenko, and L. Maleki. "Review of applications of whispering-gallery mode resonators in photonics and nonlinear optics." IPN Progress Report 42 (2005): 162.

[43] McCall, S. L., A. F. J. Levi, R. E. Slusher, S. J. Pearton, and R. A. Logan. "Whispering-gallery mode microdisk lasers." Applied physics letters 60, no. 3 (1992): 289-291.

[44] Chen, Roger, Thai-Truong D. Tran, Kar Wei Ng, Wai Son Ko, Linus C. Chuang, Forrest G. Sedgwick, and Connie Chang-Hasnain. "Nanolasers grown on silicon." Nature Photonics 5, no. 3 (2011): 170-175.

[45] Djordjev, Kostadin, Seung-June Choi, Sang-Jun Choi, and P. D. Dapkus. "Microdisk tunable resonant filters and switches." Photonics Technology Letters, IEEE 14, no. 6 (2002): 828-830.

[46] Rabiei, Payam, William H. Steier, Cheng Zhang, and Larry R. Dalton. "Polymer micro-ring filters and modulators." Journal of lightwave technology 20, no. 11 (2002): 1968.

[47] Kieu, Khanh, and Masud Mansuripur. "Fiber laser using a microsphere resonator as a feedback element." Optics letters 32, no. 3 (2007): 244-246.

[48] Matsko, A. B., A. A. Savchenkov, V. S. Ilchenko, and L. Maleki. "Optical gyroscope with whispering gallery mode optical cavities." Optics communications 233, no. 1 (2004): 107-112.

[49] Symes, Rachel, Robert M. Sayer, and Jonathan P. Reid. "Cavity enhanced droplet spectroscopy: Principles, perspectives and prospects." Physical Chemistry Chemical Physics 6, no. 3 (2004): 474-487.

[50] Vollmer, Fea, D. Braun, A. Libchaber, M. Khoshsima, I. Teraoka, and S. Arnold. "Protein detection by optical shift of a resonant microcavity." Applied Physics Letters 80, no. 21 (2002): 4057-4059.

[51] Braginsky, V. B., M. L. Gorodetsky, and V. S. Ilchenko. "Quality-factor and nonlinear properties of optical whispering-gallery modes." Physics Letters A137, no. 7 (1989): 393-397.

[52] Kippenberg, T. J., S. M. Spillane, and K. J. Vahala. "Kerr-nonlinearity optical parametric oscillation in an ultrahigh-Q toroid microcavity." Physical Review Letters 93, no. 8 (2004): 083904.

[53] Campillo, A. J., J. D. Eversole, and H. B. Lin. "Cavity quantum electrodynamic enhancement of stimulated emission in microdroplets." Physical review letters67, no. 4 (1991): 437.

[54] Vernooy, D. W., A. Furusawa, N. Ph Georgiades, V. S. Ilchenko, and H. J. Kimble. "Cavity QED with high-Q whispering gallery modes." Physical Review A 57, no. 4 (1998): R2293.

[55] Artemyev, Mikhail V., Ulrike Woggon, Reinhold Wannemacher, Heiko Jaschinski, and Wolfgang Langbein. "Light trapped in a photonic dot: Microspheres act as a cavity for quantum dot emission." Nano letters 1, no. 6 (2001): 309-314.

[56] Svelto, Orazio. "Principles of lasers." (1998): 1976.

[57] Kuwata-Gonokami, Makoto, and Kenji Takeda. "Polymer whispering gallery mode lasers." Optical materials 9, no. 1 (1998): 12-17.

[58] Tamboli, Adele C., Elaine D. Haberer, Rajat Sharma, Kwan H. Lee, Shuji Nakamura, and Evelyn L. Hu. "Room-temperature continuous-wave lasing in GaN/InGaN microdisks." Nature photonics 1, no. 1 (2007): 61-64.

[59] Duong Ta, Van, Rui Chen, Lin Ma, Yong Jun Ying, and Han Dong Sun. "Whispering gallery mode microlasers and refractive index sensing based on single polymer fiber." Laser & Photonics Reviews 7, no. 1 (2013): 133-139.

[60] Eustis, Susie, and Mostafa A. El-Sayed. "Why gold nanoparticles are more precious than pretty gold: noble metal surface plasmon resonance and its enhancement of the radiative and nonradiative properties of nanocrystals of different shapes." Chemical society reviews 35, no. 3 (2006): 209-217.

[61] Link, Stephan, and Mostafa A. El-Sayed. "Spectral properties and relaxation dynamics of surface plasmon electronic oscillations in gold and silver nanodots and nanorods." The Journal of Physical Chemistry B 103, no. 40 (1999): 8410-8426. [62] Liz-Marzán, Luis M. "Nanometals: formation and color." Materials today 7, no. 2 (2004): 26-31.

[63] Long, Nguyen Ngoc, Chu Dinh Kiem, Sai Cong Doanh, Cao Thi Nguyet, Pham Thi Hang, Nguyen Duy Thien, and Luu Manh Quynh. "Synthesis and optical properties of colloidal gold nanoparticles." In Journal of Physics: Conference Series, vol. 187, no. 1, p. 012026. IOP Publishing, 2009.

[64] Amendola, Vincenzo. "Synthesis of gold and silver nanoparticles for photonic applications." PhD diss., PhD thesis, University of Padova, Italy, 2008.

[65] Ershov, B. G., and A. Henglein. "Optical spectrum and some chemical properties of colloidal thallium in aqueous solution." The Journal of Physical Chemistry 97, no. 13 (1993): 3434-3436.

[66] Mulvaney, Paul. "Surface plasmon spectroscopy of nanosized metal particles."Langmuir 12, no. 3 (1996): 788-800.

[67] Papavassiliou, George C. "Optical properties of small inorganic and organic metal particles." Progress in Solid State Chemistry 12, no. 3 (1979): 185-271.

[68] Kerker, M. "The Scattering of Light and Other Electromagnetic Radiation (Academic, New York, 1969)." Chap 7 (1971): 311.

[69] Huffman, Donald R. "Absorption and scattering of light by small particles."Wiley Science Paperback Series, John Wiley & Sons, New York, NY, USA 7, no. 1 (1983): 7-5.

[70] Link, Stephan, and Mostafa A. El-Sayed. "Shape and size dependence of radiative, non-radiative and photothermal properties of gold nanocrystals."International Reviews in Physical Chemistry 19, no. 3 (2000): 409-453.

[71] Link, Stephan, and Mostafa A. El-Sayed. "Size and temperature dependence of the plasmon absorption of colloidal gold nanoparticles." The Journal of Physical Chemistry B 103, no. 21 (1999): 4212-4217.

[72] Kelly, K. Lance, Eduardo Coronado, Lin Lin Zhao, and George C. Schatz. "The optical properties of metal nanoparticles: the influence of size, shape, and dielectric environment." The Journal of Physical Chemistry B 107, no. 3 (2003): 668-677. [73] Kreibig, Uwe, and Michael Vollmer. Optical properties of metal clusters. Vol. 25. Berlin: Springer, 1995.

[74] Kreibig, U., and L. Genzel. "Optical absorption of small metallic particles."Surface Science 156 (1985): 678-700.

[75] Schmid, Günter. Clusters and colloids: from theory to applications. John Wiley & Sons, 2008.

[76] Mackay, Raymond A., and John Texter. "Electrochemistry in colloids and dispersions." (1992).

[77] Kamat, Prashant, and Dan Meisel. "Semiconductor Nanoclusters-Physical, Chemical, and Catalytic Aspects." Studies in Surface Science and Catalysis(1997).

[78] Edelstein, A. S., and R. C. Cammarata. "Nanoparticles: Synthesis, Properties and Applications." Institute of Physical Publishing, Philadelphia (1996): 170.

[79] Otto, A., I. Mrozek, H. Grabhorn, and W. Akemann. "Surface-enhanced Raman scattering." Journal of Physics: Condensed Matter 4, no. 5 (1992): 1143.

[80] Moskovits, Martin. "Surface-enhanced spectroscopy." Reviews of modern physics 57, no. 3 (1985): 783.

[81] Campion, Alan, and Patanjali Kambhampati. "Surface-enhanced Raman scattering." Chem. Soc. Rev. 27, no. 4 (1998): 241-250.

[82] Michaels, Amy M., Jiang Jiang, and Louis Brus. "Ag nanocrystal junctions as the site for surface-enhanced Raman scattering of single rhodamine 6G molecules." The Journal of Physical Chemistry B 104, no. 50 (2000): 11965-11971.

[83] Aslan, Kadir, Ignacy Gryczynski, Joanna Malicka, Evgenia Matveeva, Joseph R. Lakowicz, and Chris D. Geddes. "Metal-enhanced fluorescence: an emerging tool in biotechnology." Current Opinion in Biotechnology 16, no. 1 (2005): 55-62.

[84] Kang, Kyung A., Jianting Wang, Jacek B. Jasinski, and Samuel Achilefu. "Fluorescence manipulation by gold nanoparticles: from complete quenching to extensive enhancement." J. Nanobiotechnol 9 (2011): 16.

[85] Geddes, Chris D., and Joseph R. Lakowicz. Radiative decay engineering. Vol. 8. Springer Science & Business Media, 2007.

[86] El-Nour, Kholoud MM Abou, Ala'A. Eftaiha, Abdulrhman Al-Warthan, and Reda AA Ammar. "Synthesis and applications of silver nanoparticles." Arabian journal of chemistry 3, no. 3 (2010): 135-140.

[87] Yang, Guowei, ed. Laser ablation in liquids: principles and applications in the preparation of nanomaterials. CRC Press, 2012.

[88] Mafuné, Fumitaka, Jun-ya Kohno, Yoshihiro Takeda, Tamotsu Kondow, and Hisahiro Sawabe. "Formation and size control of silver nanoparticles by laser ablation in aqueous solution." The Journal of Physical Chemistry B 104, no. 39 (2000): 9111-9117.

[89] Tilaki, R. M., and S. M. Mahdavi. "The effect of liquid environment on size and aggregation of gold nanoparticles prepared by pulsed laser ablation." Journal of Nanoparticle Research 9, no. 5 (2007): 853-860.

[90] Earnshaw, Alan, and Norman Greenwood. Chemistry of the Elements. Vol. 60. Oxford: Butterworth-Heinemann, 1997.

[91] Mafuné, Fumitaka, Jun-ya Kohno, Yoshihiro Takeda, Tamotsu Kondow, and Hisahiro Sawabe. "Formation of gold nanoparticles by laser ablation in aqueous solution of surfactant." The Journal of Physical Chemistry B 105, no. 22 (2001): 5114-5120.

[92] Mafuné, Fumitaka, Jun-ya Kohno, Yoshihiro Takeda, Tamotsu Kondow, and Hisahiro Sawabe. "Formation and size control of silver nanoparticles by laser ablation in aqueous solution." The Journal of Physical Chemistry B 104, no. 39 (2000): 9111-9117.

Chapter 2 :

Fabrication and characterisation tools of metal nanoparticles and polymer fibers

---

A brief note on fabrication techniques, experimental setups and characterisation tools needed for the preparation and characterisation of metal nanoparticles and polymer optical fibers are discussed in the chapter.

2.1 Preparation of metal nanoparticles by laser ablation

Fig.2.1 depicts the schematic of LAL for the preparation of metal nanoparticles in liquid media. The two sources of laser beam used in the nanoparticle synthesis are the nanosecond (ns) and femtosecond (fs) laser pulses. A Q-switched Nd-YAG laser having a pulse width of 9ns and repetition rate of 10Hz with a spot size of 1mm is used as the source of ns laser pulses. The laser system can provide a maximum pulse energy of 0.9J at 1064nm, 0.4J at 532nm and 0.2J at 355nm. A mode locked Ti: Sapphire laser having wavelength of radiation centred around 797nm, pulse width near 80fs and repetition rate of 80MHz with a laser spot size of 7mm and average output power of 1.5W is used as source of fs laser beam. Laser pulses are then focussed onto the metal targets using a dichoric mirror and a convex lens. Two types of metals, gold and silver are chosen for the present study. A gold plate with dimensions (shown in fig.2.1 (b)) 0.38mm thickness and 14mm diameter and a silver plate of 24mm×16mm×1.2mm size are used. Metal targets are immersed in various liquid environments in a beaker where the beaker is kept on an X-Y translational stage. In order to improve the stability and uniformity of the generated nanoparticles the beaker can be kept on a magnetic stirrer.

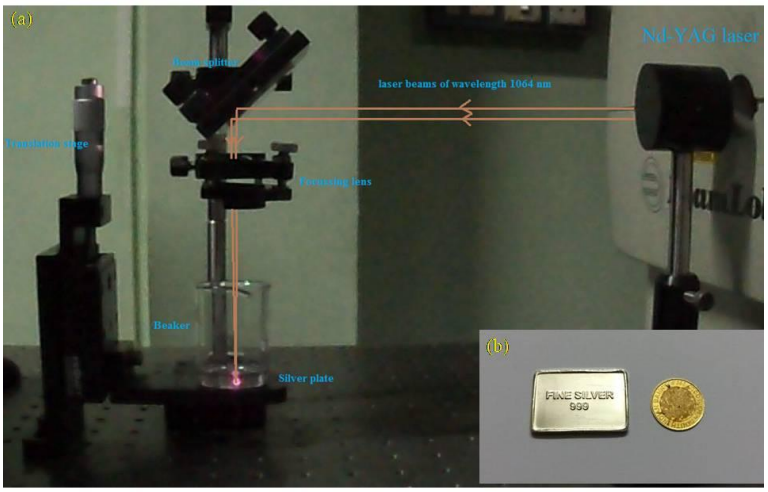

Figure 2.1: (a) Experimental setup for Laser Ablation in Liquid and (b) photograph showing the image of metal targets (left) silver and (right) gold of 99.99% purity.

The diameter of the focussed spot on the metal target is calculated using

$$2\omega_0 = \frac{2f\lambda}{D} \tag{2.1}$$

where f is the focal length of the lens, λ is the wavelength of the laser source and D is the diameter of the source beam. Thus the fluence which is energy per unit area at the metal target can be calculated using

$$\text{Fluence} = {}^{\text{Pulse energy (J)}}\Big/_{\text{Effective focal spot area (cm}^2\text{)}} \tag{2.2}$$

For a Gaussian beam the Rayleigh length, the distance from the beam waist (along the propagation direction) where the radius of the beam is increased by $\sqrt{2}$, is calculated as

$$Z_o = \frac{\pi\omega_0^2}{\lambda} \tag{2.3}$$

where ω_0 is the radius of the laser spot (radial size of the beam at its narrowest point). Variation of the spot size at a distance z from the beam waist is calculated using

$$\omega(z) = \omega_0\sqrt{1+\left(\frac{Z}{Z_0}\right)^2} \tag{2.4}$$

and thus fluence of the laser beam away from the focus can be estimated.

2.2 Characterisation of metal nanoparticles

2.2.1 Absorption spectrograph

Absorption measurements are taken using Jasco V-570 UV-VIS NIR spectrophotometer. It consists of a double beam optical system with single monochromator working in the wavelength range of 190nm to 2500nm with PbS photocell as the detector. System provides a wavelength accuracy of ± 1.5nm with a resolution of 0.5nm [1].

2.2.2 Photoluminescence Spectrograph

Photoluminescence study of the samples are carried out using VARIAN Cary Eclipse Fluorescence Spectrophotometer with a wavelength range of 200-900nm for both excitation and emission monochromator and a wavelength accuracy of ±1nm [2]. The source of excitation is xenon lamp.

2.2.3 Transmission Electron Microscopy

Transmission Electron Microscopic (TEM) images are recorded in order to visualize the size and shape of the nanoparticles. 200kV High Resolution TEM

(Model: JEM 2100) has been used with a point resolution of 0.23nm and a lattice resolution of 0.14nm [3]. TEM grids are prepared by placing a drop of the nanoparticle solution on a carbon-coated copper grid and drying under IR lamp. Electron Dispersive Spectroscopy (EDS) are also carried out for the elemental analysis of the prepared sample using the same instrument with an acceptance angle of 0.13steradian (sr) and take off angle of 25^0. Selected Area Electron Diffraction (SAED) is also recorded with the same instrument in order to identify the crystal structures. SAED is preferable over X-Ray diffraction, since in the former case areas as small as several hundreds of nanometer can be examined.

2.2.4 Time Resolved Fluorescence Spectroscopy

Time-resolved fluorescence measurements are carried out using Horiba Jobin Yuvon Fluorocube -01-NL Fluorescence Life time System. A picoseconds diode laser (469nm) is used as the excitation source, and a highly integrated picosecond PMT module is used as the detector. The instrument response function for the experimental set up is limited by the FWHM of the excitation laser pulse. The lamp profile is recorded by placing a dilute scattering solution (colloidal silica/ ludox in water) in place of the sample. Decay curves are analysed by a nonlinear least-squares iteration procedure using F900 decay analysis software. The quality of the fit is accessed by the chi square (χ^2) values and distribution of residuals. Temperature is controlled by the Quantum Northwest (TC125) instrument [4].

2.2.5 Scanning Electron Microscopy

Surface imaging of polymer fibers are done using Scanning Electron Microscope (SEM) JEOL Model JSM - 6390LV. Resolution of the system under low vacuum mode is 3nm. Magnification from 5 to 300,000 times is possible using the instrument. Samples examined in the instrument are coated with electrically conductive material using a sputter coater [5].

2.2.6 Fourier Transform Infra Red Spectroscopy (FTIR)

IR spectrum of a material is the superposition of absorption band of specific functional groups and it can be used for both quantitative as well as qualitative analysis of the sample. IR spectra of the samples in the study are recorded using Thermo Nicolet, Avatar 370 FTIR spectrometer. The instrument has a resolution of $4cm^{-1}$ with a spectral range of $4000\text{-}400cm^{-1}$ [6]. It is provided with a deuterated triglycine sulphate (DTGS) detector.

2.2.7 Particle size analyzer

Size of the nanoparticles is analysed using Horiba SZ-100 nanoparticle analyser [7]. The system makes use of dynamic light scattering (DLS) technique for particle size analysis. In DLS, fluctuations in scattered light intensity are measured

with respect to time. These fluctuations can thus be related to the diffusion of the particles and since the speed of diffusion depends on the size of the particles, it is easy to relate the particle size with fluctuations in scattered intensity.

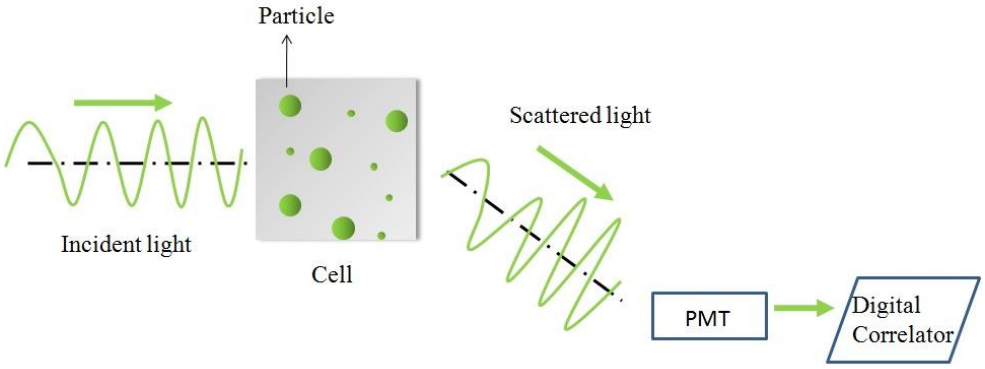

Figure 2.2: Schematic of particle size analyser.

Figure 2.2 shows the schematic of particle size analyser. The instrument makes use of high energy diode pumped green laser of 10mW power as the light source. Since the particles are in Brownian motion in the solvent, they scatter the light incident on them. Depending on the concentration of nanoparticles in the solution, scattered light is collected using a rear detector or a side detector. When the concentration of the samples is high a rear detector is used to collect the back scattered light from a scattering cross section close to the cell wall in order to avoid multiple scattering. As the concentration of the analysed sample is less, the scattered light is collected using a side detector to avoid stray light and to maximise signal to noise ratio. Scattered light is collected by a highly sensitive Photo Multiplier Tube (PMT) which is used as the detector. Autocorrelation function is measured by comparing the scattered intensity at some reference time t and after some delay time τ. For a very short τ, chances of particle motion are less and so the scattered intensity remains similar. So autocorrelation function has a high value. As the delay time is high, particles will undergo significant motion and so the autocorrelation function has a less value. This low value of autocorrelation function corresponds to the time average of scattered light intensity. The shift in the decay from high value to low value indicates the speed of particle motion (fig 2.3) and so the particle size. Diffusion coefficient (D_m) can be calculated from the autocorrelation [7] function as

$$G^{(2)}(\tau) = B + Bf \exp(-2D_m q^2 \tau) \tag{2.5}$$

where $G^{(2)}(\tau)$ is the amplitude of the autocorrelation function, B is the baseline, f is the instrument constant, q is the scattering vector and τ is the delay time. From the diffusion coefficient the particle size can be calculated using Stokes-Einstein equation

$$D_h = kT/3\pi\eta D_m \tag{2.6}$$

where D_h is the particle hydrodynamic size, k is the Boltzmann constant, T is the thermodynamic temperature and η is the viscosity of the solvent.

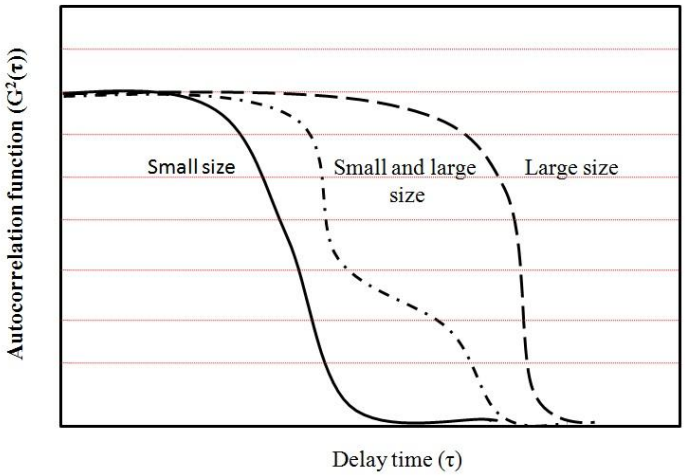

Figure 2.3: Amplitude of autocorrelation function with respect to the delay time.

2.2.8 High Resolution Raman Spectroscopy

Raman analysis is a powerful tool for the quantitative as well as qualitative analysis of materials making use of molecular deformation in the electric field of incoming light determined by molecular polarizability. It is based on the inelastic scattering of monochromatic light. Raman spectra of the samples in this study are recorded using high resolution Raman spectrometer Horiba JY [8]. In the high resolution mode, band analysis can be done with a resolution of $0.3cm^{-1}$ to $1cm^{-1}$ and the instrument has three excitation sources for Raman analysis such as Ar-ion, He-Ne and He-Cd lasers. In the present study He-Ne lasers are used as the source of excitation of Raman signals.

2.2.9 Coherent back scattering

To characterise the mean free path of the samples, coherent back scattering experiment has been carried out. The phenomenon is an interference effect occurring between the counter-propagating waves leading to a narrow cone in exact back scattering [9]. When constructive interference occurs between a wave following a certain multiple scattering path and its counter propagating wave traversing the time reversed path, a coherent light is emitted in the back scattered direction where the intensity of scattered light is enhanced [10]. Experimental setup for back scattering is shown in fig.2.4. By the expansion of a beam of 100mW from a Diode Pumped Solid State (DPSS) laser, its divergence is reduced less than 0.1mrad. The expanded beam is

passed through an aperture and is reflected onto the sample from a beam splitter. The back scattered light is measured as a function of the angle of scattering by a polymer fiber connected to Charge Coupled Device (CCD) spectrograph (0.03nm resolution) that can be moved (using rotational stage) in the focal plane of convex lens placed immediately after the beam splitter. In order to avoid the reflected beam from the cuvette interrupting the measurement, it is titled to a small angle.

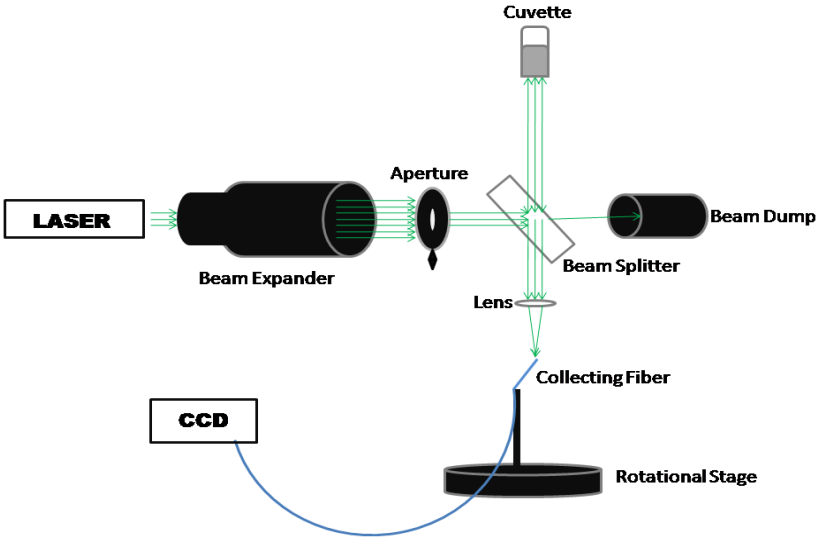

Figure 2.4: Experimental setup for coherent back scattering

2.3 Fabrication and characterisation of POFs

2.3.1 Preform fabrication

MMA which is the monomer of PMMA usually contains inhibitors like hydroquinone to prevent polymerization at room temperature. Thus the inhibitors are to be removed in order to obtain pure MMA. Inhibitors are removed by repeatedly washing the monomer with 5% NaOH solution in distilled water. This solution reacts with the inhibitor leaving MMA. Traces of NaOH if any present in MMA are removed by flushing the solution with distilled water until transparent solution of MMA are obtained. The remaining water content present in MMA is removed by adding suitable drying agents like $CaCl_2$. The monomer is then purified by distillation under reduced atmosphere to get the pure MMA [11].

MMA is then polymerised into cylindrical rods by adding BPO and n-butyl mercaptan. The test tube containing the solution is heated at a constant temperature oil bath at 70^0C for 72 hours. Polymer rods obtained by breaking the test tube is annealed

at 70^0C for improving the mechanical stability. The rods are drawn into fibers of varying thickness using a conventional polymer optical fiber drawing tower as shown in fig.2.5. Hollow preforms and thereby hollow optical fibers of PMMA are obtained by teflon technique. Here a teflon rod of 6mm thickness is fixed at the centre of the test tube of 12mm inner diameter. The test tube is then filled with solution containing proper initiator and chain transfer agents and heated at 70^0C for 72 hours in a oil bath. After polymerisation, the rod is pulled out and a hollow preform of PMMA is obtained.

2.3.2 Fiber drawing

Schematic of a conventional fiber drawing tower is represented in fig 2.5. It mainly consists of five parts namely preform feeder, furnace, temperature controller, fiber puller and winding spool. These five stages are controlled individually by an electronic controller.

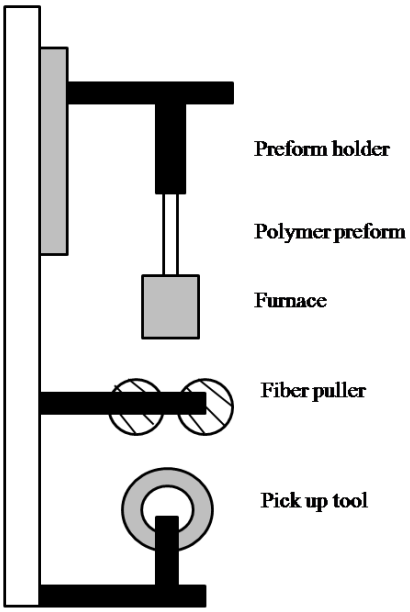

Figure 2.5: Schematic of conventional POF drawing tower.

Preform feeder consists of preform holder in which preforms of diameter upto 30mm can be held. Preform feeder is translated vertically using a stepper motor and the speed of traverse is controlled by a computer. Preform is melted using the furnace. Temperature is provided using three 75W IR lamps which provide a maximum temperature up to 250^0C. By proper slit width and controlling the amount of light inside the furnace, a proper temperature profile can be obtained. Furnace is swung up to 30^0 to provide uniform heating of the preform. Temperature control inside the

furnace is done by a thermocouple attached to the central portion of the furnace where temperature is maximum. The temperature required for drawing the preform is set manually. When the temperature is achieved, temperature controller cuts off the power to the lamp. Fiber puller pulls the drawn fiber at a uniform speed using a stepper motor connected to one of the puller. The motor is controlled by means of a computer and an electronic controller unit. The rate of draw can be programmed in the computer so that the stepper motor drives at the specified rate. By controlling the draw rate and the feed rate, the diameter of the fiber can be controlled. Winding spool attached at the lower portion of the drawing tower winds the fiber. The spool has two controlling axes along with its rotation. After one complete move along the axis, the spool will be moved perpendicular to its axis. The magnitude of this movement exactly matches with the fiber diameter and the process of winding continues [12].

2.3.3 Attenuation measurement using cut-back method

Before proceeding into the applications of POFs such as POF based lasers, sensors or amplifiers, its attenuation characteristics is performed using cut-back method which is a commonly used method [13]. Cutback method provides more accurate result than any other methods for measuring attenuation such as insertion or substitution method [14]. Accuracy lies in the fact that the launching condition of light into the fiber is fixed and remains unchanged throughout the experiment. Laser beam from a 100mW DPSS is launched into one of the ends of the fiber of 100cm length and 500μm diameter using a microscope objective which provides tight focussing of laser beam into the input side of the fiber. The output power is measured using a photo detector placed at the output end of the fiber as $P(L_1)$ where L_1 is the length of the fiber under consideration. Without disturbing the launching conditions, a small portion of the fiber is cut from the output end and it is well polished and the output power is measured again and is noted as $P(L_2)$ where L_2 is the cutback length of the fiber. The process is repeated several times and the attenuation of the test fiber is calculated using

$$\alpha_{dB} = \frac{10\log P(L_2) \big/ P(L_1)}{L_1 - L_2} \tag{2.7}$$

and is found to be 0.1dB/cm in the present case.

2.3.4 Lasing and photostability study of optical fibers

Nd-YAG laser operating at the second harmonics (532nm) having a repetition rate of 10 Hz with a pulse duration of 7ns is focussed transversely on to a fiber using a convex lens of 15mm focal length for lasing experiments. The fiber is kept at a distance of approximately 1 mm from the focus to prevent damage to the fiber that can

be caused by high output power density from the pump laser. In order to reduce the power density a cylindrical lens is also used. Spectral emission from the fiber is collected from one of the ends by using a collecting fiber connected to a CCD based spectrometer with a resolution of 0.03nm.

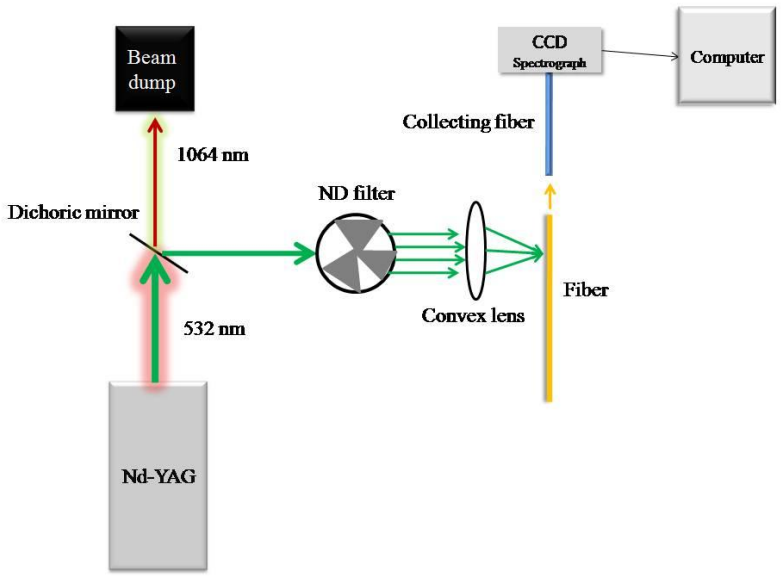

Figure 2.6: Experimental setup for lasing from POFs.

Schematic of the setup is shown in fig. 2.6. Small variations in the pump energy can be obtained using calibrated neutral density (ND) filters. The same setup is employed for measuring the photostability of the dye in the microcavity of POFs. Intensity of the emission from the dye is measured with respect to time of exposure of the fiber to the laser pulses.

2.3.5 Spontaneous Raman Scattering from POFs

Fig.2.7 represents the schematic for measuring Raman spectrum of optical fibers. CW laser emission from a DPSS of 100mW power is reflected on to a microscope objective lens using a dichoric mirror. Focussed laser beam is coupled to one of the polished ends of the POF. The output from the other end of POF is passed through a Raman notch filter (for 532nm). The filter blocks laser light and passes the Raman signals to a convex lens of 4mm focal length. The focussed signal is collected using Acton monochromator which is attached with a charged coupled device (CCD) camera. SpectrPro-500i is a 500 mm focal length monochromator with a resolution of 0.03 nm. The lens is chosen in such a way as to match the etenta with that of CCD spectrograph for maximum signal collection. The f number of the monochromator is calculated to be 7.7. The signals collected in the spectrograph are recorded using a computer.

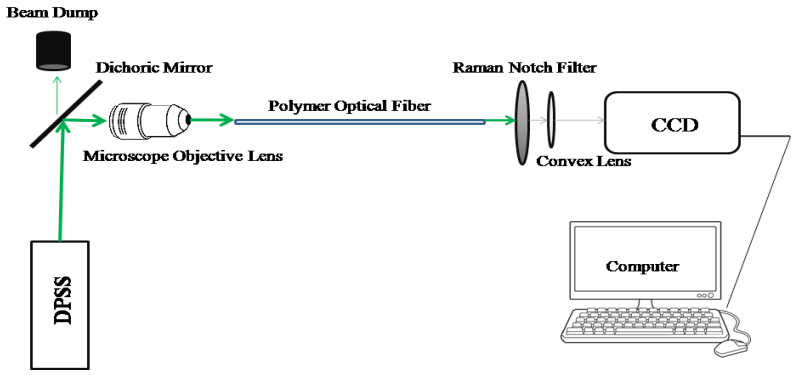

Figure 2.7: Experimental setup for spontaneous Raman Scattering.

References

[1] Model V-550/560/570 Spectrophotometer Hardware/Function manual

[2] Cary Eclipse Hardware operation manual. VARIAN. Australia

[3] Standard Operating Procedure, JEOL JEM-2100 HR Transmission Electron Microscope

[4] Horiba Jobin Yuvon Fluorocube -01-NL Fluorescence Life time System manual

[5] JEOL Model JSM - 6390LV Scanning Electron Microscopy manual

[6] Thermo Nicolet, Avatar 370 FTIR spectrometer user's guide

[7] Nano partica SZ-100 Series Nanoparticle Analyzer manual

[8] Horiba JY Raman spectrometer manual

[9] Kuga, Yasuo, and Akira Ishimaru. "Retroreflectance from a dense distribution of spherical particles." JOSA A 1, no. 8 (1984): 831-835.

[10] de Oliveira, Paulo C., Amy E. Perkins, and Nabil M. Lawandy. "Coherent backscattering from high-gain scattering media." Optics letters 21, no. 20 (1996): 1685-1687.

[11] Rajesh, Mandamparambil, Mavila Sheeba, Karinjamanna Geetha, Chakkalakkal PG Vallaban, Padmanabhan Radhakrishnan, and Vadakkedathu PN Nampoori. "Fabrication and characterization of dye-doped polymer optical fiber as a light amplifier." Applied optics 46, no. 1 (2007): 106-112.

[12] Rajesh, M., and V. P. N. Nampoori. "Fabrication and characterisation of polymer optical fibers for smart sensing and optical amplification." PhD diss., Cochin University of Science & Technology, 2006.

[13] Ghatak, Ajoy, and K. Thyagarajan. An introduction to fiber optics. Cambridge university press, 1998.

[14] Kuzyk, Mark G. Polymer Fiber Optics: materials, physics, and applications. CRC press, 2006.

Chapter 3 :

Generation of Metallic Nanoparticles by Laser Ablation- Effect of experimental parameters

---

This chapter deals with the optimization of different laser parameters such as laser wavelength, energy, number of laser shots and pulse width affecting the shape, yield and size distribution of metal nanoparticles produced by laser ablation. The effect of dielectric function and polarizability of various generation media on the stability and size distribution of nanoparticles is also studied.

3.1 Introduction

Synthesis of size and shape selected metal nanoparticles is one of the major concerns in the science and technology of nanoscale materials [1-2]. Considerable efforts have been made in developing various methods for the production of metal nanoparticles. Synthesis methods are broadly classified into chemical and physical method as described in Chapter1. Chemical method is a very powerful method and presents several advantages. Most variants to wet chemistry approach are dedicated to the generation of nanoparticles with a specific size and shape [3-4]. A high control over size and shape is possible by this method unlike in the case of any other methods. Also this method is scalable to the production of large quantities of metal nanoparticles. Apart from the various advantages, there are several limitations to the chemical reduction method such as expensive chemicals like metal precursors, reducing and stabilizing agents needed for the synthesis. Pollutant wastes are produced during the purification of final products and purification is a forced step after synthesis for its application in many fields such as sensing. Another disadvantage is the need of a chemical stabilizer around the surface of the nanoparticles to prevent them from further functionalization with other molecules in the surrounding medium.

Physical method making use of laser ablation in liquid has proved to be a useful technique to overcome the limitations with respect to chemical reduction method. LAL consists of laser ablation of a metal target immersed in a liquid environment. Since the nanoparticles generated during this technique are charged, it acts as a colloidal solution thereby avoiding the use of any stabilizing agents. Thus the method offers surfactant free nanoparticles thereby reducing the cost involved during the production. LAL allows the utilization of a wide choice of solvents as liquid media. Also any type of nanoparticles can be generated simply by ablating corresponding bulk samples. LAL in comparison to chemical method is very easy to process and do not require a constant care. LAL faces the problem with monodispersity of generated metal nanoparticles and the amount of nanoparticles generated in the media are limited.

A number of reports have come up on the formation of metal nanoparticles by LAL by varying different parameters such as pulse durations, wavelength and carrier medium [5-12]. It is thus known that the choice of laser parameters and carrier media can affect the size and shape of nanoparticles generated.

3.2 Experimental Section

Details of the experimental setup of LAL for the preparation of metal nanoparticles in liquid media are described in Chapter 2. Laser pulses from a Q-switched Nd-YAG laser having a pulse width of 9ns and repetition rate of 10Hz is focussed onto the metal targets (Au/Ag) using a dichoric mirror and a convex lens of 10cm focal length. Both the fluence (J/cm^2) as well as wavelength of the laser pulses

such as fundamental wavelength (1064nm), first (532nm) and second harmonics (355nm) are varied in the experiment. Also width of the laser pulses are changed by choosing the output from Ti:Sapphire femto second laser operating near 800nm with a pulse width around 100fs and repetition rate of 80MHz. Metal targets are immersed in various liquid media such as distilled water, ethanol, acetone and pure MMA. The experiment is further proceeded by varying the volume of the liquid media surrounding the metal targets. Shape and size distribution of nanoparticles formed in MMA, ethanol, acetone and distilled water are analysed using UV-VIS-NIR spectrometer and TEM (technical details are mentioned in the previous chapter).

3.3 Result and Discussions

3.3.1 Effect of generation media on the SPR tunability of metal nanoparticles

Four different media have been chosen with diverse properties such as dielectric constant and polarity. These properties of the media are utilised effectively for the generation of nanoparticles with different size and shape [13-15]. Fundamental wavelength of Nd-YAG laser is taken as the source of ablation. Volume of liquid environment surrounding the target, fluence at the target surface and time of ablation are all kept the same throughout this experimental section as 5ml, $10^3 J/cm^2$ and 5min respectively.

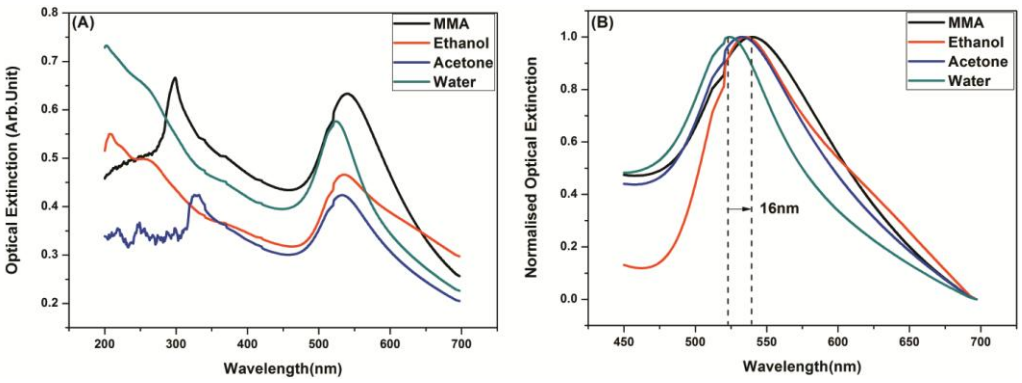

Figure 3.1: (A) Optical extinction spectra and (B) Normalised extinction spectra of Au nanoparticles generated in different media via laser ablation using 1064nm.

Fig.3.1 and fig.3.2 shows the extinction spectra of Au and Ag nanoparticles generated in various liquid media respectively. Due to the tendency of nanoparticles for aggregation and precipitation, all measurements are performed immediately after ablation. The optical absorption/extinction spectra of both Au and Ag nanoparticles are characterised by a broad spectra in the visible region and a narrow spectra in the UV region. From Mie theory, the broad spectrum is identified as the Surface Plasmon

Resonance of metal nanoparticles. SPR appears around 530nm for Au nanoparticles and around 400nm for Ag nanoparticles. The variation in the interband contribution to SPR or the difference in the polarizability of Au and Ag leads to the plasmon absorption of Ag nanoparticles around 400nm and that of Au nanoparticles around 520nm [16]. The position and number of SPR peaks in the spectrum relates to the size and shape of the nanoparticles [17]. The presence of a single SPR peak confirms that the generated nanoparticles are spherical in shape.

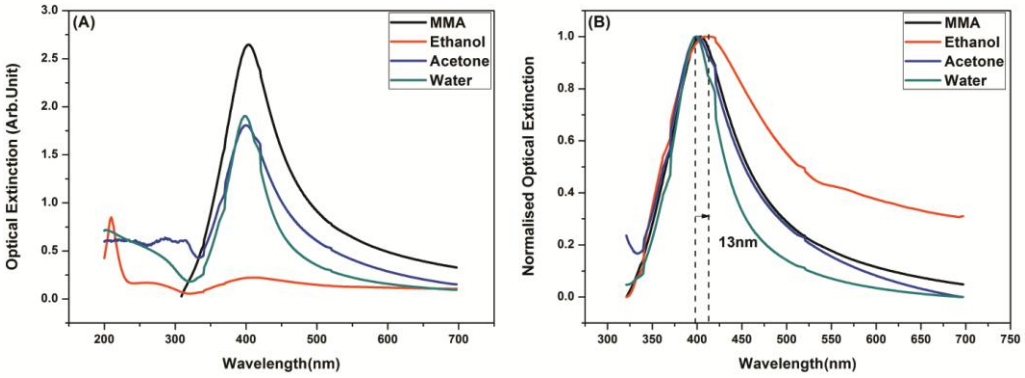

Figure 3.2: (A) Optical absorption spectra and (B) normalised extinction spectra of Ag nanoparticles in various liquid environments showing the shift of plasmon band with respect to various liquid media.

From the above figures (Fig.3.1 (A) and Fig.3.2 (B)) we can see that the SPR shifts its peak position with respect to the surrounding liquid environment. A shift of 16nm in the peak position can be noticed for Au nanoparticles as seen from Fig.3.1 (B). SPR band peaks at 524nm for Au nanoparticles in distilled water and at 540nm in pure MMA. Similarly for Ag nanoparticles SPR appears at 399nm in water medium and at 412nm in ethanolic environment. Table.3.1 gives a complete outline about the position and the full width at half maximum (FWHM) of SPR band for both Au and Ag nanoparticles in different environment.

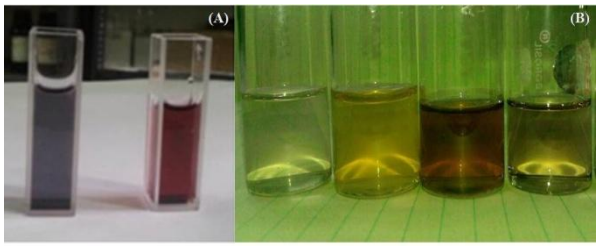

Figure 3.3: Photograph showing the colour of (A) Au nanoparticles produced in MMA (left) and in water (right) and (B) Ag nanoparticles (from left) in ethanol, water, acetone and MMA using laser ablation.

As can be clearly seen from fig.3.3 (A) production of Au nanoparticles in distilled water turns its colour to ruby red whereas its production in ethanol, acetone and MMA appears to be violet. Similarly production of Ag nanoparticles in different media changes the colour from pale yellow to deep dark yellow as in fig.3.3 (B).

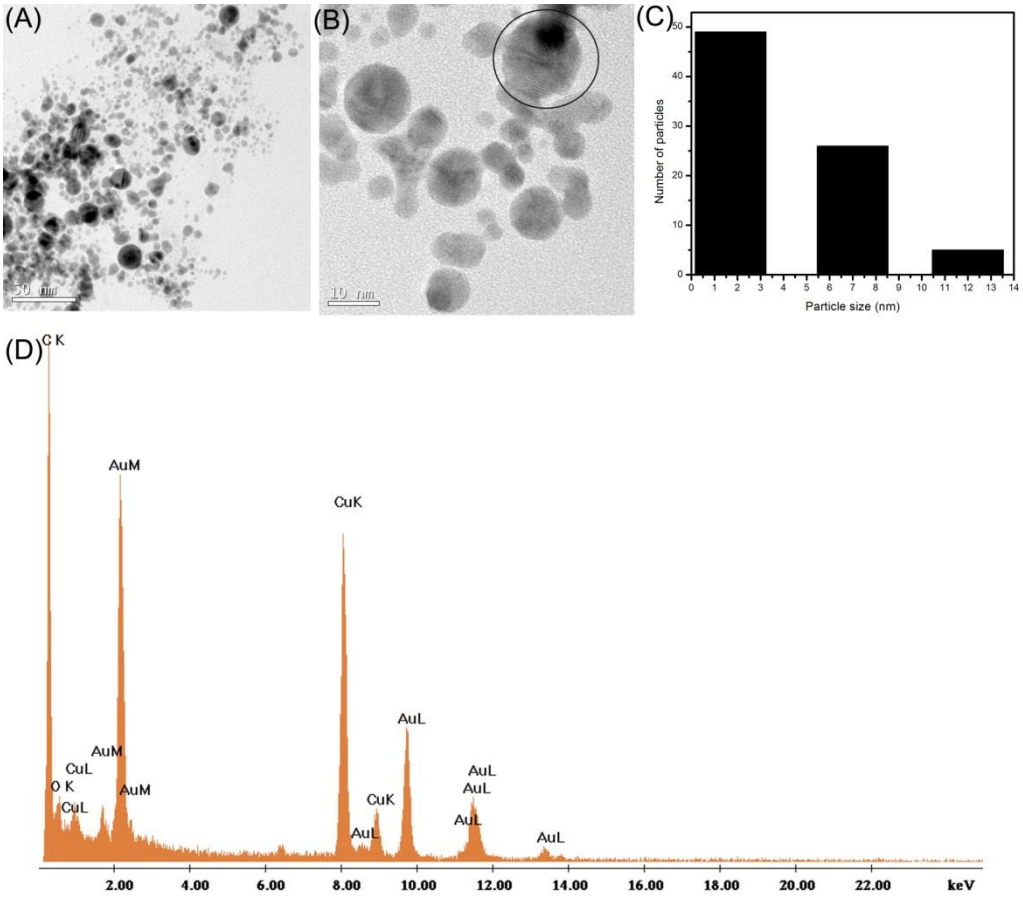

Figure 3.4: (A) Representative TEM image of Au nanoparticles in MMA (B) High Resolution TEM image indicating the polycrystalline nature of Au nanoparticles (C) Size distribution of nanoparticles showing an average size of 2nm and (D) EDS of Au nanoparticles. Presence of Copper in the EDS spectra is due to the grid.

Further it is found from the normalized extinction spectra (fig.3.1 (B) and fig.3.2 (B)) that SPR band of both Au and Ag nanoparticles in ethanol are broadened as compared to other samples. The broadening can be attributed to wide size distribution and aggregation of nanoparticles in the liquid environment [18-19]. In the case of monodispersed nanoparticles the SPR band is narrow [20]. In acetone and in water the extinction spectra of both the metal nanoparticles are narrow as compared to that in ethanol. In accordance with Mie theory of optical absorption and scattering of incoming light by spherical particles, the maximum of optical extinction and shape of

the spectra depends on the dielectric function of the surrounding medium, size, shape and type of nanoparticles [17]. Since all the liquid media under present study except MMA have similar dielectric functions and nanoparticles formed are found to be spherical in shape, the shift of SPR band of nanoparticles in ethanol as compared to water is due to an increase in size of the nanoparticles and the widening of the band is attributed to a broad size distribution.

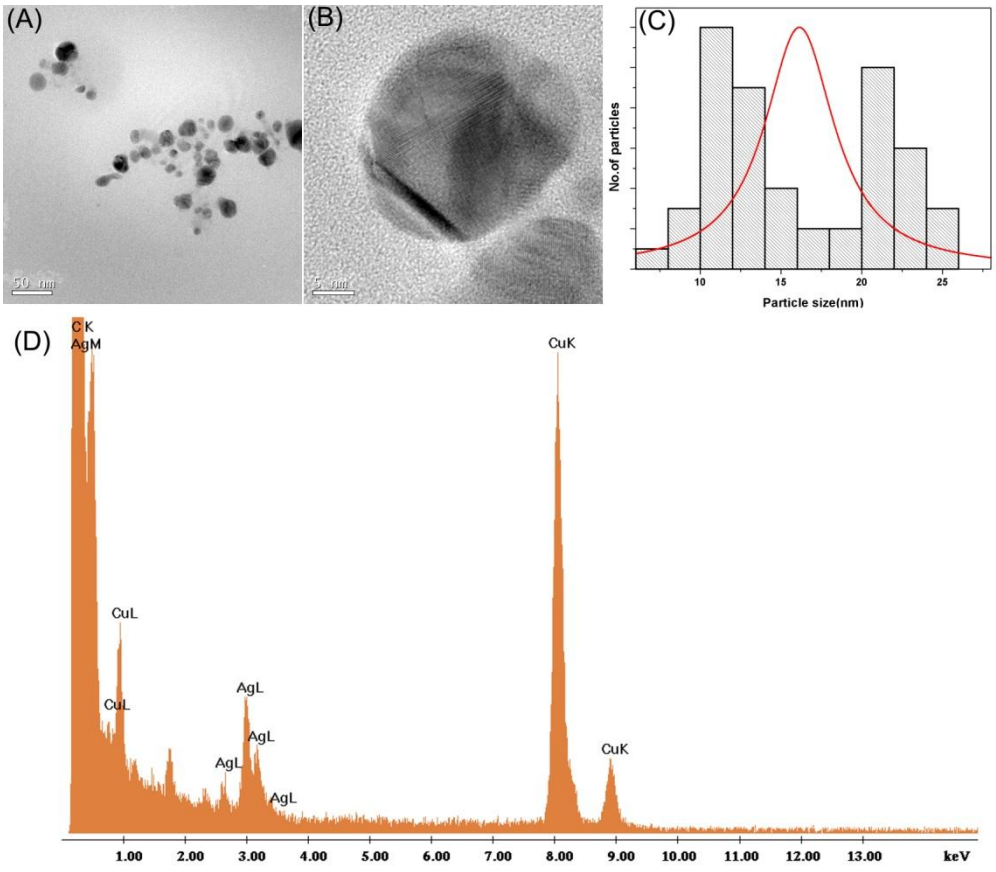

Figure 3.5: (A) TEM image of Ag nanoparticles in MMA (B) High Resolution TEM image showing the polycrystalline nature (C) Histogram showing the size distribution of Ag nanoparticles and (D) EDS showing the presence of Ag nanoparticles in MMA. Copper and carbon lines have originated from grid material.

Accordingly Au and Ag nanoparticles generated in water have the smallest size and that produced in ethanol has largest size. Metal nanoparticles produced in acetone have size in between that produced in water and in ethanol. However, maximum red shift in the SPR band is observed for Au nanoparticles in MMA since its dielectric function is much larger than other liquid media under consideration. Fig.3.4 is the representative TEM image, size distribution and EDS spectrum of Au

nanoparticles generated in MMA. Average size of Au nanoparticles is found to be 2nm and confirms that maximum red shift in the SPR band is due to large refractive index of the medium compared to other samples and not due to an enhanced size of nanoparticles. Maximum of optical extinction spectra of Ag nanoparticles in MMA is at 403nm. Fig.3.5 is the TEM image, EDS spectrum and size distribution of Ag nanoparticles in MMA produced by laser ablation. The image demonstrates a rather narrow distribution of size with mean diameter of 12nm and standard deviation of 5nm.

Metal nanoparticles formed by LAL bears a surface charge owing to partial oxidation and ablation mechanism, which fosters the ionisation of metal atoms and surrounding solvent molecules [21-23]. The development of a net charge at the surface of the nanoparticles affects the distribution of ions in the surrounding region. This results in an increased concentration of counter ions close to the surface. Thus an electrical double layer forms around each nanoparticle [24]. Fig.3.6 depicts an electrical double layer formed on the surface of metal nanoparticle. In addition, OH group has weak interaction with metal nanoparticles [25]. In water and acetone, which are having highly polarised molecules, the counter ions are strongly bound to the surface of negatively charged metal nanoparticles and species in the plume. This forms a strong electrical double layer around them thereby, reducing the Vander Waals force of attraction and thus preventing them from aggregation. This electrical double layer also prevents the further growth of nanoparticles formed during first stage of its formation (as detailed in chapter1) and hence a narrow distribution is observed in the case of water and acetone.

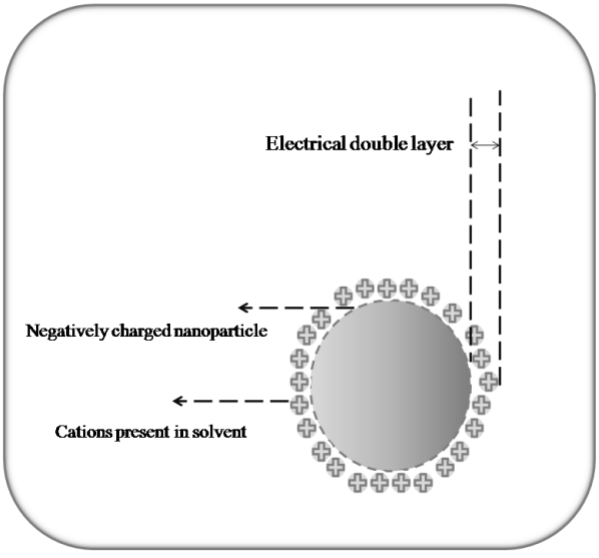

Figure 3.6: Formation of electrical double layer on the surface of nanoparticle.

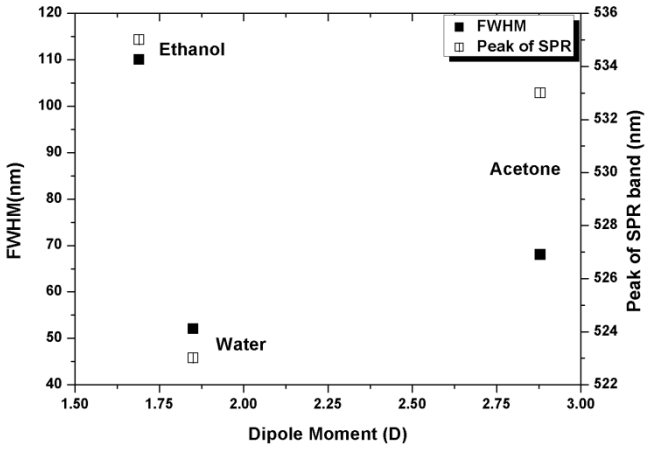

Figure 3.7: Dipole moment vs. FWHM and maximum optical extinction of Au nanoparticles in different environment.

Since the refractive index of acetone, water and ethanol are close to each other, the broadening and red shifting of SPR band in ethanol is due to the wide size distribution and large size of nanoparticles. This can be attributed to the low polarity of the medium. Since ethanol has low polar molecules, the growth mechanism of nanoparticles through the addition of metal species formed by laser ablation showed a greater effect and thus a broad distribution is observed with higher average size than the nanoparticles formed in high polar solvents. Fig.3.7 represents the broadening of SPR band with respect to the dipole moment of the solvents in the case of Au nanoparticles. Similar plot is obtained for Ag nanoparticles in different liquid media. From the figure it is clearly seen that for Au nanoparticles formed in ethanol, which is having lowest polarity, has a broad size distribution and maximum red shift in the SPR band as compared to other samples. Because of low polarity (dipole moment of 1.69D) of ethanol molecules, an asymmetric distribution of charge occurs on the surface of nanoparticles. This leads to dipole-dipole interaction between them and can subsequently result in linear assembly [19]. Thus due to the weak repulsive force and dipole-dipole interaction, the colloidal solutions of Au and Ag are found to be unstable and precipitates after 48 hours of its generation.

From fig.3.1 (A) and 3.2 (A) it can be seen that an absorption band occurs in the UV region of the optical extinction spectra which is due to the interband transitions of metal nanoparticles [21]. The shape of the band remains unchanged with respect to the particle size while its intensity is directly proportional to the number of metal atoms contained in the nanoparticles [26]. This fact takes into account of a relative abundance of nanoparticles generated in the solution. Fig.3.8 represents the relative abundance of Au nanoparticles in the various colloidal solutions. A similar plot can be drawn for Ag nanoparticles as well. Also from the molarity calculation of

metal nanoparticles generated, a comparison between densities of particles formed in various liquid environments can be done (Table.3.1). Molarity of nanoparticles produced is calculated from the measure of mass ablated during LAL.

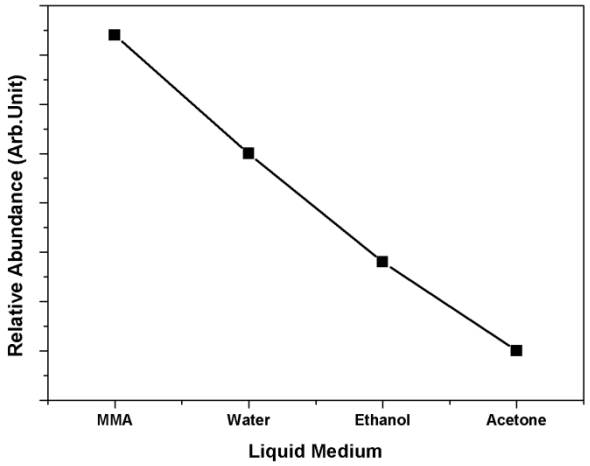

Figure 3.8: Relative abundance of Au nanoparticles generated in different liquid environment. Volume of the liquid medium, time of ablation and laser fluence are kept constant.

Table 3.1: Variation of peak of SPR band, bandwidth and mass ablated from the plate during ablation of Au and Ag nanoparticles in different liquid media. Ablation is carried out using 1064nm for 5min.

Type of metal	Medium of Ablation	Refractive index of the medium	Peak of SPR Band (nm)	Width of SPR band (nm)	Mass ablated from the plate (mg)
Au	MMA	1.41	540	72	0.6
	Ethanol	1.36	535	110	0.4
	Acetone	1.36	533	68	0.3
	Water	1.33	523	52	0.5
Ag	MMA	1.41	403	90	0.7
	Ethanol	1.36	411	155	0.2
	Acetone	1.36	400	89	0.6
	Water	1.33	398	62	0.5

It is found that relative abundance of nanoparticles formed is highest in the case of MMA. Also, metal nanoparticles in MMA have the highest plasmon band intensity since increase in dielectric function of the medium leads to an increase in the plasmon band intensity and a red shift of the plasmon band maximum [27].

3.3.2 Effect of laser wavelength

In this section an investigation on the dependence of laser wavelength on the size of Au and Ag nanoparticles generated in various liquid environments has been carried out. Fig.3.9 depicts the optical extinction spectra of colloidal solutions formed by ablating Au plate in water with 1064nm, 532nm and 355nm laser beam. Laser energy, time of ablation and volume of the liquid media are well controlled and maintained a constant during the experiment. A comparison of absorbance at inter-band transition of Au nanoparticles indicates that yield of nanoparticles increases with increase in wavelength. The mobility of generated nanoparticles is much lower in a liquid medium so that it can stay in the incoming light path. Thus if the particles have sufficient extinction coefficient at wavelength of incoming laser light, they can absorb this energy thereby reducing the energy reaching the metal target for further ablation. As seen from fig.3.9, Au nanoparticles have a strong optical extinction at around 532nm due to SPR and a considerable extinction at UV region due to interband transitions so that the energy of laser light at 532nm and 355nm reaching the surface of target for ablation is much lower than that at 1064nm. Thus due to self absorption of Au nanoparticles at shorter wavelength of laser light, the formation efficiency of nanoparticles at these wavelength is lower than that at higher wavelength [28].

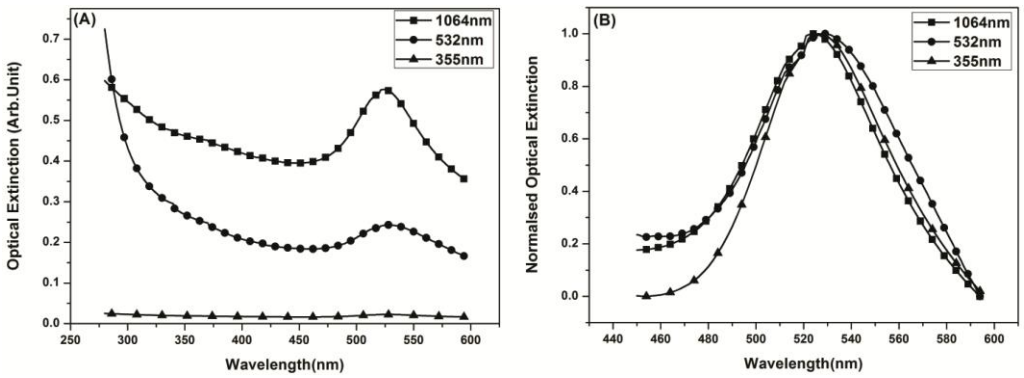

Figure 3.9: (A) Optical absorption spectra of Au nanoparticles produced by LAL in water at different wavelength and (B) Normalised extinction spectra showing the broadening of SPR spectra with respect to wavelength. Laser fluence is maintained at 250J/cm^2 and time of ablation is fixed at 5 minutes in all cases.

The shape of plasmon band of nanoparticles also changed with respect to wavelength (Fig.3.9 (B)). It can be seen that SPR band of Au nanoparticles is broadened when

ablated at 532nm as compared to 1064nm and 355nm. The broadening suggests that the morphology has altered with wavelength [29]. Size of the nanostructures can be roughly estimated using the formula given below and size of the nanoparticles calculated is given in Table.3.2.

$$R = \frac{v_f \lambda_p^2}{2\pi c \Delta\lambda} \tag{3.1}$$

where $v_f = 1.4\times10^6$ m/s is the Fermi velocity, λ_p is the peak wavelength obtained from absorption spectrum, $\Delta\lambda$ is the FWHM of the spectrum and c is the velocity of light [30]. We can see that the size of the nanoparticles produced by 532nm is lower than that at 1064nm. This suggests that the particle size of nanocolloids produced in liquid medium is significantly subjected to self-absorption. Besides, the absorbed energy can thermally excite the lattice of metal nanoparticles leading to the fragmentation of the same [29]. T. Suji et al. [28] suggests two possible mechanisms for self-absorption. One mechanism is 'inter-pulse' self absorption in which the nanoparticles produced earlier by former laser pulses can absorb the energy of subsequently arriving pulses. The other mechanism is 'intra-pulse' self absorption where the particles produced by the earlier part of one pulse immediately absorb the energy of the later section of the same pulse. This mechanism is possible only when the ablation is carried out by nanosecond laser pulses since ejection of ablated matter from the target surface begins in the picoseconds scale [31]. The contribution of this mechanism is independent of initial concentration of nanoparticles present in the liquid environment whereas the contribution of inter-pulse self absorption increases with concentration of nanoparticles produced during the earlier stage of ablation. Thus both inter-pulse and intra-pulse self absorption can be responsible for the lower efficiency and size reduction of nanoparticles produced at shorter wavelength of laser light. But ablation of Au nanoparticles at 355nm yielded nanoparticles of similar size as in the case of ablation by 1064nm since the width of the plasmon band remained almost same in both cases.

Similar results are observed in the case of Ag nanoparticles when ablation is carried out at 355nm where it has large optical absorption due to SPR. Fig. 3.10 represents the optical extinction spectra Ag nanoparticles formed in water. As seen from the figure, there is a broadening of SPR band of Ag nanoparticles when ablated by 355nm similar to Au nanoparticles when ablated at 532nm. A size reduction is also noted in this case too and is given in table 3.2. Similar results are obtained for both Au and Ag nanoparticles generated in other liquid media and are summarised in table 3.2. Ablation carried out at 532 nm for Ag yielded almost same size distribution as that obtained by 1064nm but with lower efficiency of production. Since the nanoparticles produced are polydispersive, there is an error of nearly 15% for the size of

nanoparticles calculated using the above equation and detailed analysis is possible only through TEM. However it can be concluded that the optimum wavelength for ablation of metal nanoparticles is 1064nm yielding high productivity with less size distribution as compared with other laser wavelengths.

Table 3.2: Variation of particle size with laser wavelength. The calculations are approximate to show that there is a variation of particle size with the choice of laser wavelength.

Type of metal	Liquid medium	Average size of the nanoparticles (nm) produced by		
		1064 nm	532 nm	355 nm
Au	MMA	3	2.9	3
	Ethanol	1.9	1.1	1.9
	Water	3.9	3.7	3.9
Ag	MMA	0.3	0.3	0.5
	Ethanol	1.4	1.4	0.9
	Water	1.9	1.9	1.7

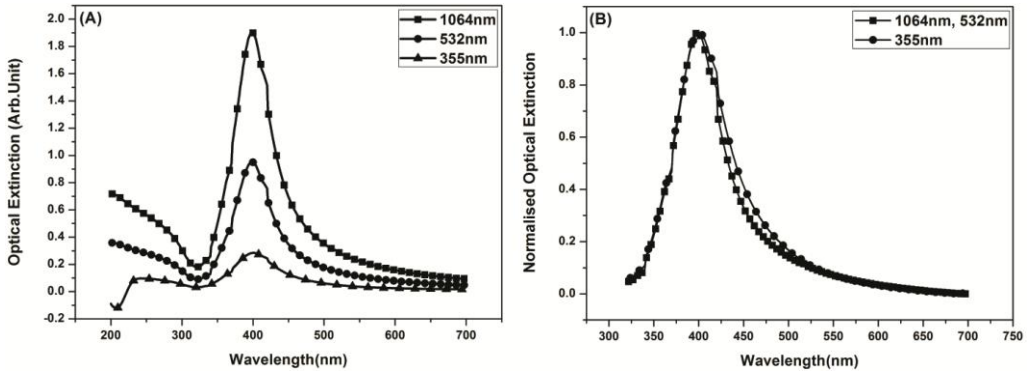

Figure 3.10: (A) Optical extinction and (B) Normalised extinction spectra of Ag nanoparticles produced in water at different wavelengths. Laser fluence is maintained at 500J/cm^2 and ablation time is fixed at 5mins in all cases.

3.3.3 Effect of energy of laser pulses

Since it is concluded that efficient laser ablation is possible at 1064nm further studies are conducted using this wavelength. It is noticed that there is a threshold energy needed for ablation process to begin. When energy of the laser pulses is low (around 50 mJ), the target gets heated due to the laser pulses but energy of the pulses is not high enough to cause ejection of the target material and so no plasma plume is observed. Above the threshold (nearly 100mJ) it is found that ablation takes place and

the relative abundance of both Au and Ag nanoparticles produced increase linearly with respect to laser energy as shown in fig.3.11 (A).

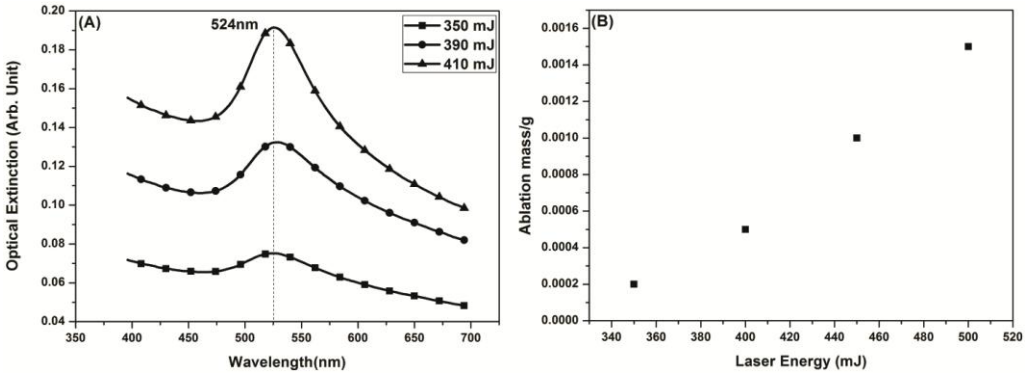

Figure 3.11: (A) Optical absorption spectra of Au nanoparticles produced in water at different laser energy and (B) Plot of ablated mass in gram, within an ablation time of 5 minutes, with increase in laser energy. Volume of the liquid is kept constant.

When the laser energy is very high, beyond a limit (around 600mJ), a self focussing effect is noticed in the liquid medium causing bubbling of the liquid leading to firing of volatile liquids like ethanol and MMA. It is well known that the refractive index of a liquid changes when it is irradiated by high energy laser beam. Due to such non-linear effects at high energy, self focussing occurs in the course of increasing refraction [32]. Beyond this focal point, laser pulses diverge out and only a portion of the energy reaches the target surface for ablation leading to a lower yield. But in the regime upto high energy leading to self focussing, the mass of target material ablated increases linearly with energy as shown in fig.3.11 (B). No appreciable broadening or shifting of SPR band in the optical extinction spectra is noticed in this regime of laser energy. Very similar results are obtained for Au as well as Ag nanoparticles generated in other liquid environments under consideration.

3.3.4 Effect of number of laser shots

Fig. 3.12 shows the absorption of Au nanocolloidal solution in MMA at the interband transitions with respect to number of laser shots. The graph is fitted by polynomial fit of order 2 and from the slope of the evolution curves it is clear that increasing rate of the relative abundance of particles decreases gradually with increase in the number of laser shots. The decrease in ablation rate with increase in the number of laser shots can be attributed to the inter-pulse colloidal absorption which becomes prominent with increase in concentration of nanoparticles (as explained in section 3.3.2). Width and peak position of plasmon band remained almost same with increase in number of laser shots upto 10,000 at a pulse energy of 300mJ. As the number of

shots increased further, plasmon band width is changed due to inter-pulse colloidal absorption. Similar results are also noticed for Ag colloidal solution in MMA.

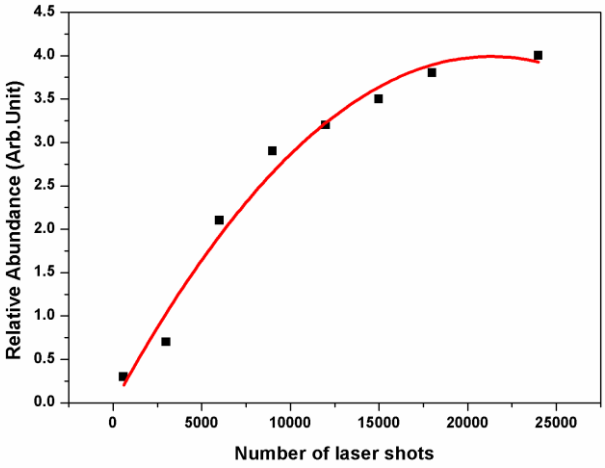

Figure 3.12: Abundance of Au nanoparticles produced in MMA with respect to number of laser shots when ablated at 300mJ using 1064nm.

3.3.5 Effect of volume of liquid media

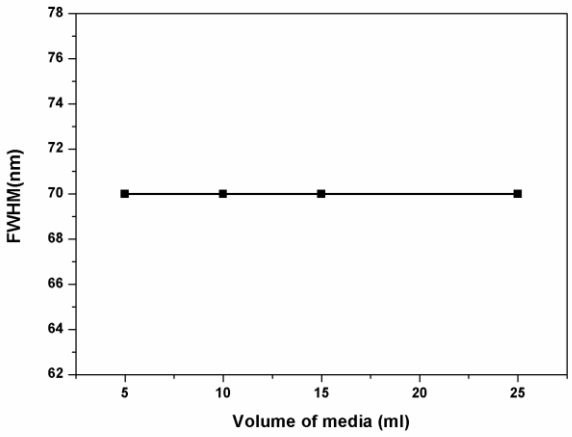

Figure 3.13: Full width at half maximum of plasmon band of Au nanoparticles produced in different volume of MMA. Nd-YAG laser of 300mJ at fundamental wavelength is used for 5min ablation of Au nanoparticles.

Volume of the liquid above the target plate plays an important role in the case of ablation using ultra-short laser pulses. In order to understand its effect in the case of

ablation using Nd-YAG laser, volume of the liquid media surrounding the metal target has been changed keeping the energy and time of ablation a constant. It is found as seen from Fig.3.13 that the width of the SPR band of Au nanoparticles remain constant with no shift in the SPR peak when the volume of the medium is varied from 5ml to 25ml. Abundance of nanoparticles generated in the liquid media varies with change in its volume. For a volume of 5ml, the molarity (keeping all other parameters constant) of Au nanoparticles generated is 6.09×10^{-4}M whereas in 10ml and 15ml it reduces to 1.52×10^{-4}M and 3.38×10^{-4}M respectively. Thus with increase in volume of the liquid medium, the productivity of metal nanoparticles decreases.

3.3.6 Effect of pulse width

Ultrashort (fs) laser pulses have been employed for the production of metal nanoparticles in various liquid environments since such pulses from laser system results in the reduction of thermal load due to decreased heat diffusion time since energy cannot be transferred to the lattice in times smaller than 1ps [33-34]. It is known that the formation mechanism of nanoparticles by ultrashort pulse and ns pulse are fundamentally different. Isochoric lattice heating occurs as a result of the rapid energy transfer from the carriers to the lattice in the case of fs pulses [35]. As a result of isochoric lattice heating, which is an ultrafast non-thermal heating, conversion of the spotted target material into a super heated fluid which along with the build up of extreme thermoelastic pressure leads to material ejection. In the case of ablation by ns laser pulses, nucleation of plasma plume materials in the vapour phase because of the condensation and cooling of the plume under adiabatic expansion leads to nanoparticle formation [35]. Since the formation mechanisms are different, nanoparticles of different size distributions are obtained in both cases. Nanoparticles produced by fs laser always showed a broadened optical extinction spectrum with a broad size distribution of nanoparticles [36-38].

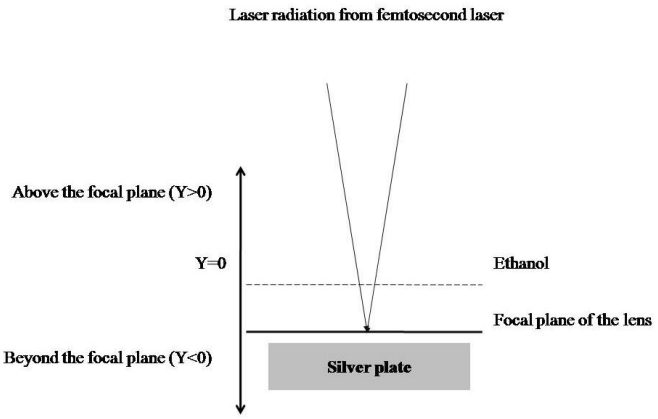

Figure 3.14: Schematic of the experimental setup for laser ablation using fs laser pulses.

It is found that the position of the target with respect to the focal point of the lens plays a crucial role for efficient ablation rate and for obtaining stable nanoparticles by fs laser pulses. In order to clarify this effect, experiment has been performed by varying the position of the target with respect to the focal plane. Throughout the experiment the laser energy is maintained a constant and the liquid level (ethanol is chosen as the medium) above the target is maintained at 2mm which is found to be the optimum level for efficient ablation. Fig. 3.14 represents a schematic of the setup used for the experiment. The fluence at the geometrical focal point of the lens is found to be 1400J/cm^2. The zero point (Y=0) in the figure corresponds to the geometric focal plane of the lens on the target. Positive value of Y corresponds to target above the focal plane and negative value of Y corresponds to target below the focal plane. Ablation is carried out for 5min in all cases. Even if the laser power is maintained a constant at 1.5 W, Power density at the target is varied due to change in position of the target. Nanoparticles produced by femtosecond laser pulses encountered problems with stability and the yellow colour of Ag nanocolloidal solution turned to grey just after a few minutes of its formation when ablation is carried out by placing the target at the geometric focal point. Similarly Au nanoparticles generated in MMA appeared ruby red just after its formation turned to violet a few minutes later.

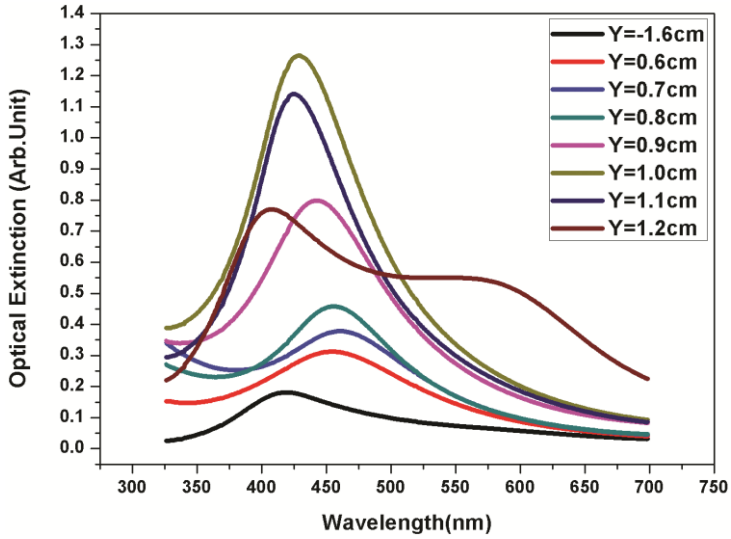

Figure 3.15: Optical extinction spectra of Ag nanoparticles in ethanol produced by positioning the target above and below the focal plane of the lens.

Fig. 3.15 shows the optical extinction spectra of Ag nanoparticles in ethanol generated by placing the target at different positions with respect to the focal plane of the objective lens. It is found that peak of SPR band is shifting when the target is

moved. Peak of SPR band is observed at 430nm when the target is 1cm above the focal point (Y=1cm) and also maximum extinction is noticed at this position. Plasma generated is greatest when the target is at this position which is attributed to the phenomenon of self-focusing, which can play an important role at relatively high laser pulse power like in this case of ultrashort laser pulses. Due to the self focusing effect, the radiation is readily absorbed in the liquid medium by non-linear phenomena and a plasma is formed in front of the target surface [32, 39]. As a result 70% of the laser energy is absorbed by the medium thereby reducing the efficiency of pure radiation related ablation [39]. When the target is in contact with the plasma formed due to self focussing (optical breakdown of liquid medium) ablation takes place which can be due to thermal melting of the target in contact with the plasma [1]. In addition, laser initiated plasma production in liquid is followed by the production of bubbles as a result of liquid evaporation which is in contact with the plasma [40]. The bubbles suddenly merge to a single larger bubble known as cavitation bubble which collapse 50-150μs after plasma initiation by releasing a significant amount of energy [41]. Sylvestre et al. [39] reason out that this energy released during the collapse of cavitation bubble is large enough to cause secondary ablation of the target. Thus ablation by thermal melting and collapse of cavitation bubble leads to the formation of nanoparticles with wide size distribution.

When the target is moved further below or above this self focussing point, lowering of ablation rate is noticed with shifting in the peak of SPR band. When the target is further above (Y=1.2cm), two absorption bands are observed at 400nm and at 570 nm. This new peak can be ascribed to the longitudinal plasmon resonance of rod-shaped silver nanostructures [42]. It is found that placing the target further above this point also yielded nanoparticles but the concentration as well as stability of the so formed nanoparticles are very less.

When the target is placed below Y=0, two centers of plasma production take place. First one, localized near the focal point, is much stronger and is related to the breakdown of ethanol and second one, associated with the ablated material, is near the target surface and is weak [39]. Because of this weak plasma production near the surface, the intensity of the plasmon resonance is weak as shown in the above figure. Also we have observed SPR at 420nm when the sample is placed Y=-1.6cm below the focal plane. Above and below this point, the nanoparticles formed are found to be unstable and agglomeration is noted just after its formation. Table.3.3 gives a summary of peak of SPR band, bandwidth, fluence of the laser and size of the nanoparticles at different target position with respect to Y=0. As can be seen from the table, the mean nanoparticle size increases as the target approach the point of most intense plasma intensity (i.e., when Y= 1 cm). It is found that nanoparticles generated at Y=1cm showed a stability for 2 days whereas Y=0.9 and 1.1cm showed a shift in the plasmon band. All other samples got precipitated a few hours after its formation.

By carefully fixing the target with respect to the geometric focal point of the objective lens, nanoparticles with less size distribution and enhanced stability can be obtained.

Table 3.3: Variation of position of plasmon band, bandwidth and particle size with target position (with respect to Y=0). Positive value corresponds to position of the target above and negative value corresponds to that below the focal plane.

Distance from Y=0 (cm)	Power density (W/cm^2)	Peak of plasmon band (nm)	Bandwidth (nm)	Particle size (nm)
-1.6	94	419	140	0.93
0.6	670	453	190	0.80
0.7	494	461	157	1.00
0.8	377	454	147	1.04
0.9	299	442	142	1.00
1.0	241	429	120	1.14
1.1	198	425	113	1.18

3.4 Conclusions

- Effect of generation media on the size distribution and stability of metal nanoparticles have been studied. Among various generation media having similar dielectric function but with different polarity, nanoparticles produced in low polar solvents showed red shift and broadening of plasmon band. It is found that polarity of the medium plays an important role in determining the size distribution and stability of nanoparticles. It is also found that maximum plasmon band intensity with highest nanoparticle productivity is observed for medium with highest dielectric function.
- Relative abundance and size distribution of nanoparticles in liquid environment is found to be dependent on the ablating wavelength. Yield is found to be maximum at the fundamental wavelength (1064nm).
- There is a threshold energy needed for ablation to take place. When the energy of laser pulses is very high, self focussing takes place which will demote the ablation efficiency. However, it is found that there is a regime of laser energy where the relative abundance of nanoparticles varies linearly with no noticeable shift in the plasmon band.

- With increase in number of laser shots, relative abundance of the nanoparticles in the medium decreases gradually due to inter-pulse colloidal absorption, leading to a broadening of band width.
- Size and shape of the plasmon band remained the same with increase in volume of the liquid medium. But relative abundance of nanoparticles is found to decrease with increase in volume.
- Ablation using femtosecond laser pulses yielded nanoparticles with less stability as compared with that obtained using nanosecond laser pulses. Also it is found that nanoparticles with different size and shape can be produced by changing the position of the target with respect to the focal point of the lens.

References

[1] Mafuné, Fumitaka, Jun-ya Kohno, Yoshihiro Takeda, Tamotsu Kondow, and Hisahiro Sawabe. "Formation of gold nanoparticles by laser ablation in aqueous solution of surfactant." The Journal of Physical Chemistry B 105, no. 22 (2001): 5114-5120.

[2] Petroski, Janet M., Zhong L. Wang, Travis C. Green, and Mostafa A. El-Sayed. "Kinetically controlled growth and shape formation mechanism of platinum nanoparticles." The Journal of Physical Chemistry B 102, no. 18 (1998): 3316-3320.

[3] Xia, Younan, and Naomi J. Halas. "Shape-controlled synthesis and surface plasmonic properties of metallic nanostructures." MRS bulletin 30, no. 05 (2005): 338-348.

[4] Amendola, Vincenzo, and Moreno Meneghetti. "Laser ablation synthesis in solution and size manipulation of noble metal nanoparticles." Physical chemistry chemical physics 11, no. 20 (2009): 3805-3821.

[5] Brito-Silva, Antonio M., Luiz A. Gómez, Cid B. De Araújo, and André Galembeck. "Laser ablated silver nanoparticles with nearly the same size in different carrier media." Journal of Nanomaterials 2010 (2010): 10.

[6] Kalyva, Maria, Giovanni Bertoni, Athanasios Milionis, Roberto Cingolani, and Athanassia Athanassiou. "Tuning of the characteristics of Au nanoparticles produced by solid target laser ablation into water by changing the irradiation parameters." Microscopy research and technique 73, no. 10 (2010): 937-943.

[7] Kabashin, A. V., and M. Meunier. "Synthesis of colloidal nanoparticles during femtosecond laser ablation of gold in water." Journal of Applied Physics 94, no. 12 (2003): 7941-7943.

[8] Muto, Hitomi, Kunihiro Yamada, Ken Miyajima, and Fumitaka Mafuné. "Estimation of surface oxide on surfactant-free gold nanoparticles laser-ablated in water." The Journal of Physical Chemistry C 111, no. 46 (2007): 17221-17226.

[9] Hahn, Anne, Stephan Barcikowski, and Boris N. Chichkov. "Influences on nanoparticle production during pulsed laser ablation." Pulse 40, no. 45 (2008): 50.

[10] Riabinina, Daria, Jianming Zhang, Mohamed Chaker, Joëlle Margot, and Dongling Ma. "Size control of gold nanoparticles synthesized by laser ablation in liquid media." ISRN Nanotechnology 2012 (2012).

[11] Nguyen The Binh, Do Thi Ly, Nguyen Thi Hue, Le Tu Quyen "Silver nanoparticles prepared by laser ablation and their optical characteristics" VNU Journal of Science, Mathematics - Physics 24 (2008): 1-5.

[12] Akman, E., B. Genc Oztoprak, M. Gunes, E. Kacar, and A. Demir. "Effect of femtosecond Ti: Sapphire laser wavelengths on plasmonic behaviour and size evolution of silver nanoparticles." Photonics and Nanostructures-Fundamentals and Applications 9, no. 3 (2011): 276-286.

[13] Dolgaev, S. I., A. V. Simakin, V. V. Voronov, G. A. Shafeev, and F. Bozon-Verduraz. "Nanoparticles produced by laser ablation of solids in liquid environment." Applied surface science 186, no. 1 (2002): 546-551.

[14] Simakin, A. V., V. V. Voronov, N. A. Kirichenko, and G. A. Shafeev. "Nanoparticles produced by laser ablation of solids in liquid environment." Applied Physics A 79, no. 4-6 (2004): 1127-1132.

[15] Sasaki, T., C. Liang, W. T. Nichols, Y. Shimizu, and N. Koshizaki. "Fabrication of oxide base nanostructures using pulsed laser ablation in aqueous solutions." Applied Physics A 79, no. 4-6 (2004): 1489-1492.

[16] Link, S., Zz L. Wang, and M. A. El-Sayed. "Alloy formation of gold-silver nanoparticles and the dependence of the plasmon absorption on their composition." The Journal of Physical Chemistry B 103, no. 18 (1999): 3529-3533.

[17] Huffman, DONALD R. "Absorption and scattering of light by small particles." Wiley Science Paperback Series, John Wiley & Sons, New York, NY, USA 7, no. 1 (1983): 7-5.

[18] Liao, Jianhui, Yu Zhang, Wei Yu, Lina Xu, Cunwang Ge, Jinhong Liu, and Ning Gu. "Linear aggregation of gold nanoparticles in ethanol." Colloids and Surfaces A: Physicochemical and Engineering Aspects 223, no. 1 (2003): 177-183.

[19] Liao, J. H., K. J. Chen, L. N. Xu, C. W. Ge, J. Wang, L. Huang, and N. Gu. "Self-assembly of length-tunable gold nanoparticle chains in organic solvents." Applied Physics A 76, no. 4 (2003): 541-543.

[20] Tilaki, R. M., and S. M. Mahdavi. "Stability, size and optical properties of silver nanoparticles prepared by laser ablation in different carrier media." Applied Physics A 84, no. 1-2 (2006): 215-219.

[21] Mafuné, Fumitaka, Jun-ya Kohno, Yoshihiro Takeda, Tamotsu Kondow, and Hisahiro Sawabe. "Formation and size control of silver nanoparticles by laser ablation in aqueous solution." The Journal of Physical Chemistry B 104, no. 39 (2000): 9111-9117.

[22] Tilaki, R. M., and S. M. Mahdavi. "The effect of liquid environment on size and aggregation of gold nanoparticles prepared by pulsed laser ablation." Journal of Nanoparticle Research 9, no. 5 (2007): 853-860.

[23] Mafuné, Fumitaka, Jun-ya Kohno, Yoshihiro Takeda, and Tamotsu Kondow. "Dissociation and aggregation of gold nanoparticles under laser irradiation." The Journal of Physical Chemistry B 105, no. 38 (2001): 9050-9056.

[24] Amendola, Vincenzo. "Synthesis of gold and silver nanoparticles for photonic applications." PhD diss., PhD thesis, University of Padova, Italy, 2008.

[25] Huang, Yunjie, Di Li, and Jinghong Li. "β-Cyclodextrin controlled assembling nanostructures from gold nanoparticles to gold nanowires." Chemical physics letters 389, no. 1 (2004): 14-18.

[26] Petit, Christophe, Patricia Lixon, and Marie Paule Pileni. "In situ synthesis of silver nanocluster in AOT reverse micelles." The Journal of Physical Chemistry97, no. 49 (1993): 12974-12983.

[27] Link, Stephan, and Mostafa A. El-Sayed. "Spectral properties and relaxation dynamics of surface plasmon electronic oscillations in gold and silver nanodots and nanorods." The Journal of Physical Chemistry B 103, no. 40 (1999): 8410-8426.

[28] Tsuji, Takeshi, Kenzo Iryo, Yukio Nishimura, and Masaharu Tsuji. "Preparation of metal colloids by a laser ablation technique in solution: influence of laser wavelength on the ablation efficiency (II)." Journal of Photochemistry and Photobiology A: Chemistry 145, no. 3 (2001): 201-207.

[29] Tsuji, Takeshi, Kenzo Iryo, Norihisa Watanabe, and Masaharu Tsuji. "Preparation of silver nanoparticles by laser ablation in solution: influence of laser wavelength on particle size." Applied surface science 202, no. 1 (2002): 80-85.

[30] Baset, Somaye, Hossein Akbari, Hossein Zeynali, and Morteza Shafie. "Size Measurement of Metal and Semiconductor Nanoparticles via UV-Vis Absorption Spectra." Digest Journal of Nanomaterials & Biostructures (DJNB) 6, no. 2 (2011).

[31] Semerok, Alexandre, Catherine Chaléard, Vincent Detalle, J-L. Lacour, Patrick Mauchien, Pierre Meynadier, Corinne Nouvellon et al. "Experimental investigations of laser ablation efficiency of pure metals with femto, pico and nanosecond pulses." Applied Surface Science 138 (1999): 311-314.

[32] Bärsch, Niko, Jurij Jakobi, Sascha Weiler, and Stephan Barcikowski. "Pure colloidal metal and ceramic nanoparticles from high-power picosecond laser ablation in water and acetone." Nanotechnology 20, no. 44 (2009): 445603.

[33] Christopher, Dennis, K. Shadak Alee, and D. Narayana Rao. "Synthesis and characterization of silver nanoparticles produced by laser ablation technique in aqueous monomer solution." Journal of Trends in Chemistry 2, no. 1 (2011): 1-5.

[34] Videla, F. A., G. A. Torchia, D. C. Schinca, L. B. Scaffardi, P. Moreno, C. Méndez, L. J. Giovanetti, JM Ramallo Lopez, and L. Roso. "Analysis of the main optical mechanisms responsible for fragmentation of gold nanoparticles by femtosecond laser radiation." Journal of Applied Physics 107, no. 11 (2010): 114308. Page-114308-1

[35] Semaltianos, N. G. "Nanoparticles by laser ablation." Critical Reviews in Solid State and Materials Sciences 35, no. 2 (2010): 105-124.

[36] Barcikowski, Stephan, Ana Menéndez-Manjón, Boris Chichkov, Marijus Brikas, and Gediminas Račiukaitis. "Generation of nanoparticle colloids by picosecond and femtosecond laser ablations in liquid flow." Applied Physics Letters 91, no. 8 (2007): 083113.

[37] Kabashin, A. V., and M. Meunier. "Femtosecond laser ablation in aqueous solutions: a novel method to synthesize non-toxic metal colloids with controllable size." In Journal of Physics: Conference Series, vol. 59, no. 1, p. 354. IOP Publishing, 2007.

[38] Kabashin, Andrei V., Michel Meunier, Christopher Kingston, and John HT Luong. "Fabrication and characterization of gold nanoparticles by femtosecond laser ablation in an aqueous solution of cyclodextrins." The Journal of Physical Chemistry B 107, no. 19 (2003): 4527-4531.

[39] Sylvestre, J-P., A. V. Kabashin, E. Sacher, and M. Meunier. "Femtosecond laser ablation of gold in water: influence of the laser-produced plasma on the nanoparticle size distribution." Applied Physics A 80, no. 4 (2005): 753-758.

[40] PKennedy, Paul K., Daniel X. Hammer, and Benjamin A. Rockwell. "Laser-induced breakdown in aqueous media." Progress in Quantum Electronics 21, no. 3 (1997): 155-248.

[41] Vogel, Alfred, Joachim Noack, Kester Nahen, Dirk Theisen, Stefan Busch, Ulrich Parlitz, D. X. Hammer, G. D. Noojin, B. A. Rockwell, and R. Birngruber. "Energy balance of optical breakdown in water at nanosecond to femtosecond time scales." Applied Physics B: Lasers and Optics 68, no. 2 (1999): 271-280.

[42] Link, Stephan, and Mostafa A. El-Sayed. "Spectral properties and relaxation dynamics of surface plasmon electronic oscillations in gold and silver nanodots and nanorods." The Journal of Physical Chemistry B 103, no. 40 (1999): 8410-8426.

Chapter 4 :

Effect of Au nanoparticles on the optical properties of laser dye

In the present work Au nanoparticles have been incorporated in MMA by Laser Ablation in Liquid technique. Rh6G is doped with this solution containing nanoparticles and studies on optical absorption, fluorescence emission, quantum yield and lifetime of the dye in its presence have been carried out. The monomer solution containing dye-nanoparticles is then polymerised into cylindrical rods and successfully drawn to Rh6G-Au nanoparticle doped Polymer Optical Fiber. Photostability of such fibers is measured subsequently. In the last section, we have developed dye doped polymer fiber lasers incorporating Au nanoparticles.

Publications

Sebastian, Suneetha, C. Ajina, CP G. Vallabhan, V. P. N. Nampoori, P. Radhakrishnan, and M. Kailasnath. "Fabrication and photostability of rhodamine-6G gold nanoparticle doped polymer optical fiber." Chinese Physics Letters 30, no. 11 (2013): 118101.

4.1 Introduction

Gold nanoparticle is one of the most widely studied nanomaterials. These are known to be the most stable among metal nanoparticles [1-3]. Apart from the optoelectronic and biomedical applications of Au nanoparticles, they can serve as ultra efficient quenchers of molecular excitation energy in fluorophore-Au nanoparticle composites [4-7]. Any process that causes a decrease in intensity can be considered as quenching. Quenching will result in dissipation of the fluorophore's electronic energy as heat. When Au nanoparticles are added to the fluorophores, it can affect the fluorescence emission in two ways. Either it can quench the emission intensity or enhance it. Recently there have been several results showing that fluorescence can be manipulated by Au nanoparticles from complete quenching to immense enhancement. The factors that affect the alteration are the size of the nanoparticles and the distance between the dye molecule and nanoparticle [8]. In previous works it is noted that Fluorescence Resonance Energy Transfer (FRET) is one of the possible mechanism for fluorescence quenching of Rh6G by Au nanoparticles [9-10]. Because of the development in the field of nanotechnology especially in the area of Au nanoparticles, organic dyes incorporating Au nanoparticles are gaining attention. Both liquid and solid media such as films with dye-nanoparticle combination [11-12] finds tremendous applications in the field of Surface Enhanced Raman Scattering [13], Radiative Decay Engineering [14] and sensing applications [15]. Several reports have already come up with Rh6G-Au nanoparticle combination in solid as well as liquid media showing how the particle size and concentration can affect the lasing activity of the dye [11-12, 16-17].

FRET happens between a donor molecule in the excited state and an acceptor in the ground state. The donor molecules typically emit radiation at shorter wavelengths that overlap with the absorption spectrum of the acceptor molecules. The rate at which energy is transferred, depends upon the magnitude of spectral overlap, quantum yield of the donor, relative orientation of the donor and acceptor transition dipoles, and the distance between the donor and acceptor molecules. FRET decreases the intensity of the donor and transfers the energy to an acceptor. The acceptor can be fluorescent or non-fluorescent, but in both cases the fluorescence intensity of the initially excited molecules is decreased. Fig.4.1 shows the molecular orbital schematic for FRET. The fluorophore initially has electrons in the ground state (S_0). Absorption of light results in the elevation of electrons to the unoccupied singlet orbitals (S_1). When FRET occurs, electrons of the excited donor return to the ground state. Simultaneously an electron in the acceptor goes into a higher excited-state orbital. If the acceptor is fluorescent it may then emit and if it is non-fluorescent the energy is dissipated as heat. The mechanism of FRET is the same whether the acceptor is fluorescent or non-fluorescent: simultaneous electron transitions in donor and acceptor [18].

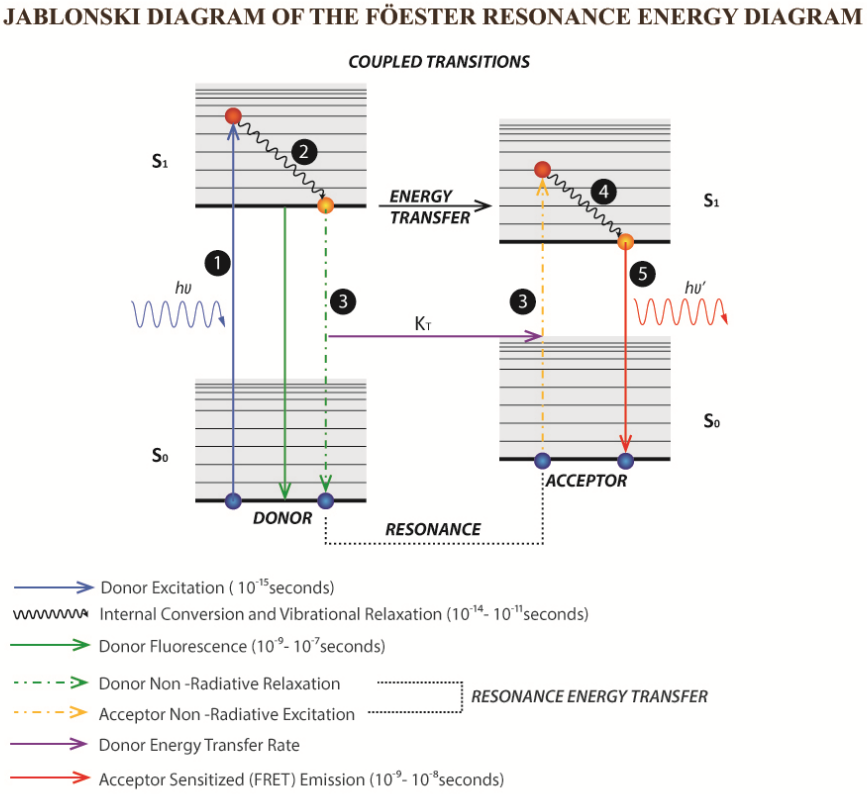

Figure 4.1: Molecular orbital schematic for resonance energy transfer.

4.2 Experimental Section

Ablation is carried out at the fundamental wavelength of Nd-YAG laser with a fluence of $10^3 J/cm^2$ at the surface of the target as optimised from the previous study. Two different generation media such as pure MMA and Rh6G doped MMA are chosen for the synthesis of Au nanoparticles. Time of ablation is varied between 10 seconds to 45 minutes. Concentration of Au nanoparticles in MMA after 45 minutes of ablation is calculated to be 10^{-3} mol/litres.

In the present study, concentration of Au nanoparticles is varied at a fixed concentration of Rh6G in the present study. Details of the concentrations of Rh6G and Au nanoparticles are listed in table.4.1. The concentration of Rh6G in MMA is fixed at a low value, i.e., 5×10^{-5} M since its solubility is less in MMA [19]. A total of 6 samples designated as R, M_1, M_2, M_3, M_4 and M_5 are considered where R is taken as the reference which contains only dye. Rh6G acts as the gain medium while constructing fiber laser.

The below designated samples are then made viscous for casting into planar waveguides by adding appropriate quantity of initiator and heating the solution at 70^0C for an hour. Thin films are made using tape-casting technique and films of 300μm are chosen for the present study. Thicknesses of the sample films are controlled by maintaining the speed of casting as well as viscosity of the solutions. Film thickness is measured using a micro gauge of 0.01mm accuracy. Laser Induced Fluorescence (LIF) of the films is recorded using the setup shown in fig.4.2 where, instead of polymer fiber, the film is placed by sandwiching between two clean micro glass slides.

Table 4.1: Sample designation, concentration of dye and concentration of Au nanoparticles.

Sample designation	**[Rh6G] in the sample**	**[Au] nanoparticle (10^{-3}M)**
R	5×10^{-5}M	-----
M_1	5×10^{-5}M	0.266
M_2	5×10^{-5}M	0.160
M_3	5×10^{-5}M	0.115
M_4	5×10^{-5}M	0.069
M_5	5×10^{-5}M	0.017

Sample solutions are further polymerised into cylindrical rods by adding appropriate quantities of initiator and chain transfer agent. Since it is found that the combination of BPO and n-butyl mercaptan resulted in agglomeration and precipitation of Au nanoparticles in MMA while polymerising, we have used AIBN instead of BPO. The solution containing Rh6G-Au nanoparticle are taken in a test tube with an inner diameter of 12mm and the system is heated in a constant heat oil bath at 90^0C for 48 hours. The rods are drawn into fibers of varying thickness using the polymer optical fiber drawing tower. Hollow preforms of pure PMMA and Au nanoparticles doped PMMA are also fabricated by properly placing a teflon rod of 6mm thickness at the centre of the test tube of 12mm inner diameter. The test tube is then filled with solutions containing proper initiator and chain transfer agents and heated at 70^0C for 72 hours in the oil bath. After polymerisation, the teflon rod is pulled out and a hollow preform of pure PMMA and PMMA doped with Au nanoparticles is obtained and the preforms are drawn into POFs.

Photostability of fibers are measured using the experimental setup shown in fig.4.2. Rh6G-Au nanoparticle doped POF sample is mounted on a fiber holder. The holder is placed at the focus of a cylindrical lens of focal length 15cm. A cw laser beam from a DPSS laser of 100mW power is focused onto the fibers having diameter of 600µm. The fiber is transversely pumped and the fluorescence emission from the fiber is collected from one end of the fiber using a collecting fiber and intensity is recorded using a spectrometer (HR 4000 with a resolution of 0.29nm).

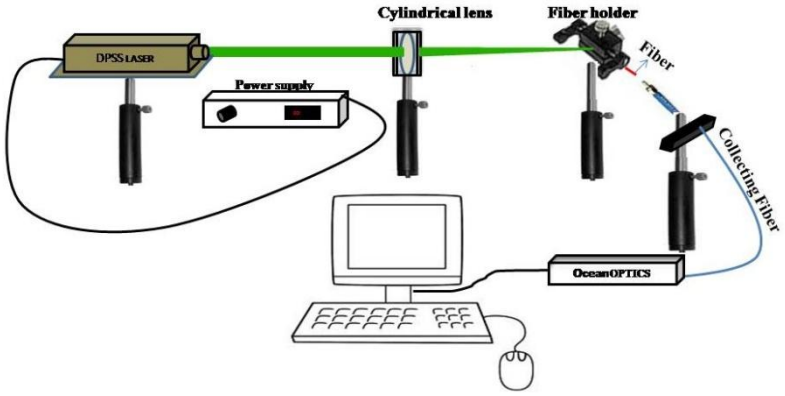

Figure 4.2: Experimental setup for photostability and LIF measurements of waveguides.

Nd-YAG laser operating at the second harmonics having a repetition rate of 10 Hz with a pulse duration of 9 ns is focussed transversely on to a fiber of 7cm length and 400µm diameter using a convex lens of 15mm focal length for lasing experiments (as detailed in chapter 2). The experiment is repeated by carefully replacing the sample fibers without changing any experimental conditions.

4.3 Result and Discussions

4.3.1 Optical characterisation of Rh6G-Au nanoparticle system

4.3.1.1 Optical absorption spectroscopy, fluorescence spectroscopy and Transmission Electron Microscopy

Gold nanoparticles generated in MMA and in Rh6G doped MMA using laser ablation showed different size distribution as depicted in the TEM image and histogram shown in Fig.4.3. From the previous chapter the average size of spherical Au nanoparticles formed in MMA is found to be 2nm whereas in the present case it is found to be 7nm. The change in the particle size is attributed to the change in dielectric function of the medium on addition of the dye. Thus a red shift in the peak intensity of plasmon band is expected for nanoparticles generated in a medium having higher dielectric function leading to larger size as predicted by Mie theory [20]. EDS (Fig.4.3 (D)) shows the presence of Rh6G as well as Au nanoparticles in the solution.

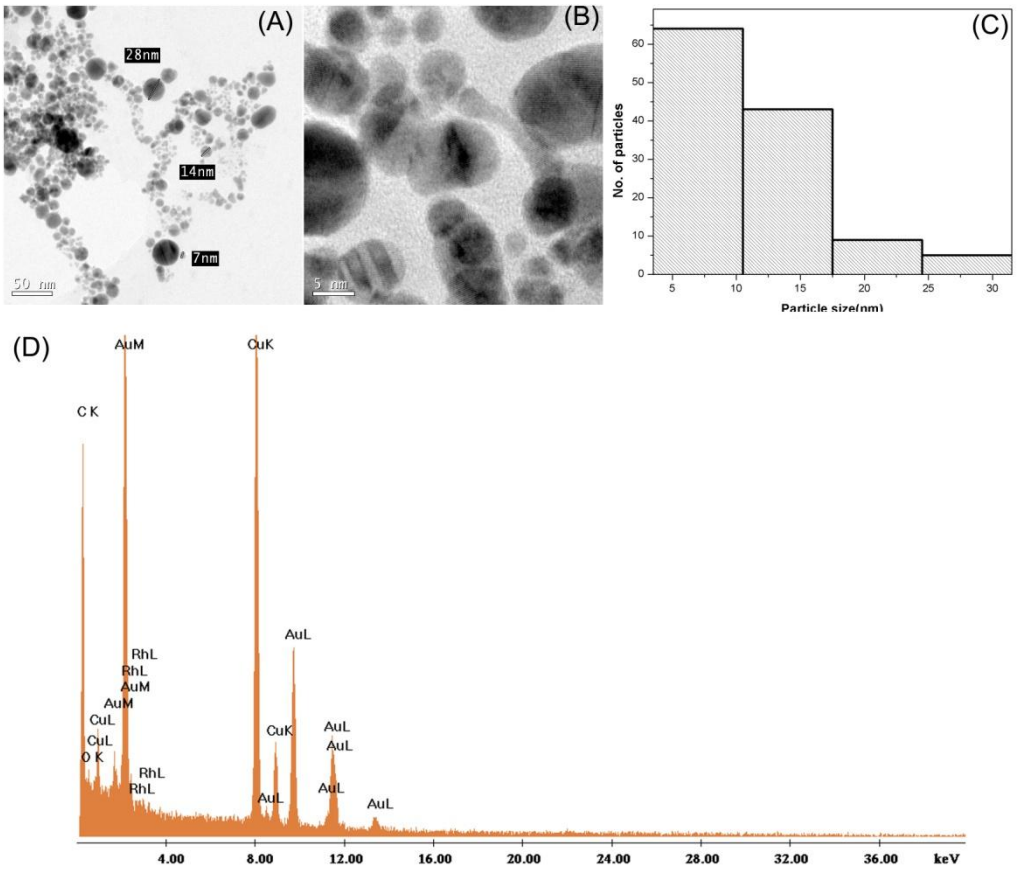

Figure 4.3: (A) Representative TEM image of Au nanoparticles produced in Rh6G doped MMA solution by laser ablation at 1064nm (B) HRTEM image showing the crystalline nature of the nanoparticles (C) Particle size distribution showing an average size of 7nm and (D) EDS showing the presence of nanoparticles and Rh6G in the solution.

As seen from Fig.4.4, two distinct extinction bands are observed for Au nanoparticles in Rh6G doped MMA. Here in this case, Rh6G doped MMA is taken as the reference. As a first inference the presence of two bands is thought of as the formation of nanorod like structures which have two bands corresponding to the oscillation of the free electrons along and perpendicular to the long axis of the rods. The transverse mode shows a resonance at about 520nm, which coincides with the plasmon band of spherical nanoparticles, while the resonance of the longitudinal mode is red shifted and strongly depends on the nanorod aspect ratio [21]. But from the TEM image shown in Fig.4.3 (A), it is confirmed that the nanoparticles formed are spherical in shape and so the distinct bands observed are due to incomplete cancellation of reference solution during recording of the spectrum.

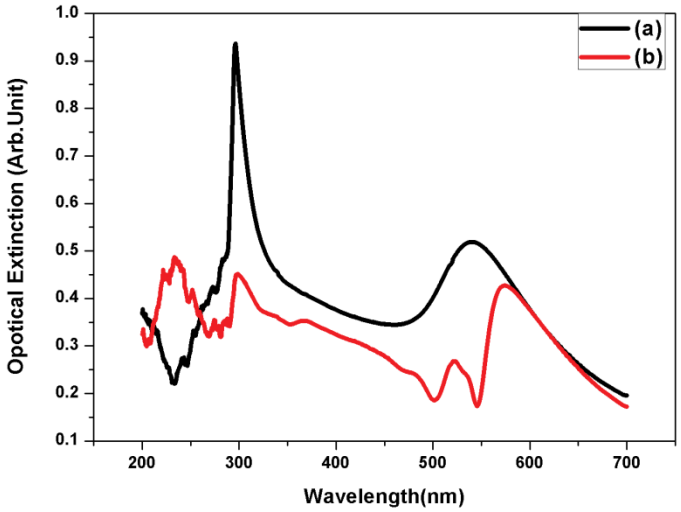

Figure 4.4: Extinction spectra showing the plasmon band of Au nanoparticles produced in (a) MMA and (b) Rh6G doped MMA solution where in the latter case Rh6G in MMA is taken as the reference.

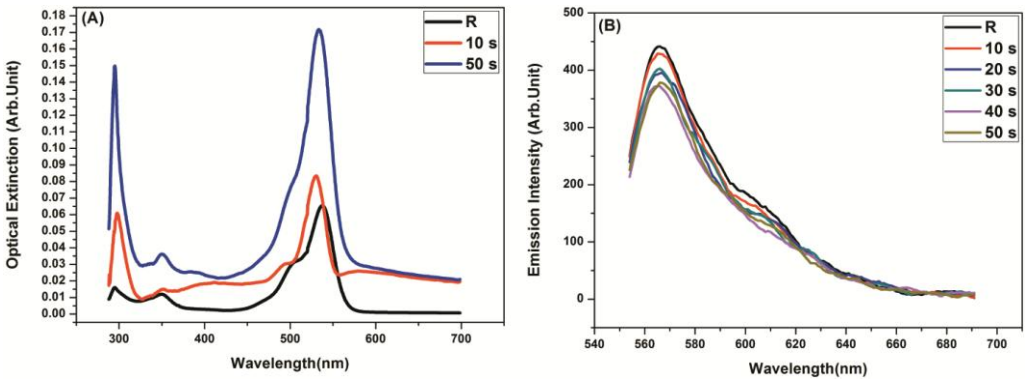

Figure 4.5: (A) Optical extinction and (B) emission spectra of Rh6G in the absence (R) and presence of Au nanoparticles formed directly in the solution by ablating for different durations.

From the optical absorption and emission spectra of Rh6G-Au nanoparticle system (Fig. 4.5(A) and Fig. 4.5 (B) respectively), it is found that the generation of nanoparticles by ablating Au plate even for a few seconds in the solution has quenched the fluorescence emission of the dye as shown in Fig.4.5 (B) whereas the net absorption of the system has enhanced (Fig.4.5 (A)). With increase in time of ablation which means increase in the concentration of Au nanoparticles in the solution, fluorescence quenching becomes prominent. Due to the difficulty and inaccuracy in the molarity calculation of Au nanoparticles formed in the solution by ablating for a few seconds, the experiment is further proceeded by adding Au nanoparticles formed

in MMA (whose molarity is already known) with Rh6G. But the average size of the nanoparticles produced in pure MMA and in Rh6G doped MMA are different.

The concentration of nanoparticles is varied as given in table.4.1. Low concentrations of Au nanoparticles are preferred to reduce its quenching effect. Low concentrations are obtained by diluting the stoke solution of Au nanoparticles produced in MMA by ablating the Au plate for 45mins. The optical extinction spectra of Au nanoparticles in MMA at such concentrations are shown in Fig.4.6. As seen from the figure, with increase in concentration of nanoparticles, the optical absorption of the plasmon band increases.

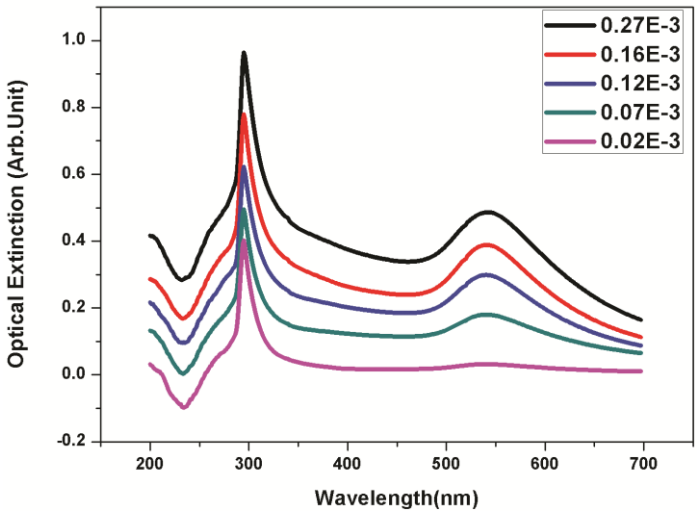

Figure 4.6: Optical extinction spectra of Au nanoparticles produced in MMA at different concentrations.

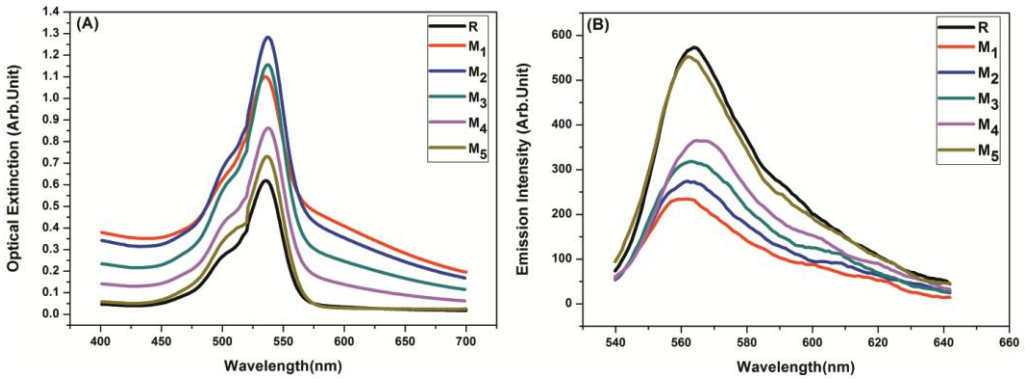

Figure 4.7: (A) Spectral absorption and (B) Emission of Rh6G-Au nanoparticle system in MMA. Excitation wavelength is 500nm.

Also the absorption spectra confirm that Au nanoparticles will be present in the solution of Rh6G even at such low concentrations. The plasmon band peaks at 540nm and the band in the UV region is due to interband transitions of Au nanoparticles as discussed in the previous chapter.

The spectral absorption and emission of Rh6G mixed with Au nanoparticles is shown in Fig.4.7. As seen from the figure, the spectral absorption of the system increases with increase in concentration of Au nanoparticles in the solution as compared to pure dye doped solution. The plasmon field generated on Au nanoparticles due to SPR strengthens the incoming field and thus the net field for exciting the fluorophore is increased so that the net absorption of Rh6G is enhanced. However, the presence of nanoparticles quenches the fluorescence intensity of the dye due to the damping of molecular dipole by the nearby metallic Au nanoparticles [9]. Rh6G molecules are adsorbed non-covalently on to the surface of Au nanoparticles [22]. The relative orientation of fluorophore's dipole with regard to metal nanoparticles determines whether the radiative rate is enhanced or quenched [9]. Luminescence quenching takes place when the energy transfer process dominates whereas enhancement occurs if the increase in radiative decay rate dominates [9, 23]. In the present case the type of energy transfer is identified as FRET due to the overlap between the emission band of Rh6G and plasmon absorption band of Au nanoparticles as shown in Fig.4.8.

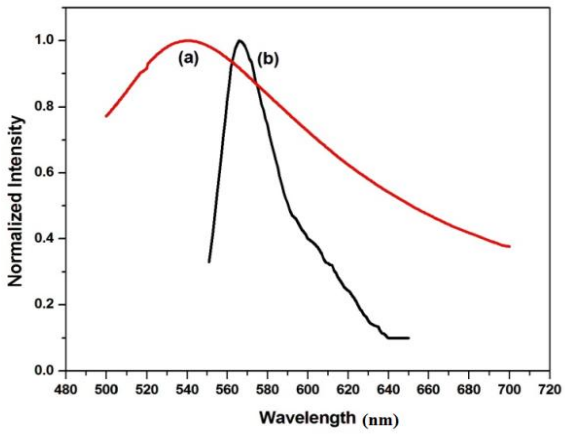

Figure 4.8: Spectral overlap between (a) plasmon band of Au nanoparticles and (b) emission band of Rh6G.

In this case Rh6G acts as the donor molecule and Au nanoparticles as the acceptor. For FRET to happen, the distance of separation between the donor and acceptor is within a few nanometers [18]. Energy transfer between the donor and acceptor takes place non-radiatively [18]. Au nanoparticles are non-fluorescent

quenchers of fluorophore's emission. Thus as seen from Fig.4.7(B), the relative intensity of Rh6G in the presence of Au nanoparticles is quenched due to the non-radiative energy transfer between the excited state molecule of the dye and the ground state Au nanoparticles. This type of process increases the total non-radiative rate of the dye due to energy transfer and radiative rate of the molecules is decreased. The dipole of the molecules and the dipole induced on Au nanoparticles radiate out of phase if the molecules are oriented tangentially to the nanoparticle's surface thereby reducing the excited state lifetime and quantum yield of the dye [24]. Quenching becomes prominent with increase in concentration of acceptor in the vicinity of the donor as seen from the Fig.4.7 (B). Thus Au nanoparticles with an average size of 2nm as well as 7nm promote quenching of the fluorescence emission of Rh6G.

4.3.1.2 Time- Resolved Fluorescence Spectroscopy

To understand the detailed mechanism of fluorescence quenching, time-resolved fluorescence spectra are recorded for all the samples. The decay curves of samples are depicted in Fig. 4.9. The decay curves are fitted with a bi exponential decay function. The intensity of decay [18] is given by

$$I(t) = \sum_i \alpha_i \exp(-t/\tau_i) \tag{4.1}$$

where $\Sigma\alpha_i$ is normalized to unity. For a large number of fluorophores, some will emit quickly following the excitation, and some will emit slowly as compared to their lifetime. This time distribution of photons which are emitted is the intensity decay curve. The lifetime obtained from the decay curve is the statistical average of the individual decays and α_i values are called the pre-exponential factors. For the same fluorophores in different environments, which usually shows the same radiative decay rates, the values of α_i represent the fractional amount of fluorophore in each environment and τ_i individual decay time [18]. From the intensity decay measurements we can calculate the lifetime (τ) of the samples. The presence of two decay times results in curvature in the plot as shown in Fig.4.9. Thus the intensity decay curves are fitted with a double exponential function rather than a single exponential function as given by the following equation.

$$I(t) = \alpha_1 e^{-t/\tau_1} + \alpha_2 e^{-t/\tau_2} \tag{4.2}$$

It is therefore concluded that the donor is partially quenched by the acceptor molecules and some of the donor molecules do not have a nearby acceptor [18]. Table

4.2 gives a complete picture of the time resolved studies of Rh6G in the absence and presence of Au nanoparticles.

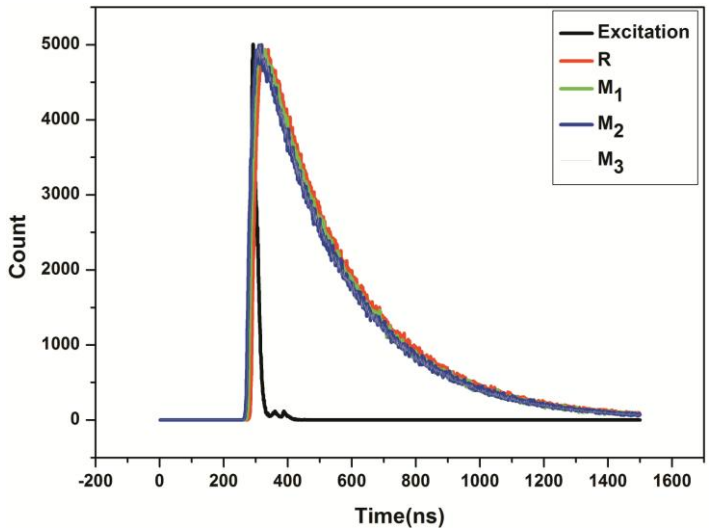

Figure 4.9: Decay curves of Rh6G doped MMA solution in the absence and presence of laser ablated gold nanoparticles. Decay curves of M_4 and M_5 are omitted due to the inappreciable change in the decay curve.

From the table it can be found that the lifetime of the sample R (containing Rh6G only) is reduced from 3.76ns to 3.6ns as observed for sample M_1. Thus with increase in the concentration of Au nanoparticles in the dye solution, much higher will be the reduction in the lifetime as evident from the table. Since lifetime changes by nearly 3% for the highest concentration of Au nanoparticles in the solution (M_1) and fluorescence intensity changes by nearly 60%, it is assumed that the rate of energy transfer is small in Rh6G-Au nanoparticle pair in MMA and there may be other types of non-radiative decay paths giving rise to complete quenching [25].

Table 4.2: Time-resolved quenching studies of Rh6G containing different concentrations of Au nanoparticles.

Sample designation	**B_1'**	**B_2'**	**τ_1(ns)**	**τ_2(ns)**	**$<\tau>=<B_1' \tau_1 + B_2' \tau_2>$ (ns)**
R	0.84	0.16	3.51	5.04	3.76
M_1	0.81	0.19	3.38	4.92	3.66
M_2	0.83	0.17	3.43	4.99	3.69
M_3	0.91	0.09	3.33	7.69	3.71

4.3.1.3 Quantum yield measurements of Rh6G in MMA

Quantum yield (QY) is an important parameter to characterize a fluorescent media in respect of device applications. It is the ratio of number of photons emitted to number of photons absorbed and its maximum value is 1. QY can be calculated through absolute method in which the radiative and non radiative rates should be known. Usually to characterize fluorescence efficiency, relative quantum yield of a fluorophore is measured by comparing with a reference fluorophore for which the quantum yield is well known. There are two methods for relative quantum yield measurements: single-point and comparative method. Using the single-point method the quantum yield is calculated from the integrated emission intensities from a single sample and reference pair at identical concentration. Comparative method of Williams et al., makes use of the slope of the line obtained by plotting the integrated fluorescence intensity against the absorption for multiple concentrations of the fluorophore [26]. In the present study comparative method is followed to calculate the quantum yield of Rh6G doped in MMA. Reference fluorophore is taken as Rh6G dissolved in distilled water for which quantum is already known. Fig.4.10 shows absorbance versus integrated fluorescence intensity of Rh6G doped in water and in MMA respectively for various concentrations of the fluorophore. From the slope of absorbance versus integrated fluorescence intensity for Rh6G in water and in MMA, the quantum yield is calculated using,

$$Q = Q_R\,(m \times n^2 / m_R \times n_R^2) \tag{4.3}$$

where R refers to the reference fluorophore of known quantum yield, m is the slope of the line obtained from the plot of absorbance versus integrated fluorescence intensity and n is the refractive index of the solvent. Refractive index of pure MMA is 1.41.

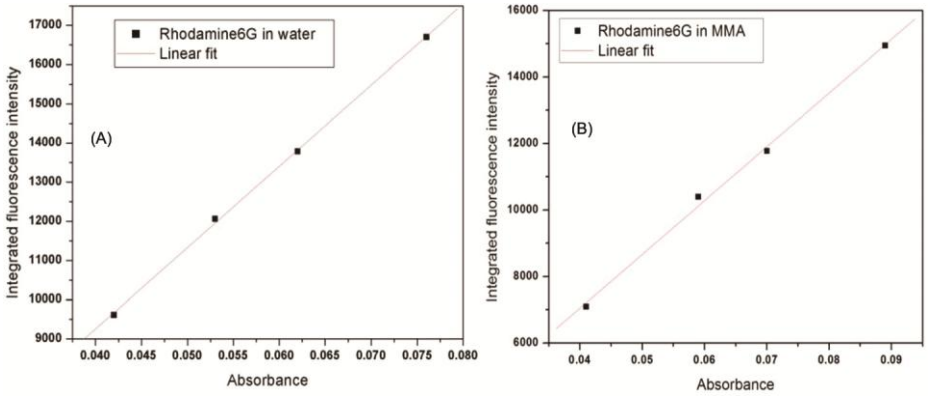

Figure 4.10: Absorbance versus integrated fluorescence intensity of Rh6G (A) in water and (B) in MMA.

Using equation (4.3), quantum yield of Rh6G in MMA is found to be 0.85. Further, the quantum yield of samples containing Au nanoparticles is determined using single point method. Quantum yield using this method is given by,

$$Q = Q_R\,(I \times OD_R \times n^2)/(I_R \times OD \times n_R^2) \tag{4.4}$$

where I is the integrated fluorescence intensity and OD is the optical density. Quantum yield of all samples are listed in table.4.3. The quantum yield of Rh6G is reduced to 80% in presence of Au nanoparticles (M_1) as compared to R. Reduction in the quantum yield of bare dye, in the presence of Au nanoparticles confirms energy transfer taking place between excited state fluorophore and nanoparticles thereby reducing the radiative emission of the dye.

4.3.1.4 Calculation of Overlap integral, Förster distance and Transfer efficiency

The overlap integral, J(λ) expresses the degree of overlap between the donor emission and the acceptor absorption [18] which is given by

$$J(\lambda) = \int F_D(\lambda)\varepsilon_A(\lambda)\lambda^4 d\lambda \tag{4.5}$$

where $F_D(\lambda)$ is the corrected fluorescence intensity of the donor in the wavelength range of λ to λ + Δ λ with the total intensity (area under the curve) normalized to unity, $\varepsilon_A(\lambda)$ is the extinction coefficient of the acceptor at λ, which is typically in units of $M^{-1}cm^{-1}$. The distance at which FRET is 50% efficient is called the Förster distance and is typically in the range of 20 to 60 Å. If the wavelength is expressed in cm and J (λ) is in units of $M^{-1}cm^3$, the Förster distance is given by

$$R_0^6 = 8.79 \times 10^{-25}\,(\kappa^2 n^{-4} Q_D\, J(\lambda))(cm^6) \tag{4.6}$$

where the term κ^2 is a factor describing the relative orientation in space of the transition dipoles of the donor and acceptor, κ^2 is usually assumed to be equal to 2/3, which is appropriate for dynamic random averaging of the donor and acceptor, n is the refractive index of the medium and Q_D is the quantum yield of the donor in the absence of the acceptor [18]. The calculated value of J(λ) and R_0 using MATLAB programme [27] for the Rh6G-Au nanoparticles system in MMA is given in table.4.3.

Efficiency of energy transfer (E) is the number of photons absorbed by the donor which are transferred to the acceptor. This is given by,

$$E = K_T(r)/(\tau_D^{-1} + K_T(r)) \tag{4.7}$$

where $K_T(r)$ is the rate of energy transfer and τ_D is the lifetime of the donor. Transfer efficiency is typically measured from the relative fluorescence intensity of the donor in the absence (D) and presence (DA) of the acceptor and is given by,

$$E = 1 - (F_{DA}/F_D) \tag{4.8}$$

Also the transfer efficiency can be calculated from the fluorescence life time of the donor in the absence and presence of the acceptor as

$$E = 1 - (\tau_{DA}/\tau_D) \tag{4.9}$$

The values obtained are given in table.4.3. The above equation (eqn 4.8) is made used for calculating the transfer efficiency. Transfer efficiency for various concentrations of the Au nanoparticles in Rh6G is also listed in Table.4.3.

Table 4.3: Variation of spectral overlap, Förster distance, lifetime, QY and transfer efficiency with respect to gold nanoparticle concentration. Concentration of Rh6G in MMA is fixed at 5×10^{-5}M.

Sample designation	**Spectral overlap (J) (10^{-14} $M^{-1}cm^3$)**	**Förster distance (R_0) (Å)**	**Lifetime τ (ns)**	**Quantum yield**	**Transfer Efficiency (E %)**
R	-----	-----	3.76	0.85	------
M_1	2.00	37.57	3.66	0.17	80
M_2	2.16	38.04	3.69	0.22	74
M_3	2.30	38.46	3.71	0.28	67
M_4	2.40	38.72	-----	0.41	52
M_5	1.79	36.88	------	0.70	18

From Table 4.3 the average value of R_0 is found to be 38 Å which is well within the range of FRET and the transfer efficiency is found to decrease with decrease in the concentration of acceptor in the solution. Because of the assumptions taken into account for the derivation of transfer efficiency calculations from photoluminescence spectra and lifetime (eqns (4.8) & (4.9)) [18], the precision in the calculation of distance of separation between the dye and the nanoparticle is not known and thus its calculation is omitted. However for a rough estimation, the calculated value of separation for M_1 is found to be 36 Å. The distance of separation

between the donor and the acceptor (r) in the present case is a few tens of Å. Since the optical properties of the system depends on the state such as liquid or solid as well as on the geometrical shape, the work is further extended to 2D and 3D structures.

4.3.2 Optical properties of Rh6G-Au nanoparticle based planar waveguide (2D structures)

Due to the transformation from liquid to solid medium, a shift in the plasmon band of Au nanoparticles is observed as shown in Fig.4.11.

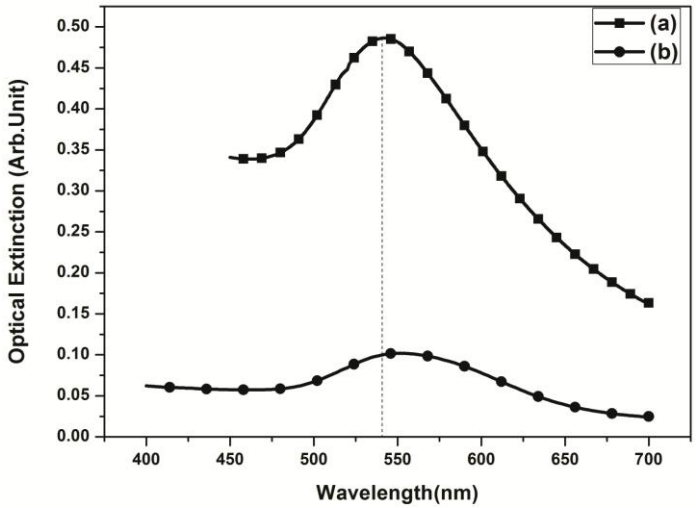

Figure 4.11: Optical absorption spectra of Au nanoparticles (a) in MMA (b) in PMMA.

A shift in peak of plasmon band from 540nm in MMA to 551nm in PMMA is noted with a corresponding broadening in the bandwidth from 72nm to 83nm respectively. Refractive index of MMA changes from 1.41 to 1.49 in PMMA. Thus the change in the plasmon band can be attributed to an increase in the dielectric function of the medium.

In order to understand the optical properties of Rh6G-Au nanoparticle system in a planar waveguide, the optical extinction and luminescence spectra are recorded for the same (not shown here). Film containing highest concentration of Au nanoparticles showed maximum absorption and minimum intensity of the emission band as observed in the case of liquid medium. LIF spectra are recorded for the film using a cw DPSS laser operating at 532nm and are shown in Fig.4.12. LIF spectra also showed a quenching of emission of the dye and this can be attributed to transfer of energy from Rh6G to Au nanoparticles by FRET. Thus it can be inferred that the separation between the donor and acceptor as well as its relative orientation is in such a way that it still favours FRET. Thus similar results are obtained as in the case of Rh6G in MMA and in PMMA.

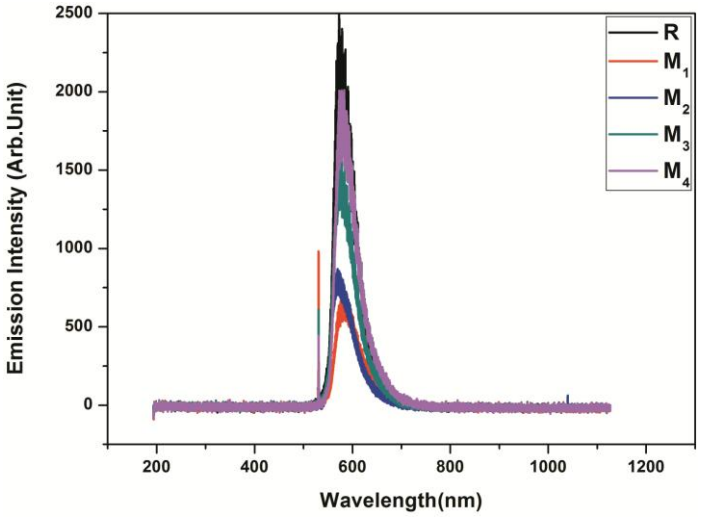

Figure 4.12: LIF of Rh6G in PMMA film with and without Au nanoparticles.

4.3.3 Rh6G-Au nanoparticles based cylindrical waveguides

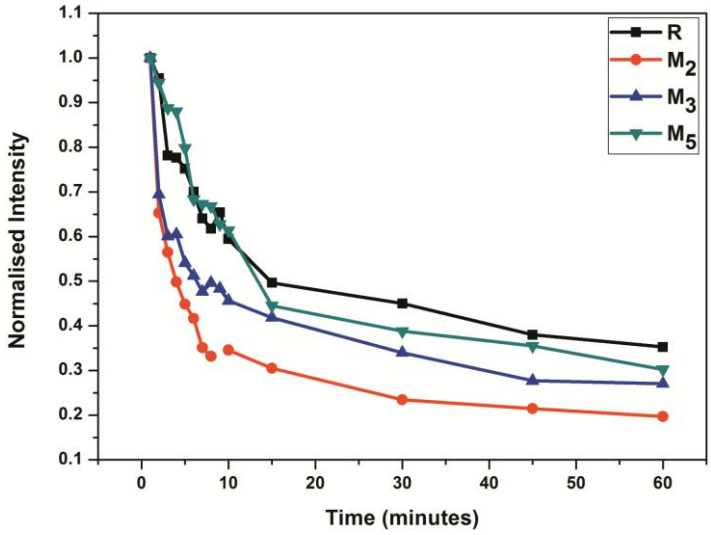

Figure 4.13: Photostability of Rh6G-Au nanoparticle based POFs having diameter of 600µm.

The photostability of the dye during its lasing action in the presence of Au nanoparticles in a microcavity is studied for making efficient fiber lasers. The rods are thus drawn to polymer fibers and its photostability (shown in Fig.4.13) in the cavity is studied using a cw laser. It is found that sample M_5 showed a slight enhancement of photostability up to 5min in the laser cavity whereas all other samples promote photobleaching as compared to bare Rh6G doped POFs (R). Half life of the dye in the

cavity increases with decrease in concentration of nanoparticles and highest half life is noted for sample R. When the concentration of the nanoparticles is high, the efficiency and thereby the rate of energy transfer is high with high deterioration of photostability. Such results reveal that enhanced photobleaching induced by metal nanoparticles is closely related to energy transfer between the dye and the nanoparticles [12, 17]. Thus it is believed that the energy transfer related photobleaching deterioration can be compensated by inducing other type of effects in the cavity which prevents quenching of the dye's emission through energy transfer mechanism. Another factor which may affect dye's stability is excessive thermal heating [12, 17] caused by the non radiative energy dissipation by the nanoparticles after FRET. Thus by reducing the rate of energy transfer, photobleaching caused by thermal heating can be reduced. For M_5, the rate of energy transfer is reduced due to low concentration of the nanoparticles and thus a better stability is exhibited during the first few minutes. However with evolution of time, the rate of bleaching increases as compared to R.

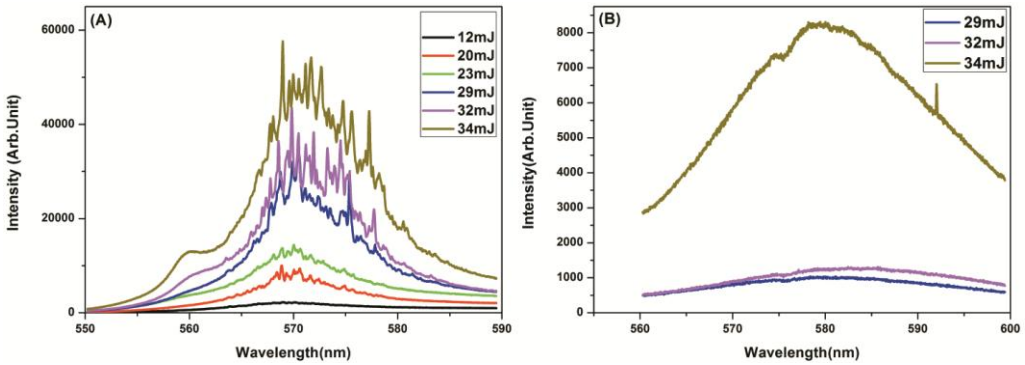

Figure 4.14: Emission from polymer fiber containing (A) Rh6G only (B) Rh6G-Au nanoparticles in the gain medium (M_5). Intensity scale on both graphs are arbitrary so cannot have a emission intensity comparison.

Thus it is concluded that the presence of Au nanoparticles in the microcavity can't promote a high photostability for a prolonged time. Photostability of the fibers with varying diameters are recorded and it is found that photostability increases with increase in diameter of the fiber. This effect is similar to increasing the concentration of the dye thereby increasing the photostability.

In order to understand the influence of Au nanoparticles in the lasing characteristics of Rh6G, both are incorporated in the optical fiber of 440µm diameter and a length of 5cm. Fig.4.14 (A) and (B) is the spectral emission characteristics of R and M_5 respectively. As seen from the figure, R exhibits a normal luminescence spectrum when pumped at 12mJ and spectral narrowing which are the characteristics of amplified spontaneous emission is observed when pumped at 20mJ. Spectral narrowing from 40nm to 11nm is observed at this pump energy. Also some lasing

modes are observed at the peak of ASE when pumped above 25mJ. Absence of well resolved WGM modes may be attributed to the low gain of the amplifying medium providing not enough gain to have well resolved and sustained WGM modes. Fig.4.14 (B) represents the spectral emission of POFs with gain medium containing Au nanoparticles (M_5) along with Rh6G. As seen from the figure, no spectral narrowing or lasing is observed even when pumped at 34mJ. Linewidth narrowing from 40nm to 32nm is observed when pumped at such high pump energy. This means that lasing action of Rh6G in presence of Au nanoparticles is deteriorated due to the energy transfer from excited state dye molecules to ground state Au nanoparticles thereby decreasing the rate of radiative emission from the dye molecule during lasing. All other samples containing even higher concentration of Au nanoparticles (such as M_2, M_3 and M_4) not even showed a linewidth narrowing when pumped at 34mJ. When pumped above 34mJ, all samples are subjected to photobleaching.

4.3.4 Lasing from Au doped hollow POFs filled with Rh6G

Further, hollow Au doped polymer optical fibers and bare hollow fibers having comparable ratio of outer to inner diameter (430µm/200µm) is filled with Rh6G (10^{-4}M) in aqueous solution. Fig.4.15 depicts the photograph of Au doped hollow optical fiber before filling the dye solution. Fig.4.16 depicts the spectral emission characteristics of such fibers when filled with Rh6G. A comparison of emission intensity cannot be done since the intensity scales are taken to be arbitrary. However it can be clearly seen that both fibers exhibits a spectral narrowing due to ASE when pumped at 20mJ.

Figure 4.15: Photograph of Au nanoparticles doped hollow fiber under a CCD camera. Violet colour is the characteristics of Au nanoparticles in MMA environment.

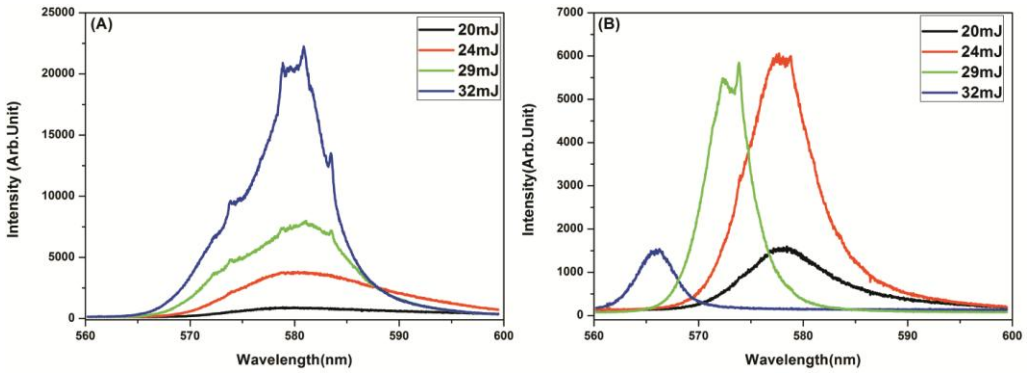

Figure 4.16: Emission spectra of (A) Hollow fiber filled with Rh6G (B) Au doped hollow fiber filled with Rh6G of same molarity when pumped at different energies.

For hollow PMMA fiber filled with dye when pumped at high energy such as 32mJ, further spectral narrowing is observed with enhanced intensity. But for Au doped hollow fiber filled with dye, as pump energy is increased, a blue shift in the emission peak with decreased intensity is observed. The reduced intensity can be attributed to the FRET mediated photobleaching of the dye in the vicinity of pump pulses. When the pump energy is further increased, quenched emission with further blue shift in the emission peak due to high rate of photobleaching is observed. This result matches with the enhanced photobleaching rate of solid fibers containing Rh6G and Au nanoparticles in the gain medium. When the pump energy is increased beyond 32mJ, a complete bleaching of the dye is observed in both cases. Thus presence of Au nanoparticles deteriorates the lasing of Rh6G doped fiber laser.

4.4 Conclusions

- Au nanoparticles produced in MMA and in Rh6G doped MMA solution by physical method showed an increment in average size of the particles, from 2nm to 7nm. This is due to change in dielectric constant of the medium in the presence of dye molecules.
- Optical emission spectra recorded for Au nanoparticles produced directly in Rh6G medium by ablating for just a few seconds showed fluorescence quenching. Similar results are observed when Au nanoparticles of 2nm are introduced in Rh6G medium with varying concentrations. From the spectral overlap between the emission of dye and absorption of nanoparticles, it is found that FRET is responsible for emission quenching by increasing the non-radiative decay rate and reducing the radiative decay rate.
- From lifetime and QY measurements, it is further confirmed that FRET type of quenching takes place in Rh6G-Au nanoparticle system. Both lifetime and

quantum yield are found to be decreased with respect to increase in concentration of Au nanoparticles in the medium.

- Spectral overlap integral, Forster distance and transfer efficiencies are also found out for Rh6G-Au nanoparticle system in MMA. Also a rough estimation of the distance of separation between the donor and acceptor are found out.
- Planar waveguides are fabricated with Rh6G-Au nanoparticles in PMMA and a fluorescence quenching is noticed in this case too.
- Cylindrical waveguides such as POFs are also fabricated with Au nanoparticles in the gain medium and lasing as well as photostability measurements are done. Both lasing as well as photostability are found to be deteriorated in the presence of Au nanoparticles.

References

[1] Borriello, Antonella, P. Agoretti, A. Cassinese, P. D'Angelo, G. T. Mohanraj, and L. Sanguigno. "Electrical bistability in conductive hybrid composites of doped polyaniline nanofibers-gold nanoparticles capped with dodecane thiol."Journal of nanoscience and nanotechnology 9, no. 11 (2009): 6307-6314.

[2] Hu, Chih-Wei, Yuming Huang, and Raymond Chien-Chao Tsiang. "Thermal and spectroscopic properties of polystyrene/gold nanocomposite containing well-dispersed gold nanoparticles." Journal of nanoscience and nanotechnology 9, no. 5 (2009): 3084-3091.

[3] Ghosh, Debanjana, and Nitin Chattopadhyay. "Gold nanoparticles: acceptors for efficient energy transfer from the photoexcited fluorophores." Optics and Photonics Journal 3, no. 01 (2013): 18-26.

[4] Dubertret, Benoit, Michel Calame, and Albert J. Libchaber. "Single-mismatch detection using gold-quenched fluorescent oligonucleotides." Nature biotechnology 19, no. 4 (2001): 365-370.

[5] Maxwell, Dustin J., Jason R. Taylor, and Shuming Nie. "Self-assembled nanoparticle probes for recognition and detection of biomolecules." Journal of the American Chemical Society 124, no. 32 (2002): 9606-9612.

[6] Dulkeith, E., A. C. Morteani, T. Niedereichholz, T. A. Klar, J. Feldmann, S. A. Levi, F. C. J. M. Van Veggel, D. N. Reinhoudt, M. Möller, and D. I. Gittins. "Fluorescence quenching of dye molecules near gold nanoparticles: radiative and nonradiative effects." Physical review letters 89, no. 20 (2002): 203002.

[7] Cheng, Pearl Pui Hang, Debbie Silvester, Gangli Wang, Gregory Kalyuzhny, Alicia Douglas, and Royce W. Murray. "Dynamic and static quenching of fluorescence by 1-4

nm diameter gold monolayer-protected clusters." The Journal of Physical Chemistry B 110, no. 10 (2006): 4637-4644.

[8] Kang, Kyung A., Jianting Wang, Jacek B. Jasinski, and Samuel Achilefu. "Fluorescence manipulation by gold nanoparticles: from complete quenching to extensive enhancement." J. Nanobiotechnol 9 (2011): 16.

[9] Karthikeyan, B. "Fluorescence quenching of Rhodamine-6G in Au nanocomposite polymers." Journal of Applied Physics 108, no. 8 (2010): 084311.

[10] Sen, Tapasi, Suparna Sadhu, and Amitava Patra. "Surface energy transfer from rhodamine 6G to gold nanoparticles: A spectroscopic ruler." Applied Physics Letters 91, no. 4 (2007): 043104.

[11] Popov, O., A. Zilbershtein, and D. Davidov. "Random lasing from dye-gold nanoparticles in polymer films: enhanced gain at the surface-plasmon-resonance wavelength." Applied physics letters 89, no. 19 (2006): 191116.

[12] Dong, Lin, Fei Ye, Adnan Chughtai, Sergei Popov, Ari T. Friberg, and Mamoun Muhammed. "Photostability of lasing process from water solution of Rhodamine 6G with gold nanoparticles." Optics letters 37, no. 1 (2012): 34-36.

[13] Xie, Zhiguo, Jun Tao, Yonghua Lu, Kaiquan Lin, Jie Yan, Pei Wang, and Hai Ming. "Polymer optical fiber SERS sensor with gold nanorods." Optics Communications 282, no. 3 (2009): 439-442.

[14] Aslan, Kadir, Ignacy Gryczynski, Joanna Malicka, Evgenia Matveeva, Joseph R. Lakowicz, and Chris D. Geddes. "Metal-enhanced fluorescence: an emerging tool in biotechnology." Current Opinion in Biotechnology 16, no. 1 (2005): 55-62.

[15] De, Mrinmoy, Partha S. Ghosh, and Vincent M. Rotello. "Applications of nanoparticles in biology." Advanced Materials 20, no. 22 (2008): 4225-4241.

[16] Dong, Lin, Fei Ye, Jun Hu, Sergei Popov, Ari T. Friberg, and Mamoun Muhammed. "Fluorescence quenching and photobleaching in Au/Rh6G nanoassemblies: impact of competition between radiative and non-radiative decay." Journal of the European Optical Society-Rapid publications 6 (2011).

[17] Dong, Lin, Fei Ye, Adnan Chughtai, Vytautas Liuolia, Sergei Popov, Ari T. Friberg, and Mamoun Muhammed. "Lasing From Water Solution of Rhodamine 6G/Gold Nanoparticles: Impact of-Coating on Metal Surface." Quantum Electronics, IEEE Journal of 48, no. 9 (2012): 1220-1226.

[18] Lakowicz, Joseph R. Principles of fluorescence spectroscopy. Springer Science & Business Media, 2007.

[19] Kurian, Achamma, Nibu A. George, Binoy Paul, V. P. N. Nampoori, and C. P. G. Vallabhan. "Studies on fluorescence efficiency and photodegradation of rhodamine 6G doped PMMA using a dual beam thermal lens technique." Laser Chemistry 20, no. 2-4 (2002): 99-110.

[20] Huffman, DONALD R., and Craig F. Bohren. "Absorption and scattering of light by small particles." Wiley Science Paperback Series, John Wiley & Sons, New York, NY, USA 7, no. 1 (1983): 7-5.

[21] Link, Stephan, and Mostafa A. El-Sayed. "Spectral properties and relaxation dynamics of surface plasmon electronic oscillations in gold and silver nanodots and nanorods." The Journal of Physical Chemistry B 103, no. 40 (1999): 8410-8426.

[22] Chang, Hsin-Yun, Tung-Ming Hsiung, Yu-Fen Huang, and Chih-Ching Huang. "Using rhodamine 6G-modified gold nanoparticles to detect organic mercury species in highly saline solutions." Environmental science & technology 45, no. 4 (2011): 1534-1539.

[23] Soller, T., M. Ringler, M. Wunderlich, T. A. Klar, J. Feldmann, H-P. Josel, Y. Markert, A. Nichtl, and K. Kürzinger. "Radiative and nonradiative rates of phosphors attached to gold nanoparticles." Nano Letters 7, no. 7 (2007): 1941-1946.

[24] Dulkeith, E., M. Ringler, T. A. Klar, J. Feldmann, A. Munoz Javier, and W. J. Parak. "Gold nanoparticles quench fluorescence by phase induced radiative rate suppression." Nano Letters 5, no. 4 (2005): 585-589.

[25] Sebastian, Suneetha, C. Ajina, CP G. Vallabhan, V. P. N. Nampoori, P. Radhakrishnan, and M. Kailasnath. "Fabrication and photostability of rhodamine-6G gold nanoparticle doped polymer optical fiber." Chinese Physics Letters 30, no. 11 (2013): 118101.

[26] Michael W. Allen, Thermo Fisher Scientific, Madison, WI, USA, Technical Note: 52019

[27] MIT online course “Calculation of R_0 from spectral overlap with MATLAB”

Chapter 5 :

Impact of Ag nanoparticles on Dye Doped Polymer Optical Fibers

---

The present chapter we have studied the impact of Ag nanoparticles produced in different media, such as MMA and ethanol, on the optical properties of Rh6G. Average size and size distributions of Ag nanoparticles are obtained from TEM images. Optical absorption and emission spectra of the system are recorded. Results supporting Metal Enhanced Fluorescence have been obtained from quantum yield measurements and Time Resolved Fluorescence Spectroscopy. Further, the dye medium along with the nanoparticles is incorporated in polymer optical fibers and the effect of nanoparticles on the lasing property of the fibers are found out.

Publications

Sebastian, S., C. L. Linslal, C. P. G. Vallabhan, V. P. N. Nampoori, P. Radhakrishnan, and M. Kailasnath. "Random lasing with enhanced photostability of silver nanoparticle doped polymer optical fiber laser." Laser Physics Letters 11, no. 5 (2014): 055108.

5.1 Introduction

Wide range of applications of dyes are mainly due to its spontaneous emission in optically transparent non-conducting media. But recently it is found that the environment of the fluorophore can be modified or engineered by the presence of conducting metal nanoparticles to alter the radiative decay rate [1-3]. This field is known as Radiative Decay Engineering (RDE). It is well known that size and geometry of the nanoparticles determines the properties of the localised surface plasmons it supports [4].

From ancient time onwards Ag has been used widespread in photography and staining of biological samples. Silver also has the highest thermal and electrical conductivity among all metals making it suitable for various applications. Among various metal nanoparticles such as gold and copper, Ag has the highest plasmon strength in the visible and NIR region i.e., 300nm-1200nm [5]. Also Ag nanoparticles have advantages such as extremely high field enhancement, which makes them useful in radiative decay engineering [6].

5.1.1 Metal Enhanced Fluorescence

When light is incident on the fluorophore, it gets excited and an excited fluorophore can be considered as an oscillating dipole. The excited fluorophore can cause oscillations of the conduction electrons in the nearby metal thus producing an electric field around the nanoparticles. The field in turn can interact with the excited state fluorophore and thereby altering its emission. The interaction is thought to be bidirectional and such interaction of fluorophore with metal nanoparticles can have a number of useful effects such as increased QY, increased photostability and decreased lifetimes [3, 5].

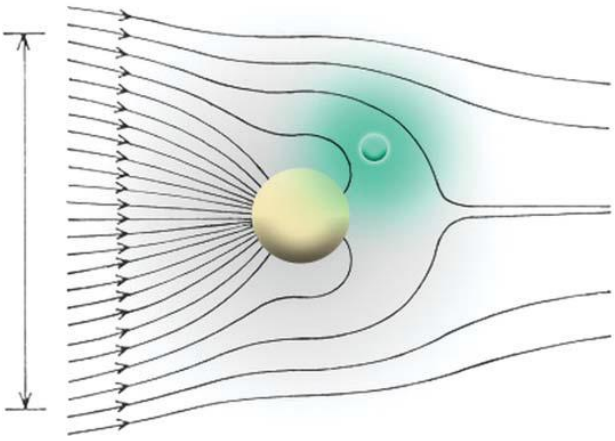

Figure 5.1: Interaction of metal nanoparticle with incident electric field. Lines represent the direction of propagation of light. Also shown in green colour is a fluorophore in the near-field of the particle [7].

The spectral properties of an excited state fluorophore are well described by Maxwell's equations for an oscillating dipole radiating into free space. In the presence of metal nanoparticles, the rate of excitation of the fluorophore can be increased due to more concentrated electric field around the particle as shown in Fig.5.1. Metal nanoparticles can also increase the radiative decay rate of the fluorophore thus leading to unusual effect on fluorophore's emission. These effects can be understood further by considering a Jablonski diagram which includes MEF as shown in Fig.5.2 [7].

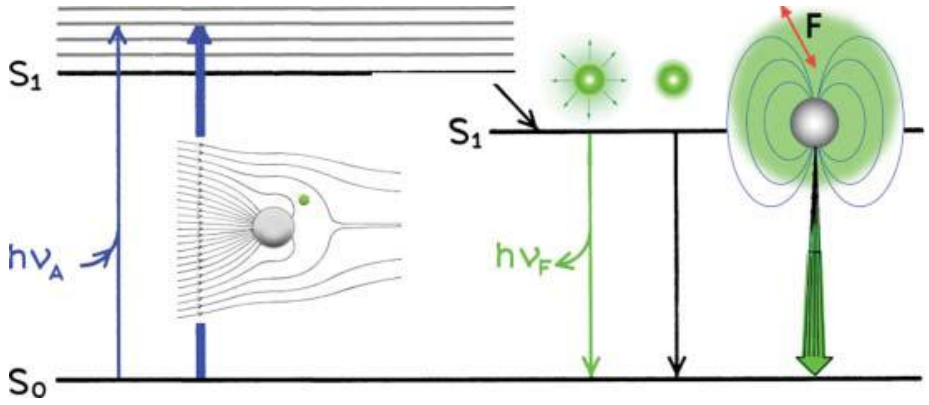

Figure 5.2: Modified Jablonski diagram which includes metal–fluorophore interactions. The thicker arrows represent increased rates of excitation and emission in presence of nanoparticles. Black line shown is the non-radiative decay path (K_{nr}) [7].

In classical fluorescence experiments any change in the quantum yield (Q_0) and lifetime (τ_0) of the fluorophore are due to changes in the non-radiative decay rates which results in altering of fluorophore's environment. The values of Q_0 and τ_0 either both increase or decrease in the same direction. But in the presence of metal nanoparticles the radiative rate is increased giving an additional radiative decay path. The equations are given in section 5.3.2. This can lead to increase in QY of the fluorophore with decrease in lifetime which is not possible in classical fluorescence experiments [2, 5, 7-9]. The solid physics behind MEF can be found elsewhere [10-11].

5.2.1 Nanomaterial Surface Energy Transfer

The quenching of the fluorescence of the dye can be attributed to the damping of the molecular dipole by metal nanoparticles and further transferring the energy between the excited state fluorophore and ground state metal nanoparticles. This leads to an increase in the non radiative decay rate of the fluorophore thereby reducing the QY and lifetime of the fluorophore. In general, the donor (fluorophore) and the acceptor (metal nanoparticles) are considered as dipoles and the energy transfer between them is explained by FRET mechanism [12]. But some of the recent research work indicates that the Nanomaterial Surface Energy Transfer (NSET) is more

adequate in explaining the energy transfer between the dye molecule and the metal nanoparticles [13-17]. Importance of SET in the present case is that it does not require a resonant electronic transition as in the case of FRET [16]. However both these mechanisms can behave as a spectroscopic ruler around the nanoparticle and can throw light on the dielectric environment around the nanoparticle in a dye-nanoparticle system [2]. Persson-Lang [18] has already illustrated the d^{-4} dependence of dye quenching at a metal surface where d is the separation between donor and acceptor. According to their model the form of dipole-surface energy transfer rate is given by,

$$K_{SET} = \frac{1}{\tau_D}\left(\frac{d_0}{d}\right)^4 \tag{5.1}$$

where τ_D is the lifetime of the donor in the absence of the acceptor and d_0 is the distance between the donor and the acceptor at which 50% quenching of donor's emission occurs. According to Persson and Lang's model, the rate of energy transfer is found out by a Fermi golden rule calculation for an excited state molecule depopulating with simultaneous scattering of an electron in the nearby metal to above the Fermi level [16]. Thus we can understand that FRET follows a d^{-6} dependence whereas NSET follows a d^{-4} dependence.

5.2 Experimental Section

Silver nanoparticles of different size distributions are produced using nanosecond and femtosecond lasers in different liquid media such as MMA and ethanol for the present study using the same experimental setup described in chapter 2. Concentrations of Ag nanoparticles are varied by dispersing various quantities of the stoke solution of nanoparticles in Rh6G doped MMA solution using a micropipette. The dispersed solution of Rh6G-Ag nanoparticles are sonicated well before experiments and it is characterised at the same time of its formation due to stability problems. Details of the concentration of Rh6G and Ag nanoparticles are given in the following sections of results and discussions.

Since the system of Rh6G-Ag nanoparticles are dispersed in MMA, it is directly polymerised into preforms and drawn to polymer optical fibers. Fig.5.3 is the schematic representation of the measurement set-up of transverse excitation and emission from the fiber. Enlarged view shows the cross-section of the fiber containing Rh6G and Ag nanoparticles. Photostability measurements of all set of fibers are also carried out. Details of the fiber diameter and length are given in the following sections.

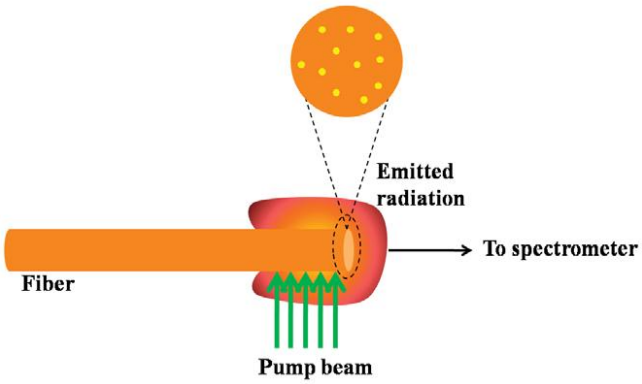

Figure 5.3: Schematic of the experimental setup for lasing from polymer fibers

5.3 Result and discussions

5.3.1 Fluorescence quenching in the presence of Ag nanoparticles by NSET

Ag nanoparticles are produced in MMA using ns Nd-YAG laser operating at 1064nm. Surface plasmon band peaks around 403nm with a width of 90nm. The average size of Ag nanoparticles is found to be 7nm (as detailed in chapter 3). It is well known that metal nanoparticles at high concentration interacting with dye molecules results in quenching of spectral emission of the dye. Therefore the concentration of the nanoparticles in the solution of Rh6G doped MMA is maintained at low.

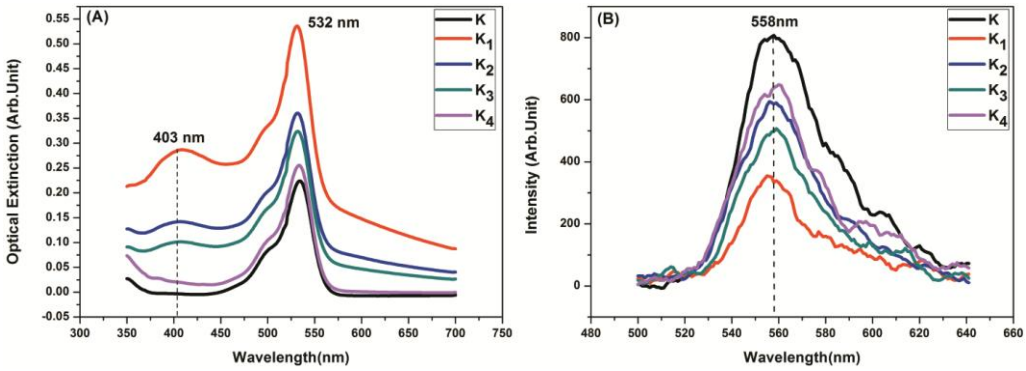

Figure 5.4: (A) Optical absorption spectra and (B) Emission spectra of Rh6G in the presence and absence of Ag nanoparticles in MMA. K (contains Rh6G only) is taken as the reference. Emission spectra are recorded by exciting the samples at 500nm.

Fig.5.4 (A) shows the absorption spectra of Rh6G dissolved in MMA in the presence and absence of Ag nanoparticles. The peak at 532nm is due to the S_0-S_1 electronic transition of the Rh6G molecules and the shoulder at 500nm is due to the vibronic transition [19]. Addition of Ag nanoparticles enhanced the electronic and vibronic

transitions of the dye and a new peak is observed around 400nm. The new peak is attributed to the plasmon band of Ag nanoparticles and the intensity of the band increases with increase in concentration of nanoparticles. Also the net absorption of the dye is increased with increase in concentration of Ag nanoparticles. The presence of Ag nanoparticles increases the local incident electric field on the dye thereby increasing its net absorption and rate of excitation of the dye molecules. Transitions of the excited state molecules residing in the electronically excited singlet state to the ground state results in the fluorescence of the dye. Emission spectra of dye molecules showed quenching effect in the presence of Ag nanoparticles produced in MMA as is depicted in Fig.5.4 (B). In the present case Rh6G acts as the donor and Ag nanoparticles act as the acceptor. Concentration details of Ag nanoparticles are given in Table.5.1 and concentration of Rh6G is taken to be 5×10^{-5}M in MMA. Since quenching effect is dominant it is assumed that the dipole of the dye molecules is damped by Ag nanoparticles through NSET. The spectral overlap between the optical absorption spectra of Ag nanoparticles and emission spectra of Rh6G both dispersed individually in MMA is shown in Fig.5.5 and we can see that there is no appreciable overlap between them, which can support NSET since it does not require a resonant electronic transition between the donor and the acceptor.

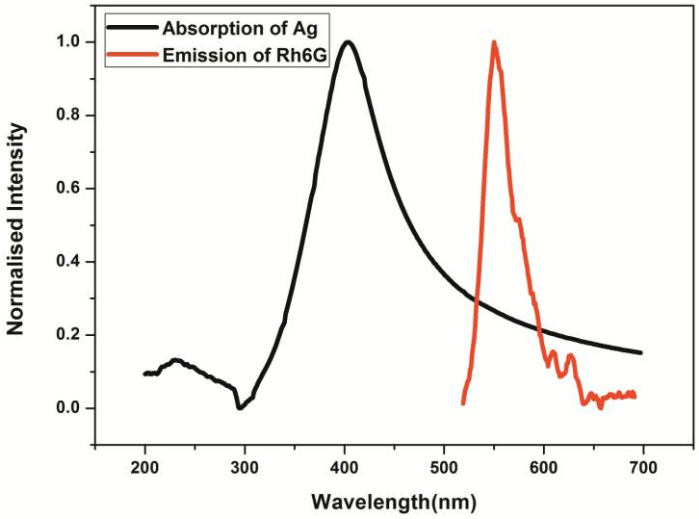

Figure 5.5: Spectral overlap between the absorption spectra of the nanoparticles and emission spectra of Rh6G. Ag nanoparticles are generated in MMA by ns laser.

A quantitative relation between the concentration of the acceptor and the emission intensity of the donor can be obtained from the well known Stern-Volmer equation

$$F_D / F_{DA} = 1 + K_{SV}[A] \tag{5.1}$$

where F_D and F_{DA} are the relative emission intensity of the donor in the absence and presence of the acceptor respectively and K_{SV} is the Stern-Volmer dynamic quenching constant and [A] is the concentration of the acceptor. Plot of ratio of intensities of the donor in the absence and presence of acceptor (F_D / F_{DA}) versus concentration of Ag nanoparticles is shown in Fig.5.6. The graph is linearly fitted and the value of the quenching constant is obtained from the slope of the line and is found to be $5.37\times10^{3}M^{-1}$. The distance between the donor and the acceptor at which 50% quenching of donor's emission occurs is calculated [20] using

$$d_0 = \frac{7.35}{([A]_{1/2})^{1/3}} \tag{5.2}$$

where $[A]_{1/2}$ is the half quenching concentration of the acceptor.

Table 5.1: Variation of efficiency of energy transfer between Rh6G and Ag nanoparticles and QY of the dye with varying concentration of Ag nanoparticles

Sample designation	**[Ag] (M)**	**ϕ_{ET} (%)**	**QY**
K_1	2.25×10^{-4}	55	0.15
K_2	1×10^{-4}	37	0.35
K_3	7.5×10^{-5}	26	0.37
K_4	2.5×10^{-5}	19	0.45

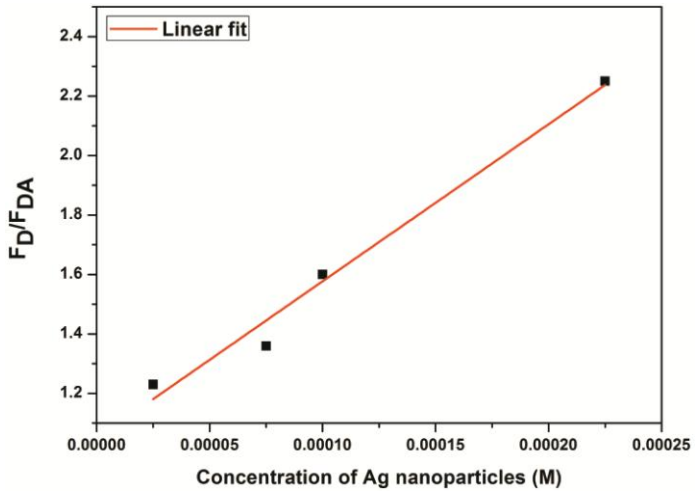

Figure 5.6: The variation of ratio of intensity of Rh6G in the presence and absence of acceptor with respect to the concentration of Ag nanoparticles.

By substituting the value of concentration of the acceptor in equation (5.2), d_0 is found to be 120Å. Theoretically the value of d_0 can be calculated using Persson model [21]

$$d_0 = \left(0.225 \frac{c^3 \phi_{dye}}{\omega_{dye}^2 \omega_F K_F} \right)^{1/4} \tag{5.3}$$

where c is the speed of light in cm s^{-1} , Φ_{dye} is the quantum efficiency of the dye in the medium, ω_{dye} is the frequency of the donor electronic transition, ω_F is the Fermi frequency and K_F is the Fermi wave vector for the metal. In the case of Rh6G–Ag NP system in MMA the quantum yield of the dye is 0.85, $\omega_{dye} = 3.6\times10^{15}$ s^{-1}, $\omega_F = 8.3\times 10^{15}$ s^{-1} and $K_F = 1.2\times10^{8}cm^{-1}$[22]. Substituting these values in the above equation yields d_0 as 80 Å. A difference of 40Å between experimentally and theoretically calculated values can be noticed. However the calculated value suggests that the quenching mechanism in the present case is NSET since in the case of FRET the typical value of d_0 is below 60Å [23]. Thus NSET can probe higher distance around the metallic nanoparticle. The efficiency of energy transfer from dye to Ag nanoparticles can be calculated using fluorescence measurement (shown in Fig.5.4 (B)) given by,

$$\phi_{ET} = 1 - \frac{F_{DA}}{F_D} \tag{5.4}$$

The values of efficiency are detailed in Table.5.1. It is found that efficiency of energy transfer increases with increase in concentration of the nanoparticles. Efficiency becomes 50% at 2.25×10^{-4}M concentration of Ag nanoparticles where the distance of separation between the dye molecules and the nanoparticles is nearly 80Å.

Decrease of QY of Rh6G with increase in concentration of Ag nanoparticles is calculated using single point method as detailed in the previous chapter and its values are given in Table.5.1. Further decrease in concentration of Ag nanoparticles below the lowest value taken in the present study yielded no further increase in the emission intensity or quantum yield. Thus it is found that Ag nanoparticles having an average diameter of 7nm generated in MMA resulted in quenching of dye's emission through NSET.

5.3.2 Metal Enhanced Fluorescence by Ag nanoparticles in lasing

It is found that Ag nanoparticles produced in ethanol by nanosecond and femtosecond lasers showed enhancement in the fluorescence emission of Rh6G. Surface plasmon resonance of Ag nanoparticles produced in ethanol by fs laser show a broad band with peak of the band at around 430nm. Low polarity of ethanol generated a weak electric double layer around the nanoparticles with non uniform distribution of

charges such that it leads to a broad size distribution with large size and less stability as compared to nanoparticles produced in high polar medium such as water. As reported in chapter 3, the stability and position of plasmon band of nanoparticles generated by femtosecond laser depend on the position of the target of silver plate with respect to the focal point of the lens. Accordingly, stable Ag nanoparticles are produced by placing the target 1cm ahead of the focal point during ablation and plasmon band of such nanoparticles peaked at around 430nm and are found to be stable for 2 days.

From Fig.5.7 we have seen that the optical absorption and emission of the dye is enhanced in the presence of Ag nanoparticles produced in ethanol. Maximum enhancement in the emission intensity is noticed for Ag nanoparticles with a concentration of 4×10^{-7}M. Presence of Ag nanoparticles below this concentration is difficult to identify since at this concentration the absorbance of Ag nanoparticles is only around 0.001. Decrease in the concentration below this optimum value yielded less fluorescence enhancement.

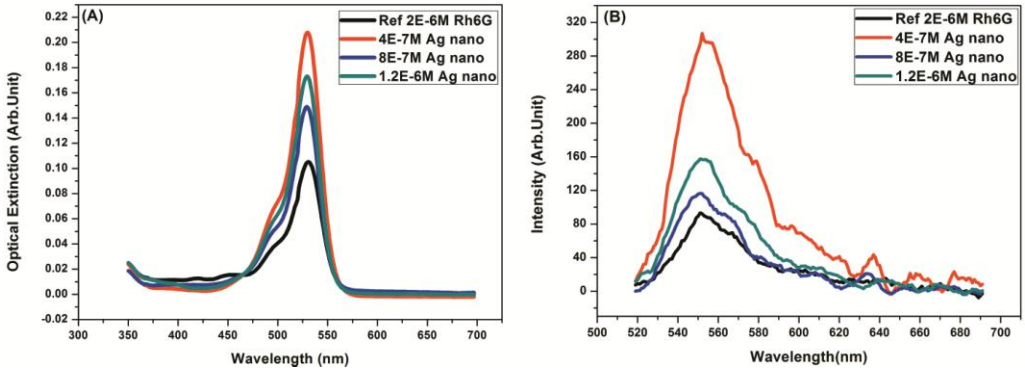

Figure 5.7: (A) Optical absorption and (B) Emission spectra of Rh6G in the absence and presence of Ag nanoparticles produced in ethanol by fs laser.

As can be seen from the previous section, Ag nanoparticles produced in MMA with nearly same concentration as discussed in this section showed fluorescence quenching whereas Ag nanoparticles produced in ethanol showed a 3-fold enhancement of emission. Increase in absorption of the dye molecules is due to the increase in the strength of the incident field on the dye due to metal nanoparticles leading to an increase in the rate of excitation. We have seen that emission of the dye is enhanced at wavelengths where Ag nanoparticles do not display a strong plasmon resonance. However it is reported that metal nanoparticles can enhance fluorescence, even if there is no plasmon resonance at the emission wavelength of the dye because of the near field interactions between the two. Absence of a resonance means that far-field radiation does not interact with the particle [24]. Increase in the rate of excitation of dye molecules in the presence of Ag nanoparticles doesn't mean that this can solely

lead to the enhancement of dye's emission since we have observed an increase in the rate of excitation leading to fluorescence quenching. An increase in excitation is not expected to change the decay time of the dye [24]. In contrast, it is reported that an increase in the radiative decay rate of a fluorophore will decrease the lifetime [8, 24].

Fig.5.8 shows the time resolved fluorescence spectra of Rh6G in the absence and presence of nanoparticles. The decay curves are fitted with double exponential function and it is found that the lifetime of the fluorophore is decreased in the presence of Ag nanoparticles produced in ethanol by fs laser. Lifetime of Rh6G alone is 3.8ns and is reduced to 3.51ns in the presence of 4×10^{-7}M concentration of Ag nanoparticles which gives maximum emission enhancement for the dye. Also the quantum yield of the dye at this concentration of Ag nanoparticles increases from 0.85 to 0.97.

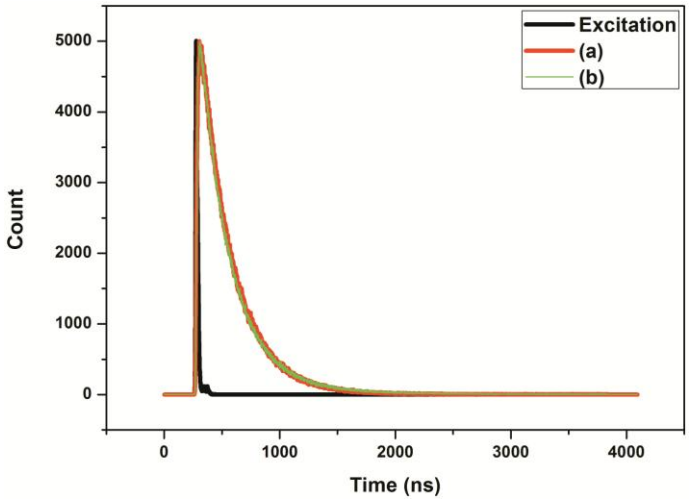

Figure 5.8: Time resolved fluorescence spectra of (a) Rh6G alone (b) Rh6G containing 4×10^{-7}M Ag nanoparticles produced in ethanol by fs laser.

In the case of free space emission of the fluorophore the quantum yield and lifetime can be expressed [9] as

$$Q_0 = \frac{\Gamma}{\Gamma + K_{nr}} \tag{5.5}$$

$$\tau_0 = \left(\Gamma + K_{nr}\right)^{-1} \tag{5.6}$$

where Γ is the radiative decay rate and K_{nr} is the non radiative decay rate of the fluorophore. In the presence of metal nanoparticles if the radiative decay rate is increased, then the above equations is modified [9] as

$$Q_m = \frac{\Gamma + \Gamma_m}{\Gamma + \Gamma_m + K_{nr}} \tag{5.7}$$

$$\tau_m = \left(\Gamma + \Gamma_m + K_{nr}\right)^{-1} \tag{5.8}$$

where Γ_m is the increased radiative rate due to metal nanoparticles. We assume that the non-radiative decay rate is unaffected by the presence of metal nanoparticles [9].These equations results in the unusual predictions of a dye near a metal surface which is not observed in classical far field fluorescence (eqn (5.5) and eqn(5.6)) where in all conditions QY and lifetime change in unison. As the value of Γ_m increases QY of the dye increases while lifetime decreases [8]. Thus in our case, metal enhanced fluorescence of Rh6G is due to an increase in the radiative decay rate of the dye molecules along with an increase in excitation rate of the fluorophore by metal nanoparticles.

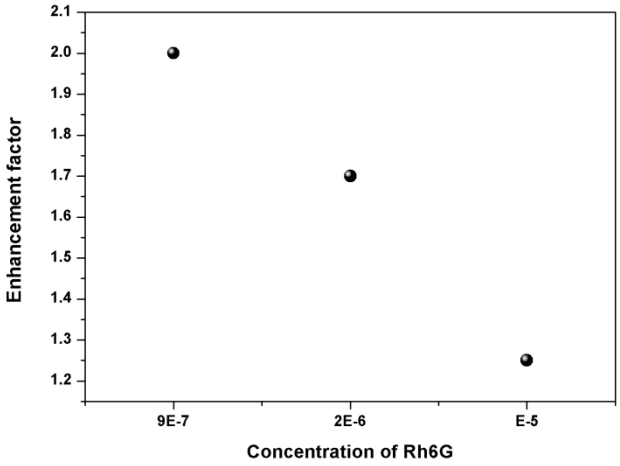

Figure 5.9: Enhancement factor of the emission with respect to the concentration of the dye at fixed concentration of Ag nanoparticles.

However it is important to consider the fact that the metal induced decay rate depends on the properties of the metal particle, fluorophore and surrounding medium which includes metal nanoparticle's size and shape, the fluorophore emission wavelength, orientation of dipole of the dye molecules with respect to the nanoparticles, distance from the nanoparticles and the properties of the surrounding medium including the refractive index near the fluorophore [24].Fluorescence enhancement factor in the present work is defined as

$$EF = \frac{I_{AgN}}{I_R} \tag{5.9}$$

where I_R is the emission intensity of bare Rh6G and I_{AgN} is the emission intensity of the dye in presence of Ag nanoparticles. It is found that at a given concentration of Ag nanoparticles, maximum fluorescence enhancement is noticed for lower concentration of Rh6G as shown in Fig.5.9. Because of the stability problems associated with Ag nanoparticles produced by fs laser further studies are carried out using Ag nanoparticles generated in ethanol by ns laser.

5.3.3 MEF in presence of Ag nanoparticles in ethanol produced by ns pulsed laser

Plasmon band of Ag nanoparticles generated in ethanol, by ns laser, peaks at 410nm with a broad band. We can see that the plasmon band of Ag nanoparticles is blue shifted to nearly 40nm as generated by femtosecond laser. Fig.5.10 represents the TEM image of Ag nanoparticles showing poly dispersive nature of nanoparticles.

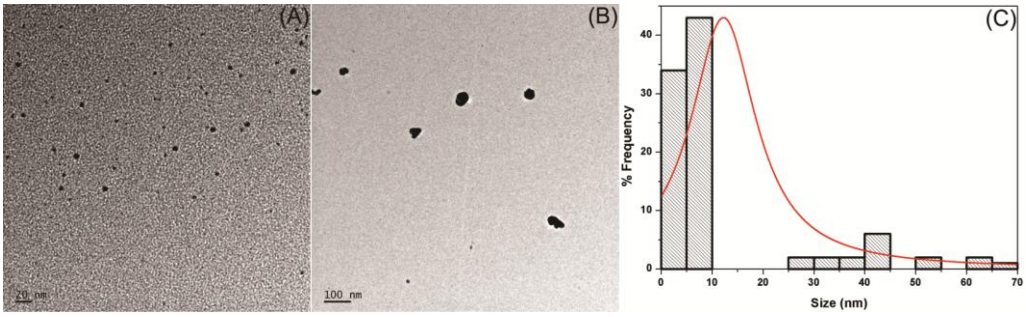

Figure 5.10: (A), (B) Representative TEM image of Ag nanoparticles generated in ethanol by nanosecond laser and (C) Histogram showing a broad size distribution.

A broad size distribution is observed in this case with an average size of 5nm. Spectral emission characteristics of Rh6G are modified in the presence of metal nanoparticles produced by ns laser in ethanol. Even though the average size is 5nm there are several large size nanoparticles present in the solution causing enhanced fluorescence as seen from Fig.5.10 (C). However the enhancement factor is much lower than that of Ag nanoparticles generated by fs laser. Thus it is concluded that enhancement factor increases with increase in size distribution of metal nanoparticles. A quantum yield enhancement of 1.7 is observed in this case for maximum emission enhancement.

5.3.4 Application of MEF in POFs

Ag nanoparticles generated in ethanol by ns pulsed laser is incorporated with Rh6G in MMA and are polymerised into cylindrical rods. Fig. 5.11 shows the corresponding spectral emission modification of Rh6G in the solid form. Enhancement factor of 3.5 is noticed in this case even with a high concentration of Rh6G since the EF is high as we move from solution phase to the solid phase. The

details of concentration of the dye and nanoparticles with emission enhancement factor are given Table.5.2.

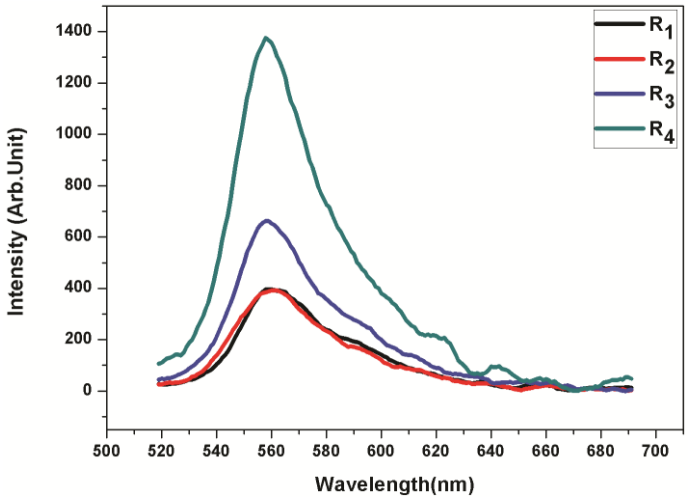

Figure 5.11: Spectral emission of cylindrical rods of Rh6G in the absence and presence of Ag nanoparticles. Excitation wavelength is at 500nm.

R_4 showed maximum enhancement factor whereas R_2 showed neither enhancement nor quenching as compared to R_1 which is taken as the reference containing only Rh6G. Due to stability problems, preforms are fabricated on the same day of generation of nanoparticles. As discussed in the previous section, this emission enhancement is due to an increased excitation rate of the fluorophore along with an increased radiative decay rate. The quantum yield has found to be increased from 0.85 which is the QY of Rh6G in MMA to 0.98 for R_4. Lifetimes obtained from time resolved fluorescence showed considerable change from 3.8ns to 3.43ns where the decay curves are fitted with double exponential function. The observed change supports the mechanism behind the metal enhanced fluorescence of the dye.

Table 5.2: Concentration of Rh6G and Ag nanoparticles with corresponding enhancement factor of emission.

Sample Designation	**Concentration of Rh6G (M)**	**Concentration of Ag nanoparticles (mol/litre)**	**Enhancement factor**
R_1	10^{-5}	--	--
R_2	10^{-5}	9×10^{-6}	1
R_3	10^{-5}	1.5×10^{-6}	1.7
R_4	10^{-5}	4.5×10^{-7}	3.5

The polymer rods drawn into fibers of varying diameter showed conspicuous changes in the emission intensity when pumped at high pump energy. Fig.5.12 depicts the spectral emission characteristics of fibers from all samples when pumped at an energy of 26mJ.

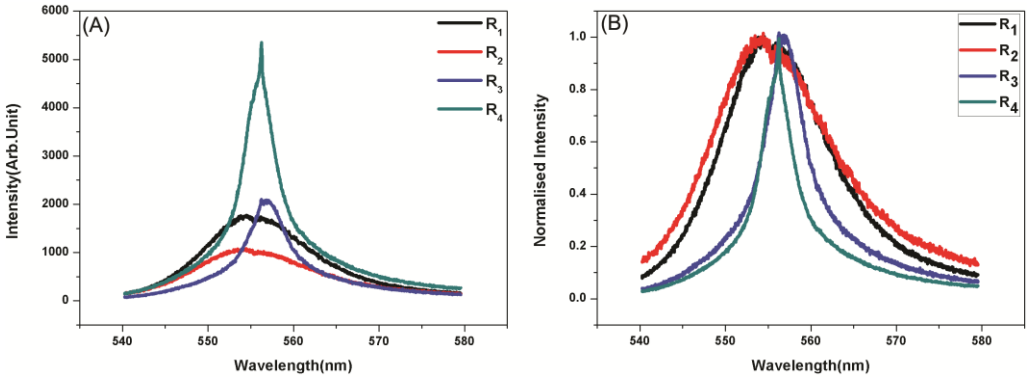

Figure 5.12: (A) Spectral emission and (B) Normalised emission spectra of fibers when pumped at 26mJ showing the linewidth narrowing of R_4 as compared to R_1.

Above figure indicates that when the pump energy reached 26mJ, a three-fold enhancement in the emission intensity is observed for R_4, whereas R_2 showed a slight quenching and R_3 showed a slight enhancement as compared to R_1. From the normalised emission spectra it is found that the linewidth of R_4 has been brought down drastically with respect to R_1. Since the emission enhancement factor is highest for R_4 in the rod form we have observed a similar result when it is transformed into optical fiber.

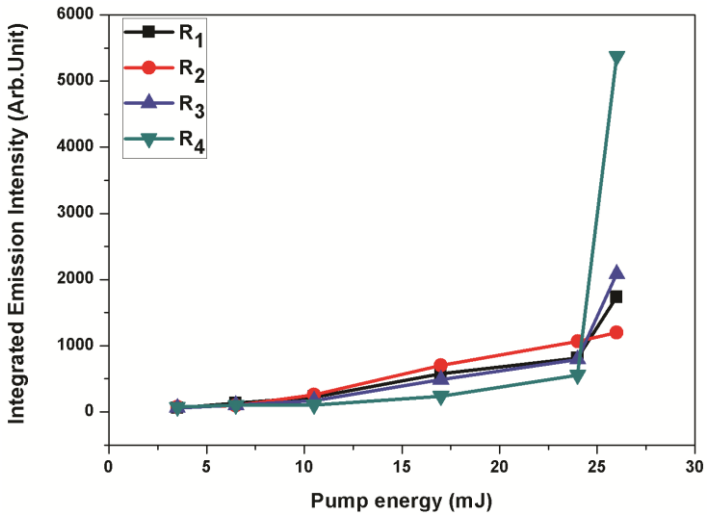

Figure 5.13: Emission intensity vs pump energy of fibers R_1, R_2, R_3 and R_4.

For R_4, the distance between the dye molecules and the Ag nanoparticles in the polymer matrix is in such a way that maximum spectral emission from the dye is obtained due to the increase in intensity of the local incident field on the dye by the SPR of the Ag nanoparticles [25, 26] along with increase in radiative decay rate. Increasing the concentration above that of R_2 resulted in quenching of the emission of the gain medium. It is expected that when the concentration of the nanoparticles in the gain medium is high, the nanoparticle will be in close proximity with respect to the dye and thus will result in quenching. Also, decreasing the concentration below that of R_4 resulted in no change in the emission intensity as compared to that of R_4.

Fig.5.13 indicates the evolution of emission intensity of all fibers with respect to pump energy of the laser. At low pump energy, the enhancement is not distinguishable due to the difficulty in controlling the precision while replacing the fibers one after another. The substantial increase in intensity for R_4 when pumped above 24mJ confirmed the threshold phenomena associated with lasing, indicating the low threshold lasing capability of Rh6G doped POF in the presence of an optimum concentration of Ag nanoparticles.

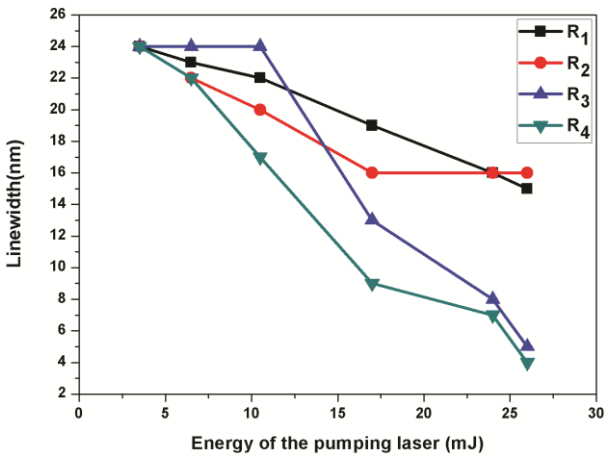

Figure 5.14: Evolution of linewidth with energy of the pumping laser.

Figure 5.14 depicts the line width of the emission of all fibers as a function of pump energy of the laser. At the minimum pump energy, all the fibers showed a broad emission band with a line width of approximately 24nm. With an increase in pump energy, R_3 and R_4 showed a spectral narrowing up to 5nm and 4nm respectively, whereas R_1 and R_2 showed no spectral narrowing at this power. With a further increase in the pump power, all samples except R_4 are photobleached and R_4 showed some lasing spikes at the peak of ASE.

Fig.5.15 shows the lasing spectra of R_4 when pumped above the threshold energy. Spectra are recorded by collecting the emission from one end of the fibers and the fibers are pumped transversely. Since well resolved modes are not observed and

also bare dye doped POF (R_1) is not showing any sign of lasing it is assumed that the nanoparticles in the gain medium of the POFs plays an important role in getting the spectral narrowing along with lasing spikes. High gain provided by the nanoparticles to the amplifier is not enough to overcome the losses in the cavity which is provided by the curved surface of the fiber.

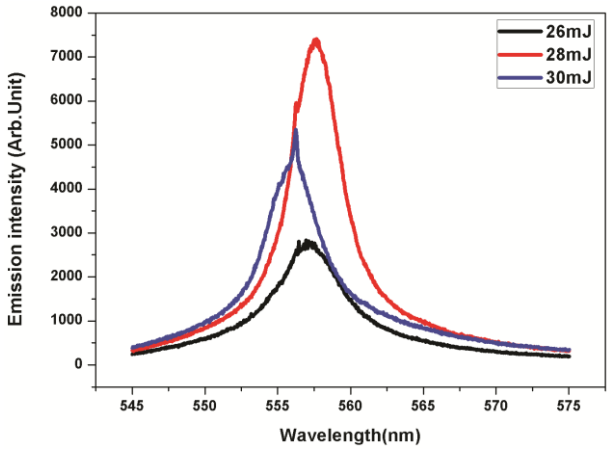

Figure 5.15: Emission spectra of R_4 with varying pump energy.

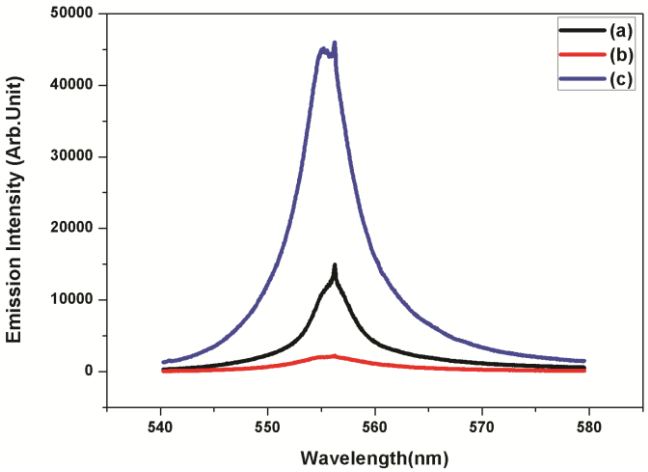

Figure 5.16: Emission spectra of R4 fibers when pumped at 26mJ with varying diameters such as (a) 300µm (b) 360µm and (c) 500µm.

Since the cavity effect is not prominent, it is assumed that the lasing observed is random lasing due to the presence of nanoparticles in the cavity [28]. Here, the random lasing behaviour of the POF is attributable to localized SPR of Ag nanoparticles at 400nm spatially confining the electric field of the pumping light near the particle surface so that it provided high gain for lasing action [28]. For a particle,

the extinction cross-section is provided as the sum of the absorption cross-section and the scattering cross-section. For nanoparticles with small diameters, as in this case (5nm), the scattering cross-section, and therefore the scattering strength, are so small that the lasing peaks are due to the highly localized optical modes caused by plasmon resonance on the surface of Ag nanoparticles [27]. Since we have observed single narrow peak in the emission spectrum with bandwidth of 4 to 5nm, this type of random lasing is identified as incoherent feedback random lasing. When pumped at high energy such as 30mJ, a blue shift in the emission spectrum with reduced intensity is noticed. Intensity reduction is due to photobleaching of the dye. Fig.5.16 depicts the evolution of lasing spectra of R_4 with varying diameter when pumped at 26mJ. Diameter is varied as 300µm, 360µm and 500µm. As the diameter of the POF is increased the emission intensity is also increased due to the increased gain medium inside the cavity.

Further lasing emission from the surface of the R_4 fiber is collected and is shown in Fig.5.17. Since no well resolved modes are observed in this case too we assume that this lasing is again due to random lasing with coherent feedback. Coherent feedback random lasing are characterized by the appearance of several sharp laser spikes of sub-nanometer bandwidths [29]. The line width of the peaks is approximately 0.06nm.

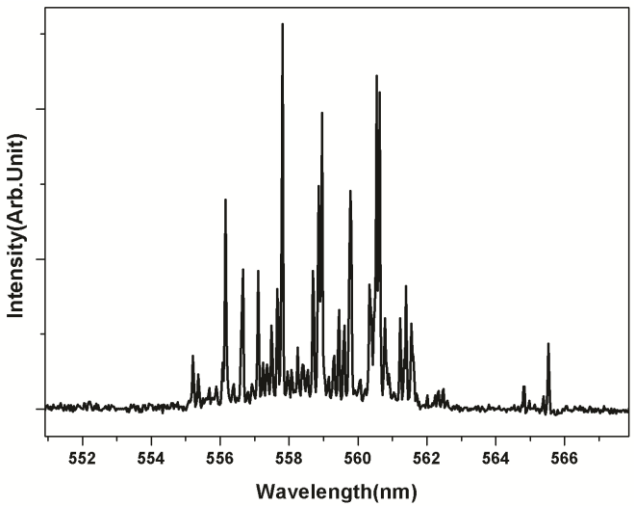

Figure 5.17: Lasing of fiber R_4 collected from the surface of the fiber when pumped at 26mJ.

POFs fabricated from all four sets (R_1, R_2, R_3, R_4) are also subjected to photostability measurements. As seen in Fig. 5.18, R_1, which is taken as the reference, withstood photobleaching up to 6000 pulses at an energy of 20mJ, thereafter, it exhibited photobleaching. However, for samples R_2 and R_3, the rate of photobleaching is high and followed an exponential decay in the output intensity. Interestingly, it is

found that for sample R_4, the damage threshold for photobleaching is so high that it showed a stability even up to 36,000 pulses, at which the reference R_1 itself reaches its half-life. For R_4, because of the maximum lightening rod effect, which is attributed to the fluorescence enhancement by metal nanoparticles, an increase in radiative decay rate is expected. This enhances the fraction of photons observed from every emitting fluorophore with reduced lifetime, which will reduce the probability of bleaching and result in a consequent increase in the photostability of the sample [26, 30]. Also, the nanoparticles provided an encapsulation effect for the dye, which may be another factor contributing to the enhanced stability [28].

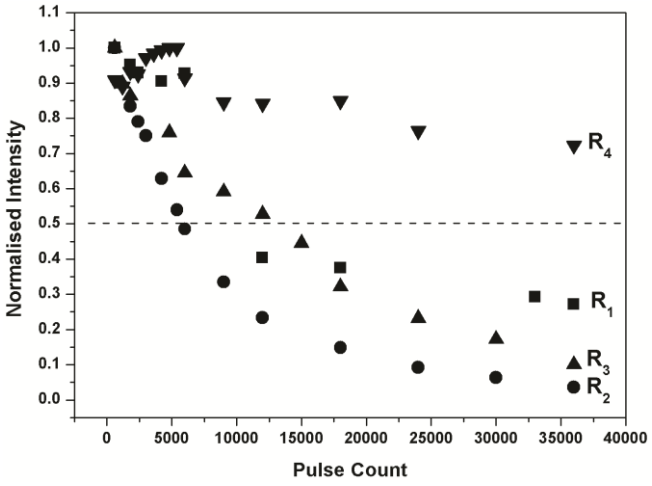

Figure 5.18: Photostability curves of pure Rh6G doped polymer optical fiber (R_1) and Rh6G–Ag nanoparticle doped POF (R_2, R_3, and R_4) when pumped at 20mJ.

5.4 Conclusions

- Ag nanoparticles produced in MMA with an average size of 7nm with plasmon band at 403nm showed a fluorescence quenching of nearby fluorophores. Even with the lowest possible concentration of nanoparticles in the medium, quenching is noticed. d_0 calculated theoretically and experimentally suggests that quenching is through NSET. From Stern-Volmer plot the value of quenching constant is found out. Also the efficiency of energy transfer between the dye molecules and nanoparticles is calculated along with the quantum yield.
- Ag nanoparticles produced in ethanol by fs and ns laser pulses showed Metal Enhanced Fluorescence of the dye molecules. Plasmon band of Ag nanoparticles produced by fs laser peaks around 430nm while that produced by ns laser pulses is around 412nm. Emission enhancement is noticed to be

maximum with nanoparticles generated by fs laser due to the large size distribution of nanoparticles. From quantum yield and lifetime measurements it is found that when MEF occurs, QY of the fluorophore is enhanced while lifetime is quenched indicating that radiative decay rate of the dye molecules is enhanced. Thus an increase in local incident electric field of the dye along with increase in radiative decay rates results in MEF. It is found that MEF is prominent at lower concentrations of fluorophores. Thus it can be concluded that larger nanoparticles with a broad size distribution favours MEF which in turn depends on the properties of the surrounding medium of the fluorophores.

- Polymer fibers doped with Ag nanoparticles, generated in ethanol by ns laser pulses, and Rh6G are subjected to lasing. When pumped at the threshold, a spectral narrowing from 16nm to 4nm is observed for Rh6G doped POF with optimum concentration of Ag nanoparticles. Also, a threefold enhancement in the emission intensity of the dye in this fiber is noticed. This is due to the strong excitement of the dye molecule by the electric field confined around the Ag nanoparticles through Localized SPR. Rh6G doped POF which shows no sign of lasing under the present conditions begins to lase randomly in the presence of Ag nanoparticles at an optimum concentration. This implies that the threshold for lasing action can be brought down in the presence of Ag nanoparticles.
- It is found that with an optimum concentration of Ag nanoparticles in the gain media, the fiber showed enhanced photostability compared to bare Rh6G doped POF due to the combined effect of increased radiative decay rate, reduced lifetime and encapsulation of dye by the nanoparticles.

References

[1] Kang, Kyung A., Jianting Wang, Jacek B. Jasinski, and Samuel Achilefu. "Fluorescence manipulation by gold nanoparticles: from complete quenching to extensive enhancement." J. Nanobiotechnol 9 (2011): 16.

[2] Basheer, N. Shemeena, B. Rajesh Kumar, Achamma Kurian, and Sajan D. George. "Thermal lens probing of distant dependent fluorescence quenching of Rhodamine 6G by silver nanoparticles." Journal of Luminescence 137 (2013): 225-229.

[3] Lakowicz, Joseph R. Principles of fluorescence spectroscopy. Springer Science & Business Media, 2007.

[4] Tam, Felicia, Glenn P. Goodrich, Bruce R. Johnson, and Naomi J. Halas. "Plasmonic enhancement of molecular fluorescence." Nano Letters 7, no. 2 (2007): 496-501.

[5] Rycenga, Matthew, Claire M. Cobley, Jie Zeng, Weiyang Li, Christine H. Moran, Qiang Zhang, Dong Qin, and Younan Xia. "Controlling the synthesis and assembly of silver

nanostructures for plasmonic applications." Chemical reviews 111, no. 6 (2011): 3669-3712.

[6] Caro, Carlos, Ana P. Zaderenko, David Pozo, Paula M. Castillo, and Rebecca Klippstein. Silver nanoparticles: sensing and imaging applications. INTECH Open Access Publisher, 2010.

[7] Lakowicz, Joseph R., Krishanu Ray, Mustafa Chowdhury, Henryk Szmacinski, Yi Fu, Jian Zhang, and Kazimierz Nowaczyk. "Plasmon-controlled fluorescence: a new paradigm in fluorescence spectroscopy." Analyst 133, no. 10 (2008): 1308-1346.

[8] Dragan, Anatoliy I., and Chris D. Geddes. "Metal-enhanced fluorescence: The role of quantum yield, Q0, in enhanced fluorescence." Applied Physics Letters100, no. 9 (2012): 093115.

[9] Bardhan, Rizia, Nathaniel K. Grady, Joseph R. Cole, Amit Joshi, and Naomi J. Halas. "Fluorescence enhancement by Au nanostructures: nanoshells and nanorods." Acs Nano 3, no. 3 (2009): 744-752.

[10] Chance, R. R., A. Prock, and R. Silbey. "Molecular fluorescence and energy transfer near interfaces." Adv. Chem. Phys 37, no. 1 (1978): 65.

[11] Ford, George W., and Willes H. Weber. "Electromagnetic interactions of molecules with metal surfaces." Physics Reports 113, no. 4 (1984): 195-287.

[12] Sebastian, Suneetha, C. Ajina, CP G. Vallabhan, V. P. N. Nampoori, P. Radhakrishnan, and M. Kailasnath. "Fabrication and photostability of rhodamine-6G gold nanoparticle doped polymer optical fiber." Chinese Physics Letters 30, no. 11 (2013): 118101.

[13] Jennings, T. L., M. P. Singh, and G. F. Strouse. "Fluorescent lifetime quenching near d= 1.5 nm gold nanoparticles: probing NSET validity." Journal of the American Chemical Society 128, no. 16 (2006): 5462-5467.

[14] Yun, C. S., A. Javier, T. Jennings, M. Fisher, S. Hira, S. Peterson, B. Hopkins, N. O. Reich, and G. F. Strouse. "Nanometal surface energy transfer in optical rulers, breaking the FRET barrier." Journal of the American Chemical Society127, no. 9 (2005): 3115-3119.

[15] Sen, Tapasi, and Amitava Patra. "Recent advances in energy transfer processes in gold-nanoparticle-based assemblies." The Journal of Physical Chemistry C 116, no. 33 (2012): 17307-17317.

[16] Sen, Tapasi, and Amitava Patra. "Resonance energy transfer from rhodamine 6G to gold nanoparticles by steady-state and time-resolved spectroscopy." The Journal of Physical Chemistry C 112, no. 9 (2008): 3216-3222.

[17] Basheer, N. Shemeena, B. Rajesh Kumar, Achamma Kurian, and Sajan D. George. "Silver nanoparticle size–dependent measurement of quantum efficiency of Rhodamine 6G." Applied Physics B 113, no. 4 (2013): 581-587.

[18] Persson, B. N. J., and N. D. Lang. "Electron-hole-pair quenching of excited states near a metal." Physical Review B 26, no. 10 (1982): 5409.

[19] Zhao, Jing, Lasse Jensen, Jiha Sung, Shengli Zou, George C. Schatz, and Richard P. Van Duyne. "Interaction of plasmon and molecular resonances for rhodamine 6G adsorbed on silver nanoparticles." Journal of the American Chemical Society 129, no. 24 (2007): 7647-7656.

[20] Kailasnath, M. "Fabrication and characterisation of dye doped polymer optical fibres with different refractive index profiles for photonic applications." PhD diss., University of Science and Technology, 2010.

[21] Haldar, Krishna Kanta, Tapasi Sen, and Amitava Patra. "Au@ ZnO Core− Shell Nanoparticles Are Efficient Energy Acceptors with Organic Dye Donors." The Journal of Physical Chemistry C 112, no. 31 (2008): 11650-11656.

[22] Hövel, H., B. Grimm, M. Bödecker, K. Fieger, and B. Reihl. "Tunneling spectroscopy on silver clusters at T= 5 K: size dependence and spatial energy shifts." Surface science 463, no. 1 (2000): L603-L608.

[23] Sen, Tapasi, Suparna Sadhu, and Amitava Patra. "Surface energy transfer from rhodamine 6G to gold nanoparticles: A spectroscopic ruler." Applied Physics Letters 91, no. 4 (2007): 043104.

[24] Zhang, Jian, Yi Fu, Mustafa H. Chowdhury, and Joseph R. Lakowicz. "Plasmon-coupled fluorescence probes: effect of emission wavelength on fluorophore-labeled silver particles." The Journal of Physical Chemistry C 112, no. 25 (2008): 9172-9180.

[25] Dominguez, Christian Tolentino, Rogério L. Maltez, Roberto Dos Reis, Luciana SA de Melo, Cid B. de Araújo, and Anderson SL Gomes. "Dependence of random laser emission on silver nanoparticle density in PMMA films containing rhodamine 6G." JOSA B 28, no. 5 (2011): 1118-1123.

[26] Geddes, Chris D., and Joseph R. Lakowicz. "Editorial: Metal-enhanced fluorescence." Journal of Fluorescence 12, no. 2 (2002): 121-129.

[27] Meng, Xiangeng, Koji Fujita, Yanhua Zong, Shunsuke Murai, and Katsuhisa Tanaka. "Random lasers with coherent feedback from highly transparent polymer films embedded with silver nanoparticles." Applied Physics Letters 92, no. 20 (2008): 201112.

[28] Sebastian, S., C. L. Linslal, C. P. G. Vallabhan, V. P. N. Nampoori, P. Radhakrishnan, and M. Kailasnath. "Random lasing with enhanced photostability of silver nanoparticle doped polymer optical fiber laser." Laser Physics Letters 11, no. 5 (2014): 055108.

[29] Sun, Yanyan, Zhaona Wang, Xiaoyu Shi, Yanrong Wang, Xiaoye Zhao, Shujing Chen, Jinwei Shi, Jing Zhou, and Dahe Liu. "Coherent plasmonic random laser pumped by nanosecond pulses far from the resonance peak of silver nanowires." JOSA B 30, no. 9 (2013): 2523-2528.

[30] Imhof, A., M. Megens, J. J. Engelberts, D. T. N. De Lang, R. Sprik, and W. L. Vos. "Spectroscopy of fluorescein (FITC) dyed colloidal silica spheres." The Journal of Physical Chemistry B 103, no. 9 (1999): 1408-1415.

Chapter 6 :

Synthesis of Au-Ag core/shell and alloy nanostructures for metal enhanced fluorescence applications

---

Au and Ag nanoparticles in ethanolic solution of Poly Vinyl Pyrrolidone are synthesised and the variation of its concentration on the ablation efficiency of nanocolloids are studied. A simple method for the formation of Au-Ag nanoalloy using laser ablation by nanosecond laser operating at the fundamental wavelength has been introduced and the mechanism behind the formation is explained. Existence of an intermediate phase of Au core/Ag shell nanostructures at the initial stage of formation of Au-Ag nanoalloy has been noticed. Concentration of the bimetallic nanocolloidal solution is controlled by simply varying the time of ablation of Ag target in the Au nanocolloidal solution. Application of alloy and core/shell nanostructures in lasing characteristics of dye doped POFs are studied and compared with bare dye doped POFs as well as POFs containing its monomeric nanoparticles in the gain medium.

Publications

Sebastian, Suneetha, C. L. Linslal, C. P. G. Vallbhan, V. P. N. Nampoori, P. Radhakrishnan, and M. Kailasnath. "Formation of Au–Ag nanoalloy through Au core/Ag shell intermediate phase by laser ablation." Chemical Physics Letters628 (2015): 25-29.

6.1 Introduction

The optical properties of metal nanoparticles depend substantially on their size, shape, composition and dielectric properties of the surrounding medium. Emergence of nanotechnology in this new era demands the generation of various types of nanoparticles. Availability of numerous methodologies to synthesise different types of nanostructures, depending on the specific requirements, leads to the fabrication of alloys, core/shell nanostructures and metal agglomerates with size, shape and composition similar to their individual counterparts but with new physical and chemical properties [1]. Alloy and core/shell structures have become a fascinating subject due to their composition dependent optical and catalytic properties [2]. Similar to the tunability of plasmon band of metal nanoparticles by varying the refractive index of the solvent media, formation of alloy nanostructures enables a wide range of tunability of the surface plasmon band in between that of their individual monometallic components. The position of the band depends on the Au/Ag weight ratio [3] and thus the tunability can easily be achieved by simply varying the concentration of its nanocomposites. One of the major differences between bimetallic core/shell and alloy nanostructures is that alloy and core/shell nanostructures show different optical properties even though the composition of Au and Ag within the nanostructures is similar [4]. As far as core/shell is concerned their optical properties depend crucially on the thickness of the core and shell. If the shell surrounding the core is slender, the surface plasmon of the core can interact with the incoming electromagnetic field and so the surface plasmon of the core is prominent. In the other case, plasmon absorption of the shell nanoparticles becomes prominent due to the dense shell around the core [4]. In all other cases, two distinct spectra can be observed for core/shell nanostructure which corresponds to the plasmon bands of Au as well as Ag monomeric components. In contrast, alloy of Au and Ag shows a single plasmon band.

There are already a number of reports on the formation of alloy nanoparticles by various methods such as chemical reduction method [5-13] utilizing chemical reagents for the formation and reduction of corresponding alloy nanostructures, capillary micro reaction [14] photochemical approach [15] to name a few. There are also reports on the formation of alloy using physical methods such as laser irradiation of a mixture of Au and Ag nanocolloids prepared independently by laser ablation of individual targets [3,16-19] or laser irradiation of nanocolloids prepared by chemical methods [1,4]. Ablation of bulk alloys of Au and Ag and thus the formation of Au-Ag nanoalloy has been reported earlier [20-23]. Han et al. [24] and Y.chen et al. [25] have recently reported the formation of Au core/Ag shell nanostructure using laser ablation of Ag plate in Au nanocolloidal solution. R.Intartaglia et al. [26] reported the formation of Au-Ag nanoalloy using complete physical method utilizing picosecond laser. Ag plate is ablated in the already existing Au nanocolloidal solution using

different wavelengths for a fixed time and the concentration of the bimetallic nanocolloidal solution is controlled by diluting the initial concentration of the mother solution (Au nanocolloidal solution). But they have not observed an alloying process of Au and Ag nanocolloids while ablating Ag with 1064nm under their experimental conditions.

6.2 Experimental Section

Neodymium-YAG laser operating at the fundamental wavelength (1064nm) with a pulse width of 9ns, repetition rate of 10Hz with a fluence of 2×10^3 J/cm^2 is used as the source for laser ablation. Both Ag and Au nanoparticles for the present study are generated in 5ml of ethanol stabilized by Poly Vinyl Pyrrolidone (PVP). Concentration of PVP having a molecular weight of 10,000 is varied in the solvent between 0.06mM to 6mM. Au-Ag core/shell and nanoalloys in the present case are prepared by ablating Au plate in the ethanolic solution of PVP for 10 minutes and replacing Au plate by Ag plate and continuing the ablation further. Concentration of Au nanoparticles present in the solution is found to be 8×10^{-5} M. Formation of nanoalloy is monitored at different times of laser ablation of Ag plate by recording the optical extinction spectra using UV-VIS NIR Spectrophotometer. Size and composition analysis are done using TEM and EDS respectively. The concentration of Ag nanocolloids in the final nanoalloy solution is found to be 2×10^{-4} M.

6.3 Results and Discussions

6.3.1 Formation of Ag nanoparticles in ethanolic solution of PVP

Ag nanoparticles produced in ethanol are subjected to agglomeration due to poor stability which is caused by its asymmetric charge distribution leading to dipole-dipole interaction between them. However, addition of suitable capping agents such as PVP in the medium can improve the formation efficiency of the colloidal nanoparticles as well as its stability [27]. The chemical composition of PVP which is essentially a polymer and which is widely used as a stabilizing agent of metal nanocolloids is shown in Fig.6.1.

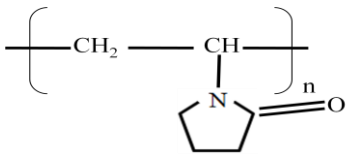

Figure 6.1: Chemical structure of Poly Vinyl Pyrrolidone.

Fig.6.2 shows the optical extinction spectra of Ag nanoparticles produced by laser ablation in ethanol as well as in ethanol containing different concentrations of

PVP. Ag nanocolloids in ethanol show a plasmon band at 408nm with a full width at half maximum of 155nm.

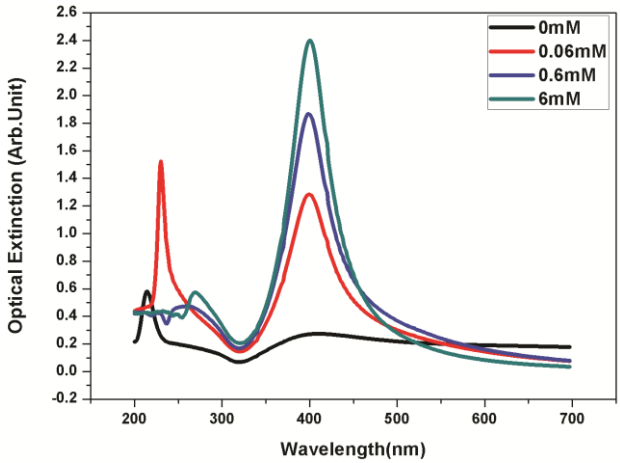

Figure 6.2: Optical absorption spectra of Ag nanoparticles produced in pure ethanol (0mM) and in ethanolic solution of PVP of various concentrations. Time of ablation is fixed a constant for 5mins in all the cases.

On the other hand, plasmon band of Ag nanocolloids in ethanolic solution of PVP peaks at around 400nm with a FWHM of 67nm (as detailed in Table 6.1). Thus, in the presence of PVP the spectral width and position of the plasmon band changes owing to its capping property. As seen from the Fig.6.2, with increase in the concentration of PVP an increase in intensity of the plasmon band is observed with no further shift in the peak position. Thus the relative abundance of the nanoparticles increases with increase in concentration of PVP. Also the mass of Ag plate ablated increases with concentration of PVP which is given in Table.6.1. The cavitation bubble formed during laser ablation is smaller in PVP solution than in ethanol which suggests that plasma species ejected during laser ablation is more confined by the solution of PVP than by pure ethanol. This enhanced confinement is due to the increased density and viscosity of the solvent in the presence of PVP [27]. It is reported that the solvent confined plasma generated near the target can etch the surface because of its high pressure [28-29]. Thus nanoparticles are generated by such a secondary ablation as well as by the direct laser ablation process. Therefore it can be concluded that increase in formation efficiency (relative abundance) of metal nanoparticles with PVP in the solvent is attributed to the increased secondary ablation efficiency. Ablation efficiency can be further increased by increasing the concentration of PVP in the solvent (shown in Fig.6.2) thereby increasing the density and viscosity. The concentration of PVP beyond 6mM resulted in highly viscous solvent which is difficult for further characterisation and so it is omitted. However it is found that increase in the formation

efficiency is moderate with a PVP concentration higher than 6mM due to the absorption of incident laser beam by the nanocolloids. As the viscosity of the solution is increased, nanocolloids generated by laser ablation stay in the vicinity of the target surface for a longer time thus absorbing the energy of the incident light and lowers the efficiency of laser ablation [27].

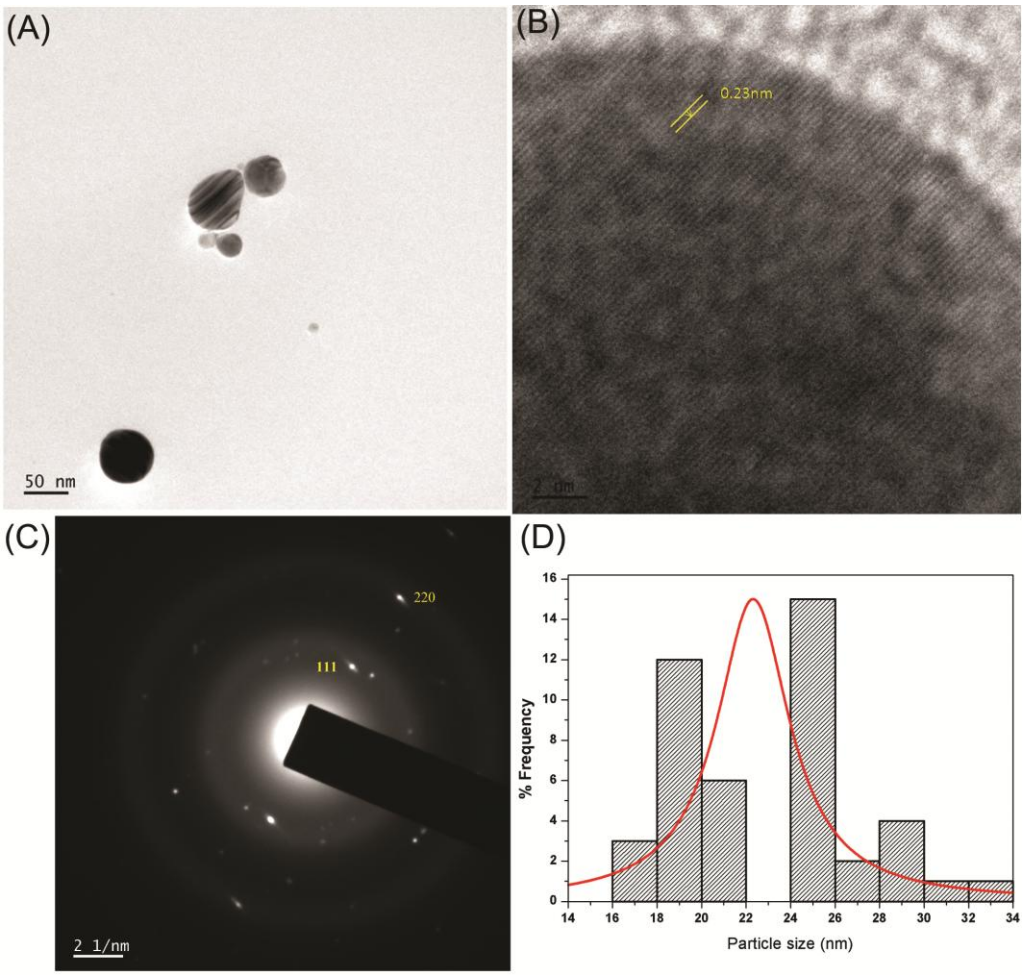

Figure 6.3: (A)Representative TEM image of Ag nanoparticles in ethanolic solution of PVP (B) HRTEM showing the inter-planar spacing and is found to be 0.23nm (C) SAED pattern showing the single crystal nature and (D) Histogram showing an average size of 14nm.

Fig.6.3 shows the representative TEM images of Ag nanocolloids generated in 6mM PVP solution ablated for 5mins. The average size of Ag is found 14nm with a standard deviation of 16nm and a mean of 28nm as seen from the histogram (Fig.6.3 (D)). It is found that the formation efficiency as well as the stability of the nanocolloidal solution is enhanced which is an important result for various

applications which demands the stability of the nanoparticles. From HRTEM shown in Fig.6.3 (B), the interplanar spacing is found to be 0.23nm which matches with the {111} d spacing of fcc lattice. Selected Area Electron Diffraction (SAED) pattern (Fig.6.3 (C)) also shows the single crystalline nature of the nanocolloids and the d spacing calculated from the pattern matches with {111} and {220} fcc lattice [30].

Table 6.1: Variation of plasmon band position, width, ablated mass of Ag nanoparticles with respect to PVP concentration in ethanol.

Type of nanocolloids	Concentration of PVP (mM)	Position of plasmon band (nm)	Plasmon band width(nm)	Mass of ablated matter (mg)
Ag	0	408	155	0.5
	0.06	400	67	1.5
	0.6	400	67	1.7
	6.0	400	67	2.0
Au	0	535	110	0.8
	0.06	524	52	1.9
	0.6	524	52	2.3
	6.0	524	52	2.9

6.3.2 Formation of Au nanoparticles in PVP solution

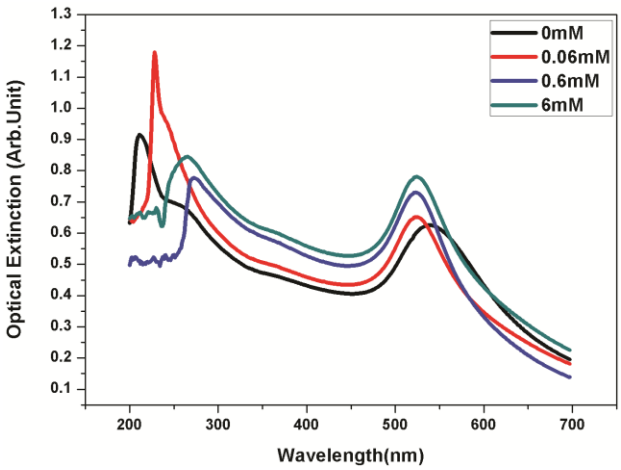

Figure 6.4: Optical absorption spectra of Au nanoparticles generated in ethanol and ethanol containing PVP.

Similar to the formation of Ag nanoparticles in PVP solution discussed in the previous section, synthesis of Au nanoparticles in PVP solution by laser ablation has also been carried out. Fig.6.4 shows the optical extinction spectra of Au nanoparticles generated in pure ethanol and in ethanolic solution of PVP. Time of ablation is fixed at 5min and all other laser parameters are also fixed, as in the earlier case. As can be seen, there is a blue shift of 11nm in the plasmon band with a reduction in the bandwidth of Au nanoparticles generated in PVP solution (as in the case of Ag nanoparticles) as compared to that produced in pure ethanol. Also the colour of the nanocolloidal solution changes from violet to red (not shown here) as we move from pure ethanol to ethanolic solution of PVP. The concentration of Au nanocolloids also increased as the concentration of PVP is increased which is calculated from the weight difference of the target plate before and after laser ablation (given in Table 6.1). Fig.6.5 represents the TEM image of Au nanoparticles generated in 0.6mM PVP solution. From the histogram the average size of the nanoparticles is found to be 8nm.

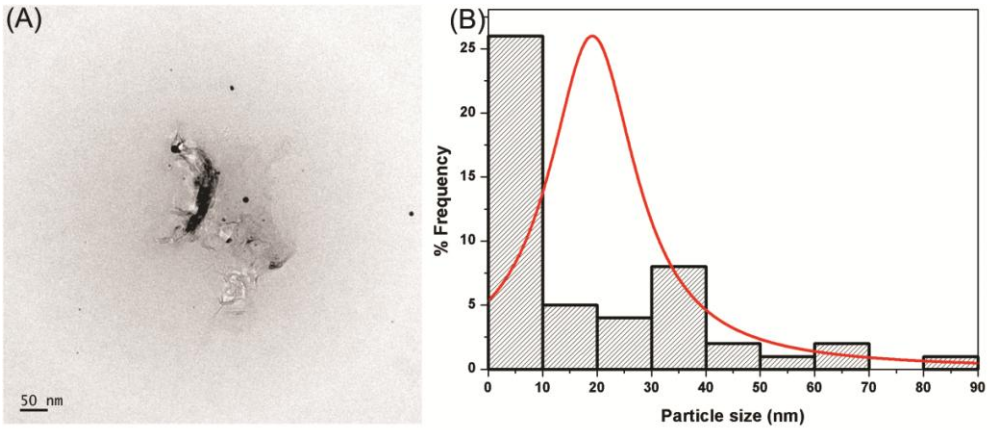

Figure 6.5: (A) TEM image of Au nanoparticles produced in 0.6mM PVP solution. The black layer is due to PVP and (B) Histogram showing an average size of 8nm.

6.3.3 Formation of Ag-Au core/shell bimetallic nanostructure by laser irradiation

Monometallic Au nanoparticles are produced in 0.6mM PVP in ethanol by laser ablation. Concentration of Au nanoparticles formed is calculated to be 6×10^{-3} mol/litre. Similarly Ag nanoparticles are also produced in the solution by the same experimental condition and the concentration of nanocolloids obtained is found to be 4×10^{-3} mol/litre. Nanocolloids of Au have plasmon band peaks at 524nm and that of Ag nanoparticles at 400nm. The variation in the interband contribution to SPR or the difference in the polarizability of Au and Ag leads to the plasmon absorption of Ag nanoparticles around 400nm and Au nanoparticles around 520nm [10]. 5ml each of

Au and Ag monometallic solutions are mixed physically and sonicated for 5min. Optical absorption spectra of the mixture showed two distinct bands corresponding to plasmon bands of individual Au and Ag nanocolloids (Fig.6.6). Since no shifting in the plasmon is observed, it is concluded that physical mixing can not form a bimetallic nanostructure. It is already reported that [31] laser irradiation of nanocolloids can modify their structure. For effective structural modification of the nanoparticles, it should absorb the incoming energy [31]. Since the plasmon band of Au nanoparticles lies near 532nm, the mixture is subjected to the second harmonics of Nd-YAG laser at a fluence of 500J/cm^2. Absorption of laser pulses occurs due to the transition of free electrons in the conduction band of nanoparticles and the energy of the electronic excitation is transferred to the nanoparticle crystal lattice after 3-5ps. If the absorbed energy is large enough, it can melt the nanoparticles. The nanoparticles in the molten state can react with the surrounding medium or with other nanoparticles already present in the medium [3, 17]. Thus laser pulses are focussed inside the colloidal mixture and irradiation is carried out for 30min and 120min and the spectra after irradiation is shown in Fig.6.6.

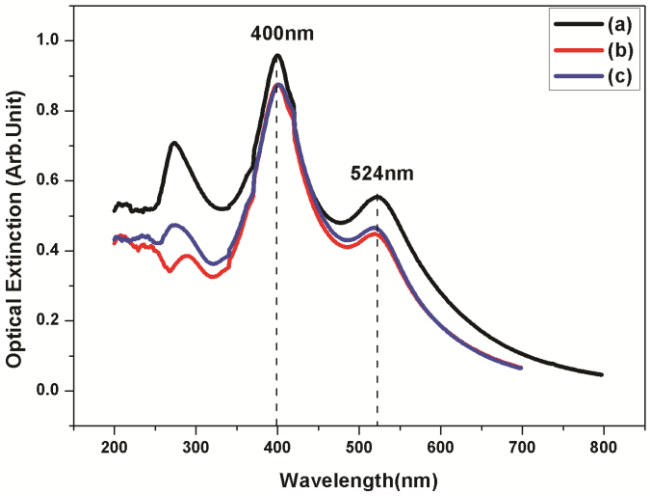

Figure 6.6: Optical absorption spectra of (a) physical mixture of Au and Ag (b) core-shell bimetallic nanostructure of Au and Ag produced by irradiating the physical mixture for 30mins and (c) 120mins.

As can be seen, when irradiated for 30min, a spectral blue shift of 7nm is noticed in the plasmon region of monomeric Au nanoparticles and a red shift of nearly 1nm is noticed for the band corresponding to Ag monomeric nanoparticles. This shifting in the bands can be thought of as the formation of a core-shell bimetallic nanostructure [32]. Since laser pulses at 532nm are focussed, it is assumed that Au nanoparticles are in the molten state and reacts with Ag nanoparticles already present in the medium leading to the formation of Ag core/Au shell nanostructures. When the irradiation is

continued for 120min, no appreciable shift in the bands is noticed. Thus it is concluded that irradiation of a mixture of Au and Ag monomeric nanocolloids under the present condition leads to the formation of a core-shell bimetallic nanostructure.

6.3.4 Formation of Au-Ag alloy through Au core/Ag shell intermediate phase in ethanolic solution of PVP by ablation

Figure 6.7: Image showing the colour of (left) Au nanoparticles (middle) Ag nanoparticles and (right) alloy of Au-Ag in PVP solvent.

Formation of bimetallic nanocomposites under laser ablation of Ag plate in the nanocolloidal solution of Au, stabilized by PVP leads to the transformation of intense ruby red colour of pure Au nanoparticles to a brown as shown in Fig.6.7. Optical absorption spectra recorded just after a minute of ablation of Ag plate (Fig.6.8) indicates that the SPR becomes complex due to the formation of a bimetallic nanostructure. Two plasmon bands can be observed leading to the formation of a core/shell nanostructure. Due to the interaction between the metals at the interface of the core/shell structure, SPR peak position shifts for both gold and silver as compared to its individual components [32].

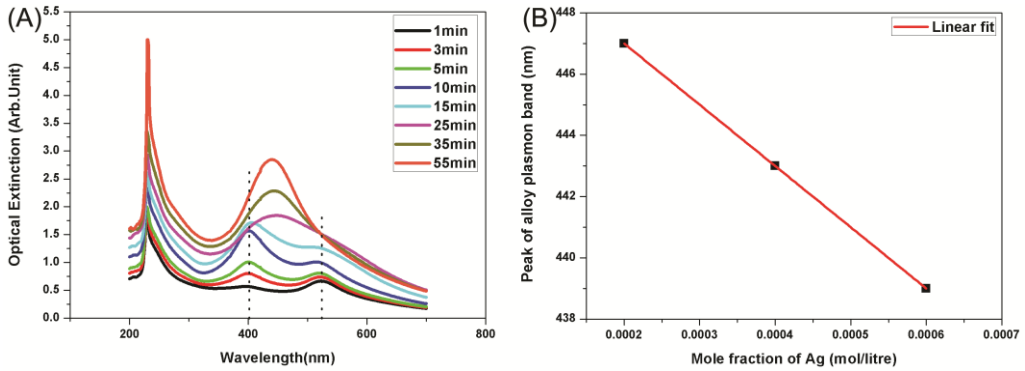

Figure 6.8: (A) Optical absorption spectra showing the formation of Au-Ag nanoalloy through the intermediate phase of Au core/Ag shell bimetallic nanostructure (B) Peak position of plasmon band of nanoalloy against the mole fraction of Ag.

Since there is a shifting of the bands which is not observed in the physical mixture of the two monomeric nanocolloidal solutions, it is assumed that core/shell nanostructure is formed. Formation of alloy of Au and Ag nanoparticles at this stage can be ruled out since this is characterised by a single absorption band tunable between the SPR band of Au and Ag nanoparticles depending on the composition of alloy nanoparticles [33-34]. From Fig.6.8 it can be seen that there is a blue shift of 7nm and 2nm respectively in the peak position of plasmon band of Au and Ag nanoparticles as they form core/shell nanostructure when the time of ablation is 5min. Au nanoparticles which are initially present in the solution act as the seeds or nucleation centres for the next coming Ag nanoclusters, ions etc and thus a Au core/Ag shell nanostructure is formed [24]. Also both Au and Ag nanoparticles are having the same fcc crystal structure and the lattice constants of Au and Ag are 4.0783 Å and 4.0862 Å respectively [25]. Hence the lattice mismatch between them is less that 5% enabling Ag atoms to attach to the surface of Au nanoparticles already present in the solution [25]. Au nanoparticles is chosen as the seeds or core for the formation of a bimetallic core/shell nanostructure due to the spherical symmetry of Au nanoparticles which is not easily attained while generating Ag nanoparticles.

Apart from the optical extinction spectra, further confirmation of core/shell nanostructure is obtained from TEM images shown in Fig.6.9. Inspection of TEM image in Fig.6.9 shows a dark centre and a lighter shell. Fig.6.9 (B) shows the higher magnification and reveals the formation of a lighter shell around Au nanoparticles. Fig.6.9 (C) is the lattice image of Ag shell and the interplanar distance calculated from the image is 0.23nm which matches well with the {111} d spacing of fcc silver [35]. Size distribution analysis is carried out for Au core/Ag shell nanocomposites (Fig.6.9. (D)) and the average diameter is found to be around 25nm. Initial sizes of 7nm and 14nm of monomeric Au nanoparticles and Ag nanoparticles respectively have become 25nm when a core/shell nanostructure is formed.

With further increase in time of ablation the amount of Ag content in the colloidal solution is increased and the plasmon band of Au nanoparticles is shifted monotonically to higher energy side while the plasmon band of Ag remains almost same with a less appreciable shift as seen from Fig.6.8. This suggests that the composition of the core is time dependent and it is modulated by the continuous interdiffusion of Ag atoms in an already existing Au core at the initial stage. Interdiffusion of Ag atoms is possible because of their similar atomic sizes [16] and so a complete miscibility between the two is possible. As the time of ablation reaches 25 min, the two bands merge to form a single plasmon band which is the characteristics of alloy formation (shown in Fig 6.8). The difference in mobility of the two constituting atomic elements, which in turn depends on their different atomic masses may be the reason for the interdiffusion of Ag atoms into Au nanoparticles [16]. Atomic mass of Ag is 107 atomic unit (a.u) where as that of Au is 197 a.u. and thus

the mobility of Ag is higher than that of Au. This explains the invariance of Ag plasmon band and the modulation of Au plasmon band as the concentration of Ag atoms in the colloidal solution increases.

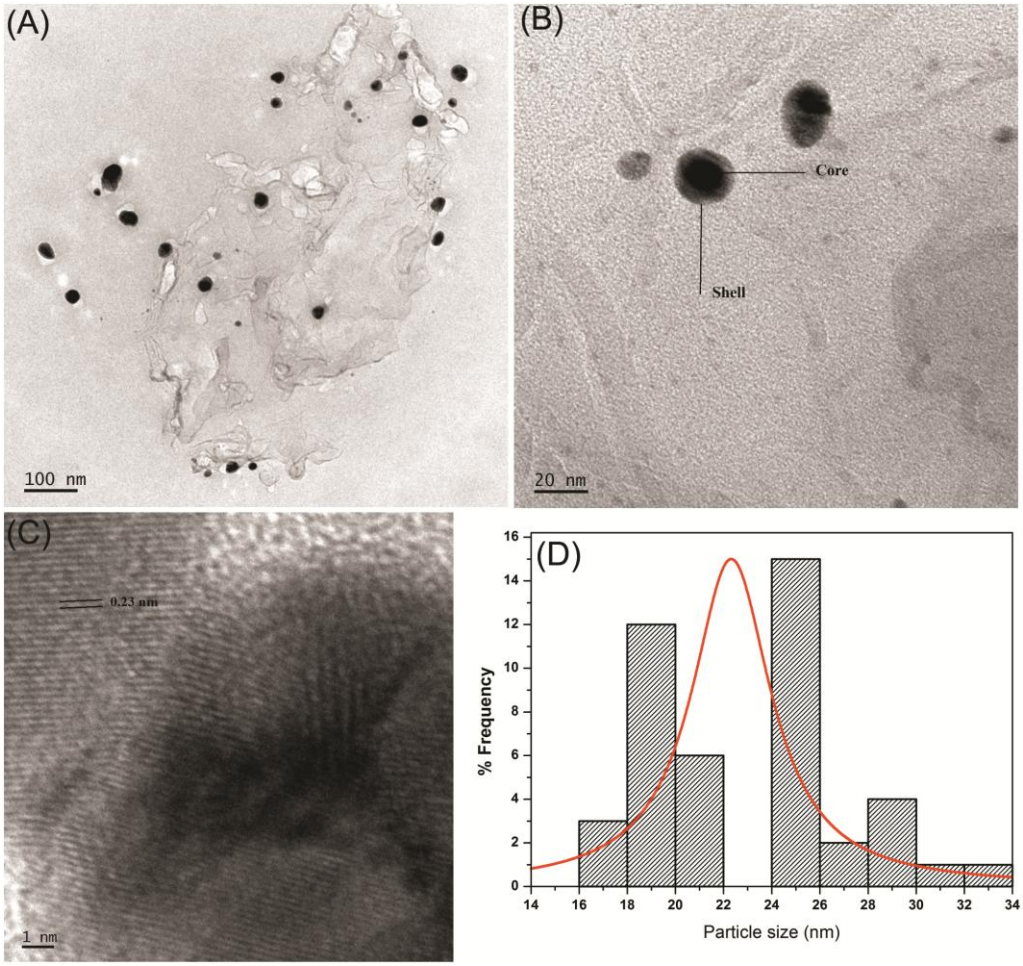

Figure 6.9: Representative TEM image of (A) Au core/Ag shell nanocomposites in ethanol stabilized by PVP (B) Magnified image of core/shell structure (C) Lattice image of Ag shell and (D) and Size distribution carried out on TEM images of Au core/Ag shell nanocomposites.

As reported by Philipp Wagener et al. [36], two different populations of nanoparticles can be formed during ablation of Ag nanoparticles, one fraction consists of compact primary nanoparticles and other fraction consists of agglomerates with larger particle size. They found that the bubble-liquid interface is penetrable by the ablated matter. The primary nanoparticles (small size) may enter the Au nanocolloidal solution during the bubble expansion phase due to high ejection velocities. Such primary particles of Ag find Au nanoparticles as the seeds or nucleation centres and so

Au-Ag core/shell nanostructure is formed. Fig 6.10 depicts a schematic of the formation of alloy through the formation of a Au core/Ag shell nanostructure.As seen from the schematic, the initial stage of the alloy formation is the formation of an Au core/Ag shell bimetallic nanostructure. With further increase in the concentration of Ag, interdiffusion of Ag atoms into the core (Au nanoparticles) can be seen. When the alloy is formed a complete miscibility between the two types of atoms is observed and the interface formed during the core/shell formation is completely vanished. Thus the nanostructure formed is an alloy of Au and Ag atoms [16]. The agglomerates of pure Ag nanoparticles with larger size present in the bimetallic nanocolloidal solution may have plasmon band close to the plasmon band of alloy since according to Mie theory, plasmon band is red shifted with increase in the size of the nanoparticles. But its presence in the final nanocolloidal solution is hardly detectable using conventional techniques such as UV-VIS spectrometer or TEM.

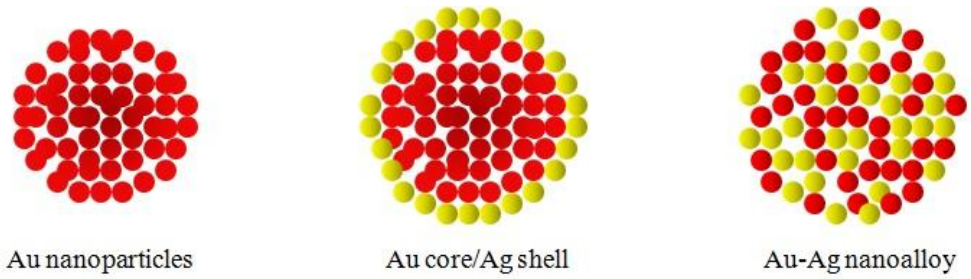

Figure 6.10: Schematic of the formation of core/shell and alloy of Au-Ag nanoparticles.

When the time of ablation is increased up to 35min, a well resolved plasmon band is observed at 443nm and with further increase in time up to 55min, an increase in the optical extinction of the alloy is noticed with a blue shift in the plasmon band. Time of ablation beyond 55min is not possible since target ablation is not observed due to absorption of incident energy by the increased concentration of alloy nanoparticles. Fig.6.8 (B) shows the peak position of plasmon band of alloy nanoparticles with increase in concentration of Ag content in the colloidal solution with respect to ablation time. The graph is fitted linearly and thus the plasmon band of alloy is shifted to the higher energy region with increase in concentration of Ag. Thus it is possible to tune the composition of the resulting bimetallic nanostructures simply by varying the initial concentration of Au nanocolloids and the time of ablation of Ag target in it. Fig.6.11 shows the TEM image of Au-Ag alloy nanostructures formed by ablating Ag plate for 35min. Due to the similar lattice constants it is difficult to identify an alloy structure even from HRTEM shown in Fig.6.11 (B). The average size of the alloy so formed is found to be 17nm which coincides with the mean and a

standard deviation of 5nm as shown in Fig.6.11 (C). EDS of the alloy nanoparticles on a small portion of the grid is recorded (Fig.6.11 (D)) and the composition of Au-Ag alloy nanostructure is found to be $Au_4Ag_{2.9}$ (weight%). A reduction of particle size from 25nm to 17nm is observed when nanostructure of core/shell is transformed to nanoalloy. Concentration details of Au and Ag nanoparticles in the final colloidal solution can be referred in the experimental section.

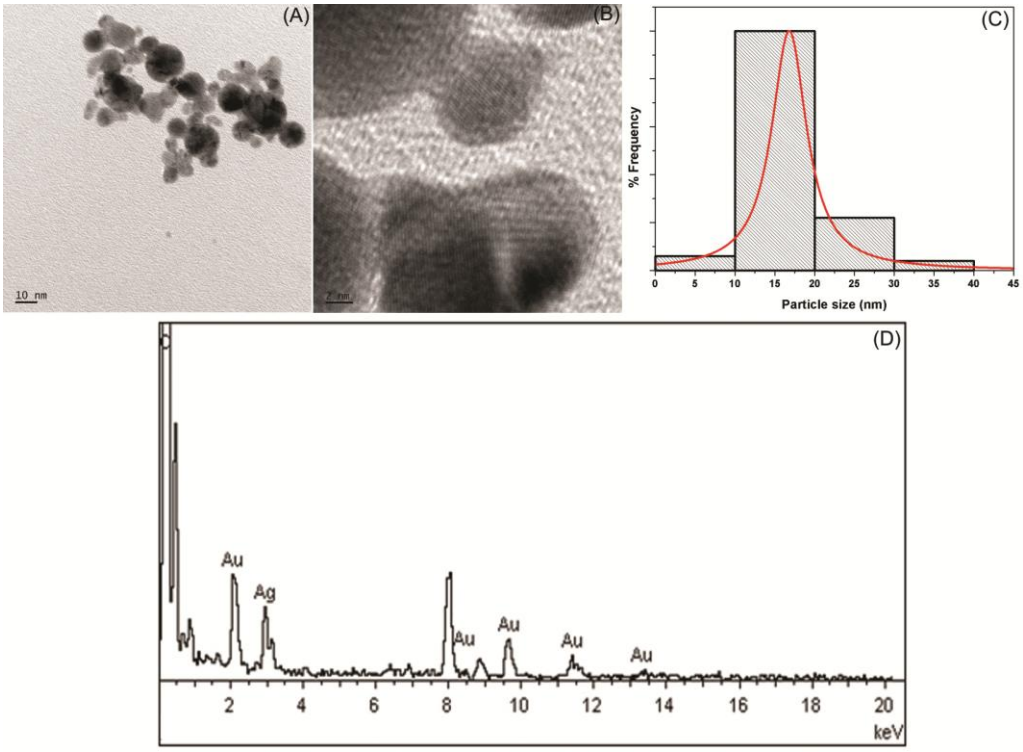

Figure 6.11: (A) Representative TEM image of Au-Ag alloy nanostructure formed by ablating Ag plate for 35 min in the nanocolloidal solution of Au nanoparticles (B) HRTEM showing the crystalline nature of the alloy (C) Size distribution showing an average size of 17 nm and (D) EDS pattern recorded on a portion on the grid with y axis normalized to unity. Presence of Carbon in the spectrum is due to the grid.

6.3.5 Formation of Au-Ag nanoalloy in ethanol by laser ablation

When Ag plate is ablated in the Au nanocolloidal solution generated in pure ethanol, a bimetallic nanostructure is observed. Similar to the above results, Au core/Ag shell bimetallic nanostructure is observed when Ag plate is ablated for a minute. As the time of ablation is increased, transformation from core/shell to alloy nanostructure is observed which is confirmed from the absorption spectra showing a single plasmon band tunable between the Au and Ag plasmon band depending on the molar concentration of the Ag nanocolloids. Time of ablation needed for the formation of alloy is less than that of nanoalloy generated in ethanolic solution of PVP. This is

because of PVP which acts as a capping agent stabilizes the nanoparticles and as the stability of the nanocolloids is increased, it is harder to perform any structural modification. But due to the instability problems of nanocolloids in ethanol, the bimetallic nanostructures precipitate completely just after its formation due to aggregation. So surfactants like PVP are used throughout the section.

6.3.6 Application of bimetallic nanostructures in MEF

As already seen in chapter 4 and 5, the presence of nanoparticles in the dye medium can enhance or quench the fluorescence depending on the type, size, shape and dielectric environment of the nanoparticles and fluorophores. Au core/Ag shell bimetallic nanostructure and its individual monomeric components such as Au and Ag nanocolloids of nearly same molarity (as present in the core/shell nanostructures) are taken and mixed with Rh6G doped in MMA. Due to the difficulty in maintaining the same composition of nanoalloy and core/shell nanostructures during the synthesis using laser ablation, a direct comparison between them can not to be taken. So the influence of alloy nanostructure in the gain medium is considered separately in the last section. Due to the low solubility of Rh6G in MMA, it is at first dissolved in ethanol where 100% miscibility is noticed and is taken as the stoke solution. From the stoke solution of Rh6G, desired quantity is mixed with MMA to get a concentration of 2.5×10^{-4}M. Concentrations of Au core/Ag shell nanocomposites as well as its components such as pure Au and Ag nanoparticles are maintained at 0.5μM in the gain medium for comparison.

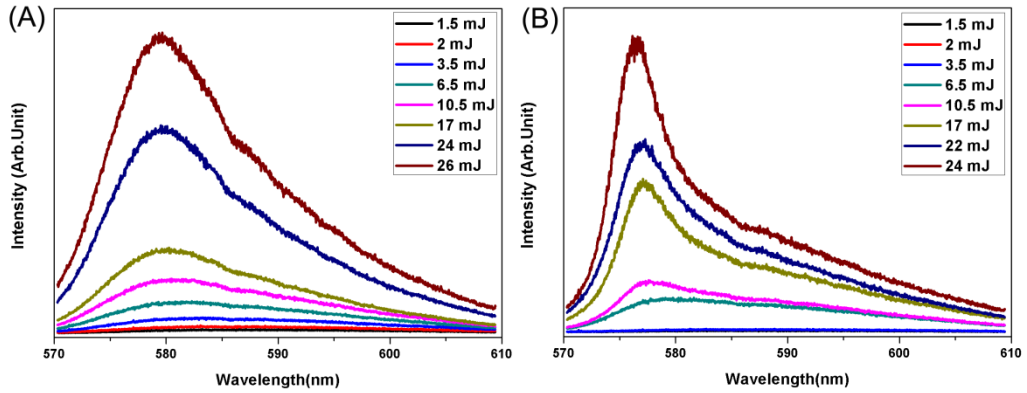

Figure 6.12: Emission spectra of 5 cm long fiber containing (A) Rh6G only and (B) Rh6G-Ag nanoparticles (P_2) in the cavity for an excitation length of 2cm. Emission is collected from one of the ends of the fiber when it is pumped axially.

From the optical absorption and emission spectra of Rh6G doped with Au, Ag and Au core/Ag shell (spectra are not shown), it is found that the absorption of Rh6G is increased maximum when core/shell is incorporated. Fluorescence enhancement factor of Rh6G in the presence of core/shell is nearly 3.9 where as in the presence of

Ag nanoparticles is 2.4. Similar results of fluorescence quenching as in the case of Au nanoparticles with 2nm and 7nm are observed when Au nanoparticles of 8nm (generated in PVP environment) are incorporated in the dye.

Spectral emission characteristics of the gain medium in POFs on addition of bimetallic core/shell nanocomposites (P_3) are compared with that of POFs containing bare gain medium (P) and gain medium containing pure Au (P_1) and Ag nanoparticles (P_2). Fibers of 50mm length and 320µm diameter are taken for the lasing study. Emission spectra of fiber samples containing Rh6G alone and Rh6G-Ag nanoparticles in the cavity is shown in Fig.6.12. For fiber containing Rh6G only, fluorescence emission is noticed at around 580nm when pumped at 2mJ. As the pump energy is increased, the linewidth of the emission starts to reduce and an ASE is observed when pump energy reaches 17mJ. Relation of linewidth of the emission from fibers with respect to pump energy is given in Fig.6.13 (A). Emission spectra of fibers containing Rh6G-Ag nanoparticle is shown in Fig.6.12 (B). ASE is noticed with linewidth reduction of the emission spectra when pumped at a low energy of 10mJ.

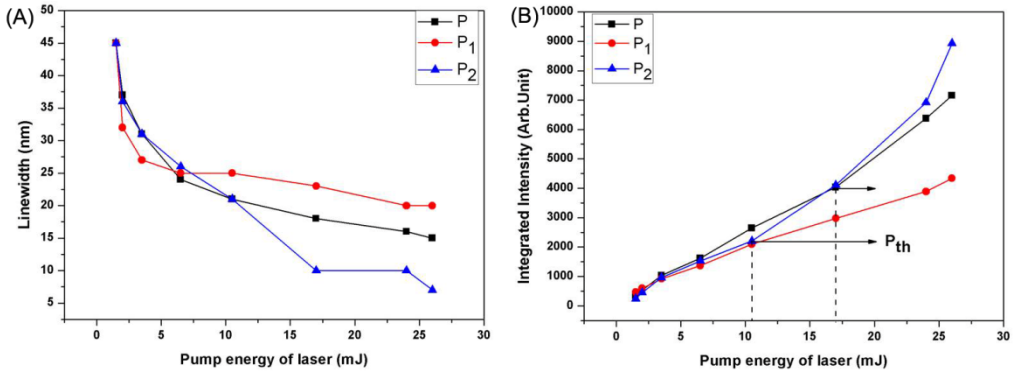

Figure 6.13: (A) Linewidth of the emission spectrum for different samples with varying pump energy and (B) Integrated intensity of emission of different POFs such as P, P_1 andP_2 versus pump energy of the laser.

As can be seen from Fig.6.13 (A), that spectral emission is narrowed down from an initial linewidth of 45nm to 20nm, 15nm and 7nm respectively for P_1, P and P_2 when pumped at 26mJ. Fig. 6.13 (B) shows the evolution of emission spectra with respect to pump energy and indicates that the threshold of ASE is minimum for P_2 at around 10mJ as compared to 17mJ for P (as evident from Fig.6.12). P_1 does not exhibit ASE even when pumped at 26mJ and its emission intensity is much lower than that of P. Thus the presence of Au nanoparticles do not bring down lasing threshold or linewidth as compared to bare dye doped POFs since it quenches the emission of dye through FRET as reported earlier [23]. But for P_2, the presence of Ag nanoparticles brings down the threshold of lasing through an increased gain of the amplifying medium due to increase in local incident electric field on the fluorophore [38]. Thus as from previous results in chapter 5, Ag nanoparticles with an average diameter of 14nm also

promotes metal enhanced fluorescence thereby enhancing the gain of the fiber laser through its plasmon field. Shift in the peak of the emission spectra for fiber P_2, with increase in pump energy, as compared to P is observed from Fig.6.12 (B). This is due to the existence of additional bands in the spectrum corresponding to de-excitation from higher vibronic level [37]. In addition, in the presence of Ag nanoparticles, additional radiative paths are present which may increases the radiative transition probability that can take place at shorter wavelength side of the spectrum. When pumped above the threshold lasing spikes are observed at the peak of ASE P_2 (as shown in Fig.6.12 (B)). However, well resolved modes are not observed.

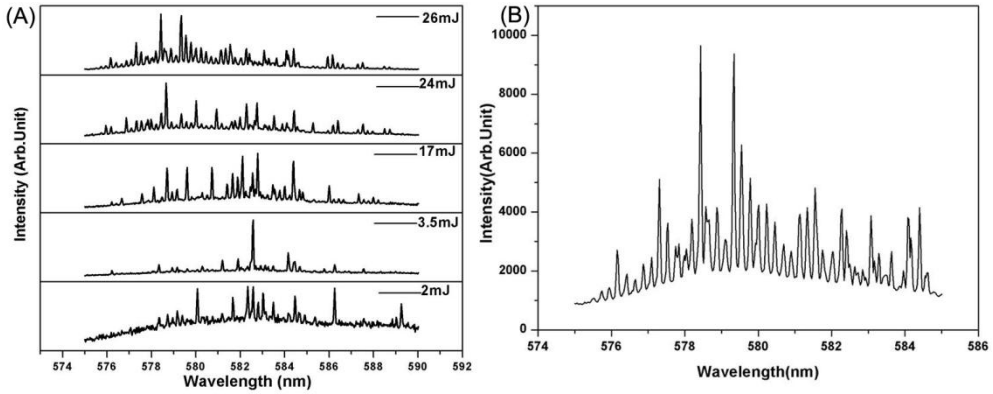

Figure 6.14: (A) WGM lasing from Au core/Ag shell incorporated POFs (P_3) with varying pump energy and (B) Enlarged version of WGM lasing at a pump energy of 26mJ.

It is found that presence of Au core/Ag shell nanostructure of nearly same concentration in the gain medium can improve the efficiency of lasing even better than its individual components. At a pump energy of 2mJ, P_3 starts lasing as shown in Fig.6.14. At the surface of complex structures like core/shell, there are hot spots near them where the electric field intensity can exceed the incident field intensity by several orders of magnitude. Thus the net gain of the amplifier is enhanced since more fluorophores are excited and emitted as compared to its individual components. Thus the threshold of lasing is brought down from 10mJ for P_2 to 2mJ for P_3. As seen from Fig.6.14 microcavity effect of POFs comes into play at such low pump energy as compared to other samples because the net gain provided by the core/shell nanostructure to the amplifier is high enough to overcome the losses in the cavity resulting in multimode WGM lasing from fibers with a Q factor as high as 7.5×10^3. The free spectral range (FSR) of whispering gallery microcavity resonator is given by

$$FSR = \frac{\lambda^2}{\pi D n_{eff}} \tag{6.1}$$

where λ is the wavelength of the strongest spectral line, n_{eff} is the effective refractive index of the cavity and D is the diameter of the cavity [39]. From the above equation the calculated value of FSR is 0.23nm which matches well with the observed FSR in Fig.6.14. With increase in pump energy more number of modes are excited in the cavity with increased intensity.

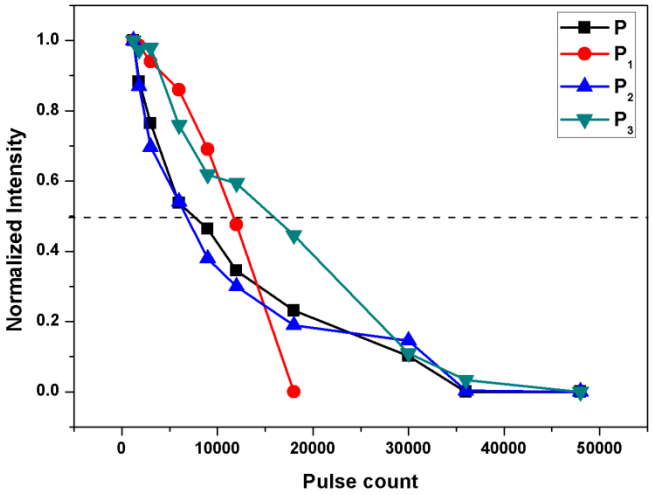

Figure 6.15: Photostability of POFs recorded with respect to pulse count. Fibers are pumped transversely at 15mJ using a biconvex lens and the emission is collected from one of the ends

Photostability of all the four fibers of same dimensions are recorded and are shown in Fig.6.15. It is found that fiber containing pure Rh6G (P) showed a half life at a pulse count of 7500 where as P_3 showed a half life at 15700. i.e., half life of fibers containing core/shell nanostructure in the gain medium has been enhanced by a factor of 2 as compared that of pure Rh6G doped POFs. This enhanced photostability is attributed to the reduced lifetime of the dye molecules in P_3 as compared to all other fibers allowing the dye to be radiated quickly from its excited state to the ground state. Even though P_1 showed a better half life, its increased photostability is deteriorated with pulse count as already mentioned in chapter 4. For P_2, the photostability is almost comparable with that of P. Thus the presence of core/shell bimetallic nanostructures in the gain medium of fiber lasers can improve the lasing efficiency as compared to its individual monomeric nanostructures.

Au-Ag nanoalloys of 0.5μM concentration with plasmon band at 440nm (containing 8×10^{-5} M Au nanoparticles and 2×10^{-4} M Ag nanoparticles) are incorporated in the gain medium of polymer fiber laser. Comparison has been made between the lasing efficiency of Rh6G doped POFs in the presence and absence of nanoalloys. Fibers of 240μm diameter are pumped axially using laser beam and the emission is collected from one of the ends. Nanoalloy doped fiber laser exhibited lasing at a low threshold of 2mJ where as bare dye doped POFs exhibits lasing at 7mJ.

Fig.6.16 shows the lasing emission from fibers when pumped at different energy. In the case of nanoalloys in the cavity, strongest mode is observed at 566.25nm with a linewidth of 0.09nm and Q factor of 6×10^3 when pumped at 7mJ. FSR is calculated to be 0.28nm which matches nearly with the mode spacing of 0.25nm obtained from the emission spectra (Fig.6.16 (B)). In the case of bare dye doped POFs, strongest mode is observed at 571.04nm when pumped at 7mJ with a Q factor of 8×10^3. Mode spacing obtained from the emission spectra is found to be 0.29nm when pumped at 7mJ. Thus presence of nanoalloy in the fiber cavity can reduce the lasing threshold which can be attributed to the plasmon field on its surface enhancing the gain of the medium. However, a comparison between core/shell and nanoalloys is not made since the composition of its monomeric nanoparticles in the nanostructure is different.

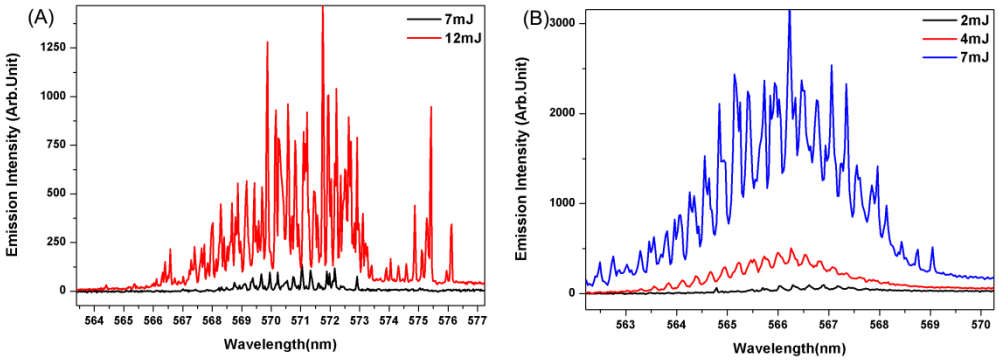

Figure 6.16: Lasing emission from (A) bare Rh6G doped POF and (B) Rh6G-Au-Ag nanoalloy doped POFs when pumped at different energy.

6.4 Conclusions

- Stability problems of nanoparticles generated in low polar solutions such as ethanol are solved by incorporating stabilising surfactants such as PVP in the solvent.
- Increasing concentration of PVP enhanced the formation efficiency of the nanoparticles in the solution due to the increased secondary ablation of the target plate in addition to the primary ablation by laser pulses.
- Core/shell bimetallic nanostructure of Au and Ag are produced by irradiating a physical mixture of individual monometallic Au and Ag nanocolloids generated in PVP solvents by laser ablation.
- A simple method of producing alloy of Au and Ag is introduced by laser ablation of the Ag plate in the already prepared nanocolloidal solution of Au. Alloy formation is supported through the formation of an intermediate phase of Au core/Ag shell nanostructure.

- Alloy of Au and Ag nanocolloids are also produced without PVP in a similar way as mentioned. But due to instability of the nanocolloids, precipitation has occurred just after its formation. However, time of ablation of Ag target plate needed for the alloy formation is less than that in the presence of PVP.
- Metal enhanced fluorescence in the presence of Au core/Ag shell nanostructures in Rh6G is compared with that of bare Rh6G and Rh6G containing its monomeric nanocolloids such as Au and Ag. A maximum emission enhancement is noticed in the presence of Au core/Ag shell.
- Au nanoparticles with an average size of 8nm deteriorated lasing action through FRET whereas Ag nanoparticles of 14nm promoted enhanced lasing efficiency.
- Polymer Optical Fibers are incorporated with Au core/Ag shell nanostructures as well as its monomeric components and its lasing properties are compared with that of pure Rh6G doped POF lasers. It is found that the efficiency of lasing has enhanced in the presence of core/shell nanostructure through the lowering of lasing threshold and increased photostability.
- Nanoalloys incorporated in the gain medium of the fiber also showed better efficiency as compared to bare Rh6G doped POF laser.

References

[1] Kuladeep, R., L. Jyothi, K. Shadak Alee, K. L. N. Deepak, and D. Narayana Rao. "Laser-assisted synthesis of Au-Ag alloy nanoparticles with tunable surface plasmon resonance frequency." Optical Materials Express 2, no. 2 (2012): 161-172.

[2] Chen, Yu-Hung, and Chen-Sheng Yeh. "A new approach for the formation of alloy nanoparticles: laser synthesis of gold–silver alloy from gold–silver colloidal mixtures." Chem. Commun 371 (2001): 372.

[3] Izgaliev, A. T., A. V. Simakin, G. A. Shafeev, and F. Bozon-Verduraz. "Intermediate phase upon alloying Au–Ag nanoparticles under laser exposure of the mixture of individual colloids." Chemical physics letters 390, no. 4 (2004): 467-471.

[4] Peng, Zhangquan, Bernd Spliethoff, Bernd Tesche, Thomas Walther, and Karl Kleinermanns. "Laser-assisted synthesis of Au-Ag alloy nanoparticles in solution." The Journal of Physical Chemistry B 110, no. 6 (2006): 2549-2554.

[5] Kim, Kwan, Kyung Lock Kim, and Seung Joon Lee. "Surface enrichment of Ag atoms in Au/Ag alloy nanoparticles revealed by surface enhanced Raman scattering spectroscopy." Chemical physics letters 403, no. 1 (2005): 77-82.

[6] Sanchez-Ramirez, J. F., U. Pal, L. Nolasco-Hernandez, J. Mendoza-Alvarez, and J. A. Pescador-Rojas. "Synthesis and optical properties of Au-Ag alloy nanoclusters with controlled composition." Journal of Nanomaterials 2008 (2008).

[7] Liu, Sha, Guanying Chen, Paras N. Prasad, and Mark T. Swihart. "Synthesis of monodisperse Au, Ag, and Au–Ag alloy nanoparticles with tunable size and surface plasmon resonance frequency." Chemistry of Materials 23, no. 18 (2011): 4098-4101.

[8] Gonzalez, Carlos Miguel, Yun Liu, and J. C. Scaiano. "Photochemical Strategies for the Facile Synthesis of Gold− Silver Alloy and Core− Shell Bimetallic Nanoparticles†." The Journal of Physical Chemistry C 113, no. 27 (2009): 11861-11867.

[9] Rivas, L., S. Sanchez-Cortes, J. V. Garcia-Ramos, and G. Morcillo. "Mixed silver/gold colloids: a study of their formation, morphology, and surface-enhanced Raman activity." Langmuir 16, no. 25 (2000): 9722-9728.

[10] Link, S., Zz L. Wang, and M. A. El-Sayed. "Alloy formation of gold-silver nanoparticles and the dependence of the plasmon absorption on their composition." The Journal of Physical Chemistry B 103, no. 18 (1999): 3529-3533.

[11] Shore, Matthew S., Junwei Wang, Aaron C. Johnston-Peck, Amy L. Oldenburg, and Joseph B. Tracy. "Synthesis of Au (Core)/Ag (Shell) nanoparticles and their conversion to AuAg alloy nanoparticles." Small 7, no. 2 (2011): 230-234.

[12] Shibata, Tomohiro, Bruce A. Bunker, Zhenyuan Zhang, Dan Meisel, Charles F. Vardeman, and J. Daniel Gezelter. "Size-dependent spontaneous alloying of Au-Ag nanoparticles." Journal of the American Chemical Society 124, no. 40 (2002): 11989-11996.

[13] Compagnini, Giuseppe, Elena Messina, Orazio Puglisi, and Valeria Nicolosi. "Laser synthesis of Au/Ag colloidal nano-alloys: Optical properties, structure and composition." Applied Surface Science 254, no. 4 (2007): 1007-1011.

[14] Sun, Li, Weiling Luan, and Yue Jin Shan. "A composition and size controllable approach for Au-Ag alloy nanoparticles." Nanoscale research letters 7, no. 1 (2012): 1-6.

[15] Mallik, Kaushik, Madhuri Mandal, Narayan Pradhan, and Tarasankar Pal. "Seed mediated formation of bimetallic nanoparticles by UV irradiation: a photochemical approach for the preparation of "core-shell" type structures."Nano Letters 1, no. 6 (2001): 319-322.

[16] Compagnini, Giuseppe, Elena Messina, Orazio Puglisi, Rosario Sergio Cataliotti, and Valeria Nicolosi. "Spectroscopic evidence of a core–shell structure in the earlier formation stages of Au–Ag nanoparticles by pulsed laser ablation in water." Chemical Physics Letters 457, no. 4 (2008): 386-390.

[17] Hajiesmaeilbaigi, F., and A. Motamedi. "Synthesis of Au/Ag alloy nanoparticles by Nd: YAG laser irradiation." Laser Physics Letters 4, no. 2 (2007): 133.

[18] Simakin, A. V., V. V. Voronov, N. A. Kirichenko, and G. A. Shafeev. "Nanoparticles produced by laser ablation of solids in liquid environment."Applied Physics A 79, no. 4-6 (2004): 1127-1132.

[19] Compagnini, G., E. Messina, and O. Puglisi. "Formation and properties of metal colloids and colloidal nano-alloys by laser ablation and irradiation of metals in liquids." Radiation Effects & Defects in Solids 163, no. 4-6 (2008): 271-276.

[20] Lee, Inhyung, Sang Woo Han, and Kwan Kim. "Production of Au–Ag alloy nanoparticles by laser ablation of bulk alloys." Chemical Communications 18 (2001): 1782-1783.

[21] Neumeister, Anne, Jurij Jakobi, Christoph Rehbock, Janine Moysig, and Stephan Barcikowski. "Monophasic ligand-free alloy nanoparticle synthesis determinants during pulsed laser ablation of bulk alloy and consolidated microparticles in water." Physical Chemistry Chemical Physics 16, no. 43 (2014): 23671-23678.

[22] Grade, Sebastian, Jörg Eberhard, Jurij Jakobi, Andreas Winkel, Meike Stiesch, and Stephan Barcikowski. "Alloying colloidal silver nanoparticles with gold disproportionally controls antibacterial and toxic effects." Gold Bulletin 47, no. 1-2 (2014): 83-93.

[23] Tiedemann, Daniela, Ulrike Taylor, Christoph Rehbock, Jurij Jakobi, Sabine Klein, Wilfried A. Kues, Stephan Barcikowski, and Detlef Rath. "Reprotoxicity of gold, silver, and gold–silver alloy nanoparticles on mammalian gametes."Analyst 139, no. 5 (2014): 931-942.

[24] Han, Huifeng, Yan Fang, Zhipeng Li, and Hongxing Xu. "Tunable surface plasma resonance frequency in Ag core/Au shell nanoparticles system prepared by laser ablation." Applied Physics Letters 92, no. 2 (2008): 023116.

[25] Chen, Yanrong, Haihua Wu, Zhipeng Li, Peijie Wang, Longkun Yang, and Yan Fang. "The study of surface plasmon in Au/Ag core/shell compound nanoparticles." Plasmonics 7, no. 3 (2012): 509-513.

[26] áDi Fabrizio, E. "Laser synthesis of ligand-free bimetallic nanoparticles for plasmonic applications." Physical Chemistry Chemical Physics 15, no. 9 (2013): 3075-3082.

[27] Tsuji, Takeshi, D-H. Thang, Yuuki Okazaki, Masataka Nakanishi, Yasuyuki Tsuboi, and Masaharu Tsuji. "Preparation of silver nanoparticles by laser ablation in polyvinylpyrrolidone solutions." Applied Surface Science 254, no. 16 (2008): 5224-5230.

[28] Tomita, Y., P. B. Robinson, R. P. Tong, and J. R. Blake. "Growth and collapse of cavitation bubbles near a curved rigid boundary." Journal of Fluid Mechanics466 (2002): 259-283.

[29] Kawaguchi, Y., X. Ding, A. Narazaki, T. Sato, and H. Niino. "Transient pressure induced by laser ablation of toluene, a highly laser-absorbing liquid."Applied Physics A 80, no. 2 (2005): 275-281.

[30] Theivasanthi, T., and M. Alagar. "Electrolytic Synthesis and Characterizations of Silver Nanopowder." arXiv preprint arXiv:1111.0260 (2011).

[31] Sebastian, Suneetha, C. L. Linslal, C. P. G. Vallabhan, V. P. N. Nampoori, P. Radhakrishnan, and M. Kailasnath. "Laser induced augmentation of silver nanospheres to nanowires in ethanol fostered by Poly Vinyl Pyrrolidone."Applied Surface Science 320 (2014): 732-735.

[32] Chandran, S. Prathap, J. Ghatak, P. V. Satyam, and Murali Sastry. "Interfacial deposition of Ag on Au seeds leading to Au core Ag shell in organic media."Journal of colloid and interface science 312, no. 2 (2007): 498-505.

[33] Zhu, Jian. "Surface plasmon resonance from bimetallic interface in Au–Ag core–shell structure nanowires." Nanoscale research letters 4, no. 9 (2009): 977-981.

[34] Sebastian, Suneetha, C. L. Linslal, C. P. G. Vallbhan, V. P. N. Nampoori, P. Radhakrishnan, and M. Kailasnath. "Formation of Au–Ag nanoalloy through Au core/Ag shell intermediate phase by laser ablation." Chemical Physics Letters628 (2015): 25-29.

[35] d = 0.235 nm, Joint Committee on Powder Diffraction Standards, File No. 04-0783

[36] Wagener, Philipp, Shyjumon Ibrahimkutty, Andreas Menzel, Anton Plech, and Stephan Barcikowski. "Dynamics of silver nanoparticle formation and agglomeration inside the cavitation bubble after pulsed laser ablation in liquid."Phys. Chem. Chem. Phys. 15, no. 9 (2013): 3068-3074.

[37] Kailasnath, M. "Fabrication and characterisation of dye doped polymer optical fibres with different refractive index profiles for photonic applications." PhD diss., University of science and Technology, 2010.

[38] Geddes, Chris D., and Joseph R. Lakowicz. "Editorial: Metal-enhanced fluorescence." Journal of Fluorescence 12, no. 2 (2002): 121-129.

[39] Linslal, C. L., S. Mathew, P. Radhakrishnan, V. P. N. Nampoori, C. P. Girijavallabhan, and M. Kailasnath. "Laser emission from the whispering gallery modes of a graded index fiber." Optics letters 38, no. 17 (2013): 3261-3263.

Chapter 7 :

Structural modification of Rhodamoine6G under femtosecond laser irradiation

---

In this chapter we have used femtosecond laser pulses to irradiate a well known dye molecule namely Rh6G in MMA solution and have noticed several interesting features related to the fluorescent emission from the irradiated system. Irradiation has also been done on Rh6G dissolved in other solvents such as water and ethanol and using other light sources such as nanosecond laser. Present work is of utmost interest since this can lead to a better sensing and detection of molecules, improved lasing properties and amplification using the pure dye itself. So we have demonstrated lasing properties of POFs containing modified Rh6G molecules and its optical characteristics.

Publications

Sebastian, Suneetha, C. Ajina, C. P. G. Vallabhan, V. P. N. Nampoori, P. Radhakrishnan, and M. Kailasnath. "Femtosecond laser induced emission enhancement in Rhodamine6G." Journal of Photochemistry and Photobiology A: Chemistry 288 (2014): 34-38

7.1 Introduction

It is well known that intense laser pulses can cause several interesting non-linear optical phenomena. Femtosecond laser pulses are known to produce high harmonics and continuum emission. They can also be used to induce many kinds of multi photon phenomena. The intense electric field of such pulses can cause bond breaking and rearrangement of molecular structure in many systems. Rh6G is the most commonly and widely used laser dye for the last four decades. Rh6G has many desirable properties such as high quantum efficiency, increased photostability and good lasing action [1,2]. Because of the widespread use of Rh6G in solid state dye lasers [3, 4], amplifiers [5, 6], and sensors [7], the continued studies on this molecule are still very much relevant. Photophysical as well as photochemical changes occurring in Rh6G due to irradiation have already been reported as early as 1971 [8]. Thereafter a number of further studies have come up in this field [9–12]. In all these reports a detailed mechanism behind the deterioration of the dye due to radiation is mentioned. But none of these works reported a spectral emission enhancement of the dye owing to its exposure to a light source. In this context the present study becomes important since it is the first such report of fluorescence enhancement of Rh6G due to radiation.

Fluorescence techniques are generally used for detection and sensing well over the last 25 years. But detection/sensing by this technology faces limitations due to quantum efficiency and photochemical stability of the fluorophore [13]. Recently there are many reports on the fluorescence enhancement of Rh6G using metal nanoparticles such as gold and silver [14–16]. Such successes in the field of radiative decay engineering overcome some of these limitations of the fluorophore. But an emission enhancement of the pure dye i.e., without the aid of metal nanoparticles is reported here.

7.2 Experimental section

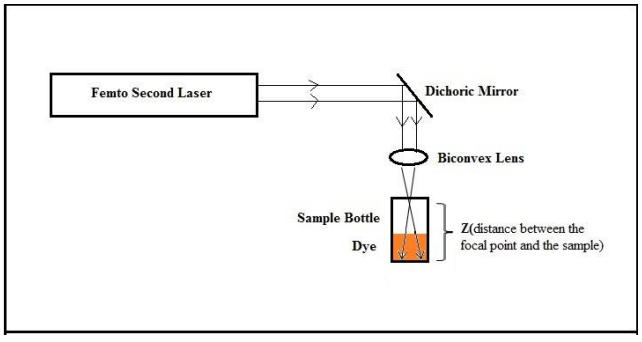

Figure 7.1: Schematic for the irradiation of Rh6G.

Rh6G is dissolved in pure Methyl Methacrylate at first in the present study. MMA is a good candidate for the POF because of its high transparency [6]. The motivation behind choosing MMA is that the whole sample can be directly polymerised. MMA is purified using the conventional purification techniques detailed in chapter 2. Fig.7.1 depicts the experimental setup used for the present study. A mode locked Ti: Sapphire femtosecond laser is used as the source of laser irradiation. Wavelength of radiation is centred around 797nm with a laser spot size of 7mm and an average output power of 1.5W. 120 fs pulsed radiation of 80MHz repetition rate is reflected using a dichoric mirror. Radiation is focussed using a biconvex lens of focal length 5cm. Irradiation has also been performed using fundamental and second harmonics of Nd-YAG laser with a repetition rate of 10Hz and pulse width of 9ns.

5ml of the dye solution is taken in a 15ml sample container for the experiment. Bottom of the sample container is placed at a distance of Z from the focal point of the lens. The experiment is repeated by varying Z from 0 to 5cm. Also the time of exposure of the sample to the laser radiation is changed from 30 seconds to 90 minutes. Further, to study the effect of concentration of the dye, the molarity of the dye is varied from 10^{-6}mol/litre to 10^{-3}mol/litre.

The photophysical characteristics of the samples are noted. Spectral absorption of the irradiated sample is recorded using Jasco UV-VIS NIR Spectrophotometer. The spectral emission of the same is recorded using Varian Cary Eclipse Fluorimeter. Fourier Transform Infra Red (FTIR) spectra are obtained using Thermo Nicolet, Avatar 370 with a resolution of 4cm^{-1}. Lasing characteristics as well as photobleaching rate of modified Rh6G molecules in step index POFs have also been recorded using the same experimental setup described in chapter 2.

7.3 Results and Discussions

7.3.1 Irradiation using femtosecond laser pulses

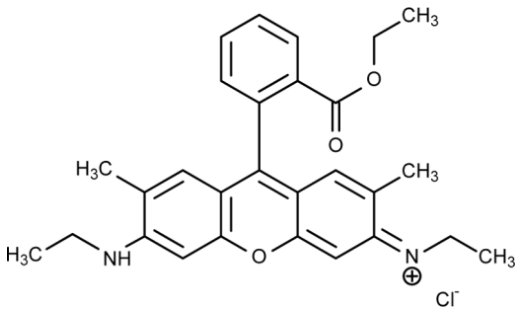

Figure 7.2: Molecular structure of Rh6G.

The molecular structure of Rh6G is widely studied by many researchers and is shown in Fig.7.2 [17]. Rh6G is a highly fluorescent xanthene dye. Xanthene ring is surrounded by phenyl and amino external groups. As is well known, the dye absorbs mainly around 530nm and emits strongly in the visible region [17-18]. It is found that irradiation of Rh6G dispersed in MMA by 797nm fs laser pulses brought changes in the optical properties of the dye and is systematically studied in the following sections.

7.3.1.1 Effect of irradiation time

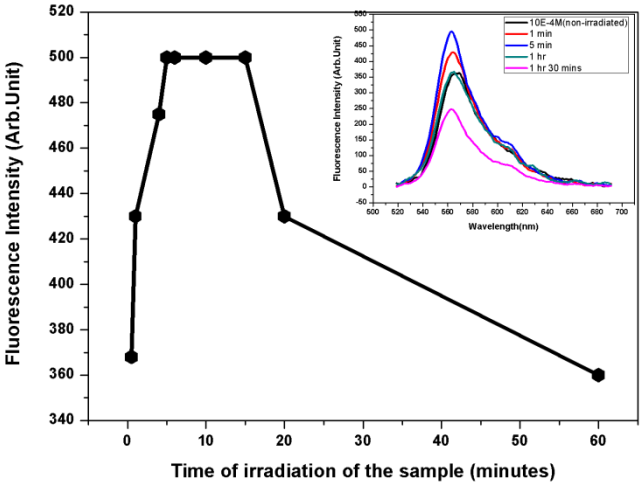

Figure 7.3: Peak fluorescence intensity of Rh6G vs. Irradiation time of the dye. Intensity corresponding to 0 min is the initial peak intensity of the dye before irradiation. Inset shows the emission spectra of Rh6G, excited at 500 nm, before and after irradiation with femtosecond laser pulses.

After irradiating the dye solution of 10^{-4}mol/l concentration kept at a distance of 2cm from the focal point for 10min, it is noted that the appearance of the sample itself has changed to more bright and fluorescent (change of colour from pinkish orange to a bright orange is noticed). To understand the phenomenon in detail the exposure time of the sample is varied. Fig. 7.3 depicts the change in the emission intensity of the dye when it is exposed to different time durations of femtosecond radiations. As seen from figure, 30% increase in the peak value of fluorescence emission of the dye is obtained when the sample is exposed for 5min. Increase in the exposure time up to 15min does not bring any further enhancement in the peak intensity as compared to 5min exposed sample. But after 15min, the emission intensity starts to decrease from the maximum and at 60min, the intensity of the irradiated sample becomes same as that of non-irradiated sample. Further exposure of the sample to the source reduces the intensity to even lower values as evident from the inset of Fig. 7.3. Thus the optimum exposure time for maximum enhancement is determined to be 5–15min and the exposure beyond this time scale reduces the dye's fluorescence.

7.3.1.2 Effect of concentration of the dye

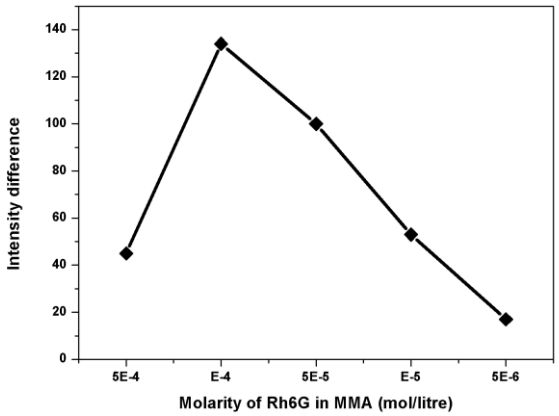

Figure 7.4: The difference in peak fluorescence intensity between the non-irradiated sample and 5min irradiated samples vs. concentration of the dye.

The experiment is repeated by changing the concentration of the dye in the solution. It is observed that the maximum enhancement is possible only for a particular concentration i.e. 10^{-4}mol/litre as is shown in Fig.7.4 which is the concentration for maximum fluorescence emission for pure dye in MMA. Even though other concentrations also showed fluorescence enhancement, the percentage of increase is found to be less.

7.3.1.3 Effect of distance from the focal point (Z)

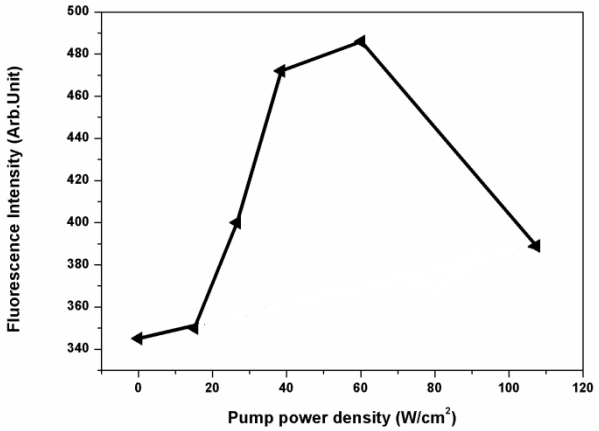

Figure 7.5: Variation of fluorescence intensity with pump power density. 0w/cm^2 corresponds to the fluorescence intensity of non-irradiated sample. All samples are irradiated for 5 minutes. Z=1.5cm, Z=2cm, Z=2.5cm, Z=3cm, Z=4cm corresponds to the pump power densities of 107W/cm^2, 60W/cm^2, 38W/cm^2, 27W/cm^2, 15W/cm^2 respectively.

Finally the influence of Z, which is the distance between the focal point of the lens and the bottom of the sample container, on the emission enhancement is taken into consideration and is depicted in Fig.7.5. It is found that when the focus is within the sample, emission intensity is drastically quenched when irradiated for 5 minutes. At the focus the diameter of the laser radiation is found to be 11.4μm and the power density is 1.47MW/cm^2. This density is so high that the molecule may get structural decomposition leading to an adverse effect on the emission intensity as compared to the non-irradiated sample. As Z is increased obviously the power density of the pump is decreased and interestingly it is found that for a power density of 60W/cm^2 (i.e. when Z=2cm) maximum fluorescence enhancement is noted. Power density above or below 60W/cm^2 resulted in decrease in dye's emission with respect to the emission at this optimized power density. Thus an optimum fluorescence enhancement of Rh6G is noticed when irradiated by fs laser pulses having a power density of 60W/cm^2 for 5min when the concentration of the dye is fixed at 10^{-4}mol/litre.

7.3.1.4 Structural modifications in Rh6G

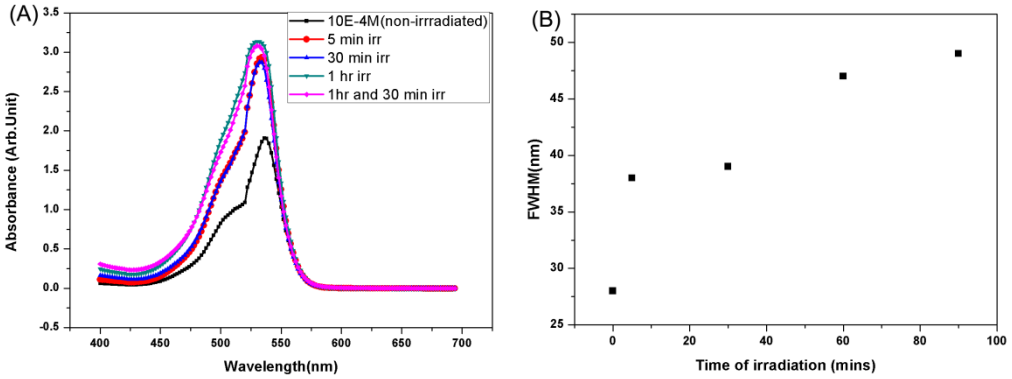

Figure 7.6: (A) Optical absorption spectra of Rh6G before and after irradiation with fs laser pulses. Sample is kept at a distance of Z=2cm from the focal point and (B) Width of absorption band of dye is plotted as a function of irradiation time. Width at 0 irradiation time corresponds to the non-irradiated dye.

Fig. 7.6(A) shows the spectral absorption of the samples before and after irradiation. It is noticed that the spectral characteristics of the irradiated dye is significantly changed. The absorption of dye before irradiation has enhanced nearly twice after irradiating for 5min and the shape of the absorption band after irradiation has changed. Also the width of the absorption band of Rh6G is increased with irradiation time as shown in. Fig.7.6 (B). When irradiated for 5min, the width is increased from 28nm to 38nm and as the irradiation is continued, the width is increased upto 48nm. The shoulder at 520nm, due to the vibronic transitions, lifts up and merges with that of the peak at 532nm which is essentially due to the electronic

transitions of its molecules. When the irradiation is continued beyond an hour with optimised parameters no further changes in the spectrum as well as hike in absorbance is noticed. The spectral change due to irradiation by fs laser pulses is thought as bringing some photo-induced structural changes of the molecules. Due to the large peak power of fs pulses, non-linear effects such as multi photon absorption is thought to occur during irradiation which causes some molecular bond breaking or re-arrangement.

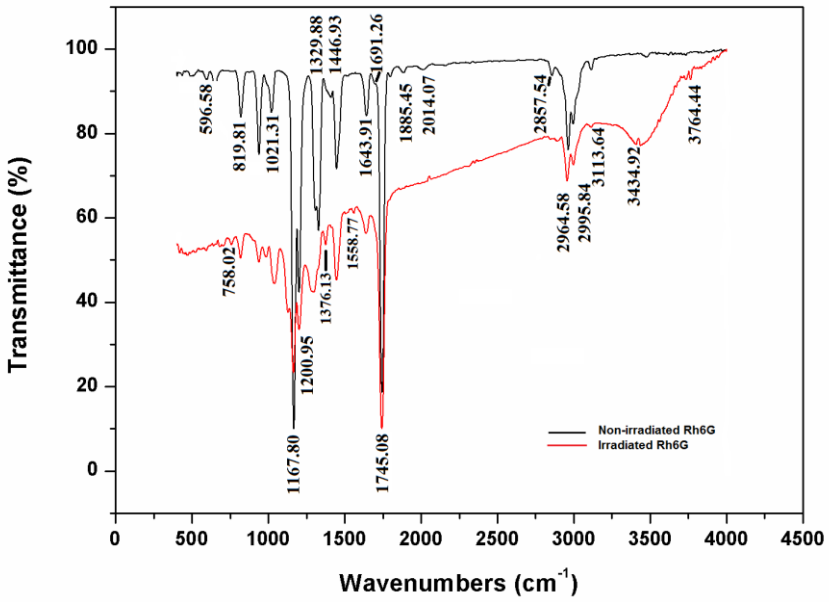

Figure 7.7: FTIR spectra of non-irradiated and irradiated Rh6G in MMA for 5 minutes at a concentration of 10^{-4} mol/litre with a pump power density of 60 W/cm^2.

Further in order to understand the structural changes happening in the irradiated dye, FTIR spectra are recorded for the bare sample and irradiated sample (Fig.7.7). As seen from Fig.7.7, the bands present in the spectrum are the combined effect of Rh6G and MMA. The bands at 596 cm^{-1},819 cm^{-1}, 1167 cm^{-1}, 1329 cm^{-1} are due to the xanthene ring, phenyl and ethylamine groups of Rh6G. The band at 1021 cm^{-1} is due to methyl, phenyl and ethylamine external groups. The sharp band at 1200 cm^{-1} is due to xanthene ring and ethylamine groups. Again the sharp peak at 1446 cm^{-1} is due to ethylamine group. The very sharp and narrow band at 1745 cm^{-1} is due to C=O stretching of the xanthene ring of Rh6G and carbonyl stretching band due to MMA. The band at 1643cm^{-1} is due to C=C bond in MMA. The band at 3000 cm^{-1} range is due to symmetric and asymmetric vibrations of methylene group present in MMA [18-24]. But in the FTIR of the irradiated sample, it can be seen that all bands

which are present in the FTIR of non-irradiated sample get reduced in intensity. Also some bands due to xanthene ring like 1691cm^{-1} and 1329cm^{-1} disappear and new bands like 758 cm^{-1} are appearing. It is reported that the new bands like 758 cm^{-1} are due to the presence of deformed xanthene ring. We have also observed other new bands in the FTIR spectrum of the irradiated dye such as 1376cm^{-1} and 1558cm^{-1} which are due to the stretching of the xanthene ring [18].

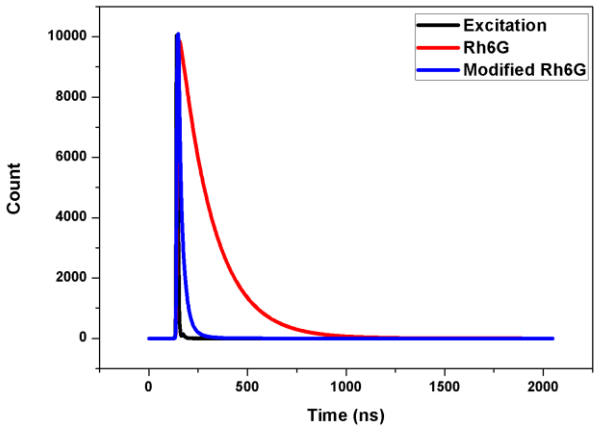

Figure 7.8: Time resolved fluorescence spectra of modified Rh6G.

From these inferences it can be thought that the photochemical reaction induced by the pump beam is initiating the breakdown and thereby the deformations of the xanthene ring in Rh6G. Also from Fig.7.7 it is evident that some new bands are also appearing in the high wavenumber range and this can be likely due to the rearrangement of molecular structure of MMA by the attachment of chromophore group from Rh6G to MMA monomers or dimmers. The new structure of Rh6G molecule is an intermediate state of the dye before it gets degraded when irradiated beyond the optimum time. The structural deformation happening to the dye under laser radiation might have reduced the rate of non-radiative relaxation of the molecules from the excited state thereby increasing the radiative decay rate resulting in fluorescence enhancement. The time resolved fluorescence spectra of the samples are recorded and given in Fig. 7.8. Lifetime calculated from the decay curves is found to be decreased from 3.71ns to 2.11ns. Rate of radiative decay and non-radiative decay are calculated using the equations for classical fluorescence given in chapter 5 and is given in Table.7.1. Rate of radiative decay is found to be increased from 0.23×10^9/s to 0.45×10^9/s and that of non-radiative decay rate is reduced (Table.7.1). Thus fs laser induced irradiation of Rh6G brought photo-induced structural changes in the dye thereby increasing the rate of radiative decay nearly twice. The intermediate state is found to be very stable for

months. With increase in irradiation time, photobleaching of the dye occurred with structural degradation.

Table7.1: Variation of QY, lifetime, radiative and non-radiative decay rate of modified Rh6G.

Sample Designation	Quantum yield	Lifetime (ns)	Rate of radiative decay (10^9/s)	Rate of non-radiative decay(10^9/s)
Rh6G	0.85	3.71	0.23	0.039
Modified Rh6G	0.95	2.11	0.45	0.023

For any fluorescent material such as dyes, quantum yield of its luminescence is a fundamental property and so its calculation is really promising for the characterisation of the material. The quantum yield is found out using the equation given below

$$Q_s = Q_R \frac{I_s \times (1-10^{-A_R}) \times n_s^2}{I_R \times (1-10^{-A_s}) \times n_R^2} \tag{7.1}$$

where the subscript S and R stands for the reference and sample respectively. Q is the quantum yield, I stands for the integrated fluorescence intensity and the term in the brackets is known as absorption factor where A is the absorbance [25]. Q_R is taken as 0.85 which is the quantum yield of Rh6G in MMA. Substituting other parameters in equation (1) using data from the spectral absorption and emission given in Fig.7.6 (A) and inset of Fig.7.3, it is found that quantum efficiency of the dye in MMA irradiated for 5min at a pump power density of 60W/cm^2 is increased from 0.85 to 0.95 (Table7.1). So the important increase in fluorescence intensity of the dye upto 30% upon irradiation results in increase of the quantum yield of the dye to nearly 10%.

In order to understand the solvent effect on the fluorescent enhancement upon fs laser irradiation, the FTIR of MMA before and after irradiation has been recorded (not shown here). It is found that bands are exactly matching with each other except for the intensity. So it is concluded that the solvent effect is not playing an important role in the structural modification of Rh6G when irradiated by fs laser. The effect is further confirmed by repeating the experiment using solvents like water and ethanol.

7.3.2 Irradiation using Nd-YAG laser

Rh6G dispersed in MMA with the optimum concentration (10^{-4}M, where maximum fluorescence enhancement is noted) is irradiated using Nd-YAG laser at 532nm with power density of 4.9W/cm^2 using the experimental setup as given in

section 7.2. Spectral emission and absorption spectra are noted after irradiation at various time durations and is depicted in Fig.7.9. It is seen that emission intensity is quenched at any time of irradiation of the dye. When irradiated for 5min, emission intensity quenches as compared to the non-irradiated reference with a blue shift of the band from 565nm to 561nm.

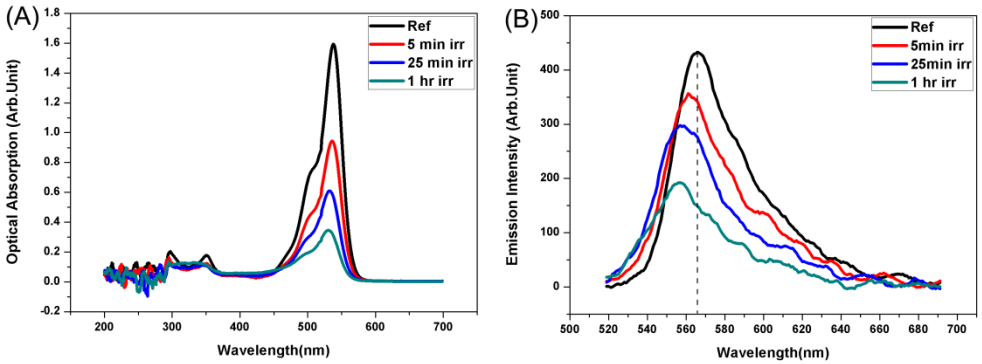

Figure 7.9: (A) Emission spectra and (B) absorption spectra of Rh6G in MMA irradiated by ns laser at various time intervals.

As the time of irradiation is increased, reduction in luminescence intensity with further blue shifting in the emission band is observed. When irradiation is continued for an hour, the fluorescence intensity quenched to less than half the initial emission intensity of the dye and further blue shift is observed. The shift in the emission band with reduction in intensity can be attributed to photobleaching of the dye due to irradiation. When irradiated by 532nm laser pulses, the dye molecules get excited due to single photon absorption and the excited state molecules in the S_1 state may undergo a transition to the triplet state through inter system crossing. Since the transition from an excited triplet state to the ground state is longer than singlet to singlet transition, reduced emission intensity is noticed. However it is found that in this case, photobleaching is not a permanent effect since most of the dye molecules return to their previous state after some days. From Fig.7.9 (B) we can see that the absorption is increased when irradiated for 5mins and 25mins with no spectral change. However when irradiated for an hour, the absorption is decreased which means that the number of dye molecules in the S_0 state has diminished since more of the excited state molecules are presented in the triplet state reducing the number of molecules returning to the ground state. Since no spectral change is observed, it can be inferred that the irradiation is not causing any photo-induced structural changes of the xanthene ring. This can be further confirmed by the FTIR spectra given in Fig.7.10. The theory of photobleaching as presented above can be proven correct since the dye molecules return to their original state after a day which is confirmed from the emission spectra recorded after some days.

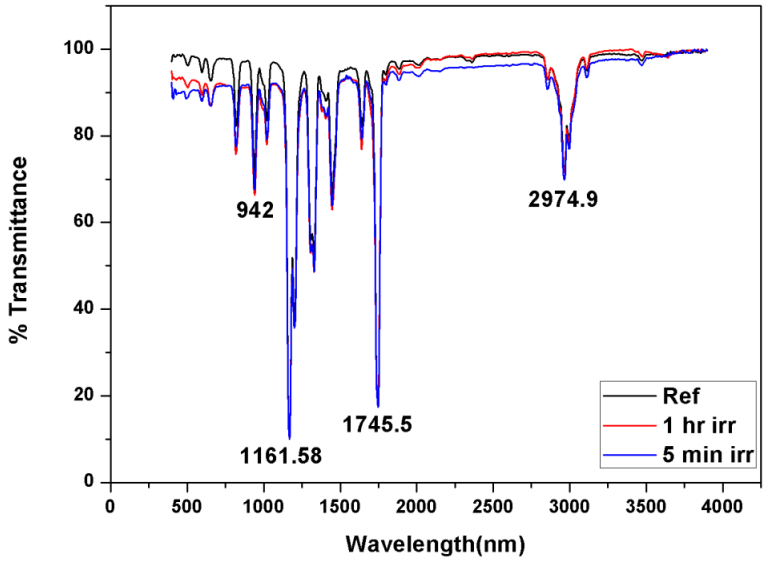

Figure 7.10: FTIR spectra of Rh6G irradiated by ns laser for 5mins and 60 minutes.

From the FTIR spectra it can be seen that all bands even after irradiation for an hour matches exactly with the non-irradiated dye and the bands corresponding to the xanthene ring are also identical. Thus it can be concluded that irradiation by ns laser at 532nm is not bringing any photo-induced structural deformation to the dye molecules even if it promotes photobleaching. Irradiation is also performed using different power density of laser and also using the fundamental wavelength of Nd-YAG laser. The results obtained are the same as above.

7.3.3 Lasing properties and photostability of modified Rh6G in POFs

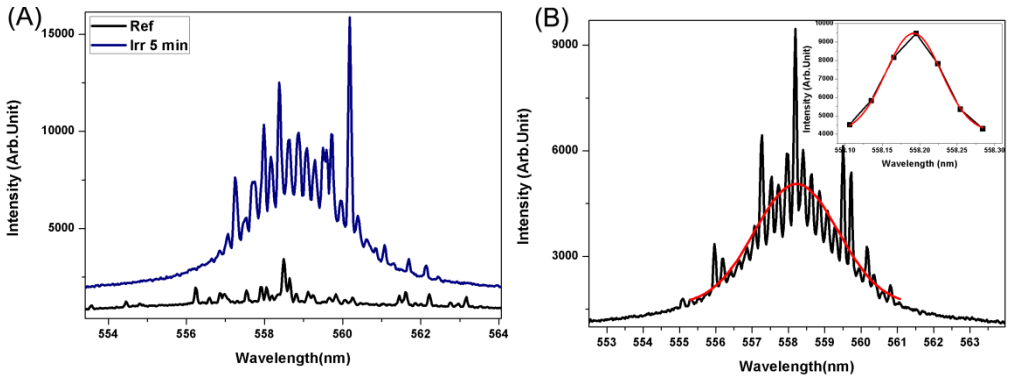

Figure 7.11: (A) Lasing emission from pure Rh6G doped POF (Ref) and modified Rh6G doped POFs (Irr 5 min) of 290µm diameter when pumped at 10mJ and (B) WGM lasing from modified Rh6G doped POF and inset shows the Gaussian fit of strongest mode at 558.19nm.

Modified Rh6G molecules produced by fs laser irradiation with optimised parameters are immobilized in step index polymer optical fibers as gain media and its lasing characteristics are studied and compared with pure Rh6G doped POFs at a concentration of 10^{-4} mol/litre. Fig.7.11 depicts the lasing emission from modified Rh6G and that from pure Rh6G doped POFs. As can be seen from the spectra, multimode lasing has been observed in both cases with a mode spacing of 0.23nm which matches with the WGM spacing calculated theoretically. Modes of both fibers match exactly such as a prominent mode at 558.48nm is observed in both cases. However we have observed a lasing emission enhancement of nearly 4 times in modified dye doped POF while considering this particular mode (Fig.7.11 (A)). The lasing emission from modified Rh6G is fitted well with a non-linear Gaussian fit with peak emission observed from the mode at 558.19 nm. The linewidth of the strongest mode is 0.08nm as seen in the inset of Fig.7.11 (B) and is also fitted with a Gaussian fit. Thus it can be inferred that deformation in the xanthene ring of Rh6G due to fs laser irradiation has not bring any changes in the laser emission of the pure dye except that the emission intensity is enhanced nearly 4 times. The enhanced emission is due to the increased radiative decay of modified Rh6G.

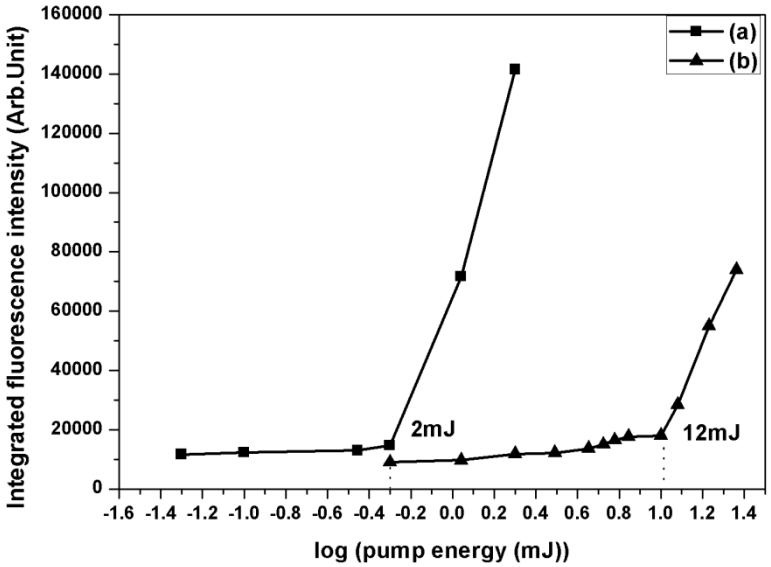

Figure 7.12: Emission of fibers containing (a) modified Rh6G and (b) pure Rh6G with respect to log of pump energy.

Emission of the fibers with modified Rh6G in the cavity is recorded w.th respect to pump energy (Fig.7.12) and it is found that the threshold energy needed for lasing has been brought down considerably from 12 mJ to 2 mJ. Thus the presence of modified Rh6G in POFs brings down threshold of lasing thereby improving the lasing efficiency of the dye without the aid of any nanoparticles in the cavity.

Photostability of fiber containing modified Rh6G is recorded at various time durations/pulse counts and the photostability curves are shown in Fig.7.13. Upto 10800 pulses the pure Rh6G doped POFs are found to be more photostable than modified Rh6G doped POFs. When pumped after this, both fibers are found to follow nearly same photostability curves and photobleaching rate.

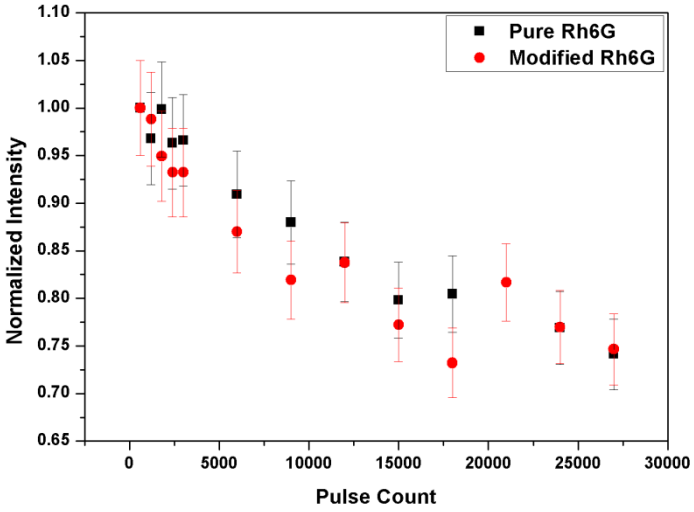

Figure 7.13: Photostability curves of modified as well as pure Rh6G doped POFs having a diameter of 440µm and pumped at 10mJ.

7.4 Conclusions

- Rh6G of 10^{-4}mol/litre when irradiated by fs laser at an optimised pump power density of 60W/cm^2 and irradiation time between 5-15min showed a peak emission enhancement of 30% with a quantum yield increase of 10%.
- Optical absorption and FTIR spectra recorded before and after irradiation showed that there is some structural deformation happening in Rh6G which can be attributed to the deformation of the xanthene ring. The structurally modified Rh6G is found to be very stable even for months.
- When irradiation is continued for an hour the intensity of luminescence emission is found to be quenched as compared to pure sample and also the width of the absorption spectra is increased leading to a complete deformation of dye molecules. Thus irradiation has caused structural deformation accompanied by photobleaching and the state of the dye is found to be permanent.
- Unlike in the case of fs laser pulses, Rh6G irradiated by ns laser at 532nm showed reduced fluorescence intensity under all experimental conditions. But both absorption as well as FTIR spectra remains unchanged in all cases indicating that photo-induced changes happened to the dye molecules is

temporary and is further confirmed from the emission spectra recorded after a few days.

- Lasing from step index POFs with pure as well as modified Rh6G as the gain media showed exactly the same modes. Modified Rh6G doped POFs showed a 4 fold increase in lasing mode intensity with a threshold reduction.
- Photostability curves of both types of Rh6G matched almost exactly at higher pulse count where as at low pulse count pure Rh6G doped POFs showed a better stability.
- Thus structural modification of Rh6G molecules caused by fs laser irradiation under optimised conditions produced more efficient step index POF lasers with stability much similar to pure Rh6G doped fiber.

References

[1] Avnir, David, David Levy, and Renata Reisfeld. "The nature of the silica cage as reflected by spectral changes and enhanced photostability of trapped rhodamine 6G." The Journal of Physical Chemistry 88, no. 24 (1984): 5956-5959.

[2] Rajesh, M., K. Geetha, M. Sheeba, CP G. Vallabhan, P. Radhakrishnan, and V. P. N. Nampoori. "Characterization of rhodamine 6G doped polymer optical fiber by side illumination fluorescence." Optical Engineering 45, no. 7 (2006): 075003-075003.

[3] Kuriki, Ken, Takeyuki Kobayashi, Nana Imai, Toshihiko Tamura, Susumu Nishihara, Yukihisa Nishizawa, Akihiro Tagaya, Yasuhiro Koike, and Yoshi Okamoto. "High-efficiency organic dye-doped polymer optical fiber lasers."Applied Physics Letters 77, no. 3 (2000): 331-333.

[4] Kuriki, Ken, Takeyuki Kobayashi, Nana Imai, Toshihiko Tamura, Yasuhiro Koike, and Yoshi Okamoto. "Organic dye-doped polymer optical fiber laser."Polymers for Advanced Technologies 11, no. 8-12 (2000): 612-616.

[5] Peng, Gang Ding, Pak L. Chu, Zhengjun Xiong, Trevor W. Whitbread, and Rod P. Chaplin. "Dye-doped step-index polymer optical fiber for broadband optical amplification." Lightwave Technology, Journal of 14, no. 10 (1996): 2215-2223.

[6] Rajesh, Mandamparambil, Mavila Sheeba, Karinjamanna Geetha, Chakkalakkal PG Vallaban, Padmanabhan Radhakrishnan, and Vadakkedathu PN Nampoori. "Fabrication and characterization of dye-doped polymer optical fiber as a light amplifier." Applied optics 46, no. 1 (2007): 106-112.

[7] Cox, Felicity M., Alexander Argyros, Maryanne CJ Large, and Srinath Kalluri. "Surface enhanced Raman scattering in a hollow core microstructured optical fiber." Optics Express 15, no. 21 (2007): 13675-13681.

[8] Ippen, Erich, C. Shank, and A. Dienes. "Rapid photobleaching of organic laser dyes in continuously operated devices." Quantum Electronics, IEEE Journal of7, no. 4 (1971): 178-179.

[9] Kato, Daisuke, and Akira Sugimura. "Deterioration of rhodamine 6G dye solution in methanol." Optics Communications 10, no. 4 (1974): 327-330.

[10] Rosenthal, I. "Photochemical stability of Rhodamine 6G in solution." Optics Communications 24, no. 2 (1978): 164-166.

[11] Arbeloa, F. López, A. Costela, and I. López Arbeloa. "Molecular structure effects on the lasing properties of rhodamines." Journal of Photochemistry and Photobiology A: Chemistry 55, no. 1 (1990): 97-103.

[12] Yamashita, Mikio, and Hiroshi Kashiwagi. "Photodegradation mechanisms in laser dyes: A laser irradiated ESR study." Quantum Electronics, IEEE Journal of 12, no. 2 (1976): 90-95.

[13] Aslan, Kadir, Ignacy Gryczynski, Joanna Malicka, Evgenia Matveeva, Joseph R. Lakowicz, and Chris D. Geddes. "Metal-enhanced fluorescence: an emerging tool in biotechnology." Current Opinion in Biotechnology 16, no. 1 (2005): 55-62.

[14] Kang, Kyung A., Jianting Wang, Jacek B. Jasinski, and Samuel Achilefu. "Fluorescence manipulation by gold nanoparticles: from complete quenching to extensive enhancement." J. Nanobiotechnol 9 (2011): 16.

[15] Liu, Gaining, Hairong Zheng, Meicen Liu, Zhenglong Zhang, Jun Dong, Xiaoqing Yan, and Xuqiang Li. "Surface-enhanced fluorescence of rhodamine 6G on the assembled silver nanostructures." Journal of nanoscience and nanotechnology11, no. 11 (2011): 9523-9527.

[16] Dong, Lin, Fei Ye, Adnan Chughtai, Vytautas Liuolia, Sergei Popov, Ari T. Friberg, and Mamoun Muhammed. "Lasing From Water Solution of Rhodamine 6G/Gold Nanoparticles: Impact of-Coating on Metal Surface." Quantum Electronics, IEEE Journal of 48, no. 9 (2012): 1220-1226.

[17] Wu, Dan, Gang-Hua Deng, Yuan Guo, and Hong-fei Wang. "Observation of the interference between the intramolecular IR− visible and visible− IR processes in the doubly resonant sum frequency generation vibrational spectroscopy of rhodamine 6G adsorbed at the air/water interface." The Journal of Physical Chemistry A 113, no. 21 (2009): 6058-6063.

[18] Majoube, M., and M. Henry. "Fourier transform Raman and infrared and surface-enhanced Raman spectra for rhodamine 6G." Spectrochimica Acta Part A: Molecular Spectroscopy 47, no. 9 (1991): 1459-1466.

[19] Sebastian, Suneetha, C. Ajina, C. P. G. Vallabhan, V. P. N. Nampoori, P. Radhakrishnan, and M. Kailasnath. "Femtosecond laser induced emission enhancement in Rhodamine6G." Journal of Photochemistry and Photobiology A: Chemistry 288 (2014): 34-38.

[20] Alshuiref, Abubker A., Hesham G. Ibrahim, Abdulmaged Abduallah, and Mohamed A. Edali. "Thermal and Mechanical Analysis of Urethane Acrylate Graft Copolymer Part A: Urethane Macromonomer Base on TDI and EG."International Journal of Chemistry 5, no. 1 (2013): p58.

[21] Crompton, Thomas Roy. Characterisation of polymers. Vol. 1. Smithers Rapra, 2008.

[22] Zheng, Yu-Ming, Rita Farida Yunus, KG Nadeeshani Nanayakkara, and J. Paul Chen. "Electrochemical decoloration of synthetic wastewater containing rhodamine 6G: behaviors and mechanism." Industrial & Engineering Chemistry Research 51, no. 17 (2012): 5953-5960.

[23] Laranjo, Marina T., Valter Stefani, Edilson V. Benvenutti, Tania MH Costa, Guilherme de O. Ramminger, and Marcia R. Gallas. "Synthesis of ORMOSIL silica/rhodamine 6G: Powders and compacts." Journal of non-crystalline solids353, no. 1 (2007): 24-30.

[24] Tripathi, S. K., Alka Monga, and G. S. S. Saini. "Characterization of thermally evaporated thin films of Rhodamine 6G." Smart Materials and Structures 18, no. 12 (2009): 125012.

[25] Brouwer, Albert M. "Standards for photoluminescence quantum yield measurements in solution (IUPAC Technical Report)." Pure and Applied Chemistry 83, no. 12 (2011): 2213-2228.

Chapter 8 :

Formation of Ag nanowires from nanospheres- its Applications in lasing and SERS

In the present work we report on the formation of well defined nanowires by laser induced irradiation of already prepared Ag nanocolloidal solution containing nanospheres. Stability of the nanocolloidal solution is provided by Poly Vinyl Pyrrolidone which also fosters the transformation of nanospheres to nanowires. Scattering strength of Ag nanowires has been calculated from scattering mean free path. MEF using Ag nanowires has been demonstrated through increase in radiative decay rate of the fluorophore and its practical application in lasing has been done. SERS of PMMA molecules with Ag nanowires has also been carried out.

Publications

Sebastian, Suneetha, C. L. Linslal, C. P. G. Vallabhan, V. P. N. Nampoori, P. Radhakrishnan, and M. Kailasnath. "Laser induced augmentation of silver nanospheres to nanowires in ethanol fostered by Poly Vinyl Pyrrolidone."Applied Surface Science 320 (2014): 732-735.

8.1 Introduction

The size and shape dependent properties of metal nanoparticles make them suitable for applications in optical and electrical devices including biosensors [1], solar cells [2-4], near field optical microscopes [5] and light emitting diodes [6]. Among various metal nanoparticles like silver, gold, platinum and copper, Ag nanoparticles have the highest surface plasmon strength across the UV- VIS- IR spectrum [7] which in turn depends on size and various shapes of nanostructures like nanosheres, nanowires and nanoprisms [8-9]. The strength of electric field caused by SP is much higher at the corners of anisotropic shaped nanostructures such as nanowires than on the surface of isotropic shaped structures such as nanospheres [10] and so its synthesis is very promising for tremendous practical plasmonic applications. Since last decade it has been expected that noble metal nanorods and nanowires are exceptional in modifying electromagnetic fields, on the basis of their apparent similarities to antennas. Schatz et al. [11] have theoretically calculated that isolated nanowires and nanorods exhibit the highest electromagnetic field enhancements at their ends compared to other nanostructures, making them very attractive substrates for MEF based applications. But only a very few reports have come up in this field so far [12-15]. In a previous report [16] it has been shown that amplification up to two orders of magnitude is possible using metal nanowires. Amplification is induced not only by the surface plasmon resonance of conduction band electrons but also due to the fact that sharp tips of the nanowires with high aspect ratio act as antennas for the radiating emission from the nearby fluorophores. Even higher amplification is possible for nanorods aligned end-to-end in one dimension where coupling of the fields can be expected [17].

Various methods are available for the synthesis of Ag nanowires such as chemical or electrochemical reduction methods [18-20]. Among the different chemical reduction routes, polyol process is the most popular for the mass production of uniform nanowires [21-25]. Another promising method other than the polyol process, for the synthesis of anisotropic Ag nanostructures is photo irradiation using a laser source [26-30]. The method offers simple and reagent free preparation of anisotropic Ag nanostructures such as nanowires and nanobelts. In these reports laser radiations are focussed onto already prepared nanocolloidal solution in which the nanoparticles are synthesised either by chemical route or by LAL technique. It is also reported that a simpler synthesis of nanostructures is possible by replacing the chemical route of preparation of nanocolloidal solution by LAL technique. T. Tsuji et al. in their work of formation of nanoclusters in PVP aqueous solution of colloidal silver nanoparticles, prepared by laser ablation, [10] reported ripening mechanism as one of the plausible mechanism behind the formation of nanostructures by laser irradiation. They also suggest that the interaction between protective reagents like PVP and silver nano atoms plays a crucial role in fostering the ripening mechanism. Also Zamiri et al. [28]

demonstrated the formation of silver microbelts in ethanol by laser irradiation. They suggested that the tendency of nanoparticles to aggregate in ethanol before irradiation is one of the possibilities for the formation of nanostructures. But the previous reports lack the formation of well defined nanowires and also some of them reported various nanostructures like nanoprisms and nanorods together in the same sample solution which may demote its use in practical applications.

8.2 Experimental Section

1 mol/litre concentration of PVP dissolved in ethanol is chosen as the medium for ablation in the present study. Ablation of a silver plate for 20min at the fundamental wavelength of Nd-YAG laser yielded Ag nanoparticles in the medium at a concentration of 2.5×10^{-4} mol/litre. Average size of Ag nanoparticles is estimated using DLS (Horiba SZ-100) nanoparticle analyser. 20ml of the colloidal solution is taken in a 30ml sample bottle and the solution is then irradiated by focussing frequency doubled laser pulses with a fluence of $500J/cm^2$ and also by xenon lamp (wavelength ranging from UV-Near IR, where IR radiations are cut to some extent using a water column placed after the source). The nanocolloidal solutions are analysed after fixed time durations for clearly monitoring and understanding the underlying mechanism of the formation of nanowires. Absorption spectra of the colloidal solution are recorded using Jasco UV-VIS NIR Spectrophotometer and TEM images are recorded using 200kV High Resolution Transmission Electron Microscopy.

Experimental setup for measuring coherent back scattering from Ag nanowires is described in chapter 2. Mono-dispersive Ag nanowires are purchased from Sigma-Aldrich having a length of 10μm and width of 60 nm. Back scattering from various concentrations of Ag nanowires dispersed in 2-propanol are measured by maintaining all other parameters constant.

Ag nanowires are incorporated in the gain medium (Rh6G) in the liquid phase (MMA) and its optical characterisations are done using optical absorption and fluorescence spectroscopy. Further the whole liquid media is polymerised into preforms and drawn to POFs and its lasing and photostability measurements are done. Scanning Electron Microscopic (SEM) (JEOL Model JSM - 6390LV) image of Ag nanowires in POFs is also recorded to ensure its presence in the fiber. Rh6G doped POFs with Ag nanowires incorporated on its outer surface are also fabricated. Fabrication is detailed as follows. At first Rh6G dispersed in MMA is polymerised using the conventional polymerisation techniques. After complete polymerisation, the preform rod is detached from the test tube and is immersed in a viscous solution of MMA containing Ag nanowires taken in a bigger test tube. Then the whole sample is left for complete polymerisation at 90^0C for 24h. Fig.8.1 shows a schematic representation of cross sections of Ag nanowires inside and outside the gain media in a

polymer rod. Lasing emission from Rh6G doped POFs with Ag nanowires inside and outside the gain medium are recorded and compared with bare Rh6G doped POFs. Photostability studies are also carried out with such fibers and a comparison with bare Rh6G doped POFs are made using the experimental setup detailed in Chapter 2.

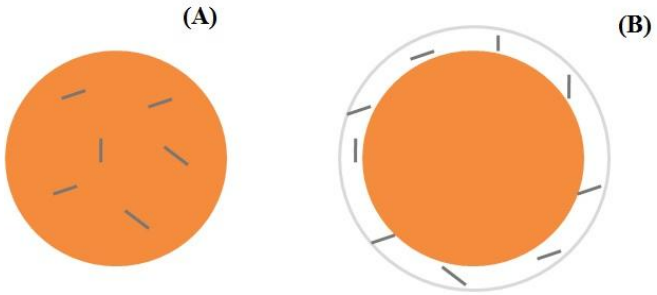

Figure 8.1: Schematic representation of Ag nanowires (A) Inside and (B) Outside the polymer preforms containing Rh6G as the gain medium

Spontaneous Raman scattering from POFs are measured using the experimental setup discussed in chapter 2. Raman scattering intensity is measured for fibers of varying diameters. Enhanced Raman signal intensity in the presence of Ag nanowires is recorded using the same experimental setup. SERS of PMMA rods with Ag nanowires are also recorded using high resolution Raman spectrometer Horiba JY for confirming the signal enhancement provided by Ag nanowires.

8.3 Results and Discussions

8.3.1 Post-irradiation of Ag nanospheres using Xenon lamp

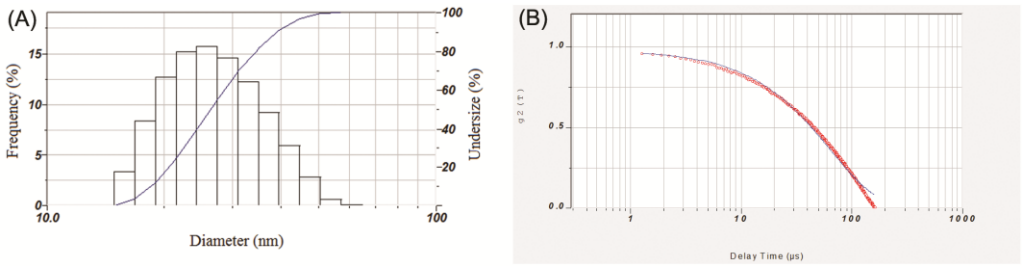

Figure 8.2: (A) Particle size distribution of Ag nanoparticles generated in ethanolic solution of PVP and (B) Amplitude of auto correlation function g2(T) vs. delay time.

From DLS, mean size of Ag nanoparticles generated in 1mM ethanolic solution of PVP is found to be 28nm with a standard deviation of 8nm as shown in Fig.8.2. Ag nanoparticles generated are subjected to irradiation from an unfocussed xenon lamp as post irradiation of metal nanoparticles can modify its nanostructure. Radiation from xenon lamp at IR region is cut using a water column and the spectra

recorded shows that the intensity of IR radiation has reduced considerably. Thus the spectrum ranges from UV to visible and near IR only.

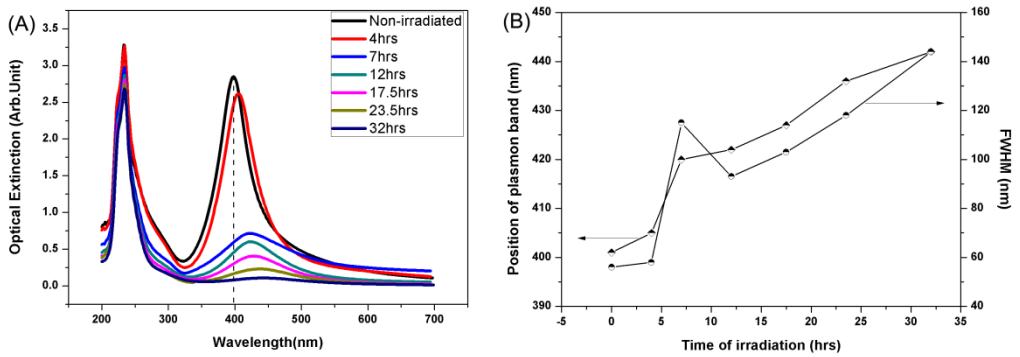

Figure 8.3: (A) Optical absorption spectra of Ag nanoparticles in ethanolic solution of PVP recorded after irradiation using xenon lamp at various time durations and (B) position and FWHM of plasmon band with respect to irradiation time.

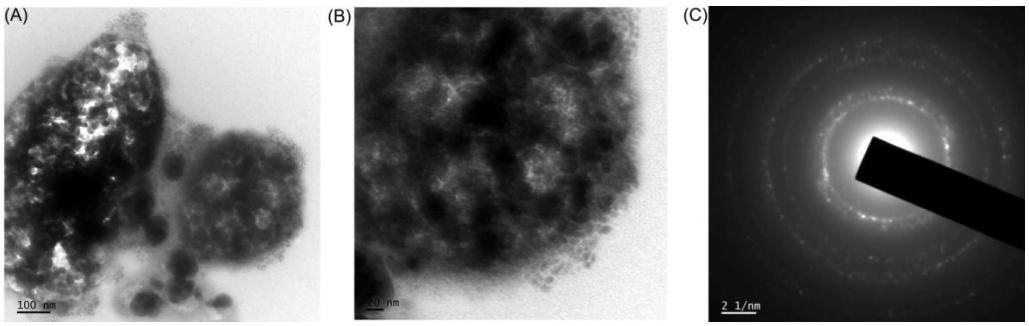

Figure 8.4: Representative TEM images of Ag nanoparticles (A) Irradiated by xenon lamp for 7h (B) Magnified image at a resolution of 20nm and (C) SAED pattern showing the polycrystalline nature.

Fig.8.3 (A) shows the optical extinction spectra of Ag nanoparticles recorded before and after irradiation at various time durations. It is found that when irradiated for 4 h the plasmon band shifts from an initial position of 401nm to 405nm with no appreciable change in the band width. As the time of irradiation is increased, the plasmon band shift increases with change in the bandwidth as depicted in Fig.8.3 (B). Since there is an appreciable blue shift in the plasmon band with increased bandwidth when irradiated for 7h, it is assumed that the irradiation is bringing some changes in the morphology of the nanoparticles. TEM image of the nanostructures recorded at this time is shown in Fig.8.4. From the image it can clearly be seen that the individual nanoparticles are aggregated. PVP in ethanol has an optical absorption in the UV region. Due to irradiation, the capping of PVP around nanoparticles has been altered and thus the nanoparticles suffer the problem of instability leading to aggregation.

Aggregated nanoparticles are found to be polycrystalline which is confirmed from the ring pattern obtained in the SAED pattern given in Fig.8.4 (C). With further increase in irradiation time, blue shift of the band is observed and when the time of irradiation is 32h, plasmon band peaks around 440nm with band intensity nearly reaching zero. Thus it is concluded that irradiation using xenon lamp promotes aggregation of metal nanostructures.

8.3.2 Post irradiation of Ag nanospheres using 532nm laser pulses

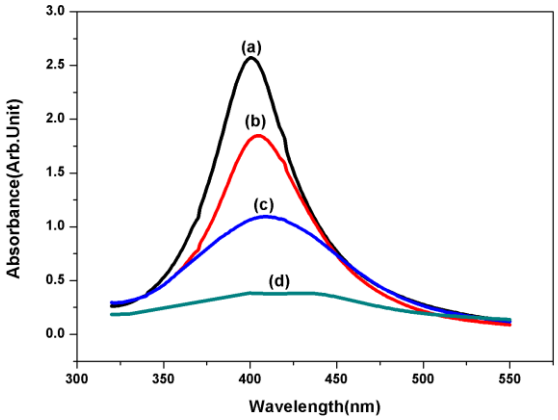

Figure 8.5: Plasmon absorption band of Ag nanocolloids (a) generated by laser ablation at the fundamental wavelength of Nd-YAG (b) nanocolloids irradiated by 532nm for 45min (c) for 9h and (d) for 18h.

Sample solution is subjected to focussed laser radiations at 532nm from Nd-YAG nanosecond pulsed laser. For effective structural modification of the nanoparticles, it should absorb the incoming radiations. Ag nanoparticles respond effectively to 355nm and 532nm radiations since the efficiency of self absorption is high at these wavelengths as compared to 1064nm [31]. After 45min of irradiation, a change in colour of the colloidal solution from light yellow to a darker one is observed and the corresponding absorption spectrum is given in Fig. 8.5. A decrease in the absorption band intensity is observed with shift of 5 nm in the SPR peak. Also no new SPR peaks are noticed in the spectrum. Fig. 8.6 shows the TEM image of the nanocolloidal solution after 45min of irradiation. From Fig.8.6 (B), we can see the fragments of Ag nanocolloids are having an average size of 5nm.

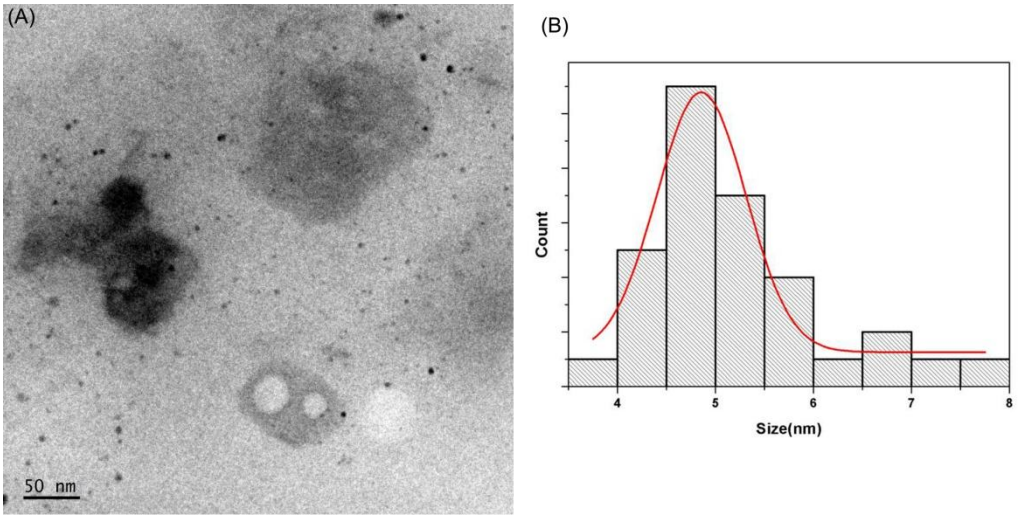

Figure 8.6: (A) TEM image of nanocolloids irradiated for 45min by laser pulses at 532nm from Nd-YAG laser and (B) Distribution of nanoparticles.

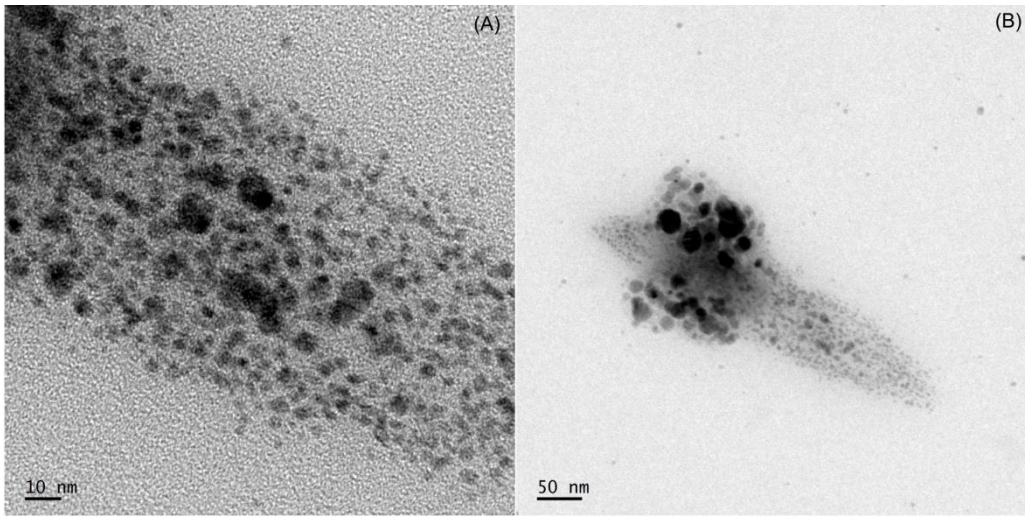

Figure 8.7: TEM image of Ag nanoparticles irradiated by laser pulses for 9 hours. (A) Assembly of unstable nanoparticles via laser radiation and (B) enlarged view of the association of nanoparticles to form stable structures.

Almost all of the larger nanoparticles are fragmented into smaller ones. Takeshi et al. reported [10] that stability of nanoparticles is directly proportional to size. So the unstable atoms of such nanoparticles move from one nanoparticle to another promoted via laser irradiation and it results in the formation of nanoparticles with stable shapes and sizes. This process is known as ripening mechanism. From the TEM images of the colloidal solution irradiated for 9h given in Fig. 8.7 (A) and (B) the process involved in ripening mechanism can be seen. The fragmented particles of size in the range of 1–5nm assemble together to form more stable shapes such as nanorod like structure

having an average width of 160nm. The corresponding absorption spectrum of Ag nanocolloids is shown in Fig. 8.5. It is seen that the absorbance is reduced by more than 50% and the FWHM is increased twice as compared with the non-irradiated sample with no obvious shift in the SPR peak [32].

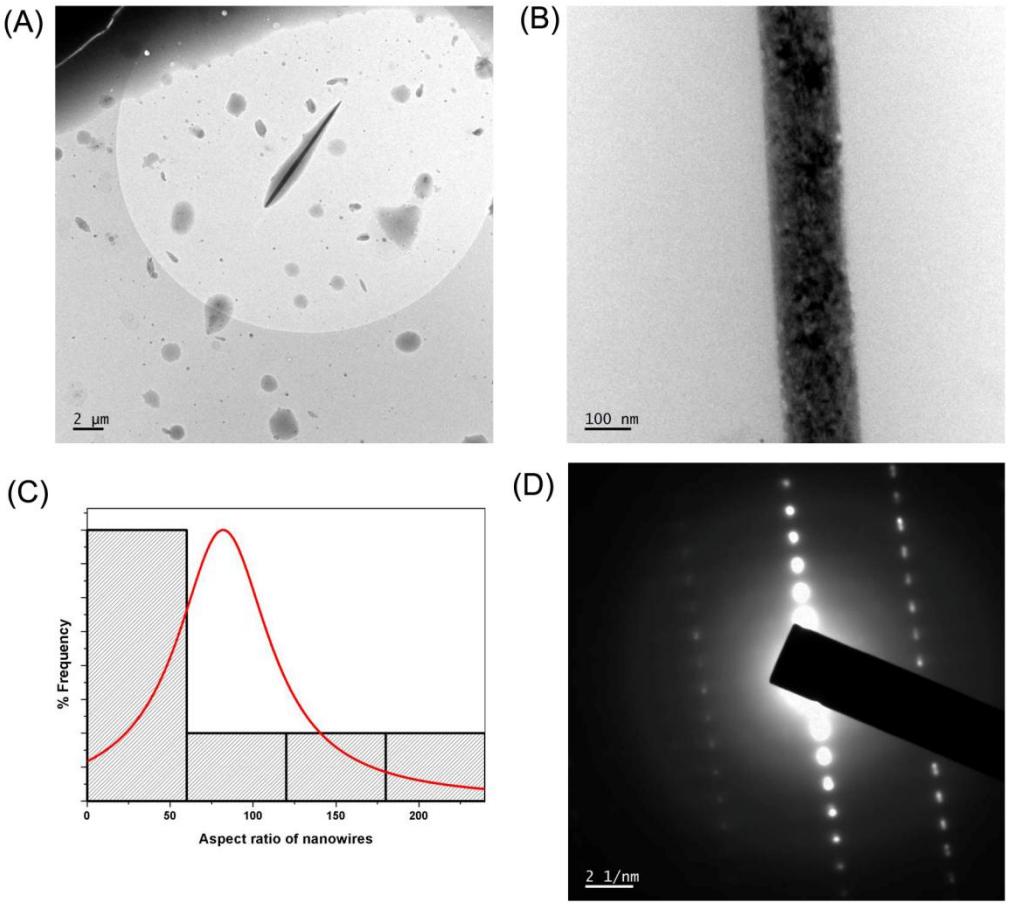

Figure 8.8: TEM images of Ag nanocolloids irradiated for 18 h. (A) Ag nanowires formed through ripening mechanism (B) Cross section of the nanowires (C) Aspect ratio distribution of nanowires and (D) SAED pattern of the nanowires.

Further irradiation of the sample has brought down the plasmon absorption to nearly 4% of the maximum and the FWHM to 170nm which is thrice that of the non-irradiated sample as is shown in Fig. 8.5. Fig.8.8 depicts the TEM image of a well defined Ag nanowire with an average diameter of 160 nm and a length of 8.7µm (average aspect ratio of 54). The darker region around the nanowires indicates the presence of PVP around them. Fig.8.8 (B) shows an enlarged view of the nanowire and the aspect ratio distribution of Ag nanowires (Fig.8.8 (C)). Average aspect ratio is around 50. However, because of the restriction in the crystallographic facets induced

by PVP for the formation of nanowires from nanostructures, only a few percentage of nanorod like structures is converted to nanowire [32]. From the SAED pattern depicted in Fig.8.8 (D), it is inferred that the nanowires so formed are polycrystalline [32]. It is inferred that these nanowires are formed through ripening mechanism promoted by the presence of PVP in the solution. The interaction strength of atoms lying on different crystallographic facets is different for various capping agents such as PVP. Yugang Sun et al. experimentally demonstrated that PVP which is a polymeric capping agent interacts more effectively with the {1 0 0} facets of the nanowires rather than {1 1 1} facets [22]. Thus the Ag nanorod like structure having an average width of 160nm formed via ripening mechanism when irradiated for 9h ends up as nanowires having the same width since the PVP in the ethanolic solution masks the surface of the nanorod like structures ({1 1 1} facets) and allows the ends ({1 0 0} facets) of them to readily react with unstable Ag atoms in the nanoparticles to form nanowires. The colour of the sample has changed from yellow to greenish yellow as shown in Fig. 8.9. This work supports the plausible mechanism behind the formation of Ag nanowires suggested by Tsuji et al. [10].

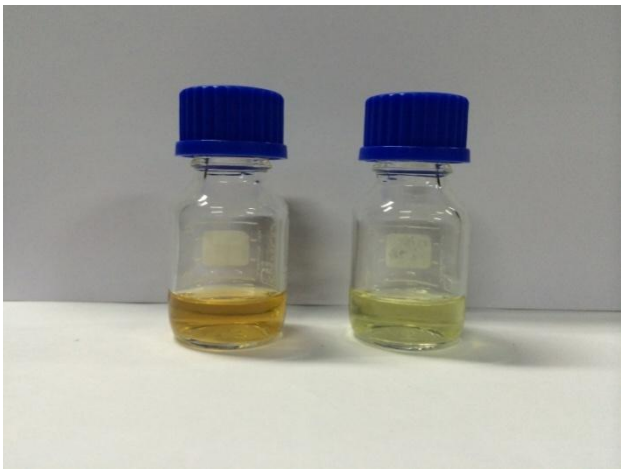

Figure 8.9: Photograph of the Ag colloidal solution before and after irradiation. 18 hours of irradiation has changed the colour from yellow to a pale green.

Thus periodic monitoring during the irradiation reveals the various steps involved in the process of nanowire formation. It involves fragmentation of larger particles to smaller ones when irradiated for 45min, formation of nanorod like structure through ripening mechanism when irradiation is continued for 9h and finally PVP assisted nanowire formation when irradiated for 18 h.

8.3.3 Optical characterisation of Ag nanowires dispersed in 2-propanol

As there are limitations in the formation of mono-dispersive Ag nanowires using the technique mentioned above, the experiments using Ag nanowires are carried out by making use of nanowires purchased from the market.

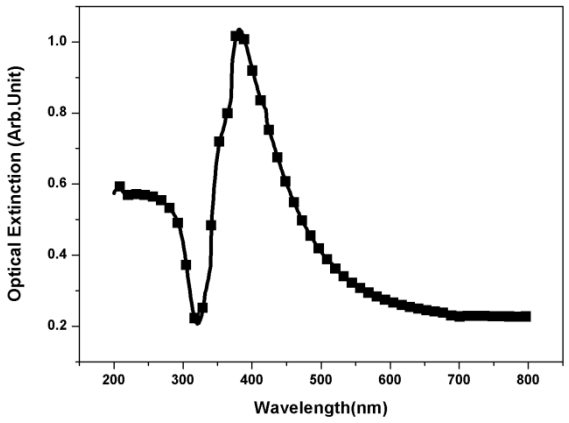

Figure 8.10: Optical absorption spectra of Ag nanowires dispersed in 2-propanol.

Fig.8.10 shows the optical extinction spectra of Ag nanowires dispersed in 2-propanol. The peak of the plasmon band is at 381nm which corresponds to the longitudinal plasmon modes of the nanowires. Fig.8.11 depicts the TEM image of nanowires and the dimensions of the nanowires are found out to be 60nm width and 10μm length. The TEM image indicates its mono-dispersive nature. HRTEM shown in Fig.8.11 (B) indicates that nanowires are polycrystalline in nature.

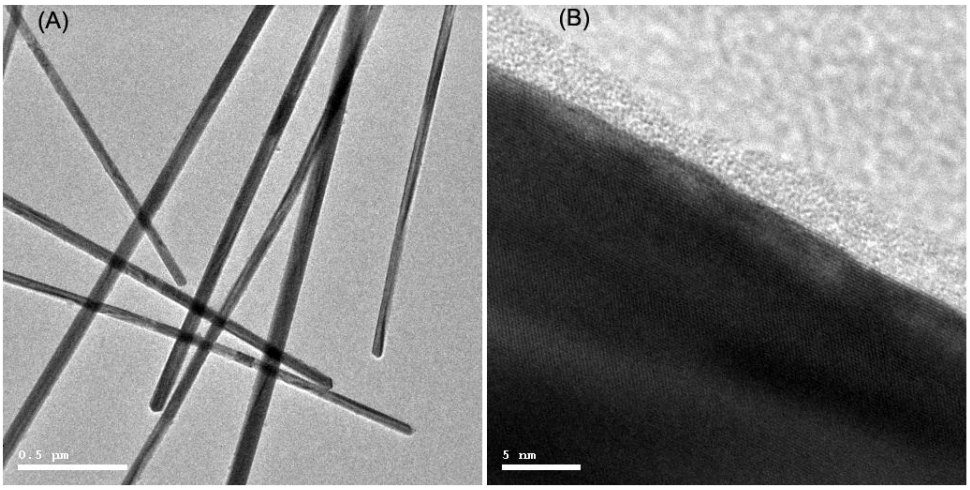

Figure 8.11: (A) Representative TEM image of Ag nanowires and (B) HRTEM indicating the polycrystalline nature.

Since the diameter of the nanowires is nearly 60nm where scattering efficiency exceeds that of absorption efficiency in the case of nanospheres [33], its scattering efficiency needs to be taken into account. An appropriate measure of scattering amount is the mean free path *l* for the light entering the medium times the magnitude of wavevector *k*. Localisation of light within the medium is expected when $kl \leq 1$ which is known as modified Ioffe-Regel criterion [34-35]. Below this value the electric field of the light cannot even perform one complete oscillation, before it is scattered. To characterise the mean free path of the samples, coherent back scattering experiment has been performed. It is an interference effect occurring between the counter-propagating waves leading to a narrow cone in exact back scattering [36-37]. The width of the backscattering cone and the angle of the cups are inversely proportional to *l* [38-41] and is given by

$$\theta = \frac{\lambda}{2\pi l} \tag{8.1}$$

where λ is the wavelength of the scattered light, *l* is the mean free path and θ is the angular width of the cups.

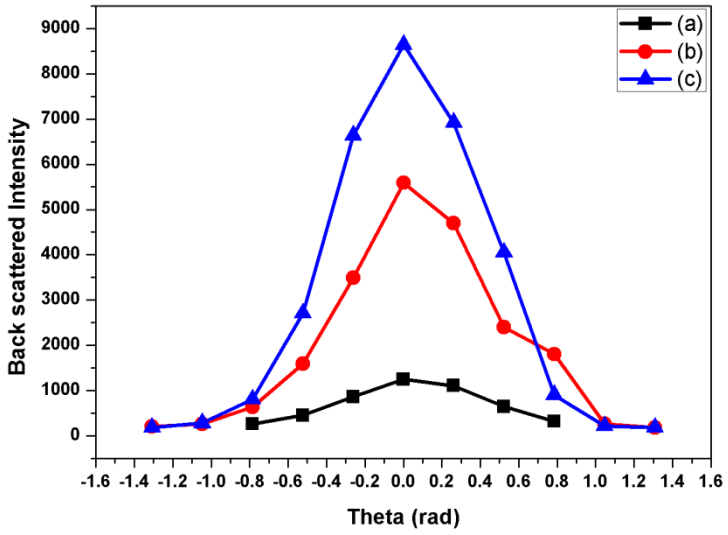

Figure 8.12: Coherent back scattering cones obtained from Ag nanowires of 60nm width and 10μm length with respect to varying concentration of nanowires where (a) 0.00032M (b) 0.0032M and (c) 0.032M.

Fig.8.12 depicts the spectra of light emitted in the backscattering direction and collected using a CCD spectrometer for varying concentrations of Ag nanowires. The spectra are obtained by subtracting the reference spectrum which is obtained from the

light scattered from the surface of the cuvette containing 2-propanol. However, any appreciable shift in the angular width of the cups with respect to the concentration of the nanowires in the solution is observed. But an appreciable variation in the intensity of the back scattered light is noticed, with maximum intensity corresponding to a concentration of 0.032M Ag nanowires. The value of mean free path obtained, by substituting necessary values in equation (8.1), is 3.7μm. The value of *kl* thus obtained is 44 which is much higher than unity. As *kl* >>1, the present system works under weakly scattering regime [42].

In order to further confirm that Ag nanowires in the gain medium are in the weakly scattering regime and that it will not support random lasing, lasing of Rh6G doped MMA solution in the absence and presence of Ag nanowires are recorded and is shown in Fig.8.13 (with concentration of Rh6G as 2.5×10^{-4}M and that of Ag nanowire 0.032M). Since lasing emission requires an external feedback, it is assumed that the wall of the cuvette acts as a Fabry-Perot (FP) like optical cavity for which length corresponds to the wall thickness. The fine structure pattern shown in the figure can be attributed to the axial modes of the Fabry-Perot cavity formed by the cuvette wall. The mode spacing can be calculated using the equation given by

$$\Delta\lambda = \frac{\lambda^2}{2nL} \tag{8.2}$$

where λ is the wavelength of the strongest lasing emission line, n is the refractive index and L is the length of the resonator cavity [43]. In the present case n is the refractive index of the quartz cuvette which is 1.46 and L is the thickness of the wall and is found to be 1.2mm and substituting these values in the equation yields mode spacing as 0.09nm which matches exactly with the mode spacing obtained from Fig.8.13 (A). As clearly seen from the same figure, a modulated output spectrum is obtained at this concentration (2.5×10^{-4}M) of Rh6G. As a result, cavity finesse is periodically modulated in Δλ with a period δλ determined by the relation [44] given by

$$\delta\lambda = \Delta\lambda \frac{n_{eff}}{\Delta n_{eff}} \tag{8.3}$$

where $\Delta n_{eff} = n_{eff} - n'_{eff}$ is the difference between the effective refractive index of quartz cuvette (n_{eff}) and gain medium (n'_{eff}) . Substituting the values in the above equation yields δλ as 3.3nm which matches nearly with the experimentally calculated value of 3.91nm. As can be seen from Fig.8.13 (B), even with a concentration of 0.032M Ag nanowire in 2.5×10^{-4}M Rh6G, no sign of random lasing is observed which

is caused by scattering in the presence of nanowires in the solution. Instead, well resolved axial modes of a FP cavity are obtained. But in this case no modulated spectrum is observed due to the variation in the effective refractive index of the medium as compared to pure dye doped gain medium.

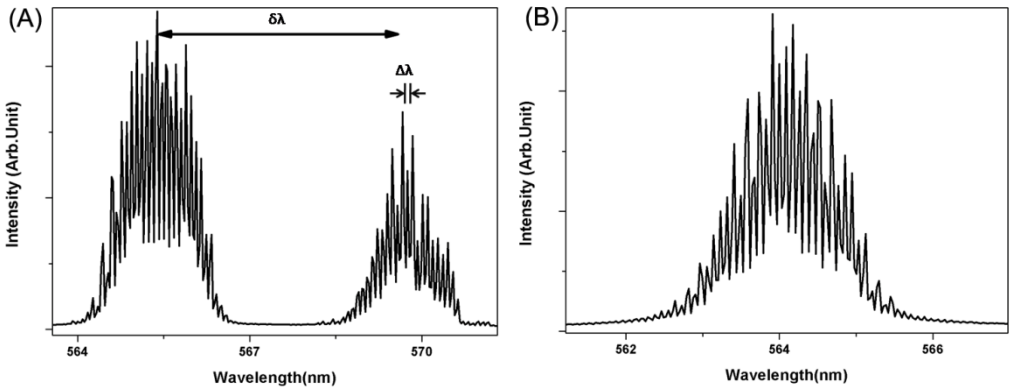

Figure 8.13: Lasing obtained from Rh6G in MMA solution (A) without Ag nanowires and (B) with 0.032M Ag nanowires pumped at an energy of 10mJ by 532nm laser pulses and emission is collected transversely from a cuvette of 1mm optical path length.

8.3.4 Ag nanowires doped polymer rods and polymer fibers

Rh6G doped polymer preforms with and without Ag nanowires of 1.2cm diameter are sliced into a thickness of 460μm and are polished by conventional techniques. Fluorescence emission from the rods (not shown here) indicates that Ag nanowires are capable of providing a large emission enhancement and EF for an optimum concentration (0.00032M) is found to be 4.5. Concentration of Ag nanowires in the polymer preforms and its designation are provided in Table.8.1. Time-resolved fluorescence spectra of the same are recorded and are shown in Fig.8.14. The curves are fitted using a triple exponential function given by

$$I(t) = \alpha_1 e^{-t/\tau_1} + \alpha_2 e^{-t/\tau_2} + \alpha_3 e^{-t/\tau_3} \tag{8.4}$$

where τ_i are observed lifetimes with amplitude or molecular fraction α_i, such that

$$\sum_i \alpha_i = 1$$

The amplitude weighted lifetime is then calculated using

$$\langle \tau \rangle = \sum_i \alpha_i \tau_i \tag{8.5}$$

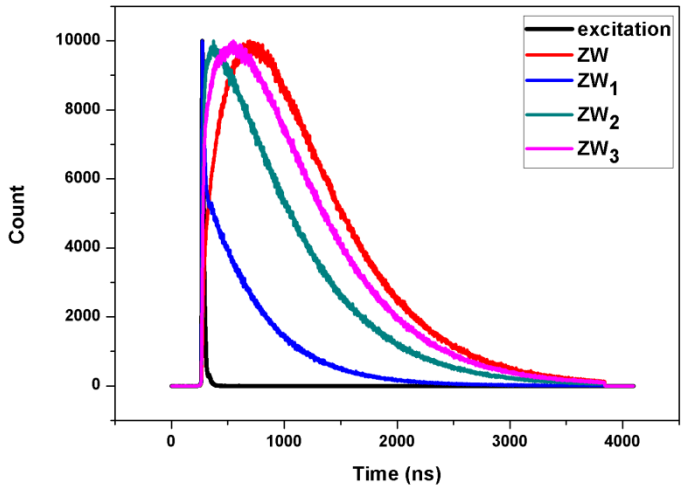

Figure 8.14: Time resolved fluorescence spectra of Rh6G doped polymer rods with and without Ag nanowires.

Table 8.1: Multi exponential analysis of intensity decay of Rh6G doped polymer rods with and without Ag nanowires showing molecular fraction (α_i), observed lifetimes (τ_i), amplitude weighted lifetime ($<\tau>$) and goodness of fit parameter (χ_R^2).

Sample	**[Rh6G] (10^{-4}M)**	**[Ag] (10^{-3} M)**	**α_1**	**α_2**	**α_3**	**τ_1 (ns)**	**τ_2 (ns)**	**τ_3 (ns)**	**$<\tau>$ (ns)**	χ_R^2
ZW	5	-----	0.49	2E-5	0.50	6.92	0.45	6.94	6.93	1.14
ZW_1	5	0.32	3E-6	0.02	0.97	2.83	6.37	0.013	0.156	1.09
ZW_2	5	3.2	0.32	0.49	0.17	5.51	7.89	0.205	5.66	1.09
ZW_3	5	32	0.50	0.06	0.43	7.36	7.92	7.24	6.72	1.06

From Table.8.1, it can be seen that in the presence of an appropriate amount of Ag nanowires (ZW_1) lifetime reduction of Rh6G from 6.93ns to 0.156ns is noticed. This reduction in lifetime is due to the fact that there are hot spots at the ends of nanowires where electric field intensity is largest as compared to that of a sphere [15, 45-46] as shown in Fig.8.15. Thus the hotspots present at the ends of the nanowires enhance the emission of the nearby fluorophores even more efficiently than that of nanospheres and thus the lifetime is reduced drastically. The reduction in lifetime for other concentrations of Ag nanowires such as ZW_2 and ZW_3 is much less as compared to ZW_1. Thus an optimum concentration of nanowires is crucial in reducing the lifetime of the dye considerably.

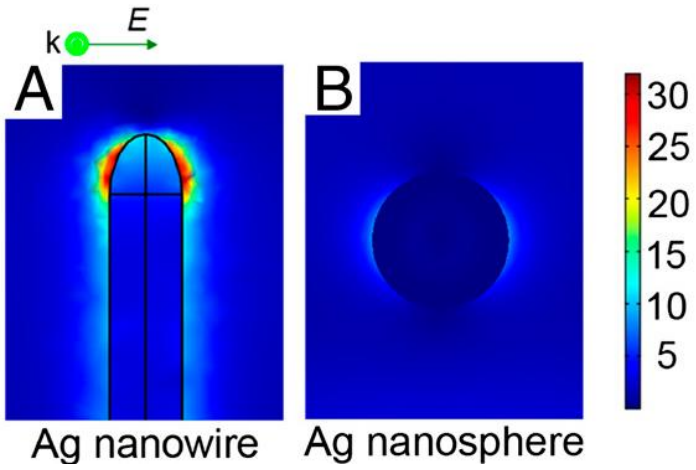

Figure 8.15: Electric field distribution at wavelength of 350nm calculated for (A) Ag nanowire (1µm length, 2nm diameter) and (B) Ag nanospheres (50nm diameter) [15].

Table 8.2: Quantum yield (QY), radiative decay rate and non-radiative decay rate of Rh6G in the presence and absence of Ag nanowires. QY obtained from the experimental data is found out using single point method.

Designation	**QY Calculated**	**QY Experimental**	**Radiative decay rate (10^9/sec)**	**Non-radiative decay rate (10^9/sec)**
ZW	0.85	0.85	0.123	0.0217
ZW_1	0.99	0.98	6.356	0.0217
ZW_2	0.88	0.90	0.155	0.0217
ZW_3	0.85	0.87	0.127	0.0217

In order to determine the radiative rate enhancement of Rh6G in the presence of nanowires, the lifetime of dye in the presence and absence of Ag nanowires and its intrinsic quantum yield are taken into consideration. Thus increased radiative decay rate ($\gamma_m \Gamma$) and quantum yield (Q_m) of the fluorophore in the presence of nanowires are calculated using the equations [47] given below and is depicted in Table 8.2.

$$\gamma_m \Gamma = \frac{1}{\tau_m} - K_{nr} \tag{8.6}$$

$$Q_m = \gamma_m \Gamma \times \tau_m \tag{8.7}$$

where τ_m is the lifetime of the fluorophore in the presence of nanowires. It is assumed that the non-radiative decay rate (K_{nr}) of the fluorophore is unchanged in the presence of nanowires and so it is taken as a constant [47]. Thus we can see that in the presence of an optimum quantity of Ag nanowires, the radiative decay rate of the dye is enhanced reducing the lifetime of the fluorophore in the excited state. This highly enhanced radiative decay rate enhances the QY of the fluorophore nearly equals 1 and thus the emission intensity is enhanced drastically.

The rods are thus drawn into POFs of varying diameters and its lasing characteristics are studied. Fig.8.16 shows the SEM image of POF containing nanowires and its presence is confirmed. Confirmation of nanowire in the SEM image is done using EDS analysis. Further location of nanowire is not identified because of the burning of polymer upon increasing the magnification. Since the pumping wavelength (532nm) is far away from the resonance (381nm), the percentage of electric field enhancement is less but there is obviously a field enhancement provided by the surface plasmons as depicted from the normalised electric field distributions shown in Fig.8.17 [48].

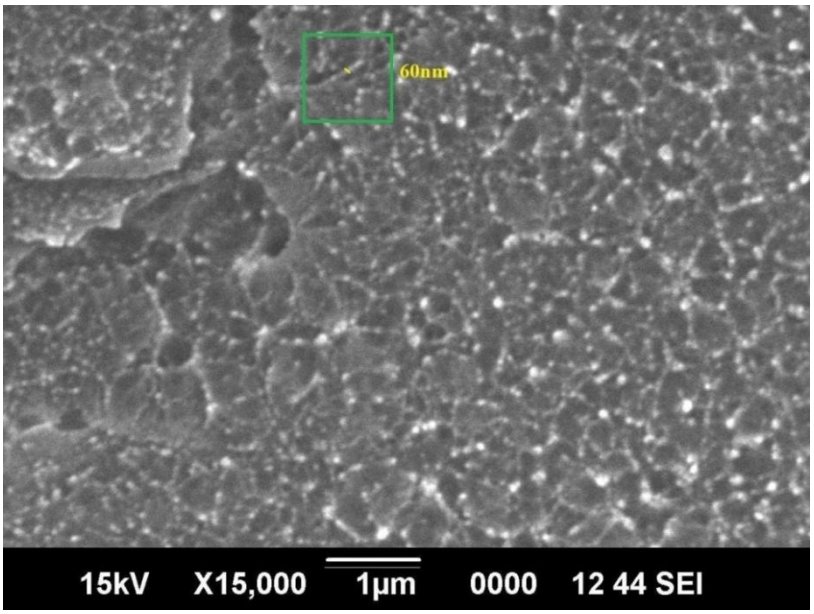

Figure 8.16: SEM image of a portion of POF containing 0.032M of Ag nanowires.

The excitation is done using a plane wave polarised along the x axis with wavelengths of (a) 383nm which matches exactly with the plasmon resonance of Ag nanowires and (b) 532nm where all of the lasing studies are done. The field enhancement factor $|E|/E_0 = \left(E_x^2 + E_y^2\right)^{1/2}/E_0$ is approximately 2.4 when excited by 532nm where as an

enhancement of nearly 4.8 is noticed when excited by 383nm [48]. However the local electromagnetic field near Ag nanowires is still enhanced.

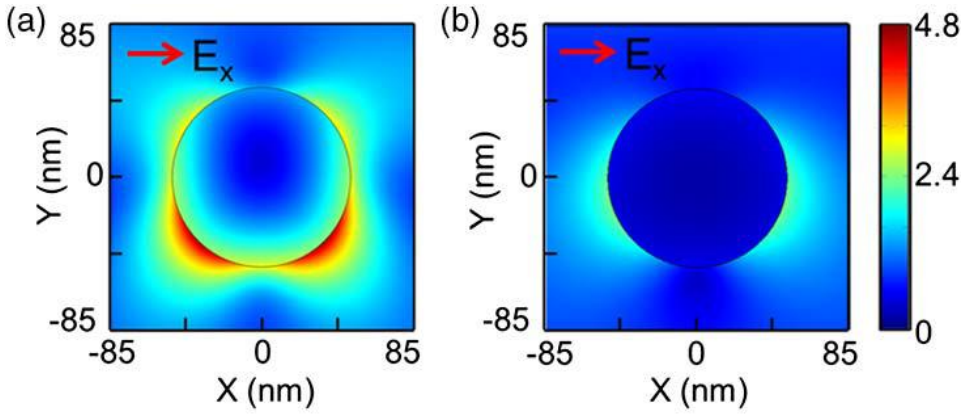

Figure 8.17: Distribution of the electric field intensity normalized by the incoming field near the pure Ag nanowires (100nm diameter and 10µm length) at the wavelengths of (a) 382 and (b) 532 nm [48].

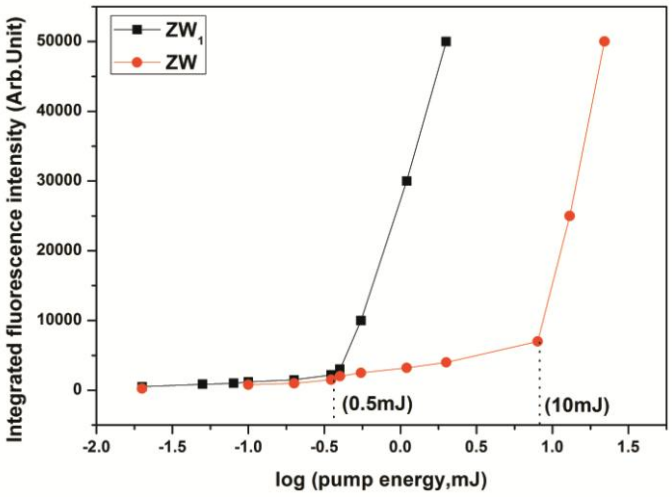

Figure 8.18: Integrated emission intensity of fibers as a log function of pump energy.

With this inference we have conducted lasing studies, using 532nm laser pulsed from Nd-YAG laser, on POFs containing Rh6G and Ag nanowires in the gain media. Fibers of 200µm diameter are pumped and the emission is collected from one of the ends of the fiber. It is found, as in the previous cases of Ag nanospheres, nanoalloy and core/shell, that the threshold for lasing has been reduced significantly from 10mJ to 0.5mJ with ZW_1 as compared to POFs containing Rh6G only (shown in Fig.8.18). For

other fiber samples (ZW_2 and ZW_3) also, the threshold of lasing is less than that of ZW at 3mJ and 6mJ respectively. WGM lasing has been observed in the case of 0.00032M Ag nanowires in the gain medium since they are in the weak scattering regime as $kl<<1$. Thus the scattering of emission of the fluorophores by the nanowires present in close proximity of them is negligible so that microcavity present in the fiber supports WGM lasing. However due to the electric field enhancement provided by the nanowires, through enhanced radiative decay rate, the threshold pump energy is reduced considerably. Thus efficient fiber lasers are demonstrated here in the presence of an optimum concentration of Ag nanowires.

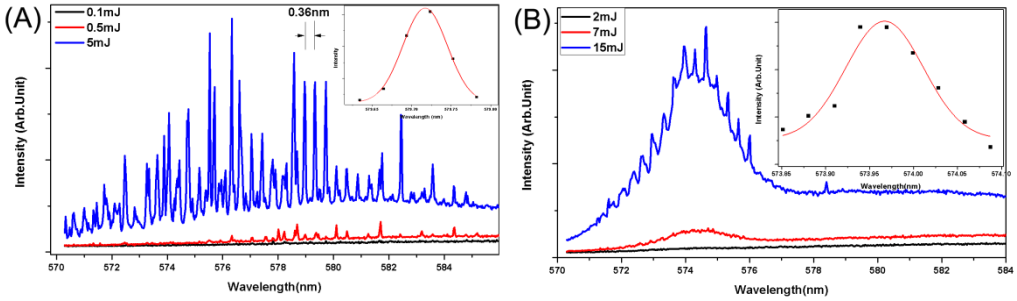

Figure 8.19: WGM lasing from (A) Ag nanowire doped POF lasers (where inset shows the Gaussian fit of mode at 580nm) and (B) Bare dye doped POFs (and inset shows the Gaussian fit of mode at 574nm) with varying pumping energy.

Fig.8.19 shows the WGM lasing from Ag nanowires doped in the gain media of POFs. Mode spacing between two adjacent modes are found to be 0.36nm which matches with the spacing calculated theoretically. Average linewidth of the WG modes are found to be 0.06nm. The quality factor of the modes are calculated using

$$Q = \frac{\lambda}{\Delta\lambda} \tag{8.8}$$

where $\Delta\lambda$ is the linewidth of the mode corresponding to the wavelength λ and is found to be 6×10^3. Lasing characteristics obtained from similar POFs without Ag nanowires matches exactly with that shown in the Fig.8.19 (B) and the Q factor obtained is 5×10^3. Studies on other fiber samples of varying diameter resulted in similar spectra as in the previous case with different mode spacing depending on the diameter of the fiber.

Fig. 8.20 compares the emission, when pumped transversely using laser at 532nm, from bare Rh6G doped POFs and Rh6G doped POF with Ag nanowire incorporated on outer surface of the fiber. It can be seen that no lasing is noticed at the threshold energy corresponding to lasing from bare Rh6G doped POFs. When pumped at 26mJ, which is well above the threshold energy (2mJ) for lasing of bare Rh6G

doped POF, only the reduction in the bandwidth from 45nm (initially) to 10nm is noticed for Rh6G doped POFs with Ag nanowires on the outer surface. Also from the photostability measurements, it is seen that bare Rh6G doped POFs are more stable than Rh6G doped POFs with Ag nanowire outside the gain medium (not shown here).

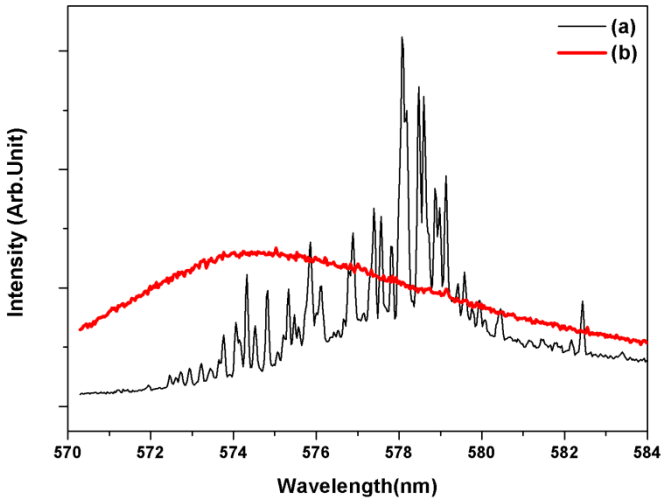

Figure 8.20: Lasing emission from (a) bare Rh6G doped POFs and (b) Ag nanowires outside bare dye doped POFs when pumped at 2mJ.

For emission enhancement of the dye, nanoparticle and the dye should be in adequate distance. Since Ag nanowires are coated outside the fiber, the distance between them may be large so that nanowires cannot influence the emission of dye molecules through its plasmon resonance. Thus Ag nanowires incorporated on the outer surface of dye doped POFs deteriorate lasing action through energy transfer mechanisms like NSET.

The photostability of all set of fibers under consideration (Ag nanowires in the gain medium) are measured and is shown in Fig.8.21. As expected, ZW_1 shows the least photobleaching rate as compared to other fibers due to the shortest lifetime exhibited by them because of the presence of an optimum concentration of Ag nanowires. Bare dye doped POFs showed a half life of 24700 shots whereas ZW_2 and ZW_3 showed a half life at lower pulse count (12990 and 9000 respectively). But ZW_1 is found to be photo stable up to a pulse count of 27000 shots.

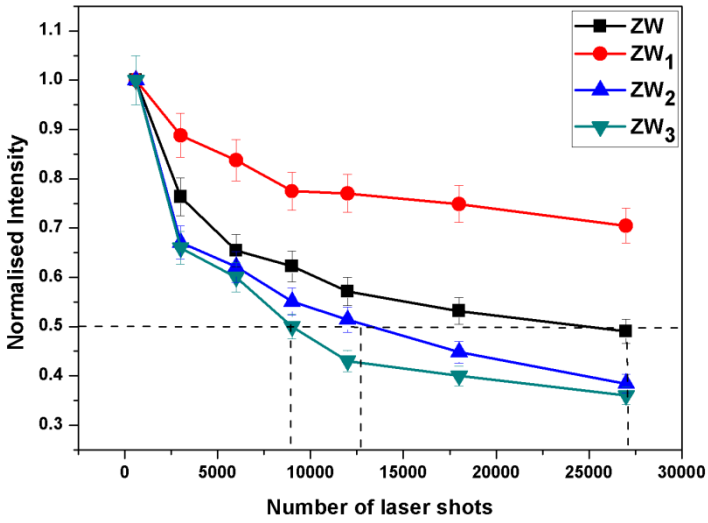

Figure 8.21: Photostability curves of Rh6G doped POFs in the presence and absence of Ag nanowires. Fibers of 200µm diameter and 5cm length are taken from all sets and are pumped at 10mJ laser energy.

8.3.4.1 Surface Enahnced Raman Scattering of PMMA by Ag nanowires

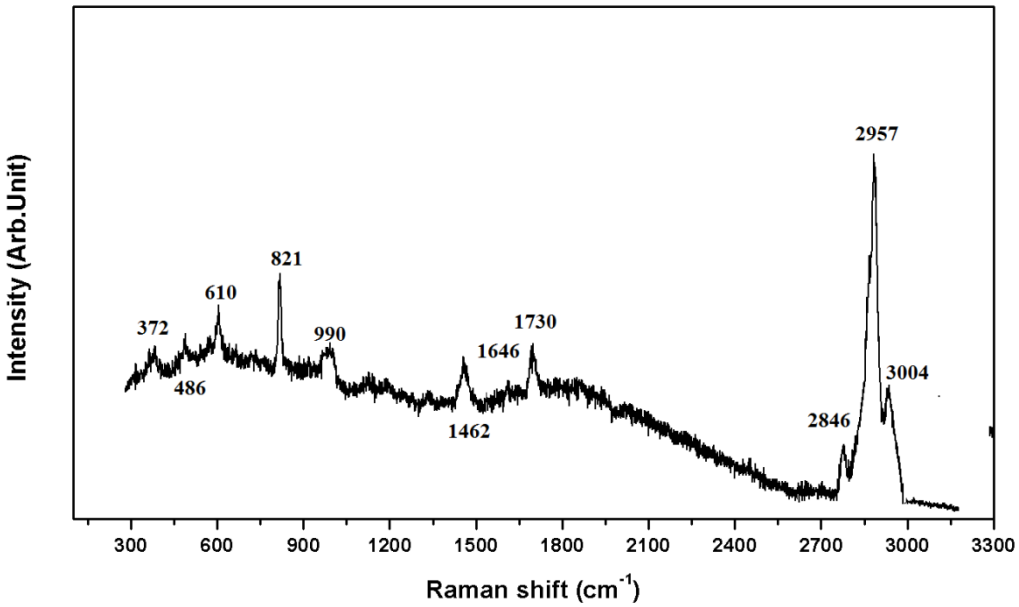

Figure 8.22: Recorded Raman spectra of PMMA based POF.

Fig.8.22 depicts the spontaneous Raman spectrum recorded from a fiber of 500µm diameter and 10cm length using the experimental setup given in chapter 2. The

observed Raman bands are stoke shifted Raman lines produced on the lower energy side of the pump laser. The most prominent Raman band is observed at 2957cm^{-1} with two shoulders at 2846cm^{-1} and 3004 cm^{-1}. The other Raman bands are observed at 372, 486, 610, 821, 990, 1462, 1646 and 1730 cm^{-1}. The band within the range of 2800-3100 cm^{-1} is identified as C-H stretching vibrations of CH_2 and CH_3 [49-52] groups of PMMA. The band at 1730cm^{-1} is due to C=O stretching and that at 1460cm^{-1} is due to C-H bending [49]. The band at 990cm^{-1} is due to C-O stretching and that at 821cm^{-1} is because of CH_3 rocking [49-52]. Two new bands at the higher energy side of the stokes spectra of PMMA are observed one at 486 cm^{-1} and another at 372 cm^{-1}.

Variation of intensity of the Raman line at 2957cm^{-1} with diameter of the fiber is plotted in Fig.8.23. It is found that as the diameter of the fiber is increased, the relative intensity of the Raman line is increased. Beyond 550μm diameter, no appreciable increase in the relative intensity is observed.

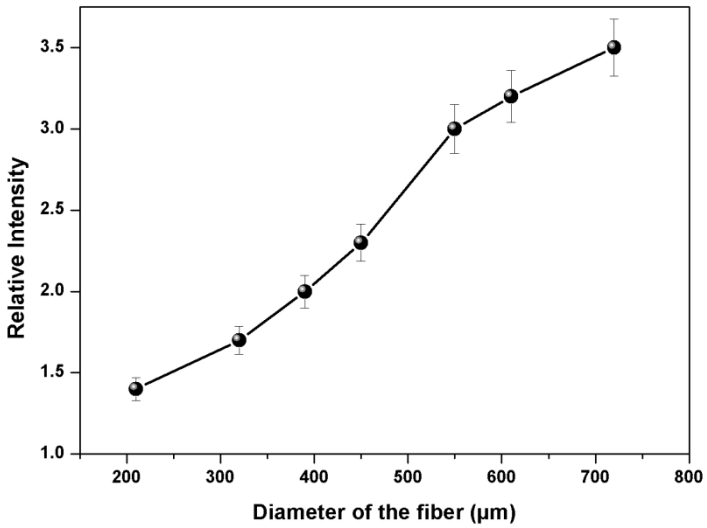

Figure 8.23: Variation of Raman intensity at 2957cm^{-1} with diameter of the polymer fiber.

As far as an amplifier is considered, gain coefficient is an important parameter since it determines the threshold power needed for stimulated Raman scattering in POF with parameters such as attenuation of the fiber, length, area of the fiber etc. The relation for gain coefficient [51] is given by

$$g = N\frac{d\sigma}{d\Omega}\frac{c^2\left[1-\exp\left(-h(\nu_p-\nu_s)/kT\right)\right]}{3h\nu_s^3 n_s \Delta\nu_N} \tag{8.9}$$

where N $d\sigma/d\Omega$ is the differential scattering cross section, c is the speed of light in vacuum, ν_s and ν_p are the stokes and pump frequencies, h is the Planck's constant, k is

the Boltzmann constant, T is the absolute temperature $\Delta\nu_N$ is the FWHM intensity and n_s is the refractive index of the material. The value of differential cross section of PMMA at 2957cm^{-1} is taken as 1.968×10^{-8} cm^{-1}sr^{-1} from a previous study by Thomas et al. [51]. Substituting the values in the above equation yields gain coefficient as 0.5×10^{-12}cmW^{-1} for POF of 550μm diameter. Higher the gain coefficient, lower is the threshold pump power needed for Stimulated Raman scattering.

SERS is a well known phenomenon of enhancing the Raman signal of molecules adsorbed on metal nanostructures. Raman peaks of PMMA based POFs (with a diameter of 420μm and length of 3cm) in normal Raman (NR) scattering and SERS due to the presence of Ag nanowires (60nm×10μm) has been recorded using the same experimental conditions (Fig. 8.24). Enhanced Raman scattering intensity of PMMA is noticed in the presence of Ag nanowires thus supporting SERS. Raman signals are enhanced by the strong electromagnetic field of nanostructures coupled to the vibration intensities of the molecules near the nanostructures [53-54]. Raman signal intensities are related to the various parameters such as size and shape of the nanostructures [55-56] and its distributions [57]. Since the plasmon field generated at the tips of nanowires are much higher than that of a sphere of comparable size [15], it is assumed that the molecules in the vicinity of the nanowires experience enhanced Raman scattering. Also at higher concentrations of Ag nanowires, there can be crossed Ag nanowires and nanowire bundles which have even higher SERS enhancement factors as compared to single nanowires. This is due to the higher density of interstitials produced by strong sp coupling when the nanowires are so close to each other [58]. Thus SERS signal intensity is found to be dependent on the concentration of Ag nanowires in the substrate. Higher concentrations of Ag nanowires (higher than 0.032M) in PMMA POFs yields scattering of the incoming laser pulses and so Raman signal are not able to be collected. Analytical enhancement factor (AEF) of the vibration peak at 2957 cm^{-1} with concentration of Ag nanowires is shown in Fig. 8.24 (B). AEF is calculated using

$$AEF = \frac{I_{SERS} C_{NR}}{I_{NR} C_{SERS}} \tag{8.10}$$

where I_{SERS} and I_{NR} are the intensity of the vibrational peak in SERS and NR measurements respectively and C_{SERS} and C_{NR} are the concentration of the analyte in SERS and NR measurements respectively [59]. An optimum concentration of 0.032M Ag nanowires is found to enhance the magnitude of signal intensity nearly 3.2 times. Since the magnitude of enhancement is of the order of tens it is assumed that among the two types of mechanism responsible for SERS (such as electromagnetic enhancement and chemical enhancement described in Chapter 1), chemical enhancement factor contributes to SERS in this case. Chemical enhancement provides

an enhancement of Raman scattering intensity upto 10^2 times and it occurs when the molecules are adsorbed strongly on the metal nanostructures, thereby changing its polarizability [59]. However, it is found that Raman scattering of PMMA is enhanced in the presence of Ag nanostructures thereby making PMMA based POFs as good substrate for remote sensing of analytes.

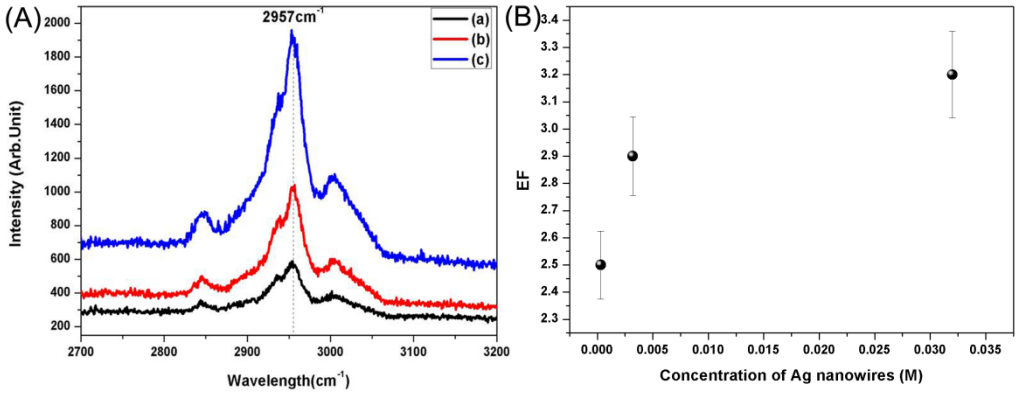

Figure 8.24: (A) Raman scattering intensity of PMMA POFs (a) normal Raman (b) SERS in the presence of 0.00032M concentration of Ag nanowires (c) 0.032M and (B) Enhancement factor of SERS with respect to concentration of Ag nanowires.

Raman signal of polished PMMA rods of 1mm thickness in the presence of Ag nanowires is also measured using high resolution Raman spectrometer Horiba JY and is shown in Fig 8.25.

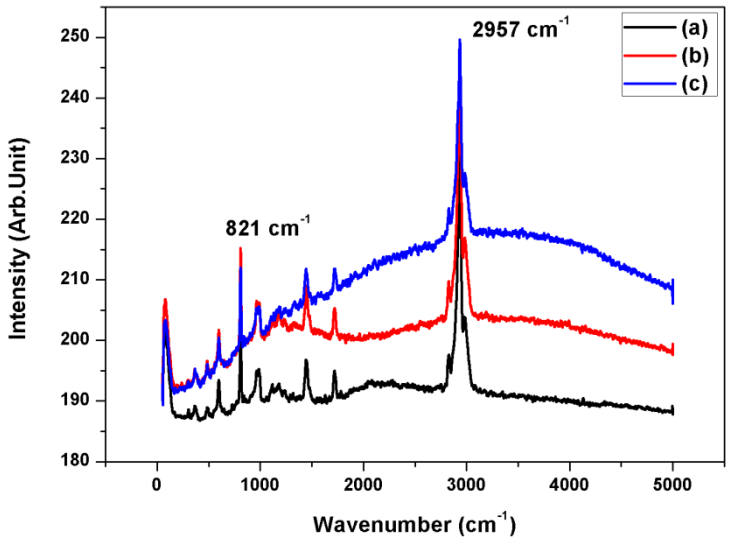

Figure 8.25: Raman scattering of PMMA rods (a) in the absence and in the presence of (b) 0.0032 M (c) 0.032 M Ag nanowires.

It is found again that Ag nanowires promote SERS and signal intensity depends on the concentration of Ag nanowires. SERS is found to be maximum for a concentration of 0.032 M Ag nanowire. However an enhancement factor of only 1.5 times is observed in this case.

8.4 Conclusions

- Average size of Ag nanospheres formed in 1mM ethanolic solution of PVP is found to be 28nm with a standard deviation of 8nm.
- Post irradiation of Ag nanospheres using xenon lamp resulted in the formation of agglomerates Ag nanoparticles.
- Irradiation of Ag nanospheres using ns pulses from Nd-YAG laser at 532nm yielded well defined Ag nanowires with an average aspect ratio of 50 which is not observed in previous reports.
- Ag nanowires of 60nm width and 10μm length are polymerised into preforms with Rh6G and from the time resolved fluorescence spectra it is found that the lifetime of Rh6G in the presence of an appropriate amount of Ag nanowires is reduced appreciably. Radiative decay rates calculated for this particular concentration of Ag nanowires indicated that the radiative decay rate is increased drastically, increasing the quantum yield of the fluorophore nearly equalling unity.
- Since the concentration of nanowires in the medium are in the weakly scattering regime, WGM lasing from POFs containing Ag nanowires in the gain media are noticed where curved surface of the fiber provides the feedback. Reduced lasing threshold as well as enhanced photostability is observed in the presence of an optimum concentration of Ag nanowires thereby demonstrating efficient fiber lasers.
- Presence of Ag nanostructures in PMMA promotes SERS. An enhancement factor of 3.2 is noticed with an appropriate quantity of Ag nanowires in PMMA based POFs.

References

[1] Haes, Amanda J., and Richard P. Van Duyne. "A unified view of propagating and localized surface plasmon resonance biosensors." Analytical and Bioanalytical Chemistry 379, no. 7-8 (2004): 920-930.

[2] Photiphitak, Chanu, Pattana Rakkwamsuk, Pennapa Muthitamongkol, Chaiyuth Sae-Kung, and Chanchana Thanachayanont. "Effect of silver nanoparticle size on efficiency enhancement of dye-sensitized solar cells." International Journal of Photoenergy 2011 (2011).

[3] Zhao, Gaoling, Hiromitsu Kozuka, and Toshinobu Yoko. "Effects of the incorporation of silver and gold nanoparticles on the photoanodic properties of rose bengal sensitized TiO 2 film electrodes prepared by sol-gel method." Solar energy materials and solar cells 46, no. 3 (1997): 219-231.

[4] Jeong, Nak Cheon, Chaiya Prasittichai, and Joseph T. Hupp. "Photocurrent enhancement by surface plasmon resonance of silver nanoparticles in highly porous dye-sensitized solar cells." Langmuir 27, no. 23 (2011): 14609-14614.

[5] Wiederrecht, G. P. "Near-field optical imaging of noble metal nanoparticles."The European Physical Journal Applied Physics 28, no. 01 (2004): 3-18.

[6] Okamoto, Koichi, Isamu Niki, Alexander Shvartser, Yukio Narukawa, Takashi Mukai, and Axel Scherer. "Surface-plasmon-enhanced light emitters based on InGaN quantum wells." Nature materials 3, no. 9 (2004): 601-605.

[7] Rycenga, Matthew, Claire M. Cobley, Jie Zeng, Weiyang Li, Christine H. Moran, Qiang Zhang, Dong Qin, and Younan Xia. "Controlling the synthesis and assembly of silver nanostructures for plasmonic applications." Chemical reviews 111, no. 6 (2011): 3669-3712.

[8] Sancho-Parramon, Jordi. "Surface plasmon resonance broadening of metallic particles in the quasi-static approximation: a numerical study of size confinement and interparticle interaction effects." Nanotechnology 20, no. 23 (2009): 235706.

[9] Junior, Amilcar Machulek, Hueder Paulo Moises De Oliveira, and Marcelo Henrique Gehlen. "Preparation of silver nanoprisms using poly (N-vinyl-2-pyrrolidone) as a colloid-stabilizing agent and the effect of silver nanoparticles on the photophysical properties of cationic dyes." Photochemical & Photobiological Sciences 2, no. 9 (2003): 921-925.

[10] Tsuji, Takeshi, Takeshi Mizuki, Shogo Ozono, and Masaharu Tsuji. "Laser-induced silver nanocrystal formation in polyvinylpyrrolidone solutions." Journal of Photochemistry and Photobiology A: Chemistry 206, no. 2 (2009): 134-139.

[11] Hao, Encai, and George C. Schatz. "Electromagnetic fields around silver nanoparticles and dimers." The Journal of chemical physics 120, no. 1 (2004): 357-366.

[12] Goldys, Ewa M., Krystyna Drozdowicz-Tomsia, Fang Xie, Tanya Shtoyko, Eva Matveeva, Ignacy Gryczynski, and Zygmunt Gryczynski. "Fluorescence amplification by electrochemically deposited silver nanowires with fractal architecture." Journal of the American Chemical Society 129, no. 40 (2007): 12117-12122.

[13] Guo, Shy-Hauh, Julia J. Heetderks, Hung-Chih Kan, and Raymond J. Phaneuf. "Enhanced fluorescence and near-field intensity for Ag nanowire/nanocolumn arrays: evidence for the role of surface plasmon standing waves." Optics express 16, no. 22 (2008): 18417-18425.

[14] Kowalska, Dorota, Bartosz Krajnik, Maria Olejnik, Magdalena Twardowska, Nikodem Czechowski, Eckhard Hofmann, and Sebastian Mackowski. "Metal-enhanced fluorescence of chlorophylls in light-harvesting complexes coupled to silver nanowires." The Scientific World Journal 2013 (2013).

[15] Yuan, Quan, Yunfei Zhang, Yan Chen, Ruowen Wang, Chaoling Du, Emir Yasun, and Weihong Tan. "Using silver nanowire antennas to enhance the conversion efficiency of photoresponsive DNA nanomotors." Proceedings of the National Academy of Sciences 108, no. 23 (2011): 9331-9336.

[16] Goldys, Ewa M., Krystyna Drozdowicz-Tomsia, Fang Xie, Tanya Shtoyko, Eva Matveeva, Ignacy Gryczynski, and Zygmunt Gryczynski. "Fluorescence amplification by electrochemically deposited silver nanowires with fractal architecture." Journal of the American Chemical Society 129, no. 40 (2007): 12117-12122.

[17] Goldys, and Krystyna Drozdowicz-Tomsia. Gold and silver nanowires for fluorescence enhancement. INTECH Open Access Publisher, 2011.

[18] Jana, Nikhil R., Latha Gearheart, and Catherine J. Murphy. "Wet chemical synthesis of silver nanorods and nanowires of controllable aspect ratio." Chemical Communications 7 (2001): 617-618.

[19] Murphy, Catherine J., Tapan K. Sau, Anand Gole, and Christopher J. Orendorff. "Surfactant-directed synthesis and optical properties of one-dimensional plasmonic metallic nanostructures." Mrs Bulletin 30, no. 05 (2005): 349-355.

[20] Zhang, J., X. Wang, X. Peng, and L. Zhang. "Fabrication, morphology and structural characterization of ordered single-crystal Ag nanowires." Applied Physics A 75, no. 4 (2002): 485-488.

[21] Sun, Yugang, Byron Gates, Brian Mayers, and Younan Xia. "Crystalline silver nanowires by soft solution processing." Nano letters 2, no. 2 (2002): 165-168.

[22] Sun, Yugang, Brian Mayers, Thurston Herricks, and Younan Xia. "Polyol synthesis of uniform silver nanowires: a plausible growth mechanism and the supporting evidence." Nano Letters 3, no. 7 (2003): 955-960.

[23] Yan, Guangqing, Li Wang, and Lei Zhang. "Recent research progress on preparation of silver nanowires by soft solution method, preparation of gold nanotubes and Pt nanotubes from resultant silver nanowires and their applications in conductive adhesive." Rev. Adv. Mater. Sci 24 (2010): 10-25.

[24] Tang, Xinling, and Masaharu Tsuji. Syntheses of silver nanowires in liquid phase. INTECH Open Access Publisher, 2010.

[25] Wiley, Benjamin, Yugang Sun, and Younan Xia. "Synthesis of silver nanostructures with controlled shapes and properties." Accounts of Chemical Research 40, no. 10 (2007): 1067-1076.

[26] Tsuji, Takeshi, Norihisa Watanabe, and Masaharu Tsuji. "Laser induced morphology change of silver colloids: formation of nano-size wires." Applied surface science 211, no. 1 (2003): 189-193.

[27] Tsuji, Takeshi, Yuuki Okazaki, Takanori Higuchi, and Masaharu Tsuji. "Laser-induced morphology changes of silver colloids prepared by laser ablation in water: Enhancement of anisotropic shape conversions by chloride ions."Journal of Photochemistry and Photobiology A: Chemistry 183, no. 3 (2006): 297-303.

[28] Zamiri, Reza, Azmi Zakaria, Mohd Shahril Husin, Zaidan Abd Wahab, and Forough Kalaei Nazarpour. "Formation of silver microbelt structures by laser irradiation of silver nanoparticles in ethanol." International journal of nanomedicine 6 (2011): 2221.

[29] Tarasenko, N. V., A. V. Butsen, and E. A. Nevar. "Laser-induced modification of metal nanoparticles formed by laser ablation technique in liquids." Applied surface science 247, no. 1 (2005): 418-422.

[30] Tsuji, Takeshi, Yuuki Okazaki, and Masaharu Tsuji. "Photo-induced morphological conversions of silver nanoparticles prepared using laser ablation in water—Enhanced morphological conversions using halogen etching." Journal of Photochemistry and Photobiology A: Chemistry 194, no. 2 (2008): 247-253.

[31] Tsuji, Takeshi, Kenzo Iryo, Yukio Nishimura, and Masaharu Tsuji. "Preparation of metal colloids by a laser ablation technique in solution: influence of laser wavelength on the ablation efficiency (II)." Journal of Photochemistry and Photobiology A: Chemistry 145, no. 3 (2001): 201-207.

[32] Sebastian, Suneetha, C. L. Linslal, C. P. G. Vallabhan, V. P. N. Nampoori, P. Radhakrishnan, and M. Kailasnath. "Laser induced augmentation of silver nanospheres to nanowires in ethanol fostered by Poly Vinyl Pyrrolidone."Applied Surface Science 320 (2014): 732-735.

[33] Evanoff, David D., and George Chumanov. "Size-controlled synthesis of nanoparticles. 2. Measurement of extinction, scattering, and absorption cross sections." The Journal of Physical Chemistry B 108, no. 37 (2004): 13957-13962.

[34] Mott, Nevill Francis, and L. Friedman. "Metal-insulator transitions in VO2, Ti2O3 and Ti2-x V x O3." Philosophical Magazine 30, no. 2 (1974): 389-402.

[35] Wiersma, Diederik S., Paolo Bartolini, Ad Lagendijk, and Roberto Righini. "Localization of light in a disordered medium." Nature 390, no. 6661 (1997): 671-673.

[36] Kuga, Yasuo, and Akira Ishimaru. "Retroreflectance from a dense distribution of spherical particles." JOSA A 1, no. 8 (1984): 831-835.

[37] de Oliveira, Paulo C., Amy E. Perkins, and Nabil M. Lawandy. "Coherent backscattering from high-gain scattering media." Optics letters 21, no. 20 (1996): 1685-1687.

[38] Van Der Mark, Martin B., Meint P. van Albada, and Ad Lagendijk. "Light scattering in strongly scattering media: multiple scattering and weak localization." Physical Review B 37, no. 7 (1988): 3575.

[39] Akkermans, E., P. E. Wolf, R. Maynard, and G. Maret. "Theoretical study of the coherent backscattering of light by disordered media." Journal de Physique49, no. 1 (1988): 77-98.

[40] Van Albada, Meint P., and Ad Lagendijk. "Observation of weak localization of light in a random medium." Physical review letters 55, no. 24 (1985): 2692-2695.

[41] Wolf, Pierre-Etienne, and Georg Maret. "Weak localization and coherent backscattering of photons in disordered media." Physical Review Letters 55, no. 24 (1985): 2696.

[42] Meng, Xiangeng, Koji Fujita, Yanhua Zong, Shunsuke Murai, and Katsuhisa Tanaka. "Random lasers with coherent feedback from highly transparent polymer films embedded with silver nanoparticles." Applied Physics Letters 92, no. 20 (2008): 201112.

[43] Du, ChaoLing, YuMeng You, XueJin Zhang, Kasim Johnson, and ZeXiang Shen. "Polarization-dependent confocal imaging of individual Ag nanorods and nanoparticles." Plasmonics 4, no. 3 (2009): 217-222.

[44] Wei, Hong, Alejandro Reyes-Coronado, Peter Nordlander, Javier Aizpurua, and Hongxing Xu. "Multipolar plasmon resonances in individual Ag nanorice." Acs Nano 4, no. 5 (2010): 2649-2654.

[45] Bardhan, Rizia, Nathaniel K. Grady, Joseph R. Cole, Amit Joshi, and Naomi J. Halas. "Fluorescence enhancement by Au nanostructures: nanoshells and nanorods." Acs Nano 3, no. 3 (2009): 744-752.

[46] Sun, Yanyan, Zhaona Wang, Xiaoyu Shi, Yanrong Wang, Xiaoye Zhao, Shujing Chen, Jinwei Shi, Jing Zhou, and Dahe Liu. "Coherent plasmonic random laser pumped by nanosecond pulses far from the resonance peak of silver nanowires." JOSA B 30, no. 9 (2013): 2523-2528.

[47] Geetha, K., M. Rajesh, V. P. N. Nampoori, C. P. G. Vallabhan, and P. Radhakrishnan. "Laser emission from transversely pumped dye-doped free-standing polymer film." Journal of Optics A: Pure and Applied Optics 8, no. 2 (2006): 189.

[48] Frolov, S. V., M. Shkunov, Z. V. Vardeny, and K. Yoshino. "Ring microlasers from conducting polymers." Physical Review B 56, no. 8 (1997): R4363.

[49] Choi, H. W., H. J. Woo, W. Hong, J. K. Kim, S. K. Lee, and C. H. Eum. "Structural modification of poly (methyl methacrylate) by proton irradiation."Applied surface science 169 (2001): 433-437.

[50] Xu, Xingsheng. "Stimulated Raman spectrum threshold in poly (methyl methacrylate) optical fibers." Optics communications 199, no. 1 (2001): 89-93.

[51] Thomas, K. J., M. Sheeba, V. P. N. Nampoori, C. P. G. Vallabhan, and P. Radhakrishnan. "Raman spectra of polymethyl methacrylate optical fibres excited by a 532 nm diode pumped solid state laser." Journal of Optics A: Pure and Applied Optics 10, no. 5 (2008): 055303.

[52] Willis, H. A., V. J. I. Zichy, and P. J. Hendra. "The laser-Raman and infra-red spectra of poly (methyl methacrylate)." Polymer 10 (1969): 737-746.

[53] Li, Jia-Han, Shih-Wen Chen, Yi Chou, Ming-Chung Wu, Chun-Hway Hsueh, and Wei-Fang Su. "Effects of gold film morphology on surface plasmon resonance using periodic P3HT: PMMA/Au nanostructures on silicon substrate for surface-enhanced raman scattering." The Journal of Physical Chemistry C 115, no. 49 (2011): 24045-24053.

[54] Tian, Zhong-Qun, Bin Ren, and De-Yin Wu. "Surface-enhanced Raman scattering: from noble to transition metals and from rough surfaces to ordered nanostructures." The Journal of Physical Chemistry B 106, no. 37 (2002): 9463-9483.

[55] Wu, Ming-Chung, Yi Chou, Chih-Min Chuang, Che-Pu Hsu, Jhih-Fong Lin, Yang-Fang Chen, and Wei-Fang Su. "High-sensitivity Raman scattering substrate based on Au/La0. 7Sr0. 3MnO3 periodic arrays." ACS applied materials & interfaces 1, no. 11 (2009): 2484-2490.

[56] Wiley, Benjamin J., Sang Hyuk Im, Zhi-Yuan Li, Joeseph McLellan, Andrew Siekkinen, and Younan Xia. "Maneuvering the surface plasmon resonance of silver nanostructures through shape-controlled synthesis." The Journal of Physical Chemistry B 110, no. 32 (2006): 15666-15675.

[57] Yu, Qiuming, Phillip Guan, Dong Qin, Greg Golden, and Paul M. Wallace. "Inverted size-dependence of surface-enhanced Raman scattering on gold nanohole and nanodisk arrays." Nano letters 8, no. 7 (2008): 1923-1928.

[58] Anh Dinh, Duc, Kwun Nam Hui, Kwan San Hui, Jai Singh, Pushpendra Kumar, and Wei Zhou. "Silver Nanowires: A Promising Transparent Conducting Electrode Material for Optoelectronic and Electronic Applications." Reviews in Advanced Sciences and Engineering 2, no. 4 (2013): 324-345.

[59] Hong, Seongmin, and Xiao Li. "Optimal size of gold nanoparticles for surface-enhanced raman spectroscopy under different conditions." Journal of Nanomaterials 2013 (2013): 49.

Chapter 9 :

General conclusions and future prospects

A glimpse of general conclusions of the work done in this thesis is discussed along with some insight to the future regarding this work.

PMMA based POFs are still in progress in the class of plastic fibers owing to thier high optical transparency in the visible region, flexibility, low birefringence and good processability. PMMA is a good host material for the incorporation of optical gain media like organic dyes. Fiber lasers incorporating laser dyes have several advantages over conventional solid state lasers such as low threshold lasing due to its light confinement in the waveguiding structure. Recently it is found that the environment of the fluorophore/dye can be engineered by the presence of conducting metal nanoparticles. Size and geometry are the main parameters of the nanoparticles that determine the properties of the localised surface plasmon it supports. Thus either enhancement or quenching of dye's emission is possible in its presence. The thesis presented in eight chapters dealt with the preparation of metal nanoparticles with various nanostructures and their influence on fiber laser properties such as lasing efficiency and photostability.

Conventional synthesis method of metal nanoparticles following chemical route suffers several disadvantages. Most of them are overcome in physical route making use of laser ablation of metal targets in various liquid environments. Metal nanoparticles of gold and silver were synthesised using laser ablation in various liquid media. Depending on the dielectric function and polarizability of the liquid environment, nanoparticles produced showed different size distribution. Nanoparticles were found to be stable with increase in polarizability of the medium. Laser parameters affecting the shape and size distribution of nanoparticles such as laser wavelength, fluence, pulse duration and number of laser shots were optimised. With optimised parameters, gold nanoparticles were synthesised in Methyl Methacrylate and its influence on the optical properties of Rh6G such as optical extinction, optical emission, lifetime and quantum yield were studied. Further, gold nanoparticles were incorporated into polymer fiber containing Rh6G as the gain media. Presence of Au nanoparticles deteriorated the lasing and photostability of dyes in the fiber cavity through FRET. Silver nanoparticles prepared by laser ablation in different media such as ethanol and MMA have shown different plasmonic properties when integrated with dyes. Silver nanoparticles produced in ethanolic environment improved the lasing efficiency of fiber laser through enhanced radiative decay rate thereby enhancing the gain of the medium whereas that produced in MMA deteriorated lasing action through NSET. Au-Ag core/shell and nanoalloys were successfully produced by laser ablation of Ag target in the already synthesised Au nanocolloids. Low threshold whispering gallery mode lasing emission from POFs with enhanced photostability have been noticed in the presence of bimetallic nanostructures as compared to their individual monomeric nanoparticles. Femtosecond laser irradiation of Rh6G has found to modify the structure thereby enhancing the emission of the dye nearly 30%. Unlike in the case of fs laser pulses, Rh6G when irradiated by ns laser showed reduced fluorescence intensity under all experimental conditions. Lasing emission from step index POFs

with pure as well as modified Rh6G as the gain medium showed exactly the same WG modes and modified Rh6G doped POFs showed a 4 fold increase in lasing mode intensity with a threshold reduction. Post irradiation of Ag nanospheres using Nd-YAG laser yielded Ag nanowires with an average aspect ratio of 50. Radiative decay rates calculated for an optimum concentration of Ag nanowires has increased the radiative decay drastically thereby increasing the quantum yield of the fluorophore nearly equalling unity. WG multimode lasing was observed from Ag nanowire incorporated in the gain media of step index POFs since Ag nanowires were in the weakly scattering regime thus avoiding scattering mediated lasing such as random lasing. Threshold reduction of nearly 20 times has been observed with high photostability upto 27000 laser shots. Also presence of Ag nanowires promoted SERS of PMMA and an enhancement factor of 3.2 was noticed with an appropriate amount of Ag nanowires. Thus efficient polymer fiber lasers incorporating various metallic nanostructures with enhanced photostability have been demonstrated in this thesis work.

One of the major advantages of preparation of metal nanoparticles by chemical route is production of mono-dispersive nanoparticles. So studies can be extended to the synthesis of mono-dispersive metal nanoparticles by laser ablation. By post-irradiation of already synthesised nanocolloidal solution, even more nanostructures such as nanobelts, nanorods can be prepared and its influence on the lasing and amplification properties of dye doped POFs can be studied. Versatility of dyes available, including natural dyes, can be utilised effectively for the fabrication of dye doped POFs. Natural dyes such as Curcumin can be replaced for synthetic dyes in the gain medium of fiber lasers and amplifiers. Photostability and quantum yield of the dyes can be improved by the presence of noble metal nanoparticles. Since graded index dye doped POFs exhibit ASE and lasing at low threshold than SI POFs, GI POFs with dye-metal nanoparticles in the gain medium can be fabricated. Optical fiber sensors based on localised Surface Plasmon Resonance, making use of metal nanoparticles, can be fabricated. Instead of depositing nanoparticles at the end of the fiber, the whole fiber fabricated with metal nanoparticles in the core/cladding of the fiber (as presented in the thesis) can be utilised. Photonic Crystal Fibers with nanoparticles embedded in its material can be fabricated for enhancing the optical non-linearity of the fiber. Metal nanoparticles incorporated in fiber can be further employed for making effective probe for SERS for the detection of remote analyte molecules.

Appendix.....

Journal of Photochemistry and Photobiology A: Chemistry 288 (2014) 34–38

Contents lists available at ScienceDirect

Journal of Photochemistry and Photobiology A: Chemistry

journal homepage: www.elsevier.com/locate/jphotochem

Femtosecond laser induced emission enhancement in Rhodamine6G

Suneetha Sebastian*, C. Ajina, C.P.G. Vallabhan, V.P.N. Nampoori, P. Radhakrishnan, M. Kailasnath

International School of Photonics, Cochin University of Science And Technology, Cochin, India

ARTICLE INFO

Article history:
Received 5 February 2014
Received in revised form 9 April 2014
Accepted 21 April 2014
Available online 9 May 2014

Keywords:
Xanthene ring
Rhodamine6G emission enhancement
Femtosecond laser irradiation

ABSTRACT

Significant enhancement in the peak intensity of fluorescent emission has been observed in dye solution of Rhodamine6G in Methyl Methacrylate on irradiation with femtosecond laser pulses. Detailed studies have been carried out by varying the parameters like exposure time, dye concentration and pump power density to determine the optimum conditions for maximum fluorescent emission enhancement. Up to 30% increase in peak intensity has been found to occur with significant increase in fluorescent quantum yield. Fourier Transform Infra Red spectra recorded before and after irradiation reveal that xanthene ring in Rhodamine6G molecule gets deformed and a new intermediate state of the dye is formed before its gets deteriorated as the exposure time is increased well above the optimum value.

1. Introduction

It is well known that intense laser pulses can cause several interesting non-linear optical phenomena. Femtosecond laser pulses are known to produce high harmonics and continuum emission. They also can be used to induce many kinds of multi photon phenomena. The intense electric field of such pulses can cause bond breaking and rearrangement of molecular structure in many systems. Rhodamine6G (Rh6G) is the most commonly and widely used laser dye for the last four decades. Rh6G has many desirable properties such as high quantum efficiency, increased photostability and good lasing action [1,2]. Because of the widespread use of Rh6G in solid state dye lasers [3,4], amplifiers [5,6], and sensors [7], the continued studies on this molecule are still very relevant.

Photophysical as well as photochemical changes occurring in Rh6G due to irradiation have already been reported as early as 1971 [8]. Thereafter a number of further studies have come up in this field [9–12]. In all these reports a detailed mechanism behind the deterioration of the dye due to radiation is mentioned. But none of these work reported a spectral emission enhancement of the dye owing to its exposure to a light source. In this context the present study becomes important since it is the first such report of fluorescence enhancement of Rhodamine6G due to radiation.

Fluorescence techniques are generally used for detection and sensing well over the last 25 years. But detection/sensing by this technology faces limitations due to quantum efficiency and photochemical stability of the fluorophore [13]. Recently there are many reports on the fluorescence enhancement of Rh6G using metal nanoparticles such as gold and silver [14–16]. Such successes in the field of radiative decay engineering (RDE) overcome some of these limitations of the fluorophore. But an emission enhancement of the pure dye i.e., without the aid of metal nanoparticles is reported here for the first time.

In this paper we have used femtosecond laser pulses to irradiate a well known dye molecule namely Rh6G in Methyl Methacrylate solution and have noticed several interesting features related to the fluorescent emission from the irradiated system. Present work is of utmost interest since this can lead to a better sensing and detection of molecules, improved lasing properties and amplification using the pure dye itself.

2. Experimental

Rh6G used in the present study is purchased from Acros, USA. The dye is dissolved in Methyl Methacrylate (supplied by Sigma–Aldrich). Methyl Methacrylate (MMA) is a good candidate for the production of polymer optical fibre (POF) because of its high transparency [6]. The motivation behind choosing MMA is that the whole sample can be directly polymerised. Methyl Methacrylate purchased from the market usually contains inhibitors like hydroquinone to prevent its polymerisation at room temperature. In order to obtain pure MMA, at first the solution is treated with 5% of sodium hydroxide (NaOH). This process is repeated several times to completely remove the effect of inhibitors. After this treatment

* Corresponding author. Tel.: +91 9745271291.
E-mail address: sunikutty@gmail.com (S. Sebastian).

http://dx.doi.org/10.1016/j.jphotochem.2014.04.021
1010-6030/

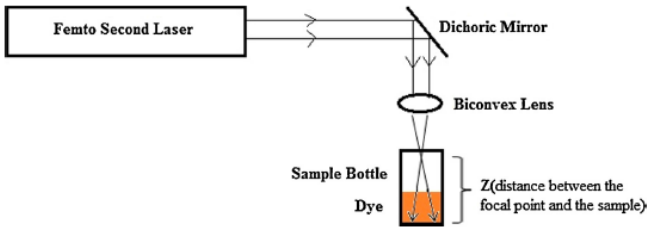

Fig. 1. Schematic for the irradiation of Rh6G.

there can be some traces of NaOH which is washed off by shaking with distilled water. Further purity of MMA is assured by distillation of the solution under vacuum [6].

Fig. 1 depicts the experimental setup used for the present study. A mode locked Ti: Sapphire femtosecond laser is used as the source of laser irradiation. Wavelength of radiation is centred around 797 nm with a laser spot size of 7 mm and an average output power of 1.5 W. 120 fs pulsed radiation of 80 MHz repetition rate is reflected using a dichoric mirror. Radiation is focussed using a biconvex lens of focal length 5 cm. 5 ml of the dye solution is taken in a 15 ml sample container for the experiment. Sample container is placed at a distance of Z from the focal point where Z is the distance between the focal point and the bottom of the sample container. The experiment is repeated by varying Z from 0 to 5 cm. Also the time of exposure of the sample to the laser radiation is changed from 30 s to 90 min. Further, to study the effect of concentration of the dye, the molarity of the dye is varied from 10^{-3} mol/l to 10^{-6} mol/l.

The photophysical characteristics of the samples are noted. Spectral absorption of the irradiated sample is recorded using Jasco UV–ViS NIR Spectrophotometer. The spectral emission of the same is recorded using Varian Cary Eclipse Fluorimeter. Fourier Transform Infra Red (FTIR) spectra are obtained using Thermo Nicolet, Avatar 370 with a resolution of 4 cm^{-1}.

3. Result and discussion

Rh6G is a highly fluorescent xanthene dye. Xanthene ring is surrounded by phenyl and amino external groups. As is well known, the dye absorbs mainly around 530 nm and emits strongly in the visible region [17,18]. After irradiating the dye solution of 10^{-4} mol/l concentration kept at a distance of 2 cm from the focal point for 10 min, it is noted that the appearance of the sample itself has changed to more bright and fluorescent. To understand the phenomena in detail the exposure time of the sample is varied. Fig. 2 shows the corresponding spectral absorbance of the samples before and after irradiation. It is noticed that the spectral characteristics of the irradiated dye is dramatically changed. From figure it is inferred that up to 30 min of irradiation the spectral shape of the dye remains unchanged and only the absorbance is increased. But after 30 min it is clearly seen that the spectral shape undergoes changes. The shoulder at 500 nm lifts up to the peak absorption range and also the full width at half maximum of the spectrum increases when the exposure time is more than an hour. This may be an indication of the destruction of the molecular structure of Rh6G due to the effect of femtosecond radiation.

Fig. 3 depicts the change in the emission intensity of the dye when it is exposed to different time durations of femtosecond radiations. As seen from figure, 30% increase in the peak value of fluorescence emission of the dye is obtained when the sample is exposed for 5 min. Increase in the exposure time up to 15 min

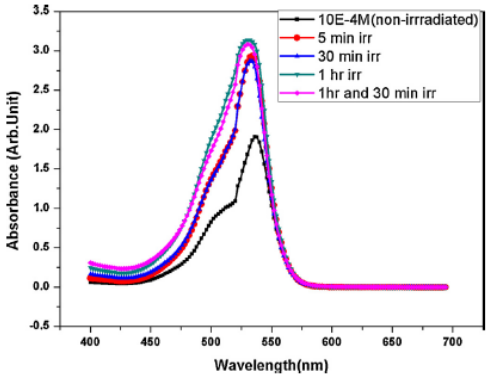

Fig. 2. Absorption spectra of Rh6G irradiated with femtosecond laser pulses for various time durations. Sample is kept at distance of $Z = 2$ cm from the focal point of the lens.

does not bring any further enhancement in the peak intensity as compared to 5 min exposed sample. But after 15 min, the emission intensity starts to quench from the maximum (30%) and at 60 min, the intensity of the irradiated sample becomes same as that of non-irradiated sample. Further exposure of the sample to the

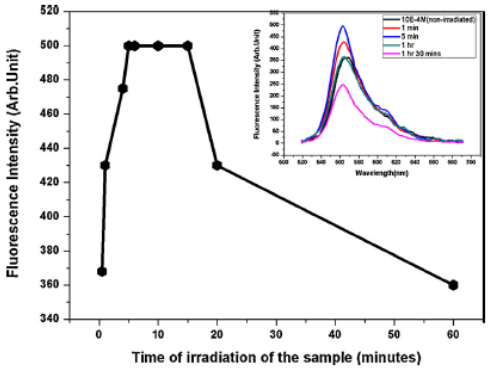

Fig. 3. Peak fluorescence intensity of Rh6G Vs. Irradiation time of the dye. Intensity corresponding to 0 min is the initial peak intensity of the dye before irradiation. Inset shows the emission spectra of Rh6G, excited at 500 nm, before and after irradiation with femtosecond laser pulses.

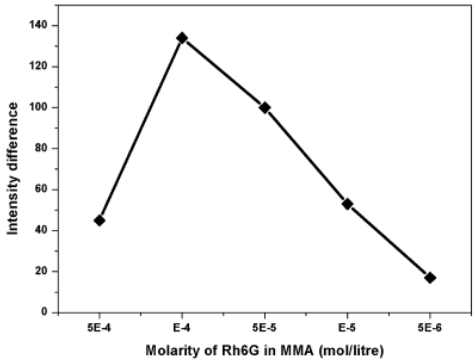

Fig. 4. The difference in peak fluorescence intensity between the non-irradiated sample and 5 min irradiated samples vs. concentration of the dye.

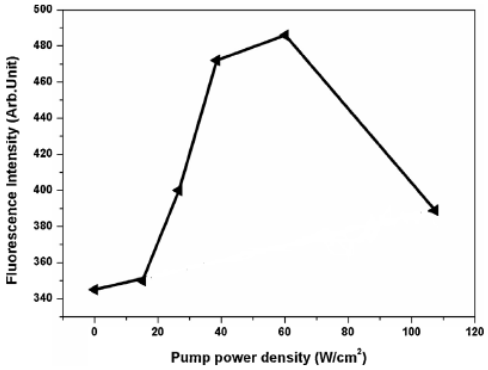

Fig. 5. Variation of fluorescence intensity with pump power density. 0 w/cm² corresponds to the fluorescence intensity of non-irradiated sample. All samples are irradiated for 5 min. $Z = 1.5$ cm, $Z = 2$ cm, $Z = 2.5$ cm, $Z = 3$ cm, $Z = 4$ cm corresponds to the pump power densities of 107 W/cm², 60 W/cm², 38 W/cm², 27 W/cm², 15 W/cm² respectively.

source quenches the intensity to even lower values as evident from the inset of Fig. 3. Thus the optimum exposure time for maximum enhancement is determined to be 5–15 min.

The experiment is repeated by changing the concentration of the dye in the solution. But it is observed that the maximum enhancement is possible only for a particular concentration i.e., 10^{-4} mol/l as is shown in Fig. 4. It is also found that the maximum fluorescence emission of the bare dye in MMA is occurring at this concentration. Thus the optimum concentration of the dye for maximum emission enhancement in MMA upon laser irradiation is 10^{-4} mol/l.

Finally the influence of Z on the emission enhancement is taken into consideration and is depicted in Fig. 5. It is found that when the focus is within the sample, emission intensity is drastically quenched when irradiated for 5 min (not shown here). At the focus the diameter of the laser radiation is found to be 11.4 μm and the power density is 1.47 MW/cm². This density is so high that the molecule may get structural decomposition leading to an adverse effect on the emission intensity as compared to the non-irradiated sample. As Z is increased obviously the power density of the pump is decreased and interestingly it is found that for a power density of 60 W/cm² (i.e., when $Z = 2$ cm) maximum fluorescence intensity enhancement is noted. Power density above or below 60 W/cm² resulted in quenching of dye's emission with respect to the emission at this optimised power density. So in order to understand the structural changes happening in the irradiated dye, FTIR spectra are recorded for the bare sample and irradiated sample (Fig. 6). As seen from Fig. 6, the bands present in the spectrum are the combined effect of Rh6G and MMA. The bands at 596 cm^{-1}, 819 cm^{-1}, 1167 cm^{-1}, 1329 cm^{-1} are due to the xanthene ring, phenyl and ethylamine groups of Rh6G. The band at 1021 cm^{-1} is due to methyl, phenyl and ethylamine external groups. The sharp band at 1200 cm^{-1} is due to xanthene ring and ethylamine groups. Again the sharp peak at 1446 cm^{-1} is due to ethylamine group. The very

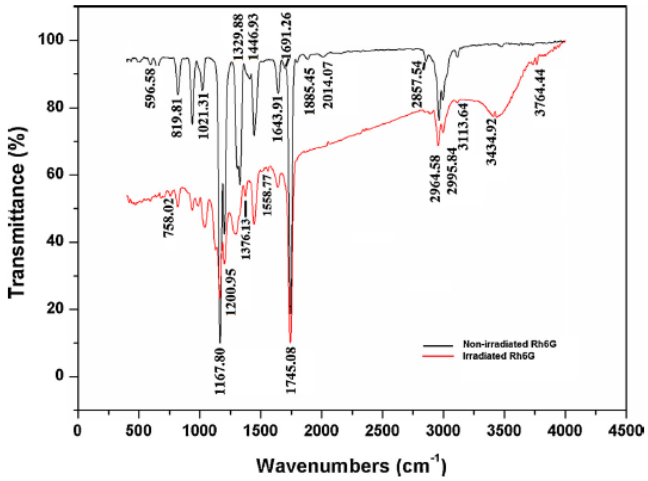

Fig. 6. FTIR spectra of non-irradiated and irradiated Rh6G in MMA for 5 min at a concentration of 10^{-4} mol/l with a pump power density of 60 W/cm².

sharp and narrow band at 1745 cm^{-1} is due to C=O stretching of the xanthene ring of Rh6G and carbonyl stretching band due to MMA. The band at 1643 cm^{-1} is due to C=C bond in MMA. The band at 3000 cm^{-1} range is due to symmetric and asymmetric vibrations of methylene group present in MMA [18–24]. But in the FTIR of the irradiated sample, it can be seen that all bands which are present in the FTIR of non-irradiated sample get reduced in intensity. Also some bands due to xanthene ring like 1691 cm^{-1} and 1329 cm^{-1} disappear and new bands like 758 cm^{-1} are appearing. It is found from the literature that the new bands like 758 cm^{-1} are due to the presence of deformed xanthene ring. We have also observed other new bands in the FTIR spectrum of the irradiated dye such as 1376 cm^{-1} and 1558 cm^{-1} which are due to the stretching of the xanthene ring [18]. From these inferences it can be thought that the photochemical reaction induced by the pump beam is initiating the breakdown and thereby the deformations of the xanthene ring in Rh6G. Also from Fig. 6 it is evident that some new bands are also appearing in the high wavenumber range and this can be likely due to the rearrangement of molecular structure of MMA by the attachment of chromophore group from Rh6G to MMA monomers or dimmers. The new structure of Rh6G molecule is an intermediate state of the dye before it gets degraded when irradiated for more than the optimum time. The structural deformation happening to the dye under laser radiation might have reduced the rate of non-radiative relaxation of the molecules from the excited state thereby increasing the radiative decay rate resulting in fluorescence enhancement of the dye. The intermediate state is found to be very stable for months.

For any fluorescent material such as dyes quantum yield of its luminescence is a fundamental property and so its calculation is really promising for the characterisation of the material. The quantum yield is found out using the equation given below

$$Q_S = Q_R \frac{I_S \times (1 - 10^{-A_R}) \times n_S^2}{I_R \times (1 - 10^{-A_S}) \times n_R^2} \quad (1)$$

where the subscript S and R stands for the reference and sample respectively. Q is the quantum yield, I stands for the integrated fluorescence intensity and the term in the brackets is known as absorption factor where A is the absorbance [25]. Q_R is taken as 0.85 which is the quantum yield of Rh6G in MMA. Substituting other parameters in Eq. (1) using data from the spectral absorption and emission given in Fig. 2 and inset of Fig. 3 it is found that quantum efficiency of the dye in MMA irradiated for 5 min at a pump power density of 60 W/cm^2 is increased from 0.85 to 0.95. So the important increase in fluorescence intensity of the dye upto 30% upon irradiation results in rather increase of the quantum yield of the dye to nearly 10%. We have noted similar effect in the case of Rh6G dissolved in other solvents also which is not included here.

4. Conclusions

Rh6G dissolved in MMA irradiated by femtosecond lase pulses resulted in a sudden deterioration of the dye's spectral emission when the sample is kept at the focus of the radiation. Deterioration took place within a short period of 5 min. But interestingly it is found that as the sample is moved away from the focus, a noticeable change in brightness took place and the maximum brightness and thus maximum emission of the dye is noticed at a distance 2 cm from the focus where the intensity of the radiation is around 60 W/cm^2. Also the concentration of the dye in the solution is varied and found that maximum enhancement is obtained for 10^{-4} mol/l. Again it is noticed that the time of exposure of the dye solution in the laser radiation plays a key role in this enhancement. The optimum time is found to be 5–15 min at the power levels mentioned here. Exposure for more than 15 min resulted in fluorescence quenching compared to 5 min irradiated sample. Further increase in the exposure time resulted in decrease compared to the non-irradiated sample. FTIR spectra of 10^{-4} mol/l concentration of Rh6G in MMA irradiated for 5 min with an intensity of 60 W/cm^2 is compared with non-irradiated sample of the same concentration. Detailed study indicated that xanthene ring in the dye may be disrupted partially giving rise to an intermediate molecular structure of the dye. The new form is found to be stable and complete breakdown of the dye occurs at the focus and also when the exposure time is increased beyond an hour. Also the quantum yield of the irradiated sample is determined and it is found to be more than that of the bare dye. The novelty in the result offers possibilities to improve the efficiency of spectral emission of Rh6G.

Acknowledgement

The author would like to thank UGC- RFSMS and DST for the financial assistance and SAIF-STIC for providing the facility for FTIR analysis. The author also thank Ms Indu Sebastian (ISP, CUSAT), Prof K.C Sebastian, Dr Thomas Lee S, Dr Jyotsna Ravi and Mr Arun (Cypress) for their inspiring discussions and helpful suggestions.

References

[1] D. Avnir, D. Levy, R. Reisfeld, The nature of the silica cage as reflected by spectral changes and enhanced photostability of trapped Rhodamine 6G, J. Phys. Chem. 88 (24) (1984).
[2] Characterization of rhodamine 6G doped polymer optical fiber by side illumination fluorescence, Opt. Eng. 45 (July (7)) (2006) 075003.
[3] KurikiK., T. Kobayashi, N. Imai, T. Tamura, S. Nishihara, et al., High-efficiency organic dye-doped polymer optical fiber lasers, Appl. Phys. Lett. 77 (July (3)) (2000).
[4] KurikiK., T. Kobayashi, N. Imai, et al., Organic dye doped polymer optical fiber lasers, Polym. Adv. Technol. 11 (2000) 612–616.
[5] G.D. Peng, P.L. Chu, Z. Xiong, T.W. Whitbread, R.P. Chaplin, Dye-doped step-index polymer optical fiber for broadband optical amplification, J. Lightw. Technol. 14 (October (10)) (1996).
[6] M. Rajesh, M. Sheeba, K. Geetha, C.P. Vallaban, P. Radhakrishnan, V.P. Nampoori, Fabrication and characterization of dye-doped polymer optical fiber as a light amplifier, Appl. Opt. 46 (January (1)) (2007) 106–112.
[7] M. Cox, A. Argyros, M.C. Large, S. Kalluri, Surface enhanced Raman scattering in a hollow core microstructured optical fiber, Opt. Exp. 15 (21) (2007) 13675–13681.
[8] E.P. Ippen, C.V. Shank, A. Dienes, IEEE J. Quant. Electron. QE-7 (1971) 178.
[9] D. Kato, A. Sugimura, Deterioration of Rhodamine 6G dye solution in methanol, Opt. Commun. 10 (4) (1974) 327–330.
[10] I. Rosenthal, Photochemical stability of Rhodamine 6G in solution, Opt. Commun. 24 (2) (1978).
[11] F. Upez Arbeloa, A. Costelab, I. Lopez Arbeloa, Molecular structure effects on the lasing properties of Rhodamines, J. Photochem. Photobiol. A: Chem. 55 (1990) 97–103.
[12] M. Yamashita, H. Kashiwagi, Photodegradation mechanisms in laser dyes: a laser irradiated ESR study, IEEE J. Quant. Electron. qe-12 (February (2)) (1976) 90–95.
[13] K. Aslan, I. Gryczynski, J. Malicka, E. Matveeva, J.R. Lakowicz, C.D. Geddes, Metal-enhanced fluorescence: an emerging tool in biotechnology, Curr. Opin. Biotechnol. 16 (February (1)) (2005) 55–62.
[14] A.K. Kyung, J. Wang, B.J. Jacek, S. Achilefu, Fluorescence manipulation by gold nanoparticles: from complete quenching to extensive enhancement, J. Nanobiotechnol. 9 (2011) 16.
[15] G. Liu, H. Zheng, M. Liu, Z. Zhang, J. Dong, X. Yan, X. Li, Surface-enhanced fluorescence of rhodamine 6G on the assembled silver nanostructures, J. Nanosci. Nanotechnol. 11 (November (11)) (2011) 9523–9527.
[16] L. Dong, F. Ye, A. Chughtai, V. Liuolia, S. Popov, A.T. Friberg, M. Muhammed, Lasing from water solution of Rhodamine6G/Gold nanoparticles: impact of SiO_2-coating on metal surface, IEEE J. Quant. Electron. 48 (September (9)) (2012).
[17] D. Wu, G.-H. Deng, Y. Guo, H.-f. Wang, Observation of the Interference between the intramolecular IR-visible and visible-IR processes in the doubly resonant sum frequency generation vibrational spectroscopy of Rhodamine 6G adsorbed at the air/water interface, J. Phys. Chem. A 113 (2009) 6058–6063.
[18] M. Majoube, M. Henry, Fourier transform Raman and infrared and surface-enhanced Raman spectra for Rhodamine 6G, Spectrochem. Acta 4lA (9/10) (1997) 1459–1466.
[19] T.G. Sunitha, K.S. Yoganand, G. Umamaheswari, M.J. Umapathy, A kinetic study on the free radical polymerization of methyl methacrylate by 1,1,4,4-tetramethyl-1,4D di ammonium chloride (TMDBEDAC) as DI-Site phase transfer catalyst, Int. J. Chem. Res. 3 (2) (2012).

[20] A.A. Abubker, G.I. Hesham, A. Abdulmaged, A.E. Mohamed, Thermal and mechanical analysis of urethane acrylate graft copolymer part A: urethane macromonomer base on TDI and EG, Int. J. Chem. 5 (1) (2013) 1916–9698.
[21] Characterisation of polymers, Vol. 2.
[22] Z. Yu-Ming, K.G. Rita Farida Yunus, N. Nadeeshani, J. Paul Chen, Electrochemical decoloration of synthetic wastewater containing Rhodamine 6G: behaviors and mechanism, Ind. Eng. Chem. Res. 51 (2012) 5953–5960, http://dx.doi.org/10.1021/ie2019273.
[23] T.L. Marina, S. Valter, V.B. Edilson, M.H.C. Tania, O.R. Guilherme de, R.G. Marcia, Synthesis of ORMOSIL silica/rhodamine 6G: powders and compacts, J. Non-Cryst. Solids 353 (2007) 24–30.
[24] S.K. Tripathi, Alka Monga, G.S.S. Saini, Characterization of thermally evaporated thin films of Rhodamine 6G, Smart Mater. Struct. 18 (2009) 125012.
[25] A.M. Brouwer, Standards for photoluminescence quantum yield measurements in solution, Pure Appl. Chem. 83 (12) (2011) 2213–2228.

IOP Publishing | Astro Ltd
Laser Physics Letters
Laser Phys. Lett. 11 (2014) 055108 (5pp)
doi:10.1088/1612-2011/11/5/055108

Letters

Random lasing with enhanced photostability of silver nanoparticle doped polymer optical fiber laser

S Sebastian, C L Linslal, C P G Vallabhan, V P N Nampoori, P Radhakrishnan and M Kailasnath

International School of Photonics, Cochin University of Science and Technology, Cochin-682022, India.

E-mail: sunikutty@gmail.com

Received 5 November 2013, revised 6 March 2014
Accepted for publication 7 March 2014
Published 9 April 2014

Abstract

We report on the realization of a silver (Ag) nanoparticle doped polymer optical fiber random laser. Lasing characteristics and photostability of the system with varying concentration of Ag nanoparticles have been investigated. It was found that there is an enhanced spectral narrowing and emission intensity in rhodamine 6G–Ag nanoparticle doped polymer optical fiber compared to that of bare rhodamine 6G doped polymer optical fiber. In contrast with the latter, low-threshold coherent feedback random lasing with improved photostability was observed for an optimum concentration of Ag nanoparticles in the gain medium.

Keywords: coherent feedback random lasing, Ag nanoparticles, rhodamine 6G, polymer optical fibers

(Some figures may appear in colour only in the online journal)

1. Introduction

Polymer optical fibers (POFs) will be able to replace silica fibers in local area networks in the near future because of their large diameter as compared to silica fibers, good ductility, low cost, and large numerical aperture that enables easy coupling required by local area networks. Progress in this field of POF can be attributed to factors such as development of new polymers with lower loss compared with the present polymers and emergence of low-threshold lasers and efficient amplifiers with improved photostability [1]. Currently, with the introduction of low-loss perfluorinated polymers for the core of POF, the problem regarding the loss in POF has been reduced to a large extent [2]. Since the implementation of polymeric lasers incorporating organic dyes in the late 1960s [3], polymer lasers and amplifiers incorporating dyes have been widely studied [4–11].

Success in the field of nanotechnology has led to the incorporation of nanoparticles, especially metal nanoparticles, into organic dyes such as rhodamine 6G (Rh6G) for various applications, such as enhancing the emission intensity of the dye [12–14]. Among metal nanoparticles, silver (Ag) nanoparticles have advantages such as extremely high field enhancement, which makes them useful in radiative decay engineering [15]. Depending on the distance of separation between the nanoparticle and the dye molecule, either fluorescence enhancement or quenching is possible. The surface plasmon of the nanoparticles excited under photon absorption influence the emission from the dye molecule in such a way that the radiative relaxation rate is increased, leading to enhanced emission when the nanoparticle is within the distance of a few nanometers with respect to the dye molecule [16]. Recently, random lasing phenomena from Rh6G in liquid suspension and polymer films in the presence of Ag nanoparticles have been reported because the latter can act as a potential candidate for the same [16–19]. Metal nanoparticles play a prominent role in random lasing, either through their

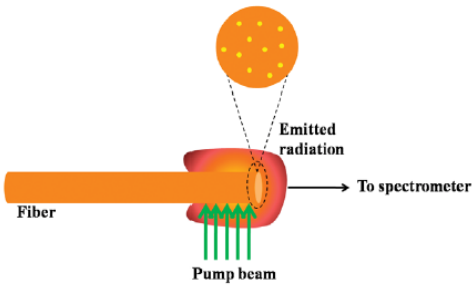

Figure 1. Schematic representation of the measurement set-up of transverse excitation and emission from the fiber. Enlarged view shows the cross-section of the fiber containing rhodamine 6G (Rh6G) and silver (Ag) nanoparticles.

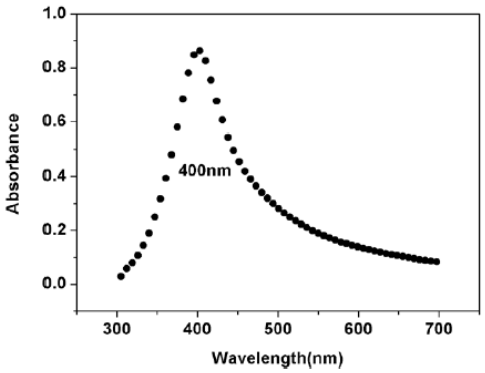

Figure 2. Absorption spectrum of silver (Ag) nanoparticles produced by laser ablation in ethanol. Surface plasmon resonance (SPR) peaks at 400 nm.

large scattering cross-section (σ_s) as compared to dielectric nanoparticles of the same dimensions or through their surface plasmon resonance (SPR) property [17]. Depending on the type of feedback provided by the nanoparticles, random lasers can be categorized into coherent and incoherent feedback random lasers. Coherent feedback random lasers are characterized by the appearance of several sharp laser spikes of sub-nanometer bandwidths, whereas incoherent feedback random lasers have a single narrow peak in the emission spectrum with a bandwidth of approximately 4 or 5 nm [20].

In the present work, we demonstrate coherent feedback random lasing from Rh6G–Ag nanoparticle doped POF. Ag nanoparticles produced by the technique of pulsed laser ablation in liquid (PLAL) using the Nd-YAG laser is incorporated into methyl methacrylate solution containing Rh6G as the active medium. The solution produced is polymerized into preforms and drawn to obtain POF containing Rh6G–Ag nanoparticles. Lasing characteristics and photostability are investigated in fibers containing different concentrations of Ag nanoparticles at a constant concentration of Rh6G.

2. Methods

Among the various techniques available for the preparation of Ag nanoparticles, the PLAL technique produces pure and agglomeration-free nanoparticles in a host medium [21–23]. In the present case, Ag nanoparticles were prepared using PLAL with ethanol as the liquid medium. Ethanol was chosen because Ag nanoparticles find poor stability in methyl methacrylate, which is the monomer candidate for preparing poly methyl methacrylate (PMMA) matrix in the form of fiber or film. The Nd-YAG laser with a pulse width of 9 ns and a repetition rate of 10 Hz operating at the fundamental wavelength was used as the source for ablation. A fine silver plate (999 purity) with thickness of 1.1 mm and an area of $2.3 \times 1.5\,\mathrm{cm}^2$ was chosen as the target. A biconvex lens with focal length of 100 mm was used to focus the laser beam on the target. Fluence at the laser–target interface was calculated to be $10^3\,\mathrm{J\,cm}^{-2}$. A beaker containing 10 ml ethanol and the silver target was placed at the focus of the lens for 30 min. Weight of the target plate before and after laser ablation was noted to obtain the concentration of Ag nanoparticles produced in ethanol. Spectral absorption of Ag nanoparticles formed was analyzed using Jasco UV-ViS NIR spectrophotometer. Size of the nanoparticles was calculated using the image obtained from 200 kV high-resolution transmission electron microscopy (model JEM2100).

Methyl methacrylate (purchased from Sigma Aldrich) was purified to remove the inhibitors using the conventional purification method [6]. Rh6G (purchased from Acros, USA) was dissolved in methyl methacrylate to get a concentration of $4 \times 10^{-5}\,\mathrm{mol\,L}^{-1}$. In each of the samples, the concentration of Rh6G was fixed and only the concentration of Ag nanoparticles varied. Samples were designated as R1, R2, R3 and R4, with R1 containing Rh6G only, R2 containing $9 \times 10^{-6}\,\mathrm{mol\,L}^{-1}$, R3 containing $1.5 \times 10^{-6}\,\mathrm{mol\,L}^{-1}$, and R4 containing $4.5 \times 10^{-7}\,\mathrm{mol\,L}^{-1}$ Ag nanoparticles. Samples R1, R2, R3 and R4 were polymerized into cylindrical rods by adding appropriate quantities of initiator and chain transfer agent. The samples in 15 ml test tubes were kept in a constant temperature oil bath at 90°C for 1 h and at 70°C for 72 h. The cylindrical rods with diameters of 10 mm were then drawn into step index multimode POF containing Rh6G and Ag nanoparticles with varying diameters using the conventional POF drawing tower.

Photostability of the fibers taken from all the four sets (R1, R2, R3 and R4) was measured using a frequency-doubled Q-switched Nd-YAG laser operating at a repetition rate of 10 Hz with a pulse duration of 9 ns. Laser pulses were focused onto the fiber with diameter of 400 μm and length of 60 mm using a biconvex lens with focal length of 150 mm. Spectral emission from one of the ends of the fiber pumped transversely was recorded using a spectrophotometer. The distance between the focusing point in the fiber and collecting end of the spectrometer was always kept constant at 35 mm.

Laser-induced spectral emission including amplified spontaneous emission (ASE) and lasing were investigated for the fibers of the same dimension as mentioned. Schematic representation of the measurement set-up is shown in figure 1.

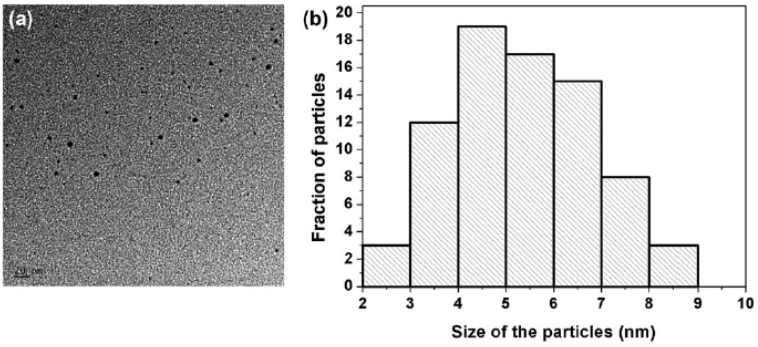

Figure 3. *(a)* Transmission electron microscopy image of silver (Ag) nanoparticles in ethanol formed by laser ablation using a Nd-YAG laser at the fundamental wavelength. *(b)* Number of nanoparticles formed versus size of the particles. Average size was found to be 5 nm.

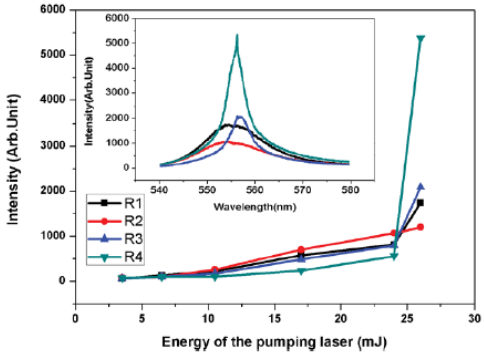

Figure 4. Laser-induced emission from the fibers as a function of pump energy. The inset shows the output intensity versus wavelength graph of all fibers R1, R2, R3 and R4 pumped at energy of 26 mJ.

The pump laser was focused in the form of a 3 mm-long stripe along the length of the fiber using a cylindrical lens with focal length of 150 mm. The fiber was kept at a distance of approximately 1 mm away from the focus to prevent damage to the fiber that could be caused by high-output power density from the pump laser. Spectral emission from the fiber was collected from one of the ends by using a collecting fiber connected to a charged coupled device (CCD) based spectrometer with a resolution of 0.03 nm.

3. Result and discussions

Thirty minutes of ablation of Ag plate in ethanol generated Ag nanoparticles with 4.6×10^{-4} mol L^{-1} concentration. The SPR spectrum recorded for the nanoparticles is shown in figure 2. The nanoparticles were found to be stable without any capping agents in ethanol for weeks.

Size and shape of the Ag nanoparticles formed in the solution using PLAL were obtained from the transmission electron microscopy image shown in figure 3(*a*). Figure 3(*b*) shows the number of nanoparticles formed compared with sizes of the particles. The nanoparticles produced were spherical, with an average size of 5 nm (figure 3).

Spectral emission characteristics of the four samples in the form of fibers were analyzed using the emission spectra provided in figure 4. Figure 4 indicates that when the pump energy reached 26 mJ, a three-fold enhancement in the emission intensity was observed for R4, whereas R2 showed a slight quenching and R3 showed a slight enhancement as compared with R1. For R4, the distance between the dye molecules and the Ag nanoparticles in the polymer matrix is in such a way that maximum spectral emission from the dye is obtained due to the increase in intensity of the local incident field on the dye by the SPR of the Ag nanoparticles [16, 24]. Increasing the concentration above that of R2 resulted in quenching of the emission of the gain medium; it was expected that when the concentration of the nanoparticles in the gain medium was high, the nanoparticle would be in close proximity with respect to the dye and thus would result in quenching. Also, decreasing the concentration above that of R4 resulted in no change in the emission intensity as compared with that of R4. The substantial increase in intensity for R4 when pumped above 24 mJ confirmed the threshold phenomena associated with lasing, indicating the lower threshold lasing capability of Rh6G doped POF in the presence of an optimum concentration of Ag nanoparticles. The inset of figure 4 shows the output intensities of all fibers at pump energy of 26 mJ, and the ASE process can be clearly seen in the case of sample R4.

Figure 5 depicts the line width of the emission of all fibers as a function of pump energy of the laser. At the minimum pump energy, all the fibers showed a broad emission band with a line width of approximately 24 nm. With an increase in pump energy, R3 and R4 showed a spectral narrowing up to 5 nm and 4 nm, respectively, whereas R1 and R2 showed no spectral narrowing at this power. With a further increase in

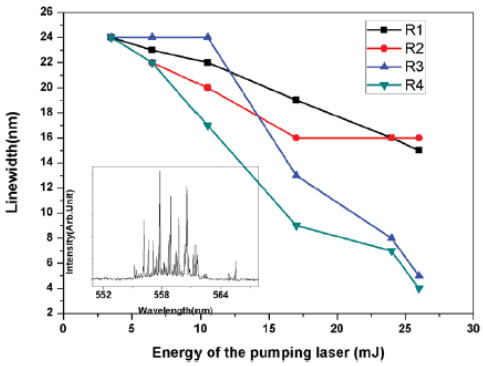

Figure 5. Emission line width versus pump energy of laser for fiber samples R1, R2, R3 and R4. The inset shows the coherent feedback random lasing from R4 at pump energy of 28 mJ.

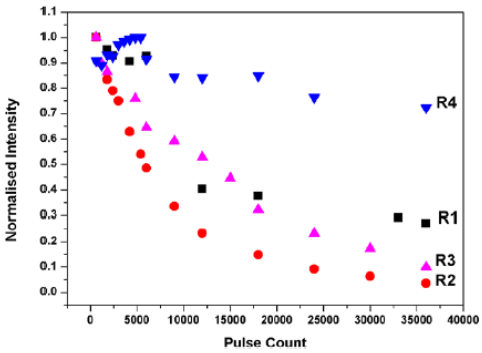

Figure 6. Photostability curves of pure rhodamine 6G (Rh6G) doped polymer optical fiber (POF) (R1) and Rh6G–Ag nanoparticle doped POF (R2, R3, and R4).

the pump power, all samples except R4 were photobleached; however, R4 continued to show lasing (inset of figure 5). The line width of the peaks was approximately 0.06 nm. The sharp and narrow peaks appearing in R4 were apparently attributable to coherent feedback random lasing, which is characterized by the appearance of several sharp peaks with sub-nanometer bandwidth [19]. Here, the random lasing behavior of Ag nanoparticles in Rh6G doped POF was attributable to localized SPR of Ag nanoparticles at 400 nm spatially confining the electric field of the pumping light near the particle surface so that it provided high gain for lasing action. For a particle, the extinction cross-section is provided as the sum of the absorption cross-section and the scattering cross-section. For nanoparticles with small diameters, as in this case (5 nm), the scattering cross-section, and therefore the scattering strength, were so small that the lasing peaks were attributable to the highly localized optical modes caused by plasmon resonance on the surface of Ag nanoparticles [17]. In contrast, R1 and R2 did not show ASE, whereas R3 showed ASE but no sharp peaks. This implies that the presence of an optimum concentration of Ag nanoparticles is crucial for random lasing from the fiber.

POFs obtained from all four sets (R1, R2, R3, R4) were also subjected to photostability measurements. As seen in figure 6, R1, which is taken as the reference, withstood photobleaching up to 6000 pulses at energy of 26 mJ; thereafter, it exhibited photobleaching. However, for samples R2 and R3, the rate of photobleaching was high and followed an exponential decay in the output intensity. Interestingly, it was found that for sample R4, the damage threshold for photobleaching was so high that it showed a stability even up to 36 000 pulses, at which point the reference R1 itself reaches its half-life. For R4, because of the maximum lightening rod effect, which is attributable to the fluorescence enhancement by metal nanoparticles, an increase in radiative decay rate was expected that would enhance the fraction of photons observed from every emitting fluorophore with reduced lifetime, which would reduce the probability of bleaching and result in a consequent increase in the photostability of the sample [24, 25]. Also, the nanoparticles provided an encapsulation effect for the dye, which may be another factor contributing to the enhanced stability.

4. Conclusions

To summarize, we have successfully incorporated Ag nanoparticles prepared by the PLAL technique with an average diameter of 5 nm into POF with Rh6G as the gain medium. When pumped at the threshold, a spectral narrowing from 16 nm to 4 nm was observed for Rh6G doped POFs with optimum concentration of Ag nanoparticles. Also, a three-fold enhancement in the emission intensity of the dye in the fiber was seen along with coherent feedback random lasing for optimum concentration of Ag nanoparticles in the gain medium because of the strong excitement of the dye molecule by the electric field confined around the Ag nanoparticles through localized SPR. Rh6G doped POFs that show no signs of lasing under the present conditions begin to lase randomly in the presence of Ag nanoparticles at an optimum concentration. This implies that the threshold for laser action can be brought down in the presence of Ag nanoparticles. It has been found that with an optimum concentration of Ag nanoparticles in the gain media, the fiber showed enhanced photostability compared to bare Rh6G doped POF because of the combined effect of increased radiative decay rate, reduced lifetime, and encapsulation of dye by the nanoparticles. The approach adopted here is promising because this is the first time, to our knowledge, that lowering of lasing threshold in Rh6G doped POF in the presence of Ag nanoparticles through coherent feedback random lasing has been reported.

Acknowledgments

The authors thank University Grants Commission-Research Fellowship in Sciences for meritorious Students and Department of Science and Technology for financial assistance and Centre for Nanoscience and Nanotechnology at Mahatma Gandhi University for providing the facility for transmission

electron microscopy analysis. The authors thank Dr Thomas S Lee (Tech Mahindra, Banglore), Dr Jyotsna (Akzo Nobel, Banglore), Ms. Indu Sebastian, Mr Arun (Cypress, Banglore), and Professor K. C. Sebastian for their great support.

References

[1] Zhang Q J, Wang P, Sun X F, Zhai Y, Dai P, Yang B, Hai M and Xie J P1998 Amplified spontaneous emission of an Nd31-doped poly(methyl methacrylate) optical fiber at ambient temperature *Appl. Phys. Lett.* **72** 407
[2] Tafur Monroy I *et al* 2003 *Opt. Fiber Technol.* **9** 159–71
[3] Singha S, Kanetkar V R, Sridhara G, Muthuswamy V and Raja K 2003 Solid-state polymeric dye lasers *J. Lumin.* **101** 285–91
[4] Somasundaram G and Ramalingam A 1999 Gain studies of coumarin 307 dye doped polymer laser *Opt. Laser Technol.* **31** 351–8
[5] Balslev S, Mironov A, Nilsson D and Kristensen A 2006 Micro-fabricated single mode polymer dye laser *Opt. Express* **14** 2170
[6] Sheeba M, Thomas K J, Rajesh M, Nampoori V P N, Vallabhan C P G and Radhakrishnan P 2007 Multimode laser emission from dye doped polymer optical fiber *Appl. Opt.* **46** 8089
[7] Geetha K, Rajesh M, Nampoori V P N, Vallabhan C P G and Radhakrishnan P 2006 Laser emission from transversely pumped dye-doped free-standing polymer film *J. Opt. A: Pure Appl. Opt.* **8** 189–93
[8] Linslal C L, Mathew S, Radhakrishnan P, Nampoori V P N, Girijavallabhan C P and Kailasnath M 2013 Laser emission from the whispering gallery modes of a graded index fiber *Opt. Lett.* **38** 3261
[9] Peng G D, Chu P K, Xiong Z, Whitebread T and Chaplin R P 1996 Dye doped step index polymer optical floor for broad band optical amplification *J. Light. Technol.* **14** 2215–23
[10] Tagaya A, Koike Y, Kinoshita T, Nihei E, Yamamoto T and Sasaki K 1993 Polymer optical fiber amplifier *Appl. Phys. Lett.* **63** 883–4
[11] Sheeba M R, Geetha K, Vallabhan C P G, Radhakrishnan P and Nampoori V P N 2007 Fabrication and characterization of dye doped polymer optical fiber as a light amplifier *Appl. Opt.* **46** 106–12
[12] Kang K A, Wang J, Jasinski J B and Achilefu S 2011 Fluorescence manipulation by gold nanoparticles: from complete quenching to extensive enhancement *J. Nanobiotechnol.* **9** 16
[13] Liu G, Zheng H, Liu M, Zhang Z, Dong J, Yan X and Li X 2011 Surface-enhanced fluorescence of rhodamine 6G on the assembled silver nanostructures *J. Nanosci. Nanotechnol.* **11** 9523–7
[14] Dong L, Ye F, Chughtai A, Liuolia V, Popov S, Friberg A T and Muhammed M 2012 Lasing from water solution of rhodamine 6G/gold nanoparticles: impact of SiO2-coating on metal surface *IEEE J. Quantum Electron.* **48** 1220
[15] Carol C, Castillo P M, Klippstein R, Pozo D, Zaderenko A P 2010 Silver nanoparticles: sensing and imaging applications (chapter 11) www.intechopen.com/books/siver-nanoparticles
[16] Dominguez C T, Maltez R L, dos Reis R M S, de Melo L S A, de Araújo C B and Gomes A S L 2011 Dependence of random laser emission on silver nanoparticle density in PMMA films containing rhodamine 6G *J. Opt. Soc. Am.* B **28** 1118
[17] Meng X, Fujita K, Zong Y, Murai S and Tanaka K 2008 Random lasers with coherent feedback from highly transparent polymer films embedded with silver nanoparticles *Appl. Phys. Lett.* **92** 201112
[18] Meng X, Fujita K, Murai S and Tanaka K 2009 Coherent random lasers in weakly scattering polymer films containing silver nanoparticles *Phys. Rev.* A **79** 053817
[19] Sun Y, Wang Z, Shi X, Wang Y, Zhao X, Chen S, Shi J, Zhou J and Liu D 2013 Coherent plasmonic random laser pumped by nanosecond pulses far from the resonance peak of silver nanowires *J. Opt. Soc. Am.* B **30** 2523
[20] Dice G D, Mujumdar S and Elezzabi A Y 2005 Plasmonically enhanced diffusive and subdiffusive metal nanoparticle-dye random laser *Appl. Phys. Lett.* **86** 131105
[21] Barcikowski S, Menéndez-Manjón A, Chichkov B, Brikas M and Račiukaitis G 2007 Generation of nanoparticle colloids by picosecond and femtosecond laser ablations in liquid flow *Appl. Phys. Lett.* **91** 083113
[22] Schwenke A, Wagener P, Nolte S and Barcikowski S 2011 Influence of processing time on nanoparticle generation during picosecond-pulsed fundamental and second harmonic laser ablation of metals in tetrahydrofuran *Appl. Phys.* A **104** 77–82
[23] Hahn A, Barcikowski S and Chichkov B N 2008 Influences on nanoparticle production during pulsed laser ablation *J. Laser Micro/Nanoeng.* **3** 73
[24] Geddes C D and Lakowicz J R 2002 Metal-enhanced fluorescence *J. Fluoresc.* **12** 121
[25] Imhof A, Megens M, Engelberts J J, de Lang D T N, Sprik R and Vos W L 1999 Spectroscopy of fluorescein (FITC) dyed colloidal silica spheres *J. Phys. Chem.* B **103** 1408–15

Applied Surface Science 320 (2014) 732–735

Contents lists available at ScienceDirect

Applied Surface Science

journal homepage: www.elsevier.com/locate/apsusc

Laser induced augmentation of silver nanospheres to nanowires in ethanol fostered by Poly Vinyl Pyrrolidone

Suneetha Sebastian*, C.L. Linslal, C.P.G. Vallabhan, V.P.N. Nampoori, P. Radhakrishnan, M. Kailasnath

International School of Photonics, Cochin University of Science and Technology, Cochin 22, India

ARTICLE INFO

Article history:
Received 15 April 2014
Received in revised form
25 September 2014
Accepted 25 September 2014
Available online 5 October 2014

Keywords:
Laser ablation
Silver nanospheres
Silver nanowire

ABSTRACT

Stable uniform silver nanospheres having an average diameter of 45 nm are synthesised in ethanol containing Poly Vinyl Pyrrolidone using Laser Ablation in Liquid technique. Further irradiation of the nanocolloidal solution by focussed laser beam produced stable well defined silver nanowires through ripening mechanism fostered by the presence of Poly Vinyl Pyrrolidone. Confirmation of the mechanism is obtained from Transmission Electron Microscopic images of the nanocolloidal solution irradiated for different time durations.

1. Introduction

The size and shape dependent properties of metal nanoparticles make them suitable for applications like Surface Enhanced Raman Scattering (SERS) [1,2], Radiative Decay Engineering [3–5] and sensors [6]. Among various metal nanoparticles like silver (Ag), gold, platinum and copper, Ag nanoparticles have the highest Surface Plasmon (SP) strength across the UV–vis–IR spectrum [7] which in turn depends on size and various shapes of nanostructures like nanospheres, nanowires and nanoprisms [8,9]. The strength of electric field caused by SP is much higher at the corners of anisotropic shaped nanostructures such as nanowires than on the surface of isotropic shaped structures such as nanospheres [10] and so its synthesis is very promising for tremendous practical plasmonic applications.

Various methods are available for the synthesis of Ag nanowires such as chemical or electrochemical reduction methods [11–13]. Among the different chemical reduction routes, polyol process is the most popular nowadays for the mass production of uniform nanowires [14–18]. Apart from the polyol process, another promising method for the synthesis of anisotropic silver nanostructures is photo irradiation using laser source [19–24]. The method offers simple and reagent free preparation of anisotropic Ag nanostructures such as nanowires and nanobelts. In these reports laser radiations are focussed onto already prepared nanocolloidal solution in which the nanoparticles are synthesised either by chemical route or by Laser Ablation in Liquid (LAL) technique. It is also reported that a simpler synthesis of nanostructures is possible by replacing the chemical route of preparation of colloidal Ag nanoparticle solution by LAL technique. T. Tsuji et al. in their work of formation of nanoclusters in Poly Vinyl Pyrrolidone (PVP) aqueous solution of colloidal silver nanoparticles, prepared by laser ablation, [10] reported ripening mechanism as one of the plausible mechanism behind the formation of nanocrystals by laser irradiation. They also suggest that the interaction between protective reagents like PVP and silver nanoatoms plays a crucial role in fostering the ripening mechanism. Also Zamiri et al. [21] demonstrated the formation of silver microbelts in ethanol by laser irradiation. They suggested that the tendency of nanoparticles to aggregate in ethanol before irradiation is one of the possibilities of the formation of nanostructures. But the previous reports lack the formation of well defined nanowires and also some of them reported various nanostructures like nanoprisms and nanorods together in the same sample solution which may demote its use in practical applications.

In the present work we report on the formation of well defined nanowires by laser induced irradiation of already prepared Ag nanocolloidal solution containing nanospheres. Stability of the nanocolloidal solution is provided by Poly Vinyl Pyrrolidone (PVP) which also fosters the transformation of nanospheres to nanowires. The work is of utmost interest since this can lead to a simple preparation method of well defined nanowires using photo irradiation technique.

* Corresponding author. Tel.: +91 9745271291.
E-mail address: sunikutty@gmail.com (S. Sebastian).

http://dx.doi.org/10.1016/j.apsusc.2014.09.163
0169-4332/

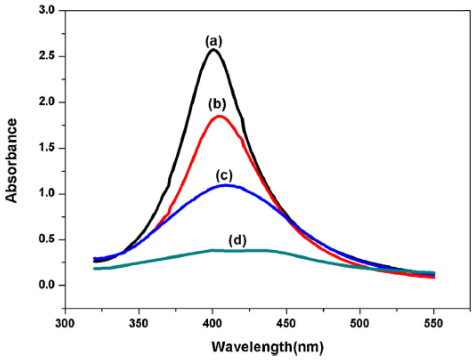

Fig. 1. Plasmon absorption band of Ag nanocolloids (a) generated by laser ablation at the fundamental wavelength from Nd-YAG laser in ethanol stabilised by PVP, (b) nanocolloids irradiated by 532 nm for 45 min, (c) irradiated for 9 h and (d) irradiated for 18 h.

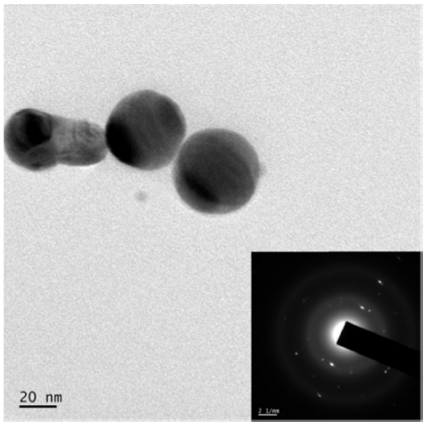

Fig. 2. TEM image of Ag nanoparticles produced in ethanol containing 6 mM PVP by Laser Ablation. Inset shows the SAED pattern of the nanoparticles.

2. Experimental

Schematic of LAL technique is same as that described elsewhere [25,26]. Nd-YAG laser having 9 ns pulse width and 10 Hz repetition rate with a spot size of 7 mm, operating at the fundamental wavelength i.e. 1064 nm is used as the source of laser ablation. Fluence of the laser pulses, after focussing with a convex lens of 100 mm focal length, at the target is calculated to be 10^3 J/cm^2. 6 mol/l concentration of PVP having a molecular weight of 10,000 dissolved in ethanol is chosen as the medium for ablation. The concentration of PVP in ethanol is optimised to 6 mol/l since it is already reported that at this molarity the viscosity which affects Transmission Electron Microscopy (TEM) analysis and the stability of Ag nanocolloids in aqueous solution are fairly maintained [10]. Silver plate of 99.99% purity (purchased from Sigma–Aldrich) which acts as the target is immersed in 30 ml of the solution for ablation. Ablation is carried out for 20 min and the weight of the silver plate is noted before and after ablation to get the molarity of the colloidal solution and is found to be 2.5×10^{-4} mol/l. 20 ml of the colloidal solution is taken in a 30 ml sample bottle and the solution is then irradiated by focussing frequency doubled i.e. 532 nm laser pulses with an energy density of 10^3 J/cm^2. The nanocolloidal solutions are analysed after fixed time durations for clearly monitoring and understanding the underlying mechanism of the formation of nanowires. Absorption spectra of the colloidal solution is recorded using Jasco UV–vis NIR Spectrophotometer and TEM images are taken using 200 kV High Resolution Transmission Electron Microscopy (Model: JEM2100).

3. Results and discussions

Nanocolloids formed in ethanol are unstable and leads to agglomeration of the particles due to dipole–dipole interaction between them [27]. PVP which acts as a suitable stabiliser can improve the formation efficiency and stability of Ag nanocolloids in the solution [28]. The SP band of stable Ag nanocolloids is depicted in Fig. 1. The plasmon absorption band peaks at 400 nm due to out of plane dipole resonance of Ag nanocolloids and the full width at half maximum of the spectrum is around 57 nm. The nanocolloids so formed in ethanolic solution of PVP by laser ablation are found to be spherical with an average diameter of 45 nm and is shown in Fig. 2. The inset of Fig. 2 shows the Selected Area Electron Diffraction (SAED) pattern of Ag nanocolloids and suggests the single crystalline nature of them. Ag nanoparticles have a face centred cubic (fcc) crystallographic structure [20].

Sample solution is subjected to focussed laser radiations at 532 nm since the irradiation can cause structural modifications of the nanoparticles. For effective structural modification of the nanoparticles, it should absorb the incoming radiations. Ag nanoparticles respond effectively to 355 nm and 532 nm since the efficiency of self absorption is high at these wavelength as compared to 1064 nm [29]. After 45 min of irradiation, we observed a change in colour of the colloidal solution from light yellow to a darker one and the corresponding absorption spectrum is given in Fig. 1. A decrease in the absorption band intensity is observed with no appreciable shift (a shift of 5 nm) in the Surface Plasmon Resonance (SPR) peak. Also no new SPR peaks are noticed in the spectrum. Fig. 3 shows the TEM image of the colloidal solution after 45 min of irradiation. From the figure we can see the fragments of Ag nanocolloids having an average size of 4 nm. Almost all of

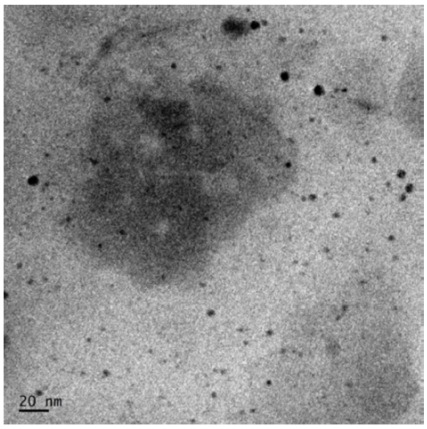

Fig. 3. TEM image of nanocolloids irradiated for 45 min by laser pulses.

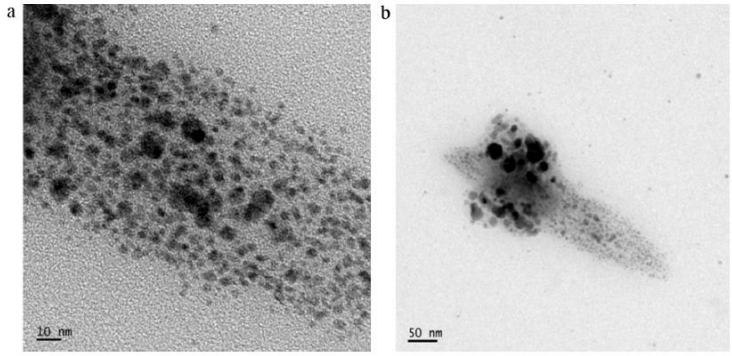

Fig. 4. TEM image of Ag nanoparticles irradiated by laser pulses for 9 h. (a) Assembly of unstable nanoparticles via laser radiation. (b) Enlarged view of the association of nanoparticles to form stable structures.

the larger nanoparticles are fragmented into smaller ones. Takeshi et al. reported [10] that stability of nanoparticles depends on size i.e. smaller the size, lesser is the stability. So the unstable atoms in such unstable nanoparticles move from one nanoparticle to another promoted via laser irradiation and it results in the formation of nanoparticles with stable shapes and sizes. This process of formation is known as ripening mechanism. From the TEM images of the colloidal solution irradiated for 9 h given in Fig. 4(a) and (b) we can see the process involved in ripening mechanism. The fragmented particles of size in the range of 1–4 nm assemble together to form more stable shapes such as nanorod like structure having an average width of 160 nm. The corresponding absorption spectrum of Ag nanocolloids is shown in Fig. 1. It is seen that the intensity of absorbance is reduced to greater than 50% and the FWHM is increased twice as compared with the non-irradiated sample with no obvious shift in the SPR peak.

Further irradiation of the sample brought down the plasmon absorption to nearly 4% and the FWHM is 170 nm which is thrice that of the non-irradiated sample as is shown in Fig. 1. Well defined Ag nanowire can be seen in the corresponding TEM image given in Fig. 5 with an average diameter of 160 nm and a length of 8.7 μm (average aspect ratio of 54). Inset is the aspect ratio distribution of Ag nanowires formed due to laser irradiation and the average aspect ratio is found to be around 50. However, because of the restriction in the crystallographic faces induced by PVP for the formation of nanowires from nanostructures, only a few percentage of nanorod like structures is converted to nanowire. The darker region around the nanowires indicates the presence of PVP around them and the inset of Fig. 5(b) shows that the nanowires so formed are polycrystalline. It is inferred that these nanowires are formed through ripening mechanism promoted by the presence of PVP in the solution. The interaction strength of atoms lying on different crystallographic facets is different for various capping agents such as PVP. Yugang Sun et al. experimentally demonstrated that PVP which is a polymeric capping agent interacts more effectively with the {1 0 0} facets of the nanowires rather than {1 1 1} facets [15]. Thus the Ag nanorod like structure having an average width of 160 nm formed via ripening mechanism when irradiated for 9 h ends up as nanowires having the same width since the PVP in the ethanolic solution masks the surface of the nanorod like structures ({1 1 1} facets) and allows the ends ({1 0 0} facets) of them to readily react with unstable Ag atoms in the unstable Ag nanoparticles to form nanowires. The colour of the sample changed from yellow to greenish yellow as shown in Fig. 6. This work supports the

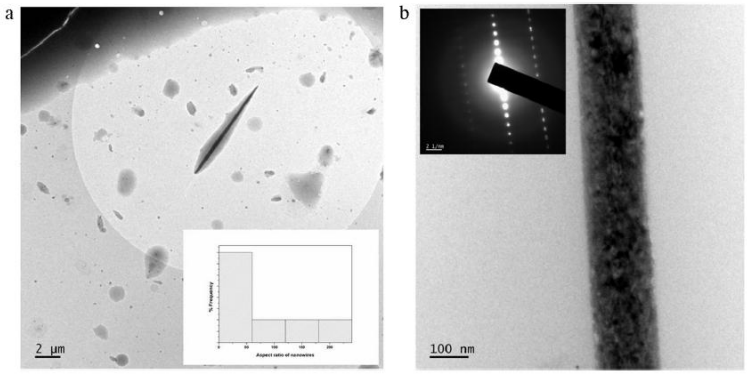

Fig. 5. TEM images of Ag nanocolloids irradiated for 18 h. (a) Ag nanowires formed through ripening mechanism. Inset shows the aspect ratio distribution of nanowires (b) cross section of the nanowires and the inset is the SAED pattern of the nanowires.

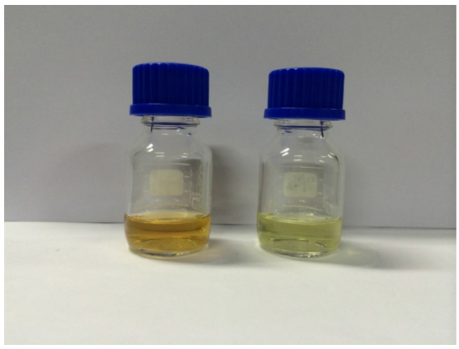

Fig. 6. Photograph of the Ag colloidal solution before and after irradiation. 18 h of irradiation changed the colour from yellow to a pale green colour.

plausible mechanism behind the formation of Ag nanowires suggested by Tsuji et al. [10].

4. Conclusions

We have conducted laser mediated augmentation of silver nanospheres, formed by laser ablation in alcoholic (ethyl alcohol) solution of PVP, to well defined silver nanowires. Periodic monitoring during the irradiation reveals the various steps involved in the process of nanowire formation namely fragmentation of larger particles to smaller ones when irradiated for 45 min, formation of nanorod like structure through ripening mechanism when irradiation is continued for 9 h and finally PVP assisted nanowire formation when irradiated for 18 h. The work is unique since it is the first such report on the formation of well defined nanowire through laser irradiation of colloidal solution of silver nanospheres formed by laser ablation.

Acknowledgment

First author would like to thank UGC-RFSMS and DST for the financial assistance and Centre for Nanoscience and Nanotechnology, M G University for providing the facility for TEM analysis. The author also thanks Dr. Thomas Lee S, Dr. Jyotsna Ravi, Prof. K.C. Sebastian and Mr. Arun (Cypress Semiconductors India) for their constant support and encouragement.

References

[1] P. Šimakova, J. Gautier, M. Prochazka, K. Herve-Aubert, I. Chourpa, Polyethylene-glycol-stabilized Ag nanoparticles for Surface Enhanced Raman Scattering spectroscopy: Ag surface accessibility studied using metalation of free-base Porphyrins, J. Phys. Chem. C 118 (2014) 7690–7697.
[2] S. Lin, W. Zhu, Y. Jin, K.B. Crozier, Surface-Enhanced Raman Scattering with Ag nanoparticles optically trapped by a photonic crystal cavity, Nano Lett. 13 (2013) 559–563.
[3] J. Dong, H. Zheng, X. Li, X. Yan, Y. Sun, Z. Zhang, Surface-enhanced fluorescence from silver fractal like nanostructures decorated with silver nanoparticles, Appl. Opt. 50 (November (31)) (2011).
[4] J. Dong, S. Qu, Z. Zhang, M. Liu, G. Liu, et al., Surface enhanced fluorescence on three dimensional silver nanostructure substrate, J. Appl. Phys. 111 (2012) 093101.
[5] A. Ianoul, A. Bergeron, Spatially inhomogeneous enhancement of fluorescence by a monolayer of silver nanoparticles, Langmuir 22 (2006) 10217–10222.
[6] J. Rohab, H.N. Umha, H.K. Sunga, B.-C. Leec, Y. Kima, Repression of photomediated morphological changes of silver nanoplates, Colloids Surf. A: Physicochem. Eng. Aspects 415 (2012) 449–453.
[7] M. Rycenga, C.M. Cobley, J. Zeng, W. Li, C.H. Moran, Q. Zhang, D. Qin, Y. Xia, Controlling the synthesis and assembly of silver nanostructures for plasmonic applications, Chem. Rev. 111 (2011) 3669–3712.
[8] J. Sancho-Parramon, Surface plasmon resonance broadening of metallic particles in the quasi-static approximation: a numerical study of size confinement and interparticle interaction effects, Nanotechnology 20 (2009) 235706, 7 pp.
[9] A. Machulek Jr., H.P. Moisés de Oliveira, M.H. Gehlen, Preparation of silver nanoprisms using poly(*N*-vinyl-2-pyrrolidone) as a colloid-stabilizing agent and the effect of silver nanoparticles on the photophysical properties of cationic dyes, Photochem. Photobiol. Sci. 2 (2003) 921–925.
[10] T. Tsuji, T. Mizukib, S. Ozono, M. Tsuji, Laser-induced silver nanocrystal formation in polyvinylpyrrolidone solutions, J. Photochem. Photobiol. A: Chem. 206 (2009) 134–139.
[11] N.R. Jana, L. Gearheart, C.J. Murphy, Wet chemical synthesis of silver nanorods and nanowires of controllable aspect ratio, Chem. Commun. (2001) 617–618.
[12] C.J. Murphy, T.K. Sau, A. Gole, C.J. Orendorff, Surfactant-directed synthesis and optical properties of one-dimensional plasmonic metallic nanostructures, MRS Bull. 30 (May) (2005).
[13] J. Zhang, X. Wang, X. Peng, L. Zhang, Fabrication, morphology and structural characterization of ordered single-crystal Ag nanowires, Appl. Phys. A 75 (2002) 485–488.
[14] Y. Sun, B. Gates, B. Mayers, Y. Xia, Crystalline silver nanowires by soft solution processing, Nano Lett. 2 (2) (2002).
[15] Y. Sun, B. Mayers, T. Herricks, Y. Xia, Polyol synthesis of uniform silver nanowires: a plausible growth mechanism and the supporting evidence, Nano Lett. 3 (7) (2003).
[16] G. Yan, L. Wang, L. Zhang, Recent research progress on preparation of silver nanowires by soft solution method. preparation of gold nanotubes and Pt nanotubes from resultant silver nanowires and their applications in conductive adhesive, Rev. Adv. Mater. Sci. 24 (2010) 10–25.
[17] X. Tang, M. Tsuji, Syntheses of Silver Nanowires in Liquid Phase, Nanowires Science and Technology, 2010 (Chapter 2).
[18] B. Wiley, Y. Sun, Y. Xia, Synthesis of silver nanostructures with controlled shapes and properties, Acc. Chem. Res. 40 (2007) 1067–1076.
[19] T. Tsujia, N. Watanabeb, M. Tsuji, Laser induced morphology change of silver colloids: formation of nano-size wires, Appl. Surf. Sci. 211 (2003) 189–193.
[20] T. Tsuji, Y. Okazaki, T. Higuchi, M. Tsuji, Laser-induced morphology changes of silver colloids prepared by laser ablation in water. Enhancement of anisotropic shape conversions by chloride ions, J. Photochem. Photobiol. A: Chem. 183 (2006) 297–303.
[21] R. Zamiri, A. Zakaria, M.S. Husin, Z.A. Wahab, F.K. Nazarpour, Formation of silver microbelt structures by laser irradiation of silver nanoparticles in ethanol, Int. J. Nanomed. 6 (2011) 2221–2224.
[22] N.V. Tarasenko, A.V. Butsen, E.A. Nevar, Laser-induced modification of metal nanoparticles formed by laser ablation technique in liquids, Appl. Surf. Sci. 247 (2005) 418–422.
[23] T. Tsuji, M. Tsuji, S. Hashimoto, Utilization of laser ablation in aqueous solution for observation of photoinduced shape conversion of silver nanoparticles in citrate solutions, J. Photochem. Photobiol. A: Chem. 221 (2011) 224–231.
[24] T. Tsuji, Y. Okazaki, M. Tsuji, Photo-induced morphological conversions of silver nanoparticles prepared using laser ablation in water – enhanced morphological conversions using halogen etching, J. Photochem. Photobiol. A: Chem. 194 (2008) 247–253.
[25] S. Sebastian, C. Ajina, C.P.G. Vallabhan, V.P.N. Nampoori, P. Radhakrishnan, M. Kailasnath, Fabrication and photostability of rhodamine-6G gold nanoparticle doped polymer optical fiber, Chin. Phys. Lett. 30 (11) (2013) 118101.
[26] F. Mafune, J.-Y. Kohno, Y. Takeda, T. Kondow, Formation and size control of silver nanoparticles by laser ablation in aqueous solution, J. Phys. Chem. B 104 (2000) 9111–9117.
[27] J. Liao, Y. Zhang, W. Yu, et al., Linear aggregation of gold nanoparticles in ethanol, Colloid Surf. A. 223 (2003) 177–183.
[28] T. Tsuji, D.-H. Thang, Y. Okazaki, M. Nakanishi, Y. Tsuboi, M. Tsuji, Preparation of silver nanoparticles by laser ablation in polyvinylpyrrolidone solutions, Appl. Surf. Sci. 254 (2008) 5224–5230.
[29] T. Tsuji, K. Iryo, Y. Nishimura, M. Tsuji, Preparation of metal colloids by a laser ablation technique in solution: influence of laser wavelength on the ablation efficiency (II), Photochem. Photobiol. A: Chem. 145 (2001) 201–207.